AN INTEGRATED COMPUTATIONAL TOOL

FOR HYPERSONIC FLOW SIMULATION

AFOSR GRANT # F49620-00-1-0219

Klaus A. Hoffmann

Department of Aerospace Engineering

Wichita State University

Wichita, KS 67260-0044

Klaus.Hoffmann@Wichita.edu

REPORT DOCUMENTATION PAGE

AFRL-SR-AR-TR-04-

0232

1. REPORT DATE 18-01-2004	2. REPORT TYPE	3. DATES COVERED (From - To) June 1999 – September 2004

4. TITLE AND SUBTITLE	5a. CONTRACT NUMBER
An Integrated Computational Tool for Hypersonic Flow Simulation	5b. GRANT NUMBER AFOSR Grant # F49620-00-1-0219
	5c. PROGRAM ELEMENT NUMBER

6. AUTHOR(S) Klaus A. Hoffmann	5d. PROJECT NUMBER
	5e. TASK NUMBER
	5f. WORK UNIT NUMBER

7. PERFORMING ORGANIZATION NAME(S) AND ADDRESS(ES) Wichita State University 1845 Fairmount Wichita , KS 67260-0044	8. PERFORMING ORGANIZATION REPORT NUMBER

9. SPONSORING / MONITORING AGENCY NAME(S) AND ADDRESS(ES) AFOSR Dr. John D. Schmisseur 4015 Wilson Blvd. , RM. 713 Arlington , VA 22203-1954	10. SPONSOR/MONITOR'S ACRONYM(S) AFOSR
	11. SPONSOR/MONITOR'S REPORT NUMBER(S)

12. DISTRIBUTION / AVAILABILITY STATEMENT

Approved for public release, distribution unlimited

13. SUPPLEMENTARY NOTES

20040423 071

14. ABSTRACT

The development of a computational tool for the solution of turbulent magnetohydrodynamic (MHD) equations, including turbulence or chemically reacting flows is presented. For the MHD solver, option is provided to solve either the full MHD equations or the low magnetic Reynolds number equations. For turbulence, the Reynolds Averaged approach is considered for its low requirement in terms of computational resources. Six turbulence models, ranging from simple algebraic model to more sophisticated two-equation models are considered to evaluate the eddy viscosity. Since the turbulence models were originally designed for non-magnetic flows, they require some modifications to account for the presence of a magnetic field. The governing equations are numerically solved by a modified Runge-Kutta scheme augmented with a Total Variation Diminishing scheme for accurate shock capturing. The numerical solutions are compared with available experimental data and existing analytical solutions. For the simulation of hypersonic high-temperature effects, two chemical models are utilized, namely a nonequilibrium model and an equilibrium model. A loosely coupled approach is implemented to communicate between the magnetogasdynamic equations and the chemical models. The nonequilibrium model is a one-temperature, five-species, seventeen-reaction model solved by an implicit flux-vector splitting scheme. The effectiveness of the chemical models for hypersonic flow over blunt body is examined in various flow conditions. It is shown that the proposed schemes perform well in a variety of test cases, though some limitations have been identified.

15. SUBJECT TERMS: Magnetohydrodynamics , Hypersonics , Turbulence , Computational Fluid Dynamics

16. SECURITY CLASSIFICATION OF:			17. LIMITATION OF ABSTRACT	18. NUMBER OF PAGES	19a. NAME OF RESPONSIBLE PERSON Klaus A. Hoffmann
a. REPORT	b. ABSTRACT	c. THIS PAGE		263	19b. TELEPHONE NUMBER (include area code) 316-978-6327

Standard Form 298 (Rev. 8-98)
Prescribed by ANSI Std. Z39.18

AN INTEGRATED COMPUTATIONAL TOOL

FOR HYPERSONIC FLOW SIMULATION

AFOSR GRANT # F49620-00-1-0219

Klaus Hoffmann

Department of Aerospace Engineering

Wichita State University

Wichita, KS 67260-0044

Abstract

The development of a computational tool for the solution of turbulent magnetohydrodynamic (MHD) equations, including turbulence or chemically reacting flows is presented. For the MHD solver, option is provided to solve either the full MHD equations or the low magnetic Reynolds number equations. For turbulence, the Reynolds Averaged approach is considered for its low requirement in terms of computational resources. Six turbulence models, ranging from simple algebraic model to more sophisticated two-equation models are considered to evaluate the eddy viscosity. Since the turbulence models were originally designed for non-magnetic flows, they require some modifications to account for the presence of a magnetic field. The governing equations are numerically solved by a modified Runge-Kutta scheme augmented with a Total Variation Diminishing scheme for accurate shock capturing. The numerical solutions are compared with available experimental data and existing analytical solutions. The calibration of the modified turbulence models is performed based on the turbulent MHD Hartmann flow, for which a relaminarization process has been experimentally observed. Original models do not accurately predict the relaminarization process, whereas modified models show good agreement with experiments. Application of the original and modified turbulence models to a supersonic flow over a flat plate leads to a reduction of the skin friction by about 20% to 30% when the fluid has a low conductivity. A complete relaminarization is observed for high conductivity fluids. The heat transfer could also be substantially reduced for the hypersonic flow over a cone, as a result of a relaminarization of the flow.

For the simulation of hypersonic high-temperature effects, two chemical models are utilized, namely a nonequilibrium model and an equilibrium model. A loosely coupled approach is implemented to communicate between the magnetogasdynamic equations and the chemical models. The nonequilibrium model is a one-temperature, five-species, seventeen-reaction model solved by an implicit flux-vector splitting scheme. The chemical equilibrium model computes thermodynamics properties using curve fit procedures. Selected results are provided, which explore the different features of the numerical algorithms. The shock capturing properties are validated for shock-tube simulations using numerical solutions reported in the literature. The computations of superfast flows over corners and in convergent channels demonstrate the performances of the algorithm in multiple dimensions. The effectiveness of the chemical models for hypersonic flow over blunt body is examined in various flow conditions. It is shown that the proposed schemes perform well in a variety of test cases, though some limitations have been identified.

Table of Contents

List of Tables

List of Figures

x

Nomenclature

Roman symbols:

A	Coefficient of damping term in modified Baldwin-Lomax model
B	Magnitude of the magnetic induction field
$\bar{\mathbf{B}} = \begin{bmatrix} B_x \\ B_y \\ B_z \end{bmatrix}$	Magnetic induction field
$\overline{B}_x, \overline{B}_y$	Transformed components of the magnetic field in the computational space
CFL	Courant-Friedrichs-Lewy number
c_p	Specific heat at constant pressure
c_s	Speed of sound or mass fraction of chemical species s
C'_{kN1}	Closure coefficient in modified $k - \epsilon$, Baseline and SST models
C_{Re_T}	Closure coefficient in modified Baldwin-Barth model
$C'_{\epsilon N1}$	Closure coefficient in modified $k - \epsilon$ model
$C'_{\omega N1}$	Closure coefficient in modified $k - \omega$ model
d	Distance to the nearest wall
D_1, D_2	Damping functions
e	Specific internal energy
$e_{e,s}$	Electronic energy mode of chemical species s
$e_{r,s}$	Rotational energy mode of chemical species s
e_t	Total energy
$e_{t,s}$	Translational energy mode of chemical species s
$e_{v,s}$	Vibrational energy mode of chemical species s
$\mathbf{E}$	Flux vector in x-direction (physical space)
E_T	Total turbulent kinetic energy
$\mathbf{E}_v$	Viscous flux vector in x-direction (physical space)
$\bar{\mathbf{E}}$	Electric field vector
$\overline{\mathbf{E}}$	Flux vector in ξ-direction (computational space)
$\overline{\mathbf{E}_v}$	Viscous flux vector in ξ-direction (computational space)
$\mathbf{F}$	Flux vector in y-direction (physical space)
$\mathbf{F}_v$	Viscous flux vector in y-direction (physical space)
F_1	Switching function
$\overline{\mathbf{F}}$	Flux vector in η-direction (computational space)
$\overline{\mathbf{F}_v}$	Viscous flux vector in η-direction (computational space)

g	TVD limiter in ξ-direction
h	TVD limiter in η-direction
$h_{0,s}$	Specific heat of formation of chemical species s
Ha	Hartmann number
$\mathbf{H}$	Source term in physical space
$\mathbf{H}_M$	Intermediate magnetic vector
$\vec{\mathbf{H}}$	Magnetic field
$\overline{\mathbf{H}}$	Source term in computational space
$\overline{\overline{\mathbf{I}}}$	Identity tensor
J	Jacobian of transformation
$\vec{\mathbf{J}}$	Current density vector
k	Thermal conductivity, turbulent kinetic energy
k_t	Turbulent conductivity
K_b	Backward chemical rate constant
K_e	Equilibrium chemical rate constant
K_f	Forward chemical rate constant
l	Characteristic turbulent length scale, mixing length
L	Characteristic length
L_k, L_ϵ	Low Reynolds number terms
m	Interaction number per unit length
M_k	Additional magnetic term in the k-equation
M_t	Turbulent Mach number
M_ϵ	Additional magnetic term in the ϵ-equation
M_ω	Additional magnetic term in the ω-equation
M_∞	Freestream Mach number
N	Interaction parameter
p	Pressure
P_k	Production term
Pr	Prandtl number
Pr_t	Turbulent Prandtl number
$\mathbf{Q}$	Unknown field vector
$\vec{\mathbf{Q}} = \begin{bmatrix} q_x \\ q_y \\ q_z \end{bmatrix}$	Heat flux vector
$\overline{\mathbf{Q}}$	Unknown field vector in computational space
r, r_s	Radius of curvature of the shock wave
R	Thermodynamic gas constant
$\mathfrak{R}$	Universal gas constant, $\mathfrak{R} = 8.314472 J.mol^{-1}K^{-1}$

Re	Reynolds number
Re_m	Magnetic Reynolds number
Re_T	Turbulent Reynolds number
S	Absolute value of vorticity
$\mathbf{S}_{MHD}$	MHD source term in physical space
$\overline{\mathbf{S}}_{MHD}$	MHD source term in computational space
t	Time
T	Temperature
Tl	Turbulent intensity
u_τ	Friction velocity
U	Magnitude of the velocity vector, ξ-component of contravariant velocity in computational space
$\vec{\mathbf{U}} = \begin{bmatrix} u \\ v \\ w \end{bmatrix}$	Velocity vector
V	η-component of contravariant velocity in computational space
V_{a_ξ}	ξ-component of Alfvén wave velocity
V_{f_ξ}	ξ-component of fast magneto-acoustic wave velocity
V_{f_η}	η-component of fast magneto-acoustic wave velocity
V_{s_ξ}	ξ-component of slow magneto-acoustic wave velocity
V_{s_η}	η-component of slow magneto-acoustic wave velocity
V_t	Characteristic turbulent velocity
x	Space coordinate
x_ξ, x_η	Metrics of transformation
$\overline{\mathbf{X}}$	Right eigenvector matrix in ξ-direction, computational space
y	Space coordinate
y_ξ, y_η	Metrics of transformation
y^+	Non-dimensional distance to the wall
$\overline{\mathbf{Y}}$	Right eigenvector matrix in η-direction, computational space

Greek symbols:

α	Intermediate components used in TVD limiter calculation
β	Intermediate components used in TVD limiter calculation
δ	Cutoff parameter in entropy correction function
δ_{ij}	Kronecker delta
δ_0	Boundary layer thickness
Δt	Time step

$\Delta\xi$	Grid spacing in ξ-direction
$\Delta\eta$	Grid spacing in η-direction
ϵ	Dissipation rate of turbulent kinetic energy
γ	Ratio of specific heats
γ_2, γ_3	Damping function in the modified Baldwin-Lomax model
κ	Von Karman constant
λ	Damping coefficients for the modified Baldwin-Lomax model
$\lambda_\xi, \lambda_\eta$	Eigenvalues of the system
μ	Dynamic viscosity
μ_{e0}	Free space magnetic permeability
μ_t	Turbulent dynamic viscosity
μ_{t_i}	Inner layer turbulent viscosity
μ_{t_o}	Outer layer turbulent viscosity
μ_w	Dynamic viscosity at the wall
ν	Kinematic viscosity
ν_e	Magnetic diffusivity
ν_t	Turbulent kinematic viscosity
$\bar{\nu}$	Turbulent variable in Spalart-Allmaras model
ψ	Entropy correction function
$\overline{\Phi}$	Flux limiter vector in ξ-direction
$\overline{\Theta}$	Flux limiter vector in η-direction
ρ	Density
ρ_w	Density at the wall
$\theta_{v,s}$	Characteristic vibrational temperature of chemical species s
σ_e	Electrical conductivity
τ_c	Chemical characteristic time scale
τ_f	Flow characteristic time scale
τ_l	Laminar shear stress
τ_w	Shear stress at the wall
$\overset{=}{\tau}$	Stress tensor
ω	Vorticity, specific turbulent dissipation rate (turbulent frequency)
Ω	Magnitude of vorticity
ξ, η	Generalized coordinates (computational space)
ξ_x, ξ_y	Metrics of transformation
η_x, η_y	Metrics of transformation

Chemical species

A_s	A Generic name of chemical species s
M	Third body in chemical reactions (O_2, N_2, NO, O or N)
N	Nitrogen (atom)
N_2	Dinitrogen (molecule)
NO	Nitric oxide (molecule)
O	Oxygen (atom)
O_2	Dioxygen (molecule)

Subscripts:

c	Chemical quantity
e	Property evaluated at the edge of the boundary layer
ref	Reference quantity for non-dimensionalization or similarity parameter
w	Property evaluated at the wall
∞	Freestream condition

Superscripts:

n	Iteration (time) level
$'$	Perturbation quantity
$*$	Non-dimensional quantity
$-$	Reynolds Averaged quantity, quantity expressed in computational space

Operators:

$\vec{\nabla}$	Del operator
$\cdot$	Dot product
$\times$	Cross product
$\otimes$	Dyadic product

List of Abbreviations

BB ....Baldwin-Barth
BL .... Baldwin-Lomax
BS...Baseline
CCT...Compressibility Correction Terms
CFD.. Computational Fluid Dynamics
CFL .... Courant-Friedrichs and Lewy
CGS .... Centimeter-Gram-Second
DES.. Detached Eddy Simulation
DNS..Direct Numerical Simulation
LES .... Large Eddy Simulation
MFD ....MagnetoFluidDynamics
MGD ....MagnetoGasDynamics
MHD ....MagnetoHydroDynamics
MKS .... Meter-Kilogram-Second
RANS..Reynolds-Averaged Navier-Stokes
RK4 ....Four-stage Runge-Kutta scheme
SA .... Spalart-Allmaras
SGS .... Subgrid Scale
SST.. Shear Stress Transport
TVD .... Total Variation Diminishing

Chapter 1

Introduction

Magnetohydrodynamics (MHD) is a branch of fluid dynamics that studies the interaction of an electrically conducting fluid with an electromagnetic field. It occurs naturally at larger scales in the sun and stars, the earth interior (dynamo effect) and ionosphere. The MHD effect has been investigated for engineering applications, e.g. for propulsion systems or power generators. Magnetohydrodynamics shows a great potential in aerospace engineering because it offers the possibility of controlling the flow around a vehicle or even extracting energy from its surrounding. Faraday was the first scientist who designed an MHD converter in 1860.

1.1 Magnetohydrodynamics

When an electrically conducting fluid moves through a magnetic field, it produces an electric field and subsequently an electric current. The interaction of the induced electric current with the electromagnetic field creates a body force, called the Lorentz force, which acts on the fluid itself. There are two approaches to treat magnetohydrodynamics. The first one is the macroscopic approach where the fluid is treated as a continuum media. It is associated with electrically conducting liquids and relatively dense gases. This is usually referred to as MHD and will be considered in this investigation. The second approach is the microscopic study of the fluid, treated in a statistical model. This approach is known as plasma dynamics.

Mathematically, magnetohydrodynamics is represented by the combination of the Maxwell's equations, governing the electromagnetic field and the Navier-Stokes equations governing the flow field. The corresponding set of equations is known as the MHD equations. These equations must be solved in order to analyze magnetohydrodynamics flows. There have been numerous attempts in solving these equations, starting from analytical or empirical methods. Since the governing equations are non-linear partial differential equations, they can be analytically solved only for simple flows with restrictive assumptions on the flow or the magnetic field. Rossow [1] developed an approximate solution for an incompressible laminar hypersonic flow over a flat plate subject to a uniform magnetic field. He showed that as the magnetic field is increased, the skin friction and heat transfer are reduced. Other investigators have shown the same trend for other types of flows. Lykoudis developed a similarity solution for boundary layer flows over a wedge [2]. Lykoudis [3] developed an analytical solution for the shock standoff distance for hypersonic flows of an electrically conducting fluid around a sphere and a cylinder. By assuming a Newtonian pressure distribution and a constant density past the shock, he was able to integrate the differential equation for an inviscid fluid and obtain a closed form solution.

With the expansion of Computational Fluid Dynamics (CFD), it has become possible to investigate MHD flows under less limiting conditions on the magnetic field or the flow properties. Since the MHD equations are hyperbolic in nature, numerical

schemes based on characteristic formulation have been widely used. High-order Godunov schemes have been used for one-dimensional cases and shock tube problems [4-9]. Riemann solvers associated with Godunov schemes have been proven to be robust and able to accurately capture the shock waves. More recently, modified Runge-Kutta schemes augmented with Total Variation Diminishing (TVD) schemes have been used for one-dimensional and two-dimensional problems [10-14]. The use of the TVD scheme as a post process stage allows good shock waves capturing with no or little spurious oscillation. This method requires the determination of the eigenvalues and eigenvectors of the system of equations. For the ideal one-dimensional case, it results in a seven-wave system, whereas for the ideal two-dimensional case, an eight-wave system is obtained. It has been shown that the determination of the eigenvalues and eigenvectors of the system requires a mathematical modification of the governing equations due to a singularity in the Jacobian matrices [15]. Recently, this scheme has been extended to the case where molecular viscosity and magnetic diffusivity are taken into consideration [16].

One of the challenges towards understanding MHD flows and its application to high-speed vehicles is the difficulty to obtain experimental results for hypersonic flows subject to a magnetic field. Encouraging results have been recently obtained in an experimental simulation of a Mach 6 flow of a weakly ionized gas over a blunt body [17]. A drag reduction was clearly observed. Another experimental study [18] has been conducted to measure the shock standoff distance for a supersonic flow around a blunt body. The experimental results matched the theoretical predictions from Lykoudis. Experimentation of an unseeded air plasma at Mach 30 subject to a transverse magnetic field has been conducted in a combustion driven hypersonic shock tube [19]. The induced electromotive force, and electrical conductivity were determined and a non-linear increase in the electrical conductivity was observed for a magnetic field of 0.65 T.

Majority of supersonic and hypersonic flows are turbulent. Therefore, inclusion of turbulence in the computation of such flowfields is essential. It has been shown that the presence of a magnetic field could decrease the drag and heat transfer for laminar flows. It is thus important to investigate turbulent supersonic flowfields subject to magnetic fields to identify the overall effect of this combination.

1.2. Turbulence and Magnetohydrodynamics

Most of the research combining the effect of turbulence with magnetohydrodynamics has been conducted for flows of liquid metals in simple geometries or in astrophysical applications, where the length scales are very large. Basic observations tend to show that the presence of a magnetic field would inhibit turbulence. Batchelor [20] showed that the equation governing the rate of change of the magnetic field intensity could be written in a similar fashion as the equation of stretching vorticity in homogeneous turbulence. He concluded from this analogy that when steady state is reached, the tension of the lines of force of the magnetic field is sufficiently large to prevent any further stretching by turbulent motion. Ferrero et al. [21] also discussed the inhibition of turbulence by a magnetic field and suggested a criterion on the magnitude of the magnetic field that would tend to inhibit the onset of turbulence.

2

Napolitano [22] developed an expression for the velocity profiles of a turbulent boundary layer of a constant property, electrically conducting fluid (without any applied electric field). He showed that the friction velocity at the wall is decreased by the magnetic field. Two physical explanations are given. First, the turbulent kinetic energy input in the outer layer is reduced due to the presence of a magnetic field (Joule's dissipation). Secondly, this energy, already reduced, has to be dissipated by both viscous and magnetic actions, such that the shear stress at the wall is decreased. These results hold for a small value of the magnetic Reynolds number. The disadvantage of the new expression for the law of the wall is that it is no longer universal since it depends on the Reynolds number. He also used the results of Chandrasekhar [23] to propose some additional assumptions on the energy transfer in turbulence with the presence of a magnetic field. First, the intensity of the turbulent magnetic energy spectrum is at any wave number one order of magnitude smaller than the turbulent kinetic energy. Besides, the probability of exchange between turbulent kinetic energy and magnetic turbulent energy is negligible compared to the transfer of turbulent kinetic energy from one wave number to another. Moreover, the intensity of the kinetic energy is lowered by the presence of a magnetic field.

Lykoudis [24] showed that for large values of the Hartmann number, the magnetic field (which enters the solution through the Hartmann number) has the same effect on the laminar layer as suction. His result was based on the laminar velocity profile in the case of a channel flow.

Turbulence has also been investigated using spectral analysis. The process of cascade of energy from larger to smaller eddies has been generalized to hydromagneto-turbulence by Chandrasekhar [25]. He postulated that (1) there is another type of turbulent energy, namely the energy of turbulent magnetic field, (2) the nonlinear terms in the magnetohydrodynamic equations could result in additional coupling among Fourier components (the nonlinear coupling between the Fourier components of the velocity are responsible for the cascade of energy), (3) the kinetic and magnetic energies can be transformed into other types of energies, and (4) the magnetic energy cannot be transferred between two wave numbers since the Maxwell's equations are linear.

For simple engineering applications, the effect of the magnetic field on turbulence has been integrated into existing turbulence concepts or even turbulence models. Lykoudis [26] generalized the Prandtl mixing length concept to MHD for a fully established turbulent channel flow, in a transverse and uniform magnetic field (electrically insulated channel). He obtained an expression for the turbulent stress in the case of MHD based on the solution of an oscillating infinite plate. Damping functions are added to the algebraic model to take the presence of a magnetic field into account. The $k-\epsilon$ two-equation model has been used in conjunction with MHD flows by several authors. Lee [27] used the $k-\epsilon$ model (with no modification) to study the effect of MHD in a three-dimensional channel flow of liquid metal. Frando [28] used the Navier-Stokes equations with the $k-\epsilon$ model to determine the steady state solution of an MHD turbulent flow in an electromagnetic valve. The breaking and accelerating of the flow was demonstrated. El-Kaddah [29] calculated the recirculating flow in an induction furnace

using the turbulent Navier-Stokes equations augmented with electromagnetic body forces. Again, the $k-\epsilon$ model (with no modification) was used to evaluate the turbulent viscosity. Shimomura [30] derived the exact equations for the turbulent kinetic energy and its dissipation rate based on the TSDIA (Two Scale Direct Interaction Approximation) approach. The resulting equations though exact, are very complex and require several closure coefficients which determination is not clear. However, in some cases, simplifications can be made based on the geometry of the problem. Kitamura [31] used a simplified version of the model derived by Shimomura. Yoshizawa and Hamba [32-34] have incorporated the effect of the magnetic field into turbulence model by considering two additional bulk turbulence quantities. In addition to the kinetic turbulent energy and dissipation rate, the cross helicity and residual helicity are considered as bulk turbulence quantities. Therefore, the resulting turbulence model is a four-equation model.

Kovasznay [35] derived a transport equation for the turbulent kinetic energy, taking both the velocity fluctuations and magnetic field fluctuations into account. This equation was derived by taking the time average of the momentum equation and the Ohm's law. The resulting equation showed that some energy could be produced from the mean electric current, transferred into the fluctuating magnetic field (magnetic turbulence) and dissipated through Joule's heating.

Shimomura [36] derived the LES formulation for MHD turbulent channel flow under uniform magnetic field. The effect of the magnetic field is to add a local damping factor in the Sub Grid Scale (SGS) eddy viscosity. He made the assumption of an incompressible flow of liquid mercury in a uniform magnetic field perpendicular to the insulated walls, at low magnetic Reynolds number. The presence of the magnetic field resulted in a negative contribution to the eddy viscosity. He was able to predict detailed structures of the MHD turbulent channel flow that the $k-\epsilon$ model was unable to resolve and showed the process of anisotropic laminarization of turbulence by the magnetic field. Sukoriansky [37] derived an approximate Sub Grid Scale model for Large Eddy Simulation of homogeneous isotropic two-dimensional turbulent. Conventional eddy viscosities that are purely dissipative fail to represent both transfers from higher to lower scales and from lower to higher scales (reverse cascade). The proposed model is able to produce a negative eddy viscosity which corresponds to the inverse cascade of energy from the unresolved (small scale) to resolved scales (larger scales). The positive eddy viscosity corresponds to dissipation of energy.

In all cases where the effect of the magnetic field was incorporated in the turbulence models, it resulted in the addition of a negative turbulent viscosity. The evidence of such a negative eddy viscosity in real phenomena has been discussed by Starr [38]. The turbulent transport of momentum is an important feature of turbulent flows. If this turbulent transport simulates a molecular viscous effect, then it is said that a turbulent viscosity is present. A positive eddy viscosity results in the dissipation of kinetic energy of the mean flow, the energy being drained into the eddy motion, then into molecular motion and finally appearing as heat. On the other hand, when negative eddy viscosity is present, the mean flow gains energy from eddies. The eddy motion either dies out or is regenerated if heat is supplied. In nature, there are some examples of flows where a

negative eddy viscosity may be encountered. The differential rotation of the photosphere of the sun is such an example. From the hydromagnetic equations, it can be shown that the magnetic forces tend to reduce the motion of solid rotation.

There are two factors that can cause a flow to become two-dimensional [39,40]: the geometry of the flow and the action of a body force that smoothes the velocity fluctuations in a preferred direction. The magnetic friction in MHD flows with low magnetic Reynolds number is an example of such a case.

Narasimha [41] discussed the phenomenon of MHD and relaminarization when the magnetic field is aligned with the flow and normal to it (the flow is assumed incompressible, and at low magnetic Reynolds number). When the magnetic field is aligned with the flow, laminarization is dissipative, the larger eddies being destroyed through electrical resistivity and the smaller one through viscosity. When a strong magnetic field is present, the Hartmann effect becomes important and the laminarization is due to the domination of the magnetic forces over the Reynolds stress gradient across the boundary layer. The critical point at which relaminarization occurs can be expressed as the value taken by the ratio of the Reynolds number and the Hartmann number. When the magnetic field is normal to mean velocity, the effect of $\left(\vec{J} \times \vec{B}\right)$ is to suppress the mean vorticity of the flow normal to $\vec{B}$.

Other investigators have studied the effect of MHD on turbulence. Eckert [42] showed that the application of a magnetic field does not lead exclusively to a suppression of the turbulent perturbations. It can be shown that velocity fluctuations remain and that an anisotropy of the MHD turbulence develops and become two-dimensional. These results are based on turbulence measurements in a sodium channel flow. Moisev [43] addressed the decrease in turbulent viscosity in flows with helical turbulence confirming it by experimental results.

1.3. Turbulence Modeling

There are mainly three approaches for the computation of turbulent flows. The Direct Numerical Simulation (DNS) approach is an "exact method" in the sense that the original governing equations are solved without any modifications, or filtering process. Assuming that the error introduced by the numerical scheme used to solve these equations can be evaluated or controlled, the use of DNS can provide high quality results, equivalent to an experiment. Note that the equations are solved on an extensive number of locations in the flow field, allowing the collection of a large amount of information that would be impossible to obtain from an experiment. For example, it is possible to numerically "probe" the flow very close to a solid surface, whereas it is relatively difficult to do so experimentally. In the case of time accurate solution, DNS also provides results in the entire flow field at a given time level, which is identical for all locations (necessary condition to evaluate the cross correlation terms). This requirement is very difficult to meet in an experiment.

5

In fluid mechanics, flows present a wide range of scales, both in length and in time. The accuracy of a simulation method relies on the ability to resolve all scales of motion. The following observations can be made: (a) the large scales are more energetic and more effective in the transport process of turbulent quantities (energy and moments) and (b) the small scales are assumed to be more universal than the large scales. They are mostly responsible for the energy dissipation.

The second approach for turbulent flow computation is the Large Eddy Simulation or LES [44,45]. Large scales are numerically computed, whereas the small scales are modeled by simple eddy viscosity models, known as Sub Grid Scale models (SGS). Algebraic models are sufficient, because the imperfections of these simple models should not greatly affect the solution.

The two methods described above are very costly in terms of computational time and storage requirement. A more affordable method consists in averaging the Navier-Stokes equations in time (also called Reynolds averaging). When the filter operation is applied to the equations, the Reynolds Averaged Navier-Stokes (RANS) equations are obtained. In this filtering process, additional terms appear, known as the Reynolds stresses. A closure model (or turbulence model) is required to close the system. Tremendous amount of investigation has been conducted in this domain, resulting in many different turbulence models, ranging from simple algebraic models to more sophisticated multi-equation models [46-63]. Unfortunately, none of the proposed models is able to accurately predict turbulent flows for a wide range of applications. The difficulty in developing such models relies in the fact that the closure constants are based on empiricism, and are calibrated to match the experimental data. This makes them non-universal and more likely to provide good results only for the type of applications they were designed for.

The RANS approach is used for simple engineering applications because of its relative low computational cost compared to other existing methods. Since the turbulence models used in RANS are mostly based on empiricism, they have to be tuned for a given application. DNS results are used to improve the turbulence models.

Other hybrid methods have been recently developed to take advantage of existing techniques. The Detached Eddy Simulation (DES) combines the RANS approach in regions of thin boundary layer where no separation occur, because this does not constitute a real challenge for RANS and switches to LES in region of massive separation [64, 65]. This method allows a reduction of the prohibitive cost of LES method and therefore, the solution of a turbulent flow field can be obtained with a reasonable time.

1.4. Chemically reacting flows and Magnetohydrodynamics

With the advent of hypersonic flight in the late 1950s, the aerospace community became interested in the application of the MGD principles for flow control of hypersonic vehicles and propulsion systems [66, 67]. In the first studies, aerospace scientists used analytical and empirical methods to solve the classical MFD problems. Particular attention was devoted to understanding the effect of magnetic fields on the velocity profiles and temperature profiles.

In 1958, Bleviss [68] investigated the magnetic hypersonic Couette flow, which admits an exact solution with few assumptions about the gas and exhibits many important features of boundary-layer flows. He considered variable thermodynamic and transport properties, in particular the electrical conductivity. He investigated two cases, namely heat-insulated wall and constant-temperature wall. For the case of a heat-insulated wall, the magnetic field leads to a decrease in the skin friction and an increase in the total drag[*]. An increase in the heat transfer at the moving wall is observed. For the heat-transfer case, application of magnetic field causes a large increase in the total drag and a moderate increase in the heat transfer. For this case, he observed that at high Mach number regimes (Mach 30), the skin friction decreases monotonically with increasing magnetic field, while at lower Mach number regimes (Mach 20), the skin friction as a function of magnetic field exhibits a hysteresis-like phenomenon. The skin friction decreases slightly as the magnetic field is increased, until a critical value is reached and then drops dramatically to a much lower value. Then, if the magnetic field is decreased, the skin friction increases slowly until a second critical value of the field is reached, and subsequently it increases sharply to a higher value. Bleviss compared the magnetic case and the nonmagnetic case using the ratio of the total drag to the average heat-transfer coefficient. His results showed that for a slender body, this ratio is of the order of unity without magnetic field, and much greater than unity in the presence of magnetic field. In other words, compared on the basis of the same total drag, the heat transfer for the magnetic case is much less than for the nonmagnetic case.

In 1960, Bush [69] solved the two-dimensional steady MGD hypersonic boundary-layer flow over a constant-temperature flat plate. Qualitative comparison of the Couette flow and boundary-layer problem showed some similarities, but some dissimilarities as well. For example, boundary-layer theory predicts that the heat transfer for a given Mach number decreases with increasing magnetic field strength, which is contrary to the phenomenon predicted by Couette-flow theory. The hysteresis effect, present in the Couette flow also occurs in the flat plate boundary-layer flow, but disappears at higher Mach numbers.

A multitude of analyses for a number of geometrical configurations has been conducted. Flows over a wedge have been studied by Chu [70] and Minura [71]. The stagnation-point flow over a flat plate and a blunt body has been the object of most of the

---

[*] The total drag can be divided into aerodynamic drag and magnetic drag. The application of the magnetic field leads to a reduction in the skin friction i.e., the aerodynamic drag, but also to a more significant increase in the magnetic drag.

7

investigations [72-82]. Indeed, in hypersonic flight, the stagnation point is where the highest degree of ionization, hence the most important magnetic interaction can be expected. In 1958, Neuringer and McIlroy [72, 73] theoretically analyzed the MGD effect on the skin friction and heat transfer in the vicinity of the stagnation point of an infinitely long flat plate. Their analysis showed that at the stagnation point, both the skin friction and heat transfer can be reduced significantly by application of a magnetic field perpendicular to the surface. They also observed that the heat transfer decreases less rapidly than the skin friction as the strength of the magnetic field is increased. Bush [77] also considered the stagnation-point flow of an axisymmetric blunt body in hypersonic regime. Results, obtained for a sphere concentric with the detached shock, indicate an increase in the shock standoff distance, decrease in the surface pressure and tangential velocity, with increasing magnetic field.

Among the various magnetic field distributions, the dipole has often been considered. In 1957, Burgers [83] investigated the flow field in the presence of a magnetic dipole. He speculated that the magnetic field strength in the immediate vicinity of the dipole is so strong that it prevents the flow from penetrating a certain region (called "frozen region") around the dipole, and the flow resembles the flow around a rigid body. In 1959, Sakurai [84] discussed the possibility of a frozen region in hypersonic flow of ideal gas with infinite electrical conductivity. His results showed that the frozen region can exist even in hypersonic flows.

All of these analytical, experimental and empirical studies led to preliminary and quantitative conclusions, as presented in a comprehensive literature review on electromagnetic control of heat transfer by Romig [85]. They clearly demonstrated the possibility of magnetic aerodynamic control. However, by the mid 1960s, enthusiasm for application of MGD principles in aerospace engineering waned, due to the lack of efficiency of magnetic systems. Since then, considerable technological progress has taken place in the field of superconducting magnets and in the enhancement of electrical conductivity by artificial ionization. As a result, electromagnetic flow control has been reconsidered for future hypersonic vehicles.

The effect of a magnetic field on the flow field of a Mars return aerobrake was investigated by Palmer [86] using CFD techniques. The solution was obtained for an axisymmetric blunt body in thermal equilibrium and chemical nonequilibrium, subject to both self-generated and externally applied magnetic fields. An explicit time marching, first-order upwind scheme for the convective terms and second-order central difference scheme for the diffusion terms were utilized. A loosely coupled approach was selected to communicate between the Navier-Stokes equations and the magnetic induction equations to avoid the prohibitive time step restriction of the fully coupled system. Investigations verified previous conclusion that a significant increase in shock standoff distance can be achieved with a relatively modest magnetic field strength, which can be provided by either a permanent or solenoid type-magnet. The numerical simulations also showed a reduction in convective heat transfer.

1.5. Objectives

The application of the MHD concept could prove valuable to the design of high-speed vehicles, by introducing a new form of flow control. The most important impact on the design is related to the possibility of drag and heat transfer reduction resulting from the application of a magnetic field. The computations of supersonic or hypersonic magnetohydrodynamic flows require the development of a versatile tool, due to the complexity of such flows. Turbulence and chemistry effects are two essential features that will affect the design process. The objective of this investigation is to utilize an affordable approach to compute turbulent and chemically reacting MHD flows. Among the available techniques to compute turbulent flows, the Reynolds Averaged approach remains more affordable than the Large Eddy Simulation or Direct Numerical Simulation. The inclusion of a magnetic field, and chemistry effects substantially increase the complexity of hypersonic MHD flows, and considerable computer resources are required to compute such flows. Therefore, the Reynolds Averaged approach appears to be the most affordable approach to represent turbulence, while it is associated with magnetohydrodynamics. One of the goals of the current investigation is to modify existing turbulence models that are not designed for MHD flows, and extend their range of application to MHD flows. Six turbulence models are modified and calibrated. The turbulent Hartmann flow serves as a reference during the calibration process. The turbulence models are applied to simple geometry flows to investigate the effect of a magnetic field on supersonic turbulent flows. Attention is focused on the possibility of reducing the turbulent skin friction and heat transfer. Two formulations for the MHD equations are considered. The full MHD equations are solved for high conductivity flows. The low magnetic Reynolds number formulation is a simpler formulation for flows characterized by a low electrical conductivity. The computational cost associated with the MHD formulations and turbulence models is evaluated to determine which one is more likely to be used in an integrated computational tool devoted to engineering MHD applications.

In addition to the effect of turbulence, the high temperature effect is also investigated. Therefore, the second goal of the present research is to develop efficient numerical schemes for computational magnetogasdynamics and simulation of hypersonic chemically reacting flows. Two models are selected, namely, a one-temperature, five-species, seventeen-reaction nonequilibrium model, and an equilibrium model based on curve-fit procedures. The loosely coupled approach used to communicate between the MHD equations and the chemistry equations is documented. Limitations and numerical issues concerning the current thermochemical nonequilibrium model are discussed.

Chapter 2
Governing Equations

In this chapter, the governing equations for MHD flows are reviewed. Two formulations are provided. First, the full MHD equations are described along with the corresponding assumptions. Next, the equations are described under the low magnetic Reynolds number approximation (i.e., for low conductivity fluids), in which case the equations can be simplified. The equations are first provided in their general form, and subsequently written in the coordinate system chosen in this investigation. Next, the parameters used to nondimensionalize the equations are specified. In order to solve the governing equations by the proposed numerical scheme, the equations must be written in a conservative form, leading to a more compact flux vector formulation. Finally, the equations are transformed into the computational space.

2.1. Full MHD Equations

2.1.1 Formulation

The MHD equations are composed of the Maxwell's equations, Ohm's law, continuity, momentum, and energy equations. The Maxwell's equations relate the basic electric and magnetic field quantities, and how they are produced. In the current study, the following assumptions are made:

- (i) The fluids are considered sufficiently dense such that they satisfy the continuum model. They have isotropic properties, and are electrically neutral.

- (ii) All velocities are small compared to that of light, i.e., the equations are considered in their non-relativistic forms.

- (iii) The fluids are considered to be in a chemically frozen state.

- (iv) The electric field is of the order of $\bar{U} \times \bar{B}$. The electric fields are always induced or of the order of the induced field.

- (v) The permeability of the fluids μ_{e0} is such that $\bar{B} = \mu_{e0}\bar{H}$. Furthermore, the permeability is considered to be a scalar quantity, such that $\bar{B}$ and $\bar{H}$ are proportional and interchangeable.

- (vi) The density of electric charges ρ_e is small.

Under these assumptions, the four basic Maxwell's equations are:

Ampere's Law: $$\vec{\nabla} \times \vec{\mathbf{H}} = \vec{\mathbf{J}}$$ (2.1)

Faraday's Law: $$\vec{\nabla} \times \vec{\mathbf{E}} = -\frac{\partial \vec{\mathbf{B}}}{\partial t}$$ (2.2)

Gauss' law for magnetism: $$\vec{\nabla} \cdot \vec{\mathbf{B}} = 0$$ (2.3)

Gauss' law for electricity: $$\vec{\nabla} \cdot \vec{\mathbf{J}} = 0$$ (2.4)

and the Ohm's Law is $$\vec{\mathbf{J}} = \sigma_e \left(\vec{\mathbf{E}} + \vec{\mathbf{U}} \times \vec{\mathbf{B}} \right)$$ (2.5)

The combination of the Maxwell's equations and the Ohm's law results in the magnetic transport equation. The electric field can be eliminated from the equations, leaving the effect of the electromagnetic field being represented only by the magnetic field. The resulting MHD equations are comprised of the continuity, momentum, magnetic transport, and energy equations:

Continuity equation:

$$\frac{\partial \rho}{\partial t} + \vec{\nabla} \cdot \left(\rho \vec{\mathbf{U}} \right) = 0$$ (2.6)

Momentum equation:

$$\frac{\partial \left(\rho \vec{\mathbf{U}} \right)}{\partial t} + \vec{\nabla} \cdot \left[\rho \vec{\mathbf{U}} \otimes \vec{\mathbf{U}} + \left(p + \frac{\left| \vec{\mathbf{B}} \right|^2}{2 \mu_{e0}} \right) \vec{\mathbf{I}} - \frac{\vec{\mathbf{B}} \otimes \vec{\mathbf{B}}}{\mu_{e0}} \right] = \vec{\nabla} \cdot \overline{\overline{\tau}}$$ (2.7)

Magnetic transport equation:

$$\frac{\partial \vec{\mathbf{B}}}{\partial t} - \vec{\nabla} \times \left(\vec{\mathbf{U}} \times \vec{\mathbf{B}} \right) = \frac{1}{\mu_{e0} \sigma_e} \nabla^2 \vec{\mathbf{B}} = v_e \nabla^2 \vec{\mathbf{B}}$$ (2.8)

Energy equation:

$$\frac{\partial}{\partial t} \left(\rho e_t \right) + \vec{\nabla} \cdot \left[\left(\rho e_t + p + \frac{\left| \vec{\mathbf{B}} \right|^2}{2 \mu_{e0}} \right) \vec{\mathbf{U}} - \frac{\vec{\mathbf{B}}}{\mu_{e0}} \left(\vec{\mathbf{U}} \cdot \vec{\mathbf{B}} \right) \right] = \vec{\nabla} \cdot \left(\vec{\mathbf{U}} \cdot \overline{\overline{\tau}} \right) - \vec{\nabla} \cdot \vec{\mathbf{Q}} + \frac{\left| \vec{\mathbf{J}} \right|^2}{\sigma_e}$$ (2.9)

where $$\rho e_t = \rho \frac{\left| \vec{\mathbf{U}} \right|^2}{2} + \frac{p}{\gamma - 1} + \frac{\left| \vec{\mathbf{B}} \right|^2}{2 \mu_{e0}}$$ (2.10)

In these equations, the term $\dfrac{\left| \vec{\mathbf{B}} \right|^2}{2 \mu_{e0}}$ is usually referred to as the magnetic pressure. This is not actually a physical pressure but enters the momentum equation as a body force and can generate mechanical stress.

The existence of cross products in the governing equations suggests that the MHD equations should be solved in a three-dimensional coordinate system. However, due to the complexity of the equations and the computational cost associated with the numerical

solution of these equations, it is more practical to write the equation in what is referred to as an extended two-dimensional form. The three components of the field vectors such as the velocity and magnetic fields are included, such that the cross product $\vec{U} \times \vec{B}$ can still be computed, but only two space coordinates are considered. Therefore, from the four vector equations, eight scalar equations are derived.

2.1.2. Nondimensionalization

The MHD equations are nondimensionalized using the following variables:

$$\left(x^*, y^*\right) = \frac{(x,y)}{L} \quad , \quad t^* = \frac{U_\infty t}{L} \quad , \quad \left(u^*, v^*, w^*\right) = \frac{(u,v,w)}{U_\infty}$$

$$\rho^* = \frac{\rho}{\rho_\infty} \quad , \quad p^* = \frac{p}{\rho_\infty U_\infty^2} \quad , \quad \left(B_x^*, B_y^*, B_z^*\right) = \frac{(B_x, B_y, B_z)}{U_\infty \sqrt{\mu_{e0} \rho_\infty}}$$

$$T^* = \frac{T}{T_\infty} \quad , \quad e_t^* = \frac{e_t}{U_\infty^2} \quad , \quad \overline{\overline{\tau}}^* = \frac{\overline{\overline{\tau}} L}{\mu_\infty U_\infty}$$

$$\mu_{e0}^* = \frac{\mu_{e0}}{\mu_{e0}} = 1 \quad , \quad \sigma_e^* = \frac{\sigma_e}{\sigma_{e\infty}} \quad , \quad \nu_e^* = \frac{\nu_e}{\nu_{e\infty}}$$

$$\mu^* = \frac{\mu}{\mu_\infty}$$

In the following sections, the asterisk superscript designating nondimensional quantities will be dropped for convenience. Therefore, all the equations will be written in nondimensional form, unless specifically stated.

2.1.3. Flux Vector Formulation

The system of eight equations (in non-dimensional form) is written in a flux vector formulation as

$$\frac{\partial \mathbf{Q}}{\partial t} + \frac{\partial \mathbf{E}}{\partial x} + \frac{\partial \mathbf{F}}{\partial y} + \mathbf{H} = \frac{\partial \mathbf{E}_v}{\partial x} + \frac{\partial \mathbf{F}_v}{\partial y} \tag{2.11}$$

where $\mathbf{Q}$ is the unknown vector, $\mathbf{E}$ and $\mathbf{F}$ are the inviscid flux vector, $\mathbf{E}_v$ and $\mathbf{F}_v$ are the viscous flux vectors. The original system of equations has been shown to be difficult to solve due to singularities in the Jacobian matrices associated with the system because of the existence of zero eigenvalues. One solution that has been proposed [15] is to modify the Jacobian matrices, leading to the introduction of an additional term in the MHD equations. Thus, the flux vector $\mathbf{H}$ is added to the left-hand side of the equation as shown in Equation (2.11). Note that the common factor $\left(\dfrac{\partial B_x}{\partial x} + \dfrac{\partial B_y}{\partial y} \right)$ appearing in the additional term is merely the divergence of the magnetic field, which is supposed to be zero. Thus, the additional term is a purely mathematical modification and does not change the physics of the problem. The unknown vector and flux vectors are given in Equations (2.12a) to (2.12g). The eight components of the flux vectors represent the

12

continuity equation, momentum equation (three components), magnetic induction equation (three components), and energy equation.

$$\mathbf{Q} = \begin{bmatrix} \rho & \rho u & \rho v & \rho w & B_x & B_y & B_z & \rho e_t \end{bmatrix}^T \qquad (2.12a)$$

$$\mathbf{E} = \begin{bmatrix} \rho u \\ \rho u^2 + p + \dfrac{-B_x^2 + B_y^2 + B_z^2}{2} \\ \rho uv - B_x B_y \\ \rho uw - B_x B_z \\ 0 \\ uB_y - vB_x \\ uB_z - wB_x \\ \left(\rho e_t + p + \dfrac{B_x^2 + B_y^2 + B_z^2}{2} \right) u \\ - B_x \left(uB_x + vB_y + wB_z \right) \end{bmatrix} \qquad (2.12b)$$

$$\mathbf{F} = \begin{bmatrix} \rho v \\ \rho vu - B_y B_x \\ \rho v^2 + p + \dfrac{B_x^2 - B_y^2 + B_z^2}{2} \\ \rho vw - B_y B_z \\ vB_x - uB_y \\ 0 \\ vB_z - wB_y \\ \left(\rho e_t + p + \dfrac{B_x^2 + B_y^2 + B_z^2}{2} \right) v \\ - B_y \left(uB_x + vB_y + wB_z \right) \end{bmatrix} \qquad (2.12c)$$

$$\mathbf{H} = \mathbf{H}_M \left(\frac{\partial B_x}{\partial x} + \frac{\partial B_y}{\partial y} \right) \qquad (2.12d)$$

13

$$\mathbf{H}_M = \begin{bmatrix} 0 \\ B_x \\ B_y \\ B_z \\ u \\ v \\ w \\ uB_x + vB_y + wB_z \end{bmatrix} \qquad (2.12e)$$

$$\mathbf{E}_v = \begin{bmatrix} 0 \\ \tau_{xx} \\ \tau_{xy} \\ \tau_{xz} \\ \dfrac{1}{Re_{m\infty}\sigma_e}\dfrac{\partial B_x}{\partial x} \\ \dfrac{1}{Re_{m\infty}\sigma_e}\dfrac{\partial B_y}{\partial x} \\ \dfrac{1}{Re_{m\infty}\sigma_e}\dfrac{\partial B_z}{\partial x} \\ u\tau_{xx} + v\tau_{xy} + w\tau_{xz} - q_x \end{bmatrix} \qquad (2.12f)$$

$$\mathbf{F}_v = \begin{bmatrix} 0 \\ \tau_{yx} \\ \tau_{yy} \\ \tau_{yz} \\ \dfrac{1}{Re_{m\infty}\sigma_e}\dfrac{\partial B_x}{\partial y} \\ \dfrac{1}{Re_{m\infty}\sigma_e}\dfrac{\partial B_y}{\partial y} \\ \dfrac{1}{Re_{m\infty}\sigma_e}\dfrac{\partial B_z}{\partial y} \\ u\tau_{yx} + v\tau_{yy} + w\tau_{yz} - q_y \end{bmatrix} \qquad (2.12g)$$

where
$$\rho e_t = \frac{1}{2}\rho\left(u^2 + v^2 + w^2\right) + \frac{p}{\gamma - 1} + \frac{B_x^2 + B_y^2 + B_z^2}{2} \qquad (2.13)$$

For a Newtonian fluid:
$$\tau_{ij} = \frac{\mu}{Re_\infty}\left(\frac{\partial u_i}{\partial x_j} + \frac{\partial u_j}{\partial x_i} - \frac{2}{3}\frac{\partial u_k}{\partial x_k}\delta_{ij}\right) \qquad (2.14)$$

and for a perfect gas
$$q_i = -\frac{\mu}{Re_\infty Pr(\gamma - 1)M_\infty^2}\frac{\partial T}{\partial x_i} \qquad (2.15)$$

The nondimensional parameters appearing in the equations are the Reynolds number $Re_\infty = \dfrac{\rho_\infty U_\infty L}{\mu_\infty}$, the Prandtl number $Pr = \dfrac{\mu_\infty c_p}{k}$, the magnetic Reynolds number $Re_{m\infty} = \sigma_{e\infty} \mu_{e0} U_\infty L$ and the free stream Mach number $M_\infty = \dfrac{U_\infty}{\sqrt{\gamma\, p_\infty / \rho_\infty}}$. The magnetic Reynolds number represents the ratio of the magnetic convection to the magnetic diffusion. It can be shown that for small values of the magnetic Reynolds number, the induced magnetic field is small compared to the applied magnetic field.

2.1.4. Generalized Coordinates

The governing equations are partial differential equations and are solved using finite difference approximations for the derivatives. This technique requires the solution of these equations at discrete points within the domain of application. These points must be uniformly spaced within a rectangular domain to yield simple formulation and simplify the application of the boundary conditions. However, most of the physical domains of interest are non rectangular. Therefore, the physical domain, in which the grid points are distributed non-uniformly, is transformed into a rectangular computational domain of constant step sizes.

The transformation between the physical and computational domain is achieved by a set of coefficients of transformation, called the metrics and Jacobian of transformation. If (x, y) is the coordinate system in the physical domain and (ξ, η) is the coordinate system in the computational domain, then the following coefficients are defined:

$$\xi_x = \frac{\partial \xi}{\partial x} \quad , \quad \eta_x = \frac{\partial \eta}{\partial x} \quad , \quad \xi_y = \frac{\partial \xi}{\partial y} \quad , \quad \eta_y = \frac{\partial \eta}{\partial y}$$

$$x_\xi = \frac{\partial x}{\partial \xi} \quad , \quad x_\eta = \frac{\partial x}{\partial \eta} \quad , \quad y_\xi = \frac{\partial y}{\partial \xi} \quad , \quad y_\eta = \frac{\partial y}{\partial \eta}$$

The terms ξ_x, ξ_y, η_x, and η_y are known as the metrics of transformation. Since ξ and η are both functions of x and y, we can write from the chain rule

$$\begin{bmatrix} d\xi \\ d\eta \end{bmatrix} = \begin{bmatrix} \xi_x & \xi_y \\ \eta_x & \eta_y \end{bmatrix} \begin{bmatrix} dx \\ dy \end{bmatrix} \tag{2.16}$$

or equivalently

$$\begin{bmatrix} dx \\ dy \end{bmatrix} = \begin{bmatrix} x_\xi & x_\eta \\ y_\xi & y_\eta \end{bmatrix} \begin{bmatrix} d\xi \\ d\eta \end{bmatrix} \tag{2.17}$$

Comparing Equations (2.16) and (2.17) leads to

$$\begin{bmatrix} \xi_x & \xi_y \\ \eta_x & \eta_y \end{bmatrix} = \begin{bmatrix} x_\xi & x_\eta \\ y_\xi & y_\eta \end{bmatrix}^{-1} \tag{2.18}$$

15

and thus
$$\xi_x = Jy_\eta$$
$$\xi_y = -Jx_\eta$$
$$\eta_x = -Jy_\xi$$ (2.19)
$$\eta_y = Jx_\xi$$

where
$$J = \frac{1}{x_\xi y_\eta - y_\xi x_\eta}$$ (2.20)

J is defined as the Jacobian of the transformation. It can be interpreted as the ratio of the areas of the cells in the physical space to that of the computational space. Since the metrics and Jacobian of transformation will be used in the finite difference approximations, their computation is recommended to be as accurate as possible and that no discontinuities be introduced in their distribution (i.e. the grid points distribution should be smooth). Typically, the metrics within the domain are calculated with second order central finite difference approximations, unless the geometry allows their analytical computation. Any spatial derivative in the physical domain can be transformed into the computational domain using the following relations:

$$\frac{\partial}{\partial x} = \xi_x \frac{\partial}{\partial \xi} + \eta_x \frac{\partial}{\partial \eta}$$ (2.21)

$$\frac{\partial}{\partial y} = \xi_y \frac{\partial}{\partial \xi} + \eta_y \frac{\partial}{\partial \eta}$$ (2.22)

Now, the governing MHD equation given by (2.11), which is written in the physical space (x, y), is transformed into the computational space (ξ, η) and expressed as follows

$$\frac{\partial \overline{Q}}{\partial t} + \frac{\partial \overline{E}}{\partial \xi} + \frac{\partial \overline{F}}{\partial \eta} + \overline{H} = \frac{\partial \overline{E}_v}{\partial \xi} + \frac{\partial \overline{F}_v}{\partial \eta}$$ (2.23)

where
$$\overline{Q} = \frac{Q}{J}$$ (2.24a)

$$\overline{E} = \frac{1}{J}(\xi_x E + \xi_y F)$$ (2.24b)

$$\overline{F} = \frac{1}{J}(\eta_x E + \eta_y F)$$ (2.24c)

$$\overline{H} = H_M \left(\frac{\partial \overline{B}_x}{\partial \xi} + \frac{\partial \overline{B}_y}{\partial \eta} \right)$$ (2.24d)

$$\overline{B}_x = \frac{1}{J}(\xi_x B_x + \xi_y B_y)$$ (2.24e)

$$\overline{B}_y = \frac{1}{J}(\eta_x B_x + \eta_y B_y)$$ (2.24f)

$$\overline{E}_v = \frac{1}{J}(\xi_x E_v + \xi_y F_v)$$ (2.24g)

$$\overline{F}_v = \frac{1}{J}(\eta_x E_v + \eta_y F_v)$$ (2.24h)

16

The computation of $\overline{E}$ and $\overline{F}$ is achieved directly from Equations (2.24b) and (2.24c). The computation of $\overline{E}_v$ and $\overline{F}_v$ requires more attention. In fact, E_v and F_v include the spatial derivatives of the velocity and magnetic field components, which must be transformed into the computational space. The resulting expressions for $\overline{E}_v$ and $\overline{F}_v$ in the computational space are provided in Appendix A.

2.1.5. Boundary Conditions

For the applications considered in this investigation, there are three types of boundary conditions, namely inflow, outflow and solid surface. The specification of the boundary conditions depends on the application considered and the type of magnetic field applied. The various possibilities for the specification of the boundary conditions are summarized below.

- Inflow:
    - Freestream conditions for density, velocity, pressure, temperature
    - Zero magnetic field or applied magnetic field for uniform distribution

- Outflow:
    - Zero-order extrapolation for all primitive variables

- Solid surface:
    - No slip condition
    - Adiabatic wall or constant temperature wall
    - Applied (electrically insulated wall) or extrapolated (perfectly conducting wall) magnetic field

2.2. Low Magnetic Reynolds Number Approximation

2.2.1. Formulation

The numerical simulation of MHD flows typically requires the solution of a system of eight equations: continuity, momentum (three components), energy, and magnetic field induction (three components). For magnetohydrodynamic flows that are characterized by a low electrical conductivity (Appendix B provides typical electrical conductivities of some fluids), the governing equations can be simplified. The validity of the simplification is monitored by a non-dimensional number known as the magnetic Reynolds number. It is defined as $Re_{m\infty} = \sigma_{e\infty} \mu_{e0} U_\infty L$, where $\sigma_{e\infty}$ is the electrical conductivity of the fluid, μ_{e0} is the magnetic permeability, U_∞ and L are respectively the reference velocity and length scale. $Re_{m\infty}$ represents the ratio of the magnetic convection to the magnetic diffusion. It can be shown that for small values of the magnetic Reynolds number ($Re_{m\infty} \ll 1$), the induced magnetic field is negligible compared to the applied magnetic field. Therefore, when this assumption is valid, the magnetic induction equations do not need to be solved. This is especially appealing since the method applied to solve these equations is source of numerical difficulties. When the

17

full system of MHD equations is solved, it has been experienced to be very difficult for the magnetic field to remain divergence-free at all time levels. Numerical techniques have been proposed [15] to alleviate this problem, but generally result in more complex equations or additional steps in the numerical procedure. The other source of difficulties is that the MHD equations become stiffer as the magnetic Reynolds number decreases. In the low magnetic Reynolds number approach, the magnetic field automatically satisfies the zero-divergence constrain, provided its initial distribution is divergence free (since it is given and remains constant through the computation). The current density is determined directly from the Ohm's law and the MHD effect is modeled by the introduction of source terms in the Navier-Stokes equations. Under the assumption of small magnetic Reynolds number, the governing equations are:

Continuity equation:

$$\frac{\partial \rho}{\partial t} + \vec{\nabla} \cdot \left(\rho \vec{U} \right) = 0 \tag{2.25}$$

Momentum equation:

$$\frac{\partial \left(\rho \vec{U} \right)}{\partial t} + \vec{\nabla} \cdot \left[\rho \vec{U} \otimes \vec{U} + p \bar{\bar{\mathbf{I}}} \right] = \vec{\nabla} \cdot \bar{\bar{\tau}} + \vec{J} \times \vec{B} \tag{2.26}$$

Energy equation:

$$\frac{\partial}{\partial t} \left(\rho e_t \right) + \vec{\nabla} \cdot \left[\left(\rho e_t + p \right) \vec{U} \right] = \vec{\nabla} \cdot \left(\vec{U} \cdot \bar{\bar{\tau}} \right) - \vec{\nabla} \cdot \vec{Q} + \vec{E} \cdot \vec{J} \tag{2.27}$$

The current density can be evaluated from the Ohm's law

$$\vec{J} = \sigma_e \left(\vec{E} + \vec{U} \times \vec{B} \right) \tag{2.28}$$

In contrast with the full MHD equations, the electric field appears explicitly in the formulation associated with the low magnetic Reynolds number approximation. This offers additional control on the flow [87-91].

2.2.2. Nondimensionalization

The MHD equations are nondimensionalized using the same quantities as described in Section 2.1.2. The electric field, which is the only additional variable, is nondimensionalized as follows

$$\left(E_x^*, E_y^*, E_z^* \right) = \frac{\left(E_x, E_y, E_z \right)}{U_\infty^2 \sqrt{\mu_{e0} \rho_\infty}}$$

Hence, the system of equations (in non-dimensional form) becomes

Continuity equation:

$$\frac{\partial \rho}{\partial t} + \vec{\nabla} \cdot \left(\rho \vec{U} \right) = 0 \tag{2.29}$$

Momentum equation:

$$\frac{\partial \left(\rho \vec{U} \right)}{\partial t} + \vec{\nabla} \cdot \left[\rho \vec{U} \otimes \vec{U} + p \bar{\bar{\mathbf{I}}} \right] = \frac{1}{Re_\infty} \vec{\nabla} \cdot \bar{\bar{\tau}} + Re_{m\infty} \vec{J} \times \vec{B} \tag{2.30}$$

18

\Energy equation:

$$\frac{\partial}{\partial t}(\rho e_t) + \vec{\nabla} \cdot \left[(\rho e_t + p)\vec{U}\right] = \frac{1}{Re_\infty}\vec{\nabla} \cdot \left(\vec{U} \cdot \overline{\overline{\tau}}\right) - \frac{1}{(\gamma-1)Pr\,M^2Re_\infty}\vec{\nabla} \cdot \vec{Q} + Re_{m\infty}\vec{E} \cdot \vec{J} \quad (2.31)$$

2.2.3. Flux Vector Formulation

The equations are solved in the same fashion as the full MHD equations, by using an extended two-dimensional approach. Although three spatial components of the velocity, magnetic and electric field are considered for the evaluation of the magnetic source terms (the Lorentz force requires the computation of several cross products), all flow variables are assumed to vary in only two dimensions. Therefore, only two spatial derivatives are taken into account. The system of equations is written in a flux vector formulation as

$$\frac{\partial \mathbf{Q}}{\partial t} + \frac{\partial \mathbf{E}}{\partial x} + \frac{\partial \mathbf{F}}{\partial y} = \frac{\partial \mathbf{E}_v}{\partial x} + \frac{\partial \mathbf{F}_v}{\partial y} + \mathbf{S}_{MHD} \quad (2.32)$$

where $\mathbf{Q}$ is the unknown vector, $\mathbf{E}$ and $\mathbf{F}$ are the inviscid flux vector, $\mathbf{E}_v$ and $\mathbf{F}_v$ are the viscous flux vectors. The additional source term is represented by $\mathbf{S}_{MHD}$. The unknown and flux vectors are given by Equations (2.33a) through (2.33f). The unknown quantities than need to be computed are the density, momentum components and total energy. The magnetic and electric fields are considered as given quantities and remain constant throughout the computations.

$$\mathbf{Q} = \begin{bmatrix} \rho & \rho u & \rho v & \rho w & \rho e_t \end{bmatrix}^T \quad (2.33a)$$

$$\mathbf{E} = \begin{bmatrix} \rho u \\ \rho u^2 + p \\ \rho u v \\ \rho u w \\ (\rho e_t + p)u \end{bmatrix} \quad (2.33b)$$

$$\mathbf{F} = \begin{bmatrix} \rho v \\ \rho v u \\ \rho v^2 + p \\ \rho v w \\ (\rho e_t + p)v \end{bmatrix} \quad (2.33c)$$

19

$$\mathbf{E}_v = \begin{bmatrix} 0 \\ \tau_{xx} \\ \tau_{xy} \\ \tau_{xz} \\ u\tau_{xx} + v\tau_{xy} + w\tau_{xz} - q_x \end{bmatrix} \qquad (2.33d)$$

$$\mathbf{F}_v = \begin{bmatrix} 0 \\ \tau_{yx} \\ \tau_{yy} \\ \tau_{yz} \\ u\tau_{yx} + v\tau_{yy} + w\tau_{yz} - q_y \end{bmatrix} \qquad (2.33e)$$

$$\mathbf{S}_{MHD} = Re_{m\infty} \begin{bmatrix} 0 \\ B_z\left(E_y + wB_x - uB_z\right) - B_y\left(E_z + uB_y - vB_x\right) \\ B_x\left(E_z + uB_y - vB_x\right) - B_z\left(E_x + vB_z - wB_y\right) \\ B_y\left(E_x + vB_z - wB_y\right) - B_x\left(E_y + wB_x - uB_z\right) \\ E_x\left(E_x + vB_z - wB_y\right) + E_y\left(E_y + wB_x - uB_z\right) + E_z\left(E_z + uB_y - vB_x\right) \end{bmatrix} \qquad (2.33f)$$

where
$$\rho e_t = \frac{1}{2}\rho\left(u^2 + v^2 + w^2\right) + \frac{p}{\gamma - 1} \qquad (2.34)$$

All other quantities have the same definitions as in Section 2.1.3.

2.2.4. Generalized Coordinates

The governing MHD equation given by (2.32), which is written in the physical space (x, y), is transformed into a computational space (ξ, η) and expressed as follows

$$\frac{\partial \overline{\mathbf{Q}}}{\partial t} + \frac{\partial \overline{\mathbf{E}}}{\partial \xi} + \frac{\partial \overline{\mathbf{F}}}{\partial \eta} = \frac{\partial \overline{\mathbf{E}}_v}{\partial \xi} + \frac{\partial \overline{\mathbf{F}}_v}{\partial \eta} + \overline{\mathbf{S}}_{MHD} \qquad (2.35)$$

where
$$\overline{\mathbf{Q}} = \frac{\mathbf{Q}}{J} \qquad (2.36a)$$

$$\overline{\mathbf{E}} = \frac{1}{J}\left(\xi_x \mathbf{E} + \xi_y \mathbf{F}\right) \qquad (2.36b)$$

$$\overline{\mathbf{F}} = \frac{1}{J}\left(\eta_x \mathbf{E} + \eta_y \mathbf{F}\right) \qquad (2.36c)$$

$$\overline{\mathbf{E}}_v = \frac{1}{J}\left(\xi_x \mathbf{E}_v + \xi_y \mathbf{F}_v\right) \qquad (2.36d)$$

$$\overline{\mathbf{F}}_v = \frac{1}{J}\left(\eta_x \mathbf{E}_v + \eta_y \mathbf{F}_v\right) \qquad (2.36e)$$

$$\overline{\mathbf{S}}_{MHD} = \frac{1}{J}\mathbf{S}_{MHD} \qquad (2.36f)$$

20

2.2.5. Boundary Conditions

The same types of boundary conditions as described in Section 2.1.5 are applied for the low magnetic Reynolds number approximation, except for the magnetic field. Since the magnetic field is a given quantity, it does not need to be updated at the boundaries.

Chapter 3
Numerical Scheme

In this section, the numerical scheme used to solve the governing equations is described. All the equations given in this section are written in the computational space. The partial derivatives appearing in the equations are approximated by finite difference formulations. The equations are solved in a discrete manner at each grid point location. Each node is referred to by the indices (i, j), which are the node locations in the computational coordinate system (ξ, η). The equations are solved by a modified fourth-order Runge-Kutta scheme augmented with a second-order TVD scheme. This numerical scheme has been employed for a wide variety of supersonic and hypersonic applications, and has shown the ability to accurately capture shock waves with no or little oscillations [10-14]. The scheme consists of four stages followed by a post-process stage where the TVD scheme is applied to stabilize the solution.

3.1. Four Stage Runge-Kutta Scheme

3.1.1. Full MHD Equations

The governing equations are solved by a four-stage Runge-Kutta scheme. It has been selected because of its high order of accuracy (fourth-order) and its low storage requirement, since only two time levels need to be stored. First, the numerical scheme is applied to the full MHD equation, given by Equation (2.11). The resulting four-stage Runge-Kutta scheme is

$$\overline{\mathbf{Q}}_{i,j}^{(0)} = \overline{\mathbf{Q}}_{i,j}^{n} \tag{3.1a}$$

$$\overline{\mathbf{Q}}_{i,j}^{(1)} = \overline{\mathbf{Q}}_{i,j}^{n} - \frac{\Delta t}{4} \left(\frac{\partial \overline{\mathbf{E}}}{\partial \xi} + \frac{\partial \overline{\mathbf{F}}}{\partial \eta} + \overline{\mathbf{H}} - \frac{\partial \overline{\mathbf{E}}_{v}}{\partial \xi} - \frac{\partial \overline{\mathbf{F}}_{v}}{\partial \eta} \right)_{i,j}^{(0)} \tag{3.1b}$$

$$\overline{\mathbf{Q}}_{i,j}^{(2)} = \overline{\mathbf{Q}}_{i,j}^{n} - \frac{\Delta t}{3} \left(\frac{\partial \overline{\mathbf{E}}}{\partial \xi} + \frac{\partial \overline{\mathbf{F}}}{\partial \eta} + \overline{\mathbf{H}} - \frac{\partial \overline{\mathbf{E}}_{v}}{\partial \xi} - \frac{\partial \overline{\mathbf{F}}_{v}}{\partial \eta} \right)_{i,j}^{(1)} \tag{3.1c}$$

$$\overline{\mathbf{Q}}_{i,j}^{(3)} = \overline{\mathbf{Q}}_{i,j}^{n} - \frac{\Delta t}{2} \left(\frac{\partial \overline{\mathbf{E}}}{\partial \xi} + \frac{\partial \overline{\mathbf{F}}}{\partial \eta} + \overline{\mathbf{H}} - \frac{\partial \overline{\mathbf{E}}_{v}}{\partial \xi} - \frac{\partial \overline{\mathbf{F}}_{v}}{\partial \eta} \right)_{i,j}^{(2)} \tag{3.1d}$$

$$\overline{\mathbf{Q}}_{i,j}^{(4)} = \overline{\mathbf{Q}}_{i,j}^{n} - \Delta t \left(\frac{\partial \overline{\mathbf{E}}}{\partial \xi} + \frac{\partial \overline{\mathbf{F}}}{\partial \eta} + \overline{\mathbf{H}} - \frac{\partial \overline{\mathbf{E}}_{v}}{\partial \xi} - \frac{\partial \overline{\mathbf{F}}_{v}}{\partial \eta} \right)_{i,j}^{(3)} \tag{3.1e}$$

The spatial derivatives are approximated by second-order central differences, such that

$$\left(\frac{\partial \overline{\mathbf{E}}}{\partial \xi} \right)_{i,j} = \frac{\overline{\mathbf{E}}_{i+1,j} - \overline{\mathbf{E}}_{i-1,j}}{2\Delta \xi} \tag{3.2a}$$

22

$$\left(\frac{\partial \overline{F}}{\partial \eta} \right)_{i,j} = \frac{\overline{F}_{i,j+1} - \overline{F}_{i,j-1}}{2\Delta\eta} \tag{3.2b}$$

$$\overline{H}_{i,j} = H_{M_{i,j}} \left(\frac{\overline{B}_{xi+1,j} - \overline{B}_{xi-1,j}}{2\Delta\xi} + \frac{\overline{B}_{yi,j+1} - \overline{B}_{yi,j-1}}{2\Delta\eta} \right) \tag{3.2c}$$

3.1.2. Low Magnetic Reynolds Number Formulation

Under, the low magnetic Reynolds number approximation, the system of MHD equations given by Equation (2.32) is solved with the same numerical scheme as the full MHD equations and is given by

$$\overline{Q}_{i,j}^{(0)} = \overline{Q}_{i,j}^{n} \tag{3.3a}$$

$$\overline{Q}_{i,j}^{(1)} = \overline{Q}_{i,j}^{n} - \frac{\Delta t}{4} \left(\frac{\partial \overline{E}}{\partial \xi} + \frac{\partial \overline{F}}{\partial \eta} - \frac{\partial \overline{E}_v}{\partial \xi} - \frac{\partial \overline{F}_v}{\partial \eta} - \overline{S}_{MHD} \right)_{i,j}^{(0)} \tag{3.3b}$$

$$\overline{Q}_{i,j}^{(2)} = \overline{Q}_{i,j}^{n} - \frac{\Delta t}{3} \left(\frac{\partial \overline{E}}{\partial \xi} + \frac{\partial \overline{F}}{\partial \eta} - \frac{\partial \overline{E}_v}{\partial \xi} - \frac{\partial \overline{F}_v}{\partial \eta} - \overline{S}_{MHD} \right)_{i,j}^{(1)} \tag{3.3c}$$

$$\overline{Q}_{i,j}^{(3)} = \overline{Q}_{i,j}^{n} - \frac{\Delta t}{2} \left(\frac{\partial \overline{E}}{\partial \xi} + \frac{\partial \overline{F}}{\partial \eta} - \frac{\partial \overline{E}_v}{\partial \xi} - \frac{\partial \overline{F}_v}{\partial \eta} - \overline{S}_{MHD} \right)_{i,j}^{(2)} \tag{3.3d}$$

$$\overline{Q}_{i,j}^{(4)} = \overline{Q}_{i,j}^{n} - \Delta t \left(\frac{\partial \overline{E}}{\partial \xi} + \frac{\partial \overline{F}}{\partial \eta} - \frac{\partial \overline{E}_v}{\partial \xi} - \frac{\partial \overline{F}_v}{\partial \eta} - \overline{S}_{MHD} \right)_{i,j}^{(3)} \tag{3.3e}$$

The similarities between the full and low magnetic Reynolds number MHD equations translate into the application of the numerical scheme. In fact, since the equations are written in a flux vector formulation, the only difference is that the term $\overline{H}$ appearing in the full MHD equations is replaced by $-\overline{S}_{MHD}$ in the low magnetic Reynolds number MHD equations. However, the definition of the flux vector is the key to the different formulations. In the full MHD equations, the magnetic terms are included in all flux vectors, the magnetic field being an unknown, resulting in a system of eight equations. In the low magnetic Reynolds number approach, the magnetic and electric field are treated as given or input quantities and are included in the term $\overline{S}_{MHD}$ only. The number of equations is therefore reduced to five.

3.2. Post-Process Stage

Some instability may arise due to the high order of accuracy associated with the numerical scheme. To alleviate this problem, a post-process stage is usually required to stabilize the solution. Such methods include the addition of artificial damping terms. Although computationally efficient and easy to implement, this technique requires a fine tuning of the amount of damping required for each possible configuration. Another method that has been successfully employed is the application of a Total Variation

23

Diminishing (TVD) scheme as a post-process stage. This method has the advantage of automatically adjusting the amount of damping (by switching from second to first order in accuracy) where needed. However, it requires the computation of the eigenvalues and eigenvectors associated with the governing equations. It is also expensive it terms of computational resources. The second order symmetric TVD scheme with Davis-Yee symmetric limiter has been chosen due to its successful application to MHD problems by previous investigators. It is particularly appealing for high-speed problems involving strong discontinuities such as shock waves.

The same post-process stage is applied for the full and low magnetic Reynolds number MHD equations. However, the eigenvalues and eigenvectors differ from one formulation to another.

3.2.1. Second Order Symmetric TVD Scheme

The post-process stage consists of correcting the latest computed unknown vector and is given by

$$
\overline{Q}_{i,j}^{n+1} = \overline{Q}_{i,j}^{n+1} - \frac{1}{2}\frac{\Delta t}{\Delta \xi}\left(\overline{X}_{i+1/2,j}^{n}\overline{\Phi}_{i+1/2,j}^{n} - \overline{X}_{i-1/2,j}^{n}\overline{\Phi}_{i-1/2,j}^{n}\right)
$$

$$
- \frac{1}{2}\frac{\Delta t}{\Delta \eta}\left(\overline{Y}_{i,j+1/2}^{n}\overline{\Theta}_{i,j+1/2}^{n} - \overline{Y}_{i,j-1/2}^{n}\overline{\Theta}_{i,j-1/2}^{n}\right)
$$

(3.4)

The eigenvector matrices $\overline{X}$ and $\overline{Y}$ are provided in Reference 14. A wide variety of TVD limiters associated with the TVD schemes has been investigated by Harada et al. [14]. In this research activity, the Davis-Yee symmetric TVD scheme is adopted, and described below.

3.2.2. Davis-Yee Symmetric TVD Limiters

The flux limiter functions are given as

$$
\Phi_{i+1/2,j} = -\left[\frac{\Delta t}{\Delta \xi}\left(\lambda_{\xi\ i+1/2,j}\right)^2 g_{i+1/2,j} + \psi\left(\lambda_{\xi\ i+1/2,j}\right)\left(\alpha_{i+1/2,j} - g_{i+1/2,j}\right)\right]
$$

(3.5a)

$$
\Phi_{i-1/2,j} = -\left[\frac{\Delta t}{\Delta \xi}\left(\lambda_{\xi\ i-1/2,j}\right)^2 g_{i-1/2,j} + \psi\left(\lambda_{\xi\ i-1/2,j}\right)\left(\alpha_{i-1/2,j} - g_{i-1/2,j}\right)\right]
$$

(3.5b)

$$
\Theta_{i,j+1/2} = -\left[\frac{\Delta t}{\Delta \eta}\left(\lambda_{\eta\ i,j+1/2}\right)^2 h_{i,j+1/2} + \psi\left(\lambda_{\eta\ i,j+1/2}\right)\left(\beta_{i,j+1/2} - h_{i,j+1/2}\right)\right]
$$

(3.5c)

$$
\Theta_{i,j-1/2} = -\left[\frac{\Delta t}{\Delta \eta}\left(\lambda_{\eta\ i,j-1/2}\right)^2 h_{i,j-1/2} + \psi\left(\lambda_{\eta\ i,j-1/2}\right)\left(\beta_{i,j-1/2} - h_{i,j-1/2}\right)\right]
$$

(3.5d)

Details of the eigenvalues λ_ξ and λ_η can be found in Section 3.3. Based on previous investigations, the following limiters are selected.

24

$$g_{i+1/2,j} = \min\mod\left[2\alpha_{i-1/2,j}, 2\alpha_{i+1/2,j}, 2\alpha_{i+3/2,j}, \frac{1}{2}\left(\alpha_{i-1/2,j} + \alpha_{i+3/2,j}\right)\right] \qquad (3.6a)$$

$$h_{i,j+1/2} = \min\mod\left[2\beta_{i,j-1/2}, 2\beta_{i,j+1/2}, 2\beta_{i,j+3/2}, \frac{1}{2}\left(\beta_{i,j-1/2} + \beta_{i,j+3/2}\right)\right] \qquad (3.6b)$$

The components α and β are defined in the generalized coordinate system as

$$\overline{\alpha}_{i+1/2,j} = 2\left(\overline{\mathbf{X}}^{-1}\right)_{i+1/2,j}\left(\mathbf{Q}_{i+1,j} - \mathbf{Q}_{i,j}\right)/\left(J_{i+1,j} + J_{i,j}\right) \qquad (3.7a)$$

$$\overline{\beta}_{i,j+1/2} = 2\left(\overline{\mathbf{Y}}^{-1}\right)_{i,j+1/2}\left(\mathbf{Q}_{i,j+1} - \mathbf{Q}_{i,j}\right)/\left(J_{i,j+1} + J_{i,j}\right) \qquad (3.7b)$$

The entropy correction function ψ is defined as

$$\psi(y) = \begin{cases} |y| & \text{for } |y| \geq \delta \\ \dfrac{\left(y^2 + \delta^2\right)}{2\delta} & \text{for } |y| < \delta \end{cases} \qquad (3.8)$$
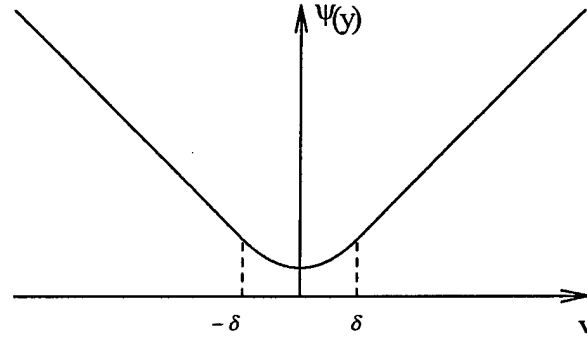
Figure 3-1. The function $\psi(y)$.

The function ψ is applied to the eigenvalues of the system. It is used to overcome difficulties when the eigenvalues become small (see Figure 3-1). Typically, the cutoff parameter δ is specified as $0 < \delta \leq 0.125$. However, it has been shown that non-physical solutions could be obtained for flows around blunt body at $M_\infty > 2.5$. In this case, δ cannot be specified as a constant and must be locally computed. The local computation of δ is given by

$$\delta_{i+1/2,j} = \overline{\delta}\left[\left|U_{i+1/2,j}\right| + \left|V_{i+1/2,j}\right| + \left(v_{f\xi}\right)_{i+1/2,j} + \left(v_{f\eta}\right)_{i+1/2,j}\right] \qquad (3.9a)$$

$$\delta_{i,j+1/2} = \overline{\delta}\left[\left|U_{i,j+1/2}\right| + \left|V_{i,j+1/2}\right| + \left(v_{f\xi}\right)_{i,j+1/2} + \left(v_{f\eta}\right)_{i,j+1/2}\right] \qquad (3.9b)$$

where U, V are the contravariant velocities and $v_{f\xi}$, $v_{f\eta}$ the fast wave velocities. $\overline{\delta}$ is a weight term and is typically specified between 0.5 and 0.7.

25

3.3. Time Stepping

When a steady state solution is sought, it is possible to accelerate the convergence of the solution by specifying a local time step at each grid point. It allows the solution to march faster where the eigenvalues of the system are small (i.e., the characteristic speed of the wave propagation are small). The time step is locally computed as a function of the eigenvalues of the system, the computational grid spacing and the Courant-Friedrichs and Lewy (*CFL*) number, which is a user-specified parameter. For stability purposes, the range of *CFL* number is typically specified between 0 and 0.2. The time step is computed according to the following procedure:

$$\Delta t = \min\left[\Delta t_\xi ; \Delta t_\eta\right] \tag{3.10}$$

where
$$\Delta t_\xi = CFL\frac{\Delta\xi}{\lambda_{\xi\,max}} \quad\text{and}\quad \Delta t_\eta = CFL\frac{\Delta\eta}{\lambda_{\eta\,max}} \tag{3.11}$$

For the full MHD equations:

$$\lambda_{\xi\,max} = \max_{i=1,8}\left[\lambda_{\xi_i}\right] \quad\text{and}\quad \lambda_{\eta\,max} = \max_{i=1,8}\left[\lambda_{\eta_i}\right] \tag{3.12}$$

$$
\begin{aligned}
\lambda_{\xi_1} &= U & \lambda_{\xi_2} &= U \\
\lambda_{\xi_3} &= U + V_{s\xi} & \lambda_{\xi_4} &= U - V_{s\xi} \\
\lambda_{\xi_5} &= U + V_{a\xi} & \lambda_{\xi_6} &= U - V_{a\xi} \\
\lambda_{\xi_7} &= U + V_{f\xi} & \lambda_{\xi_8} &= U - V_{f\xi}
\end{aligned}
\tag{3.13}
$$

where U is the contravariant velocity, $V_{a\xi}$ is the Alfvén velocity, $V_{f\xi}$ is the fast wave velocity and $V_{s\xi}$ is the slow wave velocity. They are defined in the computational space as

$$U = \xi_x u + \xi_y v \tag{3.14}$$

$$V_{a\xi} = \xi_x v_{ax} + \xi_y v_{ay} \tag{3.15}$$

$$V_{f\xi}^2 = \frac{1}{2}\left[\left(v_a^2 + c_s^2\right)a_4 + \sqrt{a_4}\sqrt{\left(v_a^2 + c_s^2\right)^2 a_4 - \frac{4p\gamma}{\rho^2}\beta_{\xi 1}^2}\right] \tag{3.16}$$

$$V_{s\xi}^2 = \frac{1}{2}\left[\left(v_a^2 + c_s^2\right)a_4 - \sqrt{a_4}\sqrt{\left(v_a^2 + c_s^2\right)^2 a_4 - \frac{4p\gamma}{\rho^2}\beta_{\xi 1}^2}\right] \tag{3.17}$$

where
$$c_s^2 = \frac{\gamma p}{\rho} \quad, \quad a_4 = \xi_x^2 + \xi_y^2 \quad, \quad \beta_{\xi 1} = \xi_x B_x + \xi_y B_y$$

$$v_a^2 = |\mathbf{B}|^2/\rho \quad, \quad v_{ax} = B_x/\sqrt{\rho} \quad, \quad v_{ay} = B_y/\sqrt{\rho}$$

For the low magnetic Reynolds number MHD equations:

$$\lambda_{\xi\,max} = \max_{i=1,5}\left[\lambda_{\xi_i}\right] \quad\text{and}\quad \lambda_{\eta\,max} = \max_{i=1,5}\left[\lambda_{\eta_i}\right] \tag{3.18}$$

$$\lambda_{\xi_1} = U \qquad\qquad \lambda_{\xi_2} = U$$
$$\lambda_{\xi_3} = U + V_{cs\xi} \qquad \lambda_{\xi_4} = U - V_{cs\xi}$$
$$\lambda_{\xi_5} = U$$

(3.19)

where $V_{cs} = c_s \sqrt{a_4}$

The eigenvalues in the η direction are expressed in a similar way as the eigenvalues in the ξ direction, by substituting ξ by η.

3.4. Grid Generation

The governing equations are solved at discrete points distributed within the domain of application. A numerical structured grid must be generated in the physical space (x, y) and then mapped onto the computational space (ξ, η). The grids are generated using an algebraic grid generator. In order to obtain good resolution of the boundary layers, grid clustering is implemented near the solid surfaces. The metrics and Jacobian of transformations are calculated by the method outlined in Section 2.1.4. For turbulent flow computations, the level of clustering is adjusted to meet the requirement that the first value of y^+ away from a solid wall is less than one. Since the value of y^+ is dependent on the solution, and cannot be known a priori, the grid is refined (if necessary) after a solution is obtained and a new computation is performed until the requirement on y^+ is satisfied. Figure 3-2 shows an example of a grid system for a 24-degree compression corner geometry.
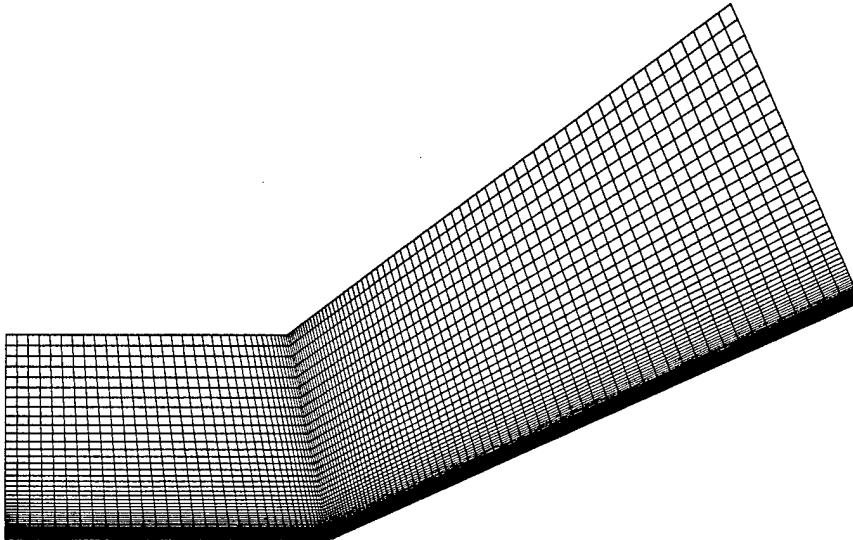
Figure 3-2. Example of two-dimensional grid system
(24-degree compression corner, 100×80 grid points).

27

Chapter 4
Turbulence Models

In this chapter, a description of the six turbulence models used for the computation of turbulent flows is reviewed. Since these models were originally derived for flows not subject to magnetic fields, they are described in their original form i.e., based on the Reynolds Averaged Navier-Stokes equations. Modifications to include compressibility effect are also provided since these models will be applied to supersonic flows. The ultimate goal is to modify these turbulence models to take the presence of the magnetic field into account. The proposed modifications for the turbulence models are provided in Chapter 5.

4.1. Introductory Remarks

The computation of turbulent flows can be achieved by various techniques. The governing equations are the Navier-Stokes equations and are given in tensor notation by Equations (4.1a) through (4.1c).

- Continuity:
$$\frac{\partial \rho}{\partial t} + \frac{\partial}{\partial x_i}(\rho u_i) = 0 \qquad (4.1a)$$

- Momentum:
$$\frac{\partial}{\partial t}(\rho u_i) + \frac{\partial}{\partial x_j}(\rho u_i u_j) = -\frac{\partial p}{\partial x_i} + \frac{\partial}{\partial x_j}\tau_{ij} \qquad (4.1b)$$

- Energy:
$$\frac{\partial}{\partial t}(\rho e_t) + \frac{\partial}{\partial x_i}(\rho u_i e_t) = \frac{\partial}{\partial x_i}(u_j \tau_{ij}) - \frac{\partial}{\partial x_i}(p u_i) - \frac{\partial q_i}{\partial x_i} \qquad (4.1c)$$

For a Newtonian fluid
$$\tau_{ij} = \mu\left(\frac{\partial u_i}{\partial x_j} + \frac{\partial u_j}{\partial x_i} - \frac{2}{3}\frac{\partial u_k}{\partial x_k}\delta_{ij}\right) \qquad (4.2)$$

and for a perfect gas
$$q_i = -k\frac{\partial T}{\partial x_i} \qquad (4.3)$$

No assumption about turbulence has been made to derive the Navier-Stokes equations. Therefore, they may be used directly to predict turbulent flows. This approach is called the Direct Numerical Simulation (DNS), where the full governing equations are solved without any modeling or limiting assumptions. However, turbulent flow fields exhibit a wide range of scales of motion, and the resolution of all these scales are necessary to accurately predict the behavior of turbulent flows. Typically, the number of grid points N, required for a three-dimensional computation is of the order of $Re^{9/4}$. For example, if $Re = 3,000$, then $N = 7.10^7$ and if $Re = 800,000$, then $N = 2.10^{13}$. Computer capacities have not yet reached levels of performance that would allow computations of complex geometries with large domains. The projection of computer's expansion shows that several decades will be required to obtain satisfactory computer capacities enabling the computation of complex flows.

The second category of turbulence computation is the Large Eddy Simulation (LES). The Navier-Stokes equations are used to simulate the large scales. The small scales (or unresolved scales) are simulated by the introduction of Sub Grid Scales models (SGS). The justification of this approach is that the smaller scales behave in a similar fashion in most flows, and they are assumed to be more homogeneous and less affected by the boundary conditions.

The third category is the Reynolds Averaged approach. This technique has been widely used for practical applications, and will be considered in this investigation. Turbulent quantities are represented by fluctuations in the flow properties. For example, one would write $u = \bar{u} + u'$, where $\bar{u}$ is the average velocity (in time), u' is the fluctuating velocity associated with turbulence, and u is the instantaneous velocity (Figure 4-1).
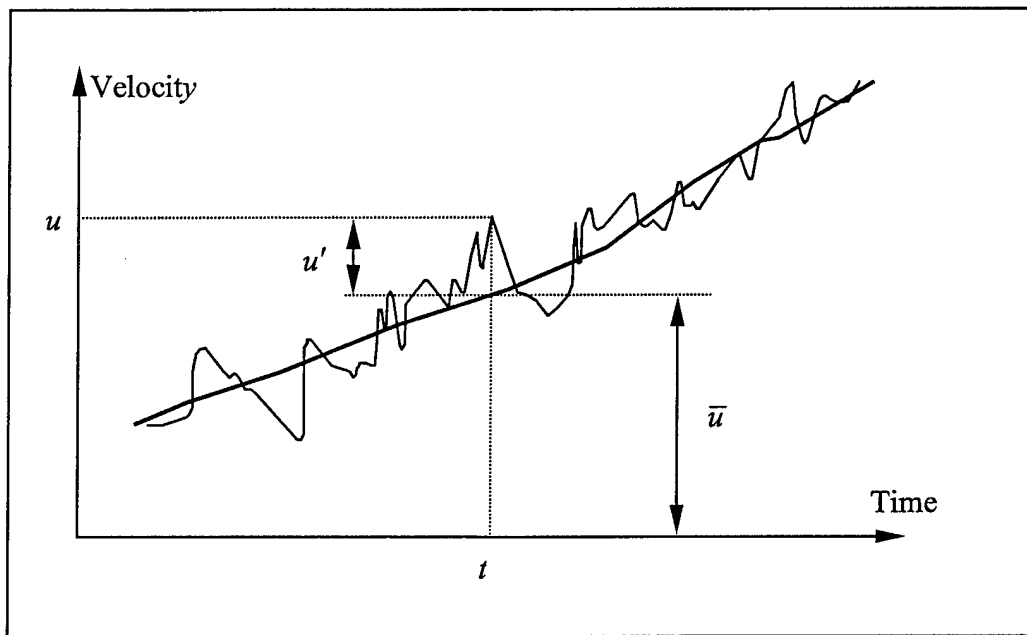
Figure 4-1. Representation of fluctuating quantities.

Once all the instantaneous quantities in the Navier-Stokes equations are written as the summation of an average and a fluctuating quantity, the equations are averaged in time. The resulting equations are known as the Reynolds Averaged Navier-Stokes equations (RANS). Additional unknowns such as $\overline{u'v'}$, $\overline{u'^2}$, etc. appear in the RANS equations, which are referred to as the turbulent or Reynolds stresses. Therefore, there are more unknowns than equations and additional equations for the Reynolds stresses are required to close the system. These equations are known as the turbulence models. They vary considerably in terms of complexity, accuracy, computational efficiency and numerical robustness. Since they are developed and calibrated based on specific conditions, they are not universal. However, the main advantage of this approach is the relatively low computational cost, and good accuracy provided the models are used within the range of application they were developed for.

29

All turbulence models are based on the Boussinesq assumption, which states that the Reynolds stresses are related to the gradient of the mean flow velocity. This assumption was made by analogy with the expression of the laminar shear stresses. For a laminar flow, the laminar shear stress is written as

$$\tau_l = \mu \frac{\partial \overline{u}}{\partial y} \tag{4.4}$$

By analogy, the Reynolds stress is written as

$$-\overline{\rho u' v'} = \mu_t \frac{\partial \overline{u}}{\partial y} \tag{4.5}$$

where μ_t is the turbulent or eddy viscosity. Similarly, the laminar and turbulent heat flux are written in an analogous way.

For a laminar flow,
$$\left(\frac{q}{A} \right)_l = -k \frac{\partial \overline{T}}{\partial y} \tag{4.6}$$

and for a turbulent flow
$$\left(\frac{q}{A} \right)_t = \overline{\rho} c_p \overline{v' T'} = -k_t \frac{\partial \overline{T}}{\partial y} \tag{4.7}$$

where k_t is the turbulent conductivity. Note that μ_t and k_t are not physical properties of the flow. They are mathematical concepts introduced to express turbulent shear stresses and heat flux in a similar form as the laminar quantities. Furthermore, a turbulent Prandtl number is introduced as $Pr_t = \frac{\mu_t c_p}{k_t}$. For air, $Pr_t = 0.90$ and is considered constant. Hence, the determination of μ_t is sufficient since, k_t is simply evaluated from $k_t = \frac{\mu_t c_p}{Pr_t}$. From a practical point of view, the implementation of turbulence in the Navier-Stokes equations is achieved by replacing μ by $\mu + \mu_t$ and $\frac{\mu}{Pr}$ by $\frac{\mu}{Pr} + \frac{\mu_t}{Pr_t}$ in the governing equations.

The main objective of a turbulence model is the determination of the turbulent viscosity μ_t, using only mean flow properties. The first attempt was made by Prandtl (1925), who wrote the turbulent viscosity in a similar way as the molecular viscosity (which can be determined from the kinetic theory of gases). The turbulent viscosity is written as the product of a characteristic velocity and a characteristic length as

$$\mu_t = \rho V_t l = \rho l^2 \left(\frac{\partial \overline{u}}{\partial y} \right) \tag{4.8}$$

where the characteristic velocity is $V_t = l \left(\frac{\partial \overline{u}}{\partial y} \right)$ and the characteristic length is l.

Turbulence models relate the characteristic velocity and length to the mean flow quantities. Zero-equation (or algebraic) models specify the turbulent characteristic velocity and length algebraically. One-equation models specify the characteristic length

30

algebraically while solving a partial differential equation for the characteristic velocity or another variable related to it. Two-equation models solve two partial differential equations for turbulent quantities. A wide variety of models have been proposed and improved throughout the years. The following sections describe six turbulence models, ranging from an algebraic model to more sophisticated two-equation models.

4.2. Baldwin-Lomax Zero-Equation Model

The Baldwin-Lomax [47] model is a two-layer model composed of an inner and an outer region. The switch between the inner and outer turbulent viscosity occurs at the y-location where both turbulent viscosities are equal. The basic assumption is that the local rate of production and dissipation of turbulence are approximately equal. This model does not include any convection of turbulence.

In the inner layer, the length scale associated with the turbulence is the mixing length. The mixing length is the distance that lumps of fluid associated with fluctuating quantities travel before they lose their identity. From experimental evidence, it is observed that turbulence damps out near the solid surfaces, within the viscous sublayer. Subsequently, turbulence grows rapidly. In this model, the mixing length is specified by an algebraic function, known as the Van-Driest function:

$$l = \kappa y (1 - e^{-y^+/A^+})$$ (4.9)

where

$$y^+ = \frac{\rho_w u_\tau y}{\mu_w}$$ (4.10)

and

$$u_\tau = \sqrt{\frac{|\tau_w|}{\rho_w}}$$ (4.11)

The characteristic velocity is given by $V_t = l\omega$ where

$$\omega = \sqrt{\left(\frac{\partial v}{\partial z} - \frac{\partial w}{\partial y}\right)^2 + \left(\frac{\partial w}{\partial x} - \frac{\partial u}{\partial z}\right)^2 + \left(\frac{\partial u}{\partial y} - \frac{\partial v}{\partial x}\right)^2}$$ (4.12)

Therefore, in the inner layer, the turbulent viscosity is given by

$$\mu_{t_i} = \rho l^2 \omega$$ (4.13)

In the outer region, the turbulent viscosity is given by

$$\mu_{t_o} = \alpha \rho U_0 L_0$$ (4.14)

where at a given x,

$$U_0 = \min\left[G_{max}, \frac{(\Delta V)^2}{G_{max}}\right]$$ (4.15)

and

$$G_{max} = \max\left(\frac{l}{\kappa}\omega\right)$$ (4.16)

$$L_0 = C_{CP} I_0 y_{max}$$ (4.17)

y_{max} is the value of y where G_{max} occurs. $\Delta V = V_{max} - V_{min}$ is the difference between the maximum and minimum velocities at a given x ($V_{min} = 0$ for boundary layer flows). I_0 is the intermittency factor:

31

$$I_0 = \left[1 + 5.5 \left(\frac{C_{kleb} y}{y_{max}} \right)^6 \right]^{-1} \tag{4.18}$$

The closure coefficients for the Baldwin-Lomax model are summarized in Table 4-1.

$\kappa = 0.41$	$A^+ = 26.0$	$C_{Kleb} = 0.3$
$C_{CP} = 1.6$	$\alpha = 0.0168$	

Table 4-1. Closure coefficients for the Baldwin-Lomax model.

4.2.1. Entropy Envelop Concept

Difficulties are encountered when the Baldwin-Lomax is implemented in regions of strong viscous / inviscid interaction and flow separation. The entropy envelope concept has been proposed by Brock et al. [92] to alleviate these problems. This method ensures the proper evaluation of the maxima of a vorticity-based function.

In the Baldwin-Lomax algebraic turbulence model, the length scale is related to the boundary layer vorticity. The length scale is the normal distance y_{max} away from the wall at which the moment of vorticity $G = l\omega/k$ is maximum. Typically, the maximum of G is found by probing the flow field from the wall and marching outward with no limits in the search height. For flow fields that are characterized with a weak viscous / inviscid interaction, only one maximum of G is found. However, several maxima may occur for more complex flows.

In separated flow fields, two maxima occur upstream and throughout separation. G can also be found maximum near strong or curved shocks outside the boundary layer, which result in a non-physical selection of the length scale.

The entropy envelope concept is based on the entropy function

$$S = \frac{p}{\rho^\gamma} \tag{4.19}$$

The edge of the entropy envelope is defined as the location where the entropy function reaches the value $S_e = S_{min}/C_s$, where C_s is user-defined constant. The search for G_{max} is then limited to the region where $S > S_{min}/C_s$, starting at the edge of the entropy envelope and moving inward. This ensures that the outer maximum above the viscous sublayer will be selected when several maxima occur. Typically, the value of C_s is problem dependent and has to be adjusted for a given application. For this investigation, a value of $C_s = 0.18$ has been used.

32

4.3. Baldwin Barth One-Equation Model

The Baldwin-Barth model [48] is a one-equation model derived from the $k-\epsilon$ model. It requires the solution of a transport partial differential equation for a new variable, which is the product of the kinematic viscosity and the turbulent Reynolds number defined as $Re_T = \dfrac{k^2}{\nu\epsilon}$. For flows in the near-wall region, the turbulent Reynolds number is split into $Re_T = \overline{Re_T} f\left(\overline{Re_T}\right)$ where f is a damping function allowing Re_T and $\overline{Re_T}$ to be equal for large values of Re_T. The transport equation in terms of $\nu\overline{Re_T}$ is given by

$$\frac{D}{Dt}\left(\nu\overline{Re_T}\right)=\left(C_{\epsilon2}f_2-C_{\epsilon1}\right)\sqrt{\nu\overline{Re_T}P_k}+\left(\nu+\frac{\nu_t}{\sigma_\epsilon}\right)\nabla^2\left(\nu\overline{Re_T}\right)-\frac{1}{\sigma_\epsilon}(\nabla\nu_t)\nabla\left(\nu\overline{Re_T}\right) \qquad (4.20)$$

Once this equation is solved, the turbulent viscosity is determined from

$$\mu_t = \rho c_\mu\left(\nu\overline{Re_T}\right)D_1 D_2 \qquad (4.21)$$

The two damping functions D_1 and D_2 are used to extend the model to the near wall region. They are

$$D_1 = 1-e^{\left(-y^+/A^+\right)} \qquad (4.22)$$

$$D_2 = 1-e^{\left(-y^+/A_2^+\right)} \qquad (4.23)$$

The production term is given by

$$P_k = \nu_t\left(\frac{\partial u_i}{\partial x_j}+\frac{\partial u_j}{\partial x_i}\right)\frac{\partial u_i}{\partial x_j}-\frac{2}{3}\nu_t\left(\frac{\partial u_k}{\partial x_k}\right)^2 \qquad (4.24)$$

The function f_2 is given by

$$f_2\left(y^+\right)=\frac{c_{\epsilon1}}{c_{\epsilon2}}+\left(1-\frac{c_{\epsilon1}}{c_{\epsilon2}}\right)\left(\frac{1}{\kappa y^+}+D_1 D_2\right)$$
$$\cdot\left[\sqrt{D_1 D_2}+\frac{y^+}{\sqrt{D_1 D_2}}\left(\frac{D_2}{A^+}e^{\left(-y^+/A^+\right)}+\frac{D_1}{A_2^+}e^{\left(-y^+/A_2^+\right)}\right)\right] \qquad (4.25)$$

and the closure coefficients are provided in Table 4-2.

$\kappa = 0.41$	$c_{\epsilon1}=1.2$	$c_{\epsilon2}=2.0$
$c_\mu = 0.09$	$A^+ = 26$	$A_2^+ = 10$
$\dfrac{1}{\sigma_\epsilon}=\left(c_{\epsilon2}-c_{\epsilon1}\right)\sqrt{c_\mu}/\kappa^2$		

Table 4-2. Closure coefficients for the Baldwin-Barth turbulence model.

33

Equation (4.20) is solved by an iterative procedure that requires the specification of initial and boundary conditions for the working variable $\overline{Re_T}$. The initial value for $\overline{Re_T}$ is the same as its freestream value $\overline{Re_{T_\infty}}$, which is specified as a small number ($\overline{Re_{T_\infty}} < 1$). The boundary conditions are specified as follows:

- Solid surface: $\overline{Re_T} = 0$
- Inflow: $\overline{Re_T} = \overline{Re_{T_\infty}}$
- Outflow: Zero-order extrapolation

The Baldwin-Barth model tends to become unstable in the separation and reattachment regions, the values of y^+ being very small and causing the damping functions to approach zero. In order to alleviate this problem, a new formulation for y^+, given by Equation (4.26) is implemented for high-speed separated flows [49]:

$$y^+ = \frac{1}{v}\left[\frac{c_\mu\left(v\overline{Re_T}\right)}{\kappa} + 0.005 Re_\infty \left|\vec{V}\right| y\right] \tag{4.26}$$

4.4. Spalart-Allmaras One-Equation Model

The Spalart-Allmaras turbulence model [50] is a one-equation model that solves a partial differential equation for the variable $\overline{v}$, which is related to the turbulent viscosity. The model is based on "empiricism, dimensional analysis, and selective dependence on molecular viscosity". The transport equation for the variable $\overline{v}$ is

$$\frac{D\overline{v}}{Dt} = C_{b1}\left(1 - f_{t2}\right)\overline{Sv} + \frac{1}{\sigma}\left\{\nabla\left[\left(v + \overline{v}\right)\nabla\overline{v}\right] + C_{b2}\left(\nabla\overline{v}\right)^2\right\}$$

$$+ \frac{C_{b1}}{\kappa^2} f_{t2}\left(\frac{\overline{v}}{d}\right)^2 - C_{w1}f_w\left(\frac{\overline{v}}{d}\right)^2 + f_{t1}(\Delta q)^2 \tag{4.27}$$

This equation states that from conservation of turbulence, the total change in v_t is equal to the sum of production, dissipation, diffusion, and destruction of v_t. The model also includes a trip function for transition from laminar to turbulent flow. The following terms can be identified in Equation (4.27):

Production term: $\qquad C_{b1}\left(1 - f_{t2}\right)\overline{Sv}$

Dissipation term: $\qquad \frac{1}{\sigma}\left\{\nabla\left[\left(v + \overline{v}\right)\nabla\overline{v}\right] + C_{b2}\left(\nabla\overline{v}\right)^2\right\}$

Diffusion term: $\qquad \frac{C_{b1}}{\kappa^2} f_{t2}\left(\frac{\overline{v}}{d}\right)^2$

Destruction term: $\quad -C_{w1}f_w\left(\dfrac{\bar{v}}{d}\right)^2$

Trip function: $\quad f_{t1}(\Delta q)^2$

The kinematic turbulent viscosity is determined from

$$v_t = \bar{v}f_{v1} \tag{4.28}$$

where

$$f_{v1} = \frac{\chi^3}{\chi^3 + C_{v1}^3} \tag{4.29}$$

and

$$\chi = \frac{\bar{v}}{v} \tag{4.30}$$

$$\bar{S} = S + \frac{\bar{v}}{\kappa^2 d^2}f_{v2} \tag{4.31}$$

$$f_{v2} = 1 - \frac{\chi}{1+\chi f_{v1}} \tag{4.32}$$

d is the distance to the wall, and S is the magnitude of the vorticity

$$S = |\omega| = \left|\frac{\partial \bar{v}}{\partial x} - \frac{\partial \bar{u}}{\partial y}\right| \tag{4.33}$$

A destruction term takes into account the destruction of Reynolds shear stress due to the effect of a wall (in case of a wall bounded flow). A dimensional analysis leads to a combination $-C_{w1}\left(\dfrac{v_t}{d}\right)^2$, where d is the distance to the wall (for free shear layer flows, d tends to infinity, so that the destruction term tends to zero). However, this destruction term results in low values of skin friction over a flat plate, indicating that the destruction term decays too slowly in the outer region of the boundary layer. Thus, the destruction term is multiplied by a non-dimensional function f_w, which equals unity in the log layer. Therefore, the destruction term is written as $-C_{w1}f_w\left(\dfrac{v_t}{d}\right)^2$, where the function for f_w is based on algebraic models as:

$$f_w = g\left(\frac{1+C_{w3}^6}{g^6 + C_{w3}^6}\right)^{\frac{1}{6}} \tag{4.34}$$

where

$$g = r + C_{w2}\left(r^6 - r\right) \tag{4.35}$$

$$r = \frac{\bar{v}}{\bar{S}\kappa^2 d^2} \tag{4.36}$$

A final set of terms includes control over the laminar regions and the transition. They maintain laminar flow where required and include transition at a specified location. In the laminar region, $\bar{v}$ must be in the order of v. Therefore, the production term is altered as follows:

$$P = C_{b1}(1 - f_{t2})\bar{S}\bar{v} \tag{4.37}$$

where
$$f_{t2} = C_{t3} \exp\left(-C_{t4}\chi^2\right)$$
(4.38)

The other trip function is given by the source term $f_{t1}(\Delta q)^2$, which was derived from dimensional analysis, and where

$$f_{t1} = C_{t1}g_t \exp\left[-C_{t2}\frac{\omega_t^2}{(\Delta q)^2}\left(d^2 + g_t^2 d_t^2\right)\right]$$
(4.39)

Δq is the difference between velocities at the trip (zero at the wall) and the point in the field that is considered, ω_t is the vorticity at the wall at the trip point, d_t is the distance from the field point to the trip point, g_t and is given by

$$g_t = \min\left(0.1, \frac{\Delta q}{\omega_t \Delta x}\right)$$
(4.40)

where Δx is the grid spacing on the wall at the trip point. The closure coefficients are provided in Table 4-3.

$\sigma = \dfrac{2}{3}$	$C_{b1} = 0.1355$	$C_{b2} = 0.622$	$C_{v1} = 7.1$
$C_{t1} = 1.0$	$C_{t2} = 2.0$	$C_{t3} = 1.1$	$C_{t4} = 2.0$
$C_{w1} = \dfrac{C_{b1}}{\kappa^2} + \dfrac{(1+C_{b2})}{\sigma}$	$C_{w2} = 0.3$	$C_{w3} = 2.0$	$\kappa = 0.41$

Table 4-3. Closure coefficients for the Spalart-Allmaras turbulence model.

The initial value for $\overline{v}$ is the same as its freestream value $\overline{v_\infty}$, which is specified as a small number ($0.0 \le \overline{v_\infty} \le v_\infty$). The boundary conditions are specified as follows:

- Solid surface: $\overline{v} = 0.0$
- Inflow: $\overline{v} = \overline{v_\infty}$
- Outflow: Zero-order extrapolation

For wall-bounded flows, the source term $\overline{S}$ becomes singular in the near wall region. The original model was modified by Edwards and Chandra [51]. The terms $\overline{S}$ and r are calculated as follows:

$$\overline{S} = \sqrt{S}\left(\frac{1}{\chi} + f_{v1}\right),$$
(4.41)

$$r = \frac{\tanh\left[\overline{v}/(\kappa d)^2 \overline{S}\right]}{\tanh(1.0)}$$
(4.42)

and

$$S^2 = \left(\frac{\partial u_i}{\partial x_j} + \frac{\partial u_j}{\partial x_i}\right)\frac{\partial u_i}{\partial x_j} - \frac{2}{3}\left(\frac{\partial u_k}{\partial x_k}\right)^2$$
(4.43)

4.5. k-ϵ Two-Equation Model (Jones & Launder)

The $k-\epsilon$ model [52,53] is a set of two partial differential equations for the turbulent kinetic energy k and its dissipation rate ϵ .

k -equation:

$$\frac{D(\rho k)}{Dt} = P_k - \rho\left(1 + \alpha M_t^2\right)\epsilon + \frac{\partial}{\partial x_i}\left[\left(\mu + \frac{\mu_t}{\sigma_k}\right)\frac{\partial k}{\partial x_i}\right] + L_k \tag{4.44}$$

ϵ -equation:

$$\frac{D(\rho\epsilon)}{Dt} = \left[C_{\epsilon 1}f_1 P_k - C_{\epsilon 2}f_2\rho\epsilon\right]\frac{\epsilon}{k} + \frac{\partial}{\partial x_i}\left[\left(\mu + \frac{\mu_t}{\sigma_\epsilon}\right)\frac{\partial\epsilon}{\partial x_i}\right] + L_\epsilon \tag{4.45}$$

The production term is

$$P_k = \tau_{ij}\frac{\partial u_i}{\partial x_j} = \left[\mu_t\left(\frac{\partial u_i}{\partial x_j} + \frac{\partial u_j}{\partial x_i} - \frac{2}{3}\frac{\partial u_k}{\partial x_k}\delta_{ij}\right) - \frac{2}{3}\rho k\delta_{ij}\right]\frac{\partial u_i}{\partial x_j} \tag{4.46}$$

The turbulent Mach number $M_t^2 = \dfrac{2k}{\gamma RT}$ is used as a compressibility term. It is designed for shear layer flows and should be turned off for wall-bounded flows, by setting $\alpha = 0$. The turbulent viscosity is calculated according to:

$$\mu_t = c_\mu f_\mu \frac{\rho k^2}{\epsilon} \tag{4.47}$$

In the Jones-Launder model, the following functions are defined:

$$f_1 = 1.0 \qquad\qquad f_2 = 1 - 0.3e^{-Re_t^2}$$

$$f_\mu = e^{-\frac{2.5}{1+0.02 Re_t}} \qquad\qquad Re_t = \frac{\rho k^2}{\mu\epsilon}$$

$$L_k = -2\mu\left(\frac{\partial\sqrt{k}}{\partial x_j}\right)^2 \qquad\qquad L_\epsilon = \frac{2\mu\mu_t}{\rho}\left(\frac{\partial^2 u_i}{\partial x_i x_j}\right)^2$$

The closure coefficients are provided in Table 4-4:

$c_{\epsilon 1} = 1.44$	$c_{\epsilon 2} = 1.92$	$c_\mu = 0.09$
$\sigma_k = 1.0$	$\sigma_\epsilon = 1.3$	$\alpha = 1.0$

Table 4-4. Closure coefficients for the $k - \epsilon$ model.

The turbulent quantities k and ϵ are initiated as their freestream values: $k = k_\infty = 1.5\left(TI.U_\infty\right)^2$ and $\epsilon = \epsilon_\infty = c_\mu f_{\mu\infty}\bar{\rho}_\infty\dfrac{k_\infty^2}{\mu_{t\infty}}$, where TI is the freestream turbulence intensity $(10^{-5} \leq TI \leq 10^{-3})$, U_∞ is the freestream velocity, and $\bar{\rho}_\infty$ is the freestream density. $\mu_{t\infty}$ is the freestream turbulent viscosity and is specified as a small fraction of the

37

freestream viscosity, e.g., $\mu_{t_\infty} = 0.001\mu_\infty$. The boundary conditions are specified as follows:

- Solid surface: $k = 0$, $\epsilon = 0$, $\mu_t = 0$
- Inflow: $k = k_\infty$, $\epsilon = \epsilon_\infty$, $\mu_t = \mu_{t\infty}$
- Outflow: Zero-order extrapolation

The modification proposed by Coakley and Huang [54] is designed to predict more accurately the separation region. The production term in the ϵ equation is modified to ensure that the turbulent length scale does not change too abruptly through a shock wave. The term $C_{\epsilon 1}f_1 P_k$ is replaced by $C_{\epsilon 1}f_1\mu_t S^2 - \alpha_\epsilon \rho \epsilon D$ in the ϵ equation, which becomes

$$\frac{D(\rho\epsilon)}{Dt} = \left[C_{\epsilon 1}f_1\mu_t S^2 - \alpha_\epsilon \rho \epsilon D - C_{\epsilon 2}f_2\rho\epsilon\right]\frac{\epsilon}{k} + \frac{\partial}{\partial x_i}\left[\left(\mu + \frac{\mu_t}{\sigma_\epsilon}\right)\frac{\partial \epsilon}{\partial x_i}\right] + L_\epsilon \qquad (4.48)$$

where

$$S^2 = \left(\frac{\partial u_i}{\partial x_j} + \frac{\partial u_j}{\partial x_i}\right)\frac{\partial u_i}{\partial x_j} - \frac{2}{3}\left(\frac{\partial u_k}{\partial x_k}\right)^2 \qquad (4.49)$$

and

$$D = \frac{\partial u_k}{\partial x_k} \qquad (4.50)$$

The closure coefficient associated with this modification is $\alpha_\varepsilon = 2.0$.

4.6. Combined k-ϵ / k-ω Two-Equation Model (Menter's)

One of the shortcomings of the $k - \epsilon$ model is its stiffness in the viscous sublayer. Wilcox [55-58] proposed the $k - \omega$ model composed of one equation for the turbulent kinetic energy and one equation for the specific turbulent dissipation rate (or turbulent frequency). This model performs better than the $k - \epsilon$ in the near wall regions but is very sensitive to freestream values of ω. On the other hand, the $k - \epsilon$ model is not sensitive to freestream values. Menter [59-62] proposed to combine the $k - \epsilon$ and the $k - \omega$ models to use the best features of both models. The model switches to the $k - \omega$ model in the inner region of the boundary layer and switches to the $k - \epsilon$ model in the outer region of the boundary layer. Therefore, the model will be well behaved in the near wall region and will stay insensitive to freestream conditions outside the boundary layer.

The combined model is written such that both models are blended together through a switching function. The switching function F_1 is designed such that $F_1 = 1$ in the near-wall region to activate the $k - \omega$ model and $F_1 = 0$ at the boundary layer edge to activate the $k - \epsilon$ model and ensure the freestream independence of the model.

The resulting two partial differential equations are given by

$$\frac{D(\rho k)}{Dt} = P_k - \beta^* \rho \omega k + \frac{\partial}{\partial x_i}\left[\left(\mu + \frac{\mu_t}{\sigma_k}\right)\frac{\partial k}{\partial x_i}\right] \tag{4.51}$$

$$\frac{D(\rho \omega)}{Dt} = \frac{\alpha \rho}{\mu_t}P_k - \beta \rho \omega^2 + \frac{\partial}{\partial x_i}\left[\left(\mu + \frac{\mu_t}{\sigma_\omega}\right)\frac{\partial \omega}{\partial x_i}\right]$$
$$+ 2\rho(1 - F_1)\sigma_{\omega 2}\frac{1}{\omega}\frac{\partial k}{\partial x_i}\frac{\partial \omega}{\partial x_i} \tag{4.52}$$

The switching function is given by

$$F_1 = \tanh(\arg_1{}^4) \tag{4.53}$$

$$\arg_1 = \min\left[\max\left(\frac{\sqrt{k}}{0.09\omega y}, \frac{500\nu}{\omega y^2}\right), \frac{4\rho\sigma_{\omega 2}k}{CD_{k\omega}y^2}\right] \tag{4.54}$$

where y is the distance to the closest wall and $CD_{k\omega}$ is the positive portion of the cross-diffusion term.

$$CD_{k\omega} = \max\left[2\rho\sigma_{\omega 2}\frac{1}{\omega}\frac{\partial k}{\partial x_i}\frac{\partial \omega}{\partial x_i}, 10^{-20}\right] \tag{4.55}$$

The production term is similar to that of the $k - \epsilon$ model:

$$P_k = \tau_{ij}\frac{\partial u_i}{\partial x_j} = \left[\mu_t\left(\frac{\partial u_i}{\partial x_j} + \frac{\partial u_j}{\partial x_i} - \frac{2}{3}\frac{\partial u_k}{\partial x_k}\delta_{ij}\right) - \frac{2}{3}\rho k\delta_{ij}\right]\frac{\partial u_i}{\partial x_j} \tag{4.56}$$

The model constants are also affected by the switching function. Since two sets of constants exist (one for the $k - \omega$ model and one for the $k - \epsilon$ model), the overall constant is given in the generic form as $\phi = \phi_1 + (1 - F_1)\phi_2$, where ϕ_1 represents a model constant for the $k - \omega$ model and ϕ_2 represents a model constant for the $k - \epsilon$ model. Menter proposed two versions of the combined $k - \epsilon / k - \omega$ model. They differ in the determination of the turbulent viscosity and the specification of the model constants.

4.6.1. Baseline Model

In the Baseline model, the turbulent viscosity is computed from

$$\mu_t = \rho \frac{k}{\omega} \qquad (4.57)$$

The model constants are given by Tables 4-5 and 4-6:

$\sigma_{k1} = 0.1$	$\sigma_{\omega1} = 0.5$	$\beta_1 = 0.0750$
$\beta^* = 0.09$	$\kappa = 0.41$	$\alpha_1 = \dfrac{\beta_1}{\beta^*} - \dfrac{\sigma_{\omega1}\kappa^2}{\sqrt{\beta^*}}$

Table 4-5. Constants associated with $k-\omega$ or ϕ_1.

$\sigma_{k2} = 1.0$	$\sigma_{\omega2} = 0.856$	$\beta_2 = 0.0828$
$\beta^* = 0.09$	$\kappa = 0.41$	$\alpha_2 = \dfrac{\beta_2}{\beta^*} - \dfrac{\sigma_{\omega2}\kappa^2}{\sqrt{\beta^*}}$

Table 4-6. Constants associated with $k-\epsilon$ or ϕ_2.

4.6.2. Shear Stress Transport

This model is a modified version of the Baseline model. It is based on the assumption of the Johnson-King model where the turbulent shear stress is proportional to the turbulent kinetic energy in the log and wake region of the turbulent boundary layer. The eddy viscosity is limited by the turbulent kinetic energy to ensure the proportionality condition. Therefore, the turbulent viscosity is given by

$$\mu_t = \frac{\rho a_1 k}{\max(a_1\omega, \Omega F_2)} \qquad (4.58)$$

where $a_1 = 0.31$, Ω is the absolute value of the vorticity,

$$\Omega = \left| \frac{\partial v}{\partial x} - \frac{\partial u}{\partial y} \right| \qquad (4.59)$$

$$F_2 = \tanh\left(\text{arg}_2^{\,2}\right) \qquad (4.60)$$

$$\text{arg}_2 = \max\left(\frac{2\sqrt{k}}{0.09\omega y}, \frac{500\nu}{\omega y^2} \right) \qquad (4.61)$$

The same model constants as for the Baseline model are used except for σ_{k1}, which is set equal to $\sigma_{k1} = 0.85$.

The initial conditions are given as follows: $\omega_\infty = m\dfrac{u_\infty}{L}$, $v_{t_\infty} = 10^{-n} v_\infty$, $k_\infty = v_{t_\infty}\omega_\infty$ where $1 \le m \le 10$ and $2 \le n \le 5$. L is a characteristic length of the problem. It is typically chosen as the length of the computational domain (it is the same as the reference length used to nondimensionalize the equations). The boundary conditions are specified as follows:

- Solid surface: $k = 0$, $\omega = 10\dfrac{6v}{\beta_1(\Delta y_1)^2}$, where Δy_1 is the distance of the first point away from the wall.
- Inflow: $k = k_\infty$, $\omega = \omega_\infty$
- Outflow: Zero-order extrapolation

Similar to the $k-\epsilon$ model, a compressibility correction is introduced for the production term in the ω equation. The production term is rewritten in terms of the proper variables through the relation $\omega = \dfrac{\epsilon}{\beta^* k}$ and the constants are adjusted accordingly. This modification is designed to increase the size of the separation region and is only applied for the Baseline model since the Shear Stress Transport model already includes a procedure to increase the size of the separation region.

A compressibility correction term and a pressure dilatation term were also introduced in the model. They were modified by Suzen and Hoffmann [63] for the $k-\epsilon$ model. Note that the modifications are applied to the $k-\epsilon$ model such that the $k-\omega$ model remains unchanged in the near-wall region where it performs well. Indeed, the modifications are fully activated when the model switches to the $k-\epsilon$ model (i.e. when $F_1 = 0$). The resulting modified equations are:

$$\frac{D(\rho k)}{Dt} = P_k - \beta^* \rho \omega k \left[1 + \alpha_1 M_t^2 (1 - F_1)\right] + \frac{\partial}{\partial x_i}\left[\left(\mu + \frac{\mu_t}{\sigma_k}\right)\frac{\partial k}{\partial x_i}\right]$$
$$+ (1 - F_1)\overline{p''d''} \tag{4.62}$$

$$\frac{D(\rho \omega)}{Dt} = \frac{\gamma \rho}{\mu_t} P_k - \beta \rho \omega^2 + \frac{\partial}{\partial x_i}\left[\left(\mu + \frac{\mu_t}{\sigma_\omega}\right)\frac{\partial \omega}{\partial x_i}\right]$$
$$+ 2\rho(1 - F_1)\sigma_{\omega 2}\frac{1}{\omega}\frac{\partial k}{\partial x_i}\frac{\partial \omega}{\partial x_i} \tag{4.63}$$
$$+ (1 - F_1)\beta^* \alpha_1 M_t^2 \rho \omega^2 - (1 - F_1)\frac{\overline{p''d''}}{v_t}$$

The pressure dilatation term is given by

$$\overline{p''d''} = -\alpha_2 \tau_{ij} \frac{\partial u_i}{\partial x_j} M_t^2 + \alpha_3 \rho \epsilon M_t^2 \qquad (4.64)$$

M_t is the turbulent Mach number,

$$M_t = \sqrt{\frac{2k}{\gamma RT}} \qquad (4.65)$$

and the following constants have been obtained based on DNS of isotropic turbulence.

$$\alpha_1 = 1.0 \qquad , \qquad \alpha_2 = 0.4 \qquad , \qquad \alpha_3 = 0.2$$

4.7. Numerical Issues

When the turbulence model is expressed by a differential equation (i.e., for the one-equation and the two-equation models), some numerical issues need to be addressed. The time scales associated with turbulence are typically much smaller than those associated with the mean flow. The Reynolds Averaged Navier-Stokes equations are solved for the mean flow variables, and the turbulence models relate them to the turbulent quantities. Two numerical approaches can be used. The first one consists in solving the entire system of mean flow and turbulence quantities simultaneously. This is called a coupled scheme. In this case, the same time step must be used for the entire system (see Figure 4-2). Since the turbulence models require a smaller time step than the mean flow solver, the convergence of the numerical solution is very slow.
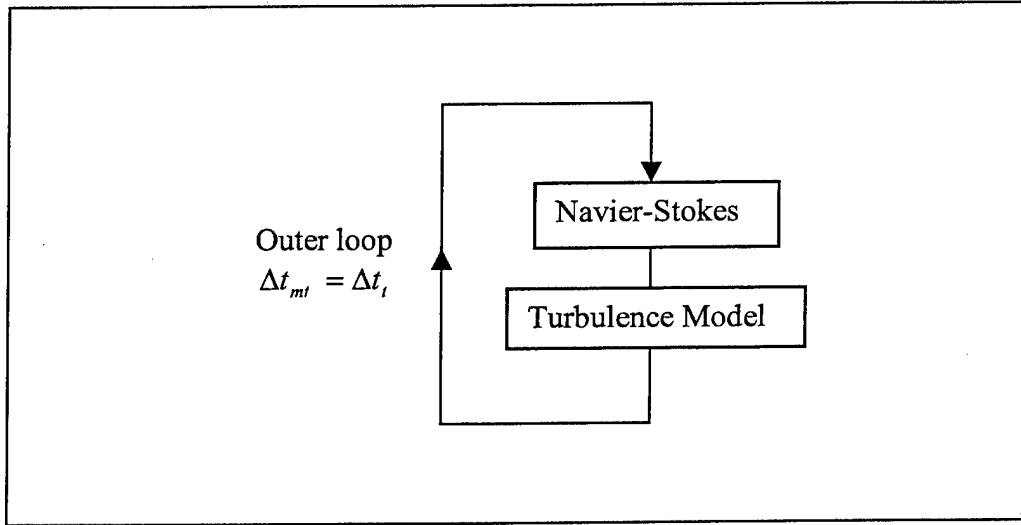
Figure 4-2. Illustration of the coupled approach in turbulence modeling.

In the second approach, the system is solved in an uncoupled fashion. First, the Reynolds Averaged Navier-Stokes equations are solved in an outer loop, with a time step Δt_{mf}. Then, the turbulence model is integrated with a time step $\Delta t_t < \Delta t_{mf}$. Next, a new outer iteration is resumed and the same procedure is applied (see Figure 4-3). This

approach is implemented with a typical turbulent time step that is five times smaller than the mean flow time step.
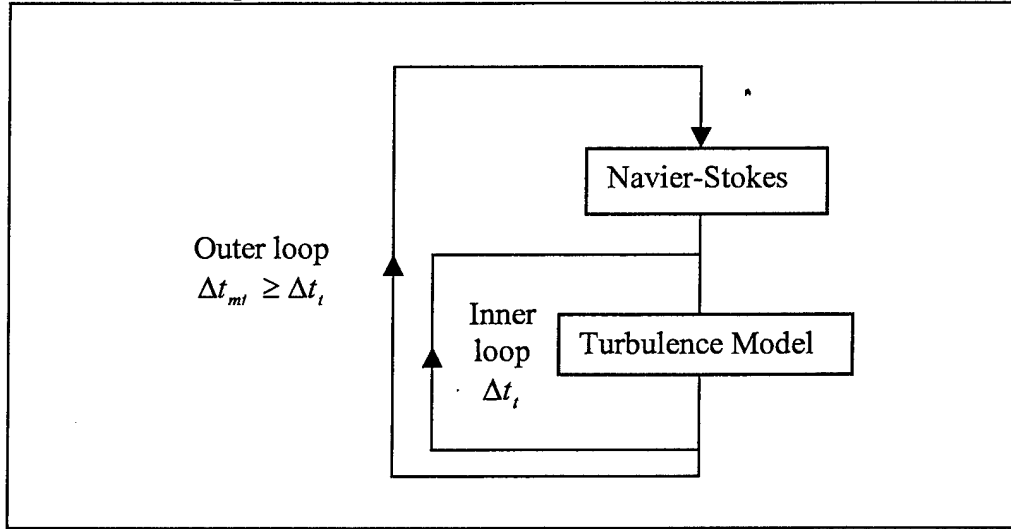
Figure 4-3. Illustration of the decoupled approach in turbulence modeling.

For all models involving the solution of a partial differential equation, the convective terms have been approximated by a first order upwind scheme and the diffusion terms by a second order central difference scheme. The equations have been written in their non-dimensional form and transformed into the computational space using the same procedure as described in Section 2.1.4. The turbulent quantities are nondimensionalized as follows:

$$\mu_t^* = \frac{\mu_t}{\mu_\infty} \quad , \quad k^* = \frac{k}{u_\infty^2} \quad , \quad \epsilon^* = \epsilon \frac{L}{u_\infty^3}$$

$$Re_T^* = \frac{k^{*2}}{v^* \epsilon^*} \quad , \quad \overline{v}^* = \frac{\overline{v}}{v_\infty} \quad , \quad \omega^* = \frac{\omega L}{u_\infty}$$

4.8. Comparison of Computational Times

Two computer programs have been developed for this investigation. A code is based on the low magnetic Reynolds number formulation (LRMHD) and a code is based on the full MHD equations (RAMHD). Both programs contain the six turbulence models described in this chapter (original forms) and in Chapter 5 (modified versions to account for the presence of a magnetic field). The selection of a turbulence model for the computation of a given application should be primarily based on the physics / geometry of the problem and the level of accuracy that the turbulence model would provide. It is expected that from the six available turbulence models, some will perform better than others, and some will exhibit similar level of accuracy. When two models provide comparable satisfactory results, the turbulence model that provides the solution in the fastest computational time is preferable. The objective of this section is to provide some guidelines toward the selection of a turbulence model, based on the computational cost associated with it.

43

The computer resource has been provided by the High Performance Computing Center at Wichita State University, which operates a Silicon Graphics Origin 2000 machine. It contains 24 processors (16 operate at 300 MHz and 8 at 250 MHz), with 10 Gigabytes of RAM. All programs have been timed on the 300 MHz processors. The programs have been written in FORTRAN 77 and optimization directives have been supplied to the compiler to increase the execution speed.
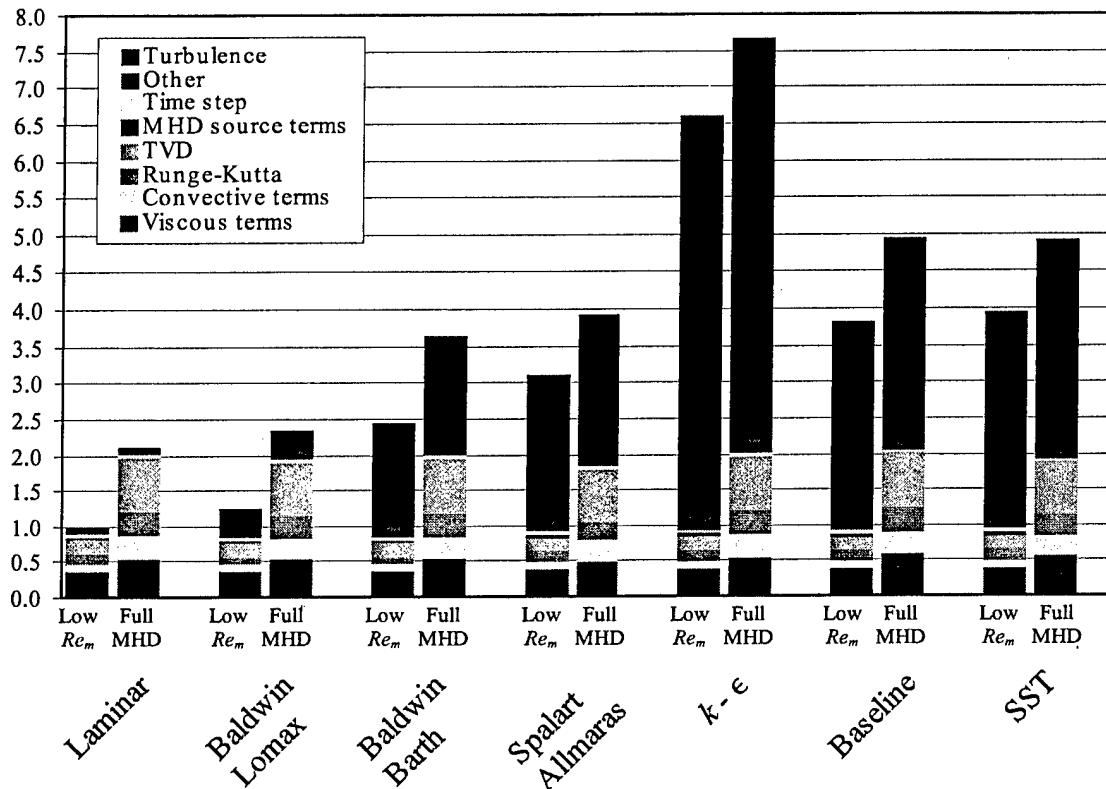
Figure 4-4. Load distribution of various program tasks.

Figure 4-4 illustrates the CPU time spent on each key-task performed by the computer codes developed for this investigation. All CPU times have been normalized with the CPU time obtained with the LRMHD code while computing a laminar solution.

For a laminar flow, the full MHD equation solver takes a little more than twice as much time as the code based on the low magnetic Reynolds number. Computation of the viscous and convective terms require more computational time when the full MHD equations are solved because there are eight components to the flux vectors as opposed to five for the low magnetic Reynolds number formulation. Similarly, the implementation of the Runge-Kutta scheme is more costly when the full equations are solved. There exist also a substantial difference in the evaluation of the TVD terms. This difference is due to the larger complexity of the eigenstructure associated with the full MHD equations, as opposed to the eigenstructure of the low magnetic Reynolds number formulation, which

44

is identical to the Navier-Stokes eigenstructure. Note that only the low magnetic Reynolds number formulation requires the computation of the MHD source terms. However, the additional time spent to compute these terms is negligible compared to the computational time saved in all other sections of the code. The computation of the time step (for steady state solution) is not significantly affected by the type of formulation. The category "Other" includes the grid generation, reading of the input data, writing the output data, and implementation of the boundary conditions. These tasks are also independent of the formulation.

When a turbulent computation is performed, the choice of the turbulence model has a substantial impact on the computational load of the codes. When the Baldwin-Lomax model is used, it results in an increase of 30% of the computational time, both for the low magnetic Reynolds number formulation or the full MHD equations formulation. Indeed, the computational time devoted to the turbulence model does not depend on the MHD formulation. The Baldwin-Barth model results in an increase of 150% compared to the laminar case. The large increase in computational time compared to the Baldwin-Lomax is due to the nature of the turbulence model. The Baldwin-Lomax model is an algebraic model that evaluates the turbulent viscosity explicitly from the mean flow quantities. The Baldwin-Barth model solves a partial differential equation in terms of a turbulent variable related to the turbulent viscosity. Due to numerical stability consideration, the turbulent equation must be solved with a smaller time step than the mean flow solver. Subsequently, for each mean flow iteration, several turbulent sub-iterations are required to produce a concurrent marching of all flow quantities. It has been determined that a turbulent time step five times smaller than the mean flow time step, associated with five sub-iterations for the turbulent equation(s) is the most efficient combination. This results in shifting most of the computational load to the turbulence model. However, it is preferable to utilize this decoupled approach rather than solving both mean flow and turbulent equations with a prohibitively small time step.

Similar to the Baldwin-Barth model, the Spalart-Allmaras model, which is also a one-equation model results in an increase of about 200% compared to the laminar case. Next, the two-equations models are investigated. The $k - \epsilon$ model is the model that requires the most CPU time. In fact, the $k - \epsilon$ model requires about 5.5 times more computational time than the mean flow solver. The Baseline and SST models need a little less than three times as much CPU time as the mean flow solver. Note that for two-equations models, most of the computational time is spent on the turbulence model, not the mean flow solver.

The previous comments merely reflect the computational time devoted to individual tasks within the codes. It allows the comparison of the full MHD and low magnetic Reynolds number formulations and each turbulence models. For the computation of a time accurate solution, the CPU time required to reach a given time level will exactly scale with the timing presented in Figure 4-4. For a steady state solution, it is more difficult to compare the performances of the codes and turbulence models. Figure 4-4 does not provide any information on how fast the codes converge. For example, it takes about twice as much time for the Spalart-Allmaras model to execute one

45

iteration as it takes for the Baldwin-Lomax model (low magnetic Reynolds number formulation). However, that does not mean that a converged solution will be obtained by the Spalart-Allmaras in twice as much CPU time as by the Baldwin-Lomax model, since the number of iterations required to reach convergence is likely to depend on the turbulence model.

It is however very difficult to assess the convergence rate for each turbulence models. Many factors affect the convergence rate. Initial conditions, geometry, freestream conditions, numerical scheme, boundary conditions, time stepping method, and numerical stability influence the way a converged solution is reached. It is therefore impossible to predict with certainty which turbulence model would provide a converged solution in the least computational time. However, based on the experience gained with the utilization of the codes, the following comments can be made:

- The low magnetic Reynolds number formulation assumes a constant magnetic field (in time). It results in faster convergence rate than the full MHD equations solver because it eliminates the mutual interaction between the magnetic and velocity field. In the low magnetic Reynolds number formulation, only the magnetic field has an effect on the other flow properties, whereas when the full MHD equations are solved, the velocity field influences the magnetic field and vice-versa. This strong coupling results in a slower rate of convergence for the full MHD equations than for the low magnetic Reynolds number formulation.

- The Baldwin-Lomax model, which is an algebraic model, depends explicitly on the mean flow variables. Therefore, the build up of turbulent viscosity occurs rapidly. In comparison, one-equation and two-equation models require more computational time to generate the same amount of turbulent viscosity. Thus, the Baldwin-Lomax model tends to converge faster than one and two-equation models.

- The $k-\epsilon$ model has been found to be more unstable than other turbulence models. It usually requires a time step (or a CFL number for steady state solutions) two to ten times smaller than that of the Baldwin-Lomax model. Therefore, the $k-\epsilon$ model, which already requires the most computational time per iteration, usually requires also more iterations to converge. The $k-\epsilon$ turbulence model is by far the model that will converge the slowest.

- In order to accelerate the convergence of a given computation, the solution must be initialized with the most appropriate data. The first step in any investigation is to start by computing a laminar non-magnetic solution. Then, the magnetic field can be turned on and the solution is initialized from the previously computed laminar non-magnetic case. Similarly, a turbulent computation should be started from the laminar solution, and not from a cold start (constant freestream conditions within the entire domain).

46

The code based on the low magnetic Reynolds number formulation is more stable than the code solving the full MHD equations. The *CFL* number associated with LRMHD is typically two to five times larger than the *CFL* number associated with RAMHD.

Overall, the Baldwin-Lomax algebraic turbulence model is able to provide a converged solution in less computational time than any other turbulence models, due to its rapidity of execution and good stability. The $k - \epsilon$ two-equation model is the slowest and most unstable model. For applications where these two models provide the same level of accuracy, preference should be given to the Baldwin-Lomax model.

Chapter 5
Modifications of Turbulence Models For
Magnetohydrodynamic Flows

The turbulence models described in Chapter 4 are developed for the Reynolds Averaged Navier-Stokes equations. They are required because additional unknowns (Reynolds stresses) appear in the Reynolds Averaged Navier-Stokes equations. When investigating turbulent magnetohydrodynamic flows, the same filtering operations can be performed on the MHD equations. The resulting Reynolds Averaged MHD equations contain the Reynolds stresses that still require modeling, and additional unknowns usually referred to as magnetic Reynolds stresses, involving the fluctuations of the magnetic field. Due to the limited experimental data and theoretical investigation on how to model the magnetic Reynolds stresses, a simplified approach is considered where the effect of the magnetic field is modeled by modifying existing turbulence models.

5.1. Baldwin Lomax Model

The generalization of Prandtl mixing length concept was extended to MHD flows at low magnetic Reynolds number by Lykoudis and Brouillette [26]. In the inner region, the turbulent viscosity is now written as

$$\mu_{t_i} = \rho \kappa^2 y^2 (1 - e^{-y^+/A^+}) \gamma_2 \gamma_3 \omega \tag{5.1}$$

where

$$\gamma_2 = 1 - \exp\left\{ -\frac{y^+}{A^+}\left[\sqrt{\frac{1}{2}(A^+\lambda)^4 + 1} + \frac{1}{2}(A^+\lambda)^2 \right]^{1/2} \right\} \tag{5.2}$$

and

$$\gamma_3 = \exp(-A\lambda^2), \quad A = 700 \tag{5.3}$$

$$\lambda^2 = \frac{\sigma_e B^2 \mu}{\rho \tau_w} \tag{5.4}$$

The damping function and corresponding constants have been designed to match their experimental investigation of a channel flow of an electrically conducting fluid subject to a uniform transverse magnetic field [93]. It has been observed that when the skin friction is plotted versus the Hartmann number (while keeping the Reynolds number constant), all curves coincide on the same laminar line when the ratio Ha/Re is larger than $1/225$. This illustrates that the presence of a magnetic field tends to inhibit turbulence or initiates a relaminarization process. The main idea behind the damping function introduced by Lykoudis is that the magnetic field leads to a suppression of the correlation term $\overline{u'v'}$. The damping function was designed for flows with a transverse magnetic field, such that the damping acts directly on the u' fluctuation (the v' fluctuation is parallel to the transverse magnetic field).

5.2. Baldwin-Barth Model

The derivation of the modified Baldwin-Barth turbulence model is presented in this section. The Baldwin-Barth model was originally derived from the standard form of the $k-\epsilon$ model. Therefore, the modified version of the Baldwin-Barth model is derived from the modified $k-\epsilon$ model, which is described in Section 5.4.

Consider the incompressible $k-\epsilon$ model with magnetic terms:
k-equation:

$$\frac{Dk}{Dt} = P_k - \epsilon + \frac{\partial}{\partial x_i}\left[\left(v + \frac{v_t}{\sigma_k}\right)\frac{\partial k}{\partial x_i}\right] + \frac{NM_k}{\rho} \tag{5.5}$$

ϵ-equation:

$$\frac{D\epsilon}{Dt} = C_{\epsilon 1}\frac{\epsilon}{k}P_k - C_{\epsilon 2}\frac{\epsilon^2}{k} + \frac{\partial}{\partial x_i}\left[\left(v + \frac{v_t}{\sigma_\epsilon}\right)\frac{\partial \epsilon}{\partial x_i}\right] + \frac{NM_\epsilon}{\rho} \tag{5.6}$$

The effects of the magnetic field are modeled by the terms NM_k and NM_ϵ.

$$M_k = C'_{KN1}kB_iB_i \tag{5.7}$$

$$M_\epsilon = C'_{\epsilon N1}\epsilon B_iB_i \tag{5.8}$$

N is the interaction parameter

$$N = \frac{\sigma B^2 L}{\rho U} \tag{5.9}$$

In the Baldwin-Barth model, a new turbulent quantity is introduced, namely the turbulent Reynolds number, Re_T, which is defined as

$$Re_T = \frac{k^2}{v\epsilon} \tag{5.10}$$

or

$$vRe_T = \frac{k^2}{\epsilon} \tag{5.11}$$

Therefore

$$\frac{d(vRe_T)}{vRe_T} = 2\frac{dk}{k} - \frac{d\epsilon}{\epsilon} \tag{5.12}$$

This transformation can be applied for both the local derivative $\dfrac{\partial}{\partial t}$ and the convective derivative $\vec{U}\cdot\vec{\nabla}(vRe_T)$. Therefore, the substantial derivative satisfies the same transformation, i.e.,

$$\frac{1}{vRe_T}\frac{D(vRe_T)}{Dt} = \frac{2}{k}\frac{Dk}{Dt} - \frac{1}{\epsilon}\frac{D\epsilon}{Dt} \tag{5.13}$$

Substitution of Equations (5.5) and (5.6) in Equation (5.13) yields

49

$$\frac{1}{vRe_T}\frac{D(vRe_T)}{Dt} = \frac{2}{k}\left(P_k - \epsilon + \frac{\partial}{\partial x_i}\left[\left(v + \frac{v_t}{\sigma_k}\right)\frac{\partial k}{\partial x_i}\right] + \frac{NM_k}{\rho}\right)$$

$$-\frac{1}{\epsilon}\left(C_{\epsilon 1}\frac{\epsilon}{k}P_k - C_{\epsilon 2}\frac{\epsilon^2}{k} + \frac{\partial}{\partial x_i}\left[\left(v + \frac{v_t}{\sigma_\epsilon}\right)\frac{\partial \epsilon}{\partial x_i}\right] + \frac{NM_\epsilon}{\rho}\right) \qquad (5.14)$$

Equation (5.14) can be rearranged by omitting some terms according to the discussion by Baldwin and Barth [48]:

$$\frac{D(vRe_T)}{Dt} = (2 - C_{\epsilon 1})vRe_T\frac{P_k}{k} + (C_{\epsilon 2} - 2)k + \left(v + \frac{v_t}{\sigma_k}\right)\frac{\partial^2}{\partial x_i^2}(vRe_T)$$

$$-\frac{1}{\sigma_\epsilon}\frac{\partial}{\partial x_i}(v_t)\left[\frac{\partial}{\partial x_i}(vRe_T)\right] + vRe_T\left(\frac{2}{\rho k}NM_k - \frac{1}{\rho\epsilon}NM_\epsilon\right) \qquad (5.15)$$

From Equations (5.7) and (5.8):

$$\frac{2}{\rho k}NM_k = \frac{2}{\rho}NC'_{KN1}B_iB_i \qquad (5.16)$$

$$\frac{1}{\rho\epsilon}NM_\epsilon = \frac{N}{\rho}C'_{\epsilon N1}B_iB_i \qquad (5.17)$$

which can be combined into

$$\frac{2}{\rho k}NM_k - \frac{1}{\rho\epsilon}NM_\epsilon = \frac{N}{\rho}(2C'_{KN1} - C'_{\epsilon N1})B_iB_i \qquad (5.18)$$

Therefore, we obtain

$$\frac{D(vRe_T)}{Dt} = (2 - C_{\epsilon 1})vRe_T\frac{P_k}{k} + (C_{\epsilon 2} - 2)k + \left(v + \frac{v_t}{\sigma_k}\right)\frac{\partial^2}{\partial x_i^2}(vRe_T)$$

$$-\frac{1}{\sigma_\epsilon}\frac{\partial}{\partial x_i}(v_t)\left[\frac{\partial}{\partial x_i}(vRe_T)\right] + \frac{N}{\rho}(2C'_{KN1} - C'_{\epsilon N1})B_iB_i(vRe_T) \qquad (5.19)$$

For convenience, the following constant is defined

$$C_{Re_T} = 2C'_{KN1} - C'_{\epsilon N1} \qquad (5.20)$$

Thus, the effect of the magnetic field is modeled by the addition of the magnetic source term $\frac{N}{\rho}C_{Re_T}B_iB_i(vRe_T)$. The treatment of wall-bounded flows involves the introduction of damping terms in the production term and is assumed not to modify the magnetic term. Finally, the Baldwin-Barth turbulence model that accounts for the presence of a magnetic field is expressed as

50

$$\frac{D(vRe_T)}{Dt} = (C_{\epsilon 1} - C_{\epsilon 2})\sqrt{vRe_T P_k} + \left(v + \frac{v_t}{\sigma_k}\right)\frac{\partial^2}{\partial x_i^2}(vRe_T)$$

$$-\frac{1}{\sigma_\epsilon}\frac{\partial}{\partial x_i}(v_t)\left[\frac{\partial}{\partial x_i}(vRe_T)\right] + \frac{N}{\rho}C_{Re_T}B_iB_i(vRe_T) \qquad (5.21)$$

The closure coefficient associated with the additional magnetic term has been calibrated for the MHD Hartmann flow (Section 7.3) and its proposed value is $C_{Re_T} = 6.0$.

5.3. Spalart-Allmaras Model

The approach to modify the Spalart-Allmaras turbulence model in the presence of a magnetic field is different from the proposed modification concerning the other turbulence models. Here, no additional magnetic term is added to the partial differential equation governing the variable $\overline{v}$. Rather, the effect of the magnetic field is accounted for within the closure coefficient C_{v1}, which becomes a function of the magnetic field. The motivation behind this approach lies in the fact that the Spalart-Allmaras model is the model that performs the best in the prediction of the relaminarization process of the MHD Hartmann flow. In fact, when the model is used in its original form, it only slightly over predicts the relaminarization process. Therefore, instead of designing an additional magnetic term, it is proposed that an adjustment in the closure coefficient would be sufficient to extend the Spalart-Allmaras model to MHD flows.

As for the Baldwin-Lomax model, the objective of the proposed modification is to reduce the amount of turbulent viscosity. This can be accomplished by several mechanisms. The Spalart-Allmaras model solves an equation in terms of the turbulent quantity $\overline{v}$, which is directly related to the turbulent viscosity through the function f_{v1}. Therefore, it would be suitable to make f_{v1} a decreasing function of the magnetic strength. Another option would be to decrease the production of $\overline{v}$, or increase the dissipation of $\overline{v}$, or a combination of both.

Based on the analysis of the Hartmann flow (Section 7.3), it is proposed to modify the closure coefficient C_{v1} according to Equation (5.22):

$$C_{v1} = 7.1\min\left[2.6 + 1.6\tanh\left(4.43\frac{Ha}{Re} - 19.345\right) + 0.022\frac{Ha}{Re}, 4.225\right] \qquad (5.22)$$

The effect of this modification on the production, dissipation, and diffusion terms in the Spalart-Allmaras turbulence model is illustrated in Figure 5-1. All quantities have been normalized with their non-magnetic counterparts. As the coefficient C_{v1} increases, the production and diffusion terms are reduced, up to a little less than 10%. On the other hand, the dissipation term increases by about 10 %, leading to a reduction of the turbulent quantity $\overline{v}$ by about 20%.
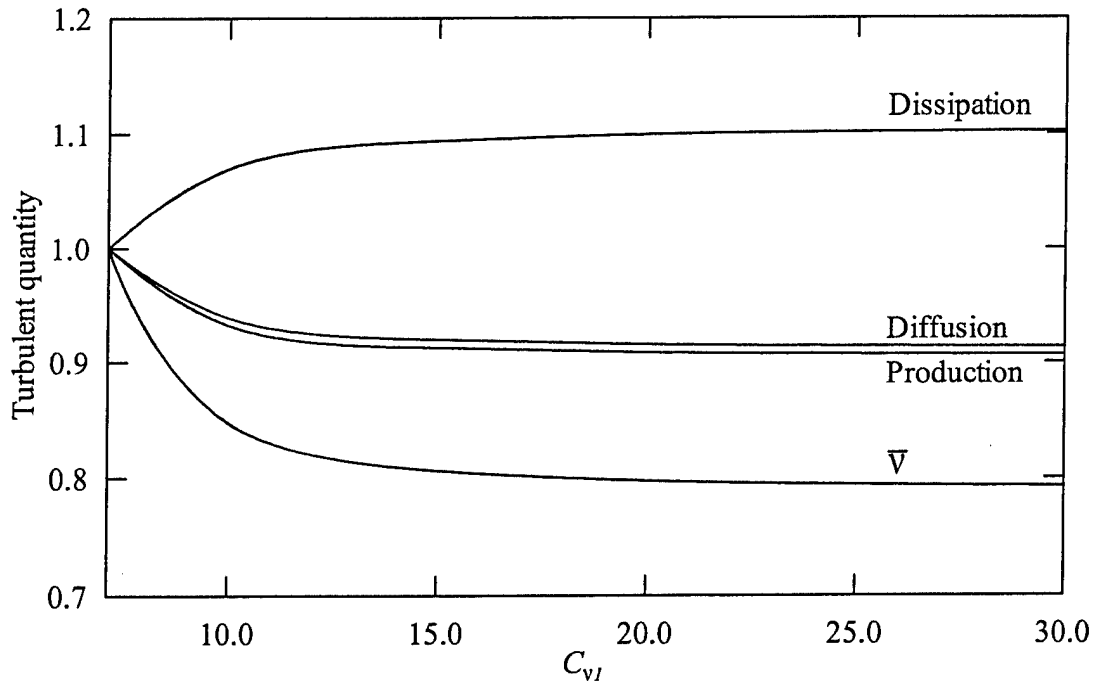
51

Figure 5-1. Effect of the closure coefficient C_{v1} on the turbulent terms
of the Spalart-Allmaras model.

5.4. k-ϵ Model

The $k - \epsilon$ model solves one equation for the turbulent kinetic energy and one equation for its dissipation rate. In the presence of a magnetic field, the fluctuations of the magnetic field must be incorporated into the model. The turbulent kinetic energy cannot be considered alone. A new turbulent variable is defined as the total turbulent energy composed of the turbulent kinetic energy and the turbulent magnetic energy. Mathematically, it is written as

$$E_t = \frac{1}{2}\overline{u_i' u_i'} + \frac{1}{2}S\overline{b_i' b_i'} \tag{5.23}$$

where

$$S = \frac{1}{\rho_\infty \mu_\infty}\left(\frac{B_\infty}{U_\infty}\right)^2 \tag{5.24}$$

and b_i are the fluctuations of the magnetic field. The first term in Equation (5.23) represents the turbulent kinetic energy and the second term represents the turbulent magnetic energy. The dissipation of the total turbulent energy is achieved by friction and Joule's heating. The dissipation rate ϵ must take into account these two mechanisms. However, since the magnitude of the fluctuations of the magnetic field is usually small, they are neglected and the total turbulent energy remains the same as the kinetic turbulent energy.

The effect of the magnetic field is incorporated into the $k - \epsilon$ model according to Kitamura et al [31] by adding magnetic terms to the k and ϵ equations. This model was designed for MHD channel flows at low magnetic Reynolds number. The fluctuation of

52

the electric field has been neglected and a more complex model was proposed by Shimomura [30]. Since the electric field is not modeled in this investigation, its fluctuations are not taken into account. Therefore, the magnetic terms developed by Kitamura are added to the $k - \epsilon$ model described in Section 4.5. The model becomes:

k-equation:

$$\frac{D(\rho k)}{Dt} = P_k - \rho\left(1 + \alpha M_t^2\right)\epsilon + \frac{1}{Re_\infty}\frac{\partial}{\partial x_i}\left[\left(\mu + \frac{\mu_t}{\sigma_k}\right)\frac{\partial k}{\partial x_i}\right] + L_k + NM_k \qquad (5.25)$$

ϵ-equation:

$$\frac{D(\rho\epsilon)}{Dt} = \left[C_{\epsilon 1}f_1 P_k - C_{\epsilon 2}f_2\rho\epsilon\right]\frac{\epsilon}{k} + \frac{1}{Re_\infty}\frac{\partial}{\partial x_i}\left[\left(\mu + \frac{\mu_t}{\sigma_\epsilon}\right)\frac{\partial\epsilon}{\partial x_i}\right] + L_\epsilon + NM_\epsilon \qquad (5.26)$$

where N is the interaction parameter

$$N = \frac{\sigma B^2 L}{\rho U} \qquad (5.27)$$

The magnetic effects are modeled by the terms NM_k and NM_ϵ,

$$M_k = C'_{KN1}kB_iB_i$$

$$M_\epsilon = C'_{\epsilon N1}\epsilon B_iB_i \qquad (5.28)$$

with

$$C'_{kN1} = -0.5$$

$$C'_{\epsilon N1} = -1.0$$

5.5. Combined k-ϵ/k-ω (Baseline and Shear Stress Transport) Model

The $k - \epsilon / k - \omega$ is a combination of the $k - \epsilon$ model, for which a modification has already been proposed in Section 5.4 and the $k - \omega$ model. The specific turbulent dissipation rate ω is directly related to the turbulent kinetic energy and its dissipation rate by the relation

$$\omega = \frac{\epsilon}{\beta^* k} \qquad (5.29)$$

Therefore, it is possible to transform the additional term in the ϵ-equation by using the change of variable (5.29) to obtain a magnetic term for the ω-equation. Subsequently, the following $k - \epsilon / k - \omega$ model is proposed. This modification applies to both the Baseline and Shear Stress Transport models.

53

$$\frac{D(\rho k)}{Dt} = P_k - \beta^* \rho \omega k + \frac{\partial}{\partial x_i}\left[\left(\mu + \frac{\mu_t}{\sigma_k}\right)\frac{\partial k}{\partial x_i}\right] + NM_k \tag{5.30}$$

$$\frac{D(\rho \omega)}{Dt} = \frac{\gamma \rho}{\mu_t} P_k - \beta \rho \omega^2 + \frac{\partial}{\partial x_i}\left[\left(\mu + \frac{\mu_t}{\sigma_\omega}\right)\frac{\partial \omega}{\partial x_i}\right]$$
$$+ 2\rho(1 - F_1)\sigma_{\omega 2}\frac{1}{\omega}\frac{\partial k}{\partial x_i}\frac{\partial \omega}{\partial x_i} + NM_\omega \tag{5.31}$$

The effect of the magnetic field is introduced in the following two additional terms

$$M_k = C'_{KN1} k B_i B_i$$
$$M_\omega = C'_{\omega N1} \omega B_i B_i$$

The closure constants need to be determined and tailored for the application they are designed for. The numerical investigation performed in Section 7.3 on the turbulent Hartmann flow leads to the following values:

Baseline model:
$$C'_{KN1} = 3.0$$
$$C'_{\omega N1} = -1.5$$

SST model:
$$C'_{KN1} = 1.0$$
$$C'_{\omega N1} = -0.5$$

Chapter 6
Hypersonic Chemistry

6.1. General Background

The definition of hypersonic is not as clearly defined as supersonic. The edge of the hypersonic regime, or the "heat barrier" lies between Mach 3 and Mach 5. The hypersonic realm starts when the air behind shock waves reaches extremely high pressures and temperatures. Some phenomena, such as increasing temperature and the formation of a shock layer[*] become considerable at about Mach 3. Others, such as chemical reactions, do not have a significant effect until about Mach 7 or more. The most notable chemical changes that air undergoes as temperature increases are summarized in Table 6-1.

Temperature [K]	Chemical change
800	Molecular vibration
2500	Oxygen molecules (O_2) dissociate
4000	Nitrogen molecules (N_2) dissociate
6000	Nitric oxide (NO) forms
9000	Oxygen and nitrogen atoms ionize

Table 6-1. High-temperature effects on air at standard conditions.

In the hypersonic regime, the assumption of air as a calorically perfect gas is no longer valid. For a calorically perfect gas, the ratio of specific heats γ is constant and the internal energy e is typically a function of temperature only. For chemically reacting flow, e is a function of both temperature and pressure, and γ is no longer a constant.

Three chemical states may be defined, namely frozen, equilibrium and nonequilibrium. The determination of the chemical states is based on the relative importance of the following characteristic times: τ_f, the time for a fluid element to traverse the flow field of interest and τ_c, the time for the chemical reactions and / or vibrational energy to approach equilibrium. In chemically frozen flow, no chemical
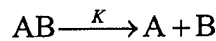
---

[*] The distance between the shock wave and the surface of a hypersonic body decreases with Mach number. The resulting flow field between the surface and shock is referred to as a shock layer.

reactions take place. In other words, τ_c tends to infinity. On the other hand, in chemical equilibrium, reactions are assumed to be instantaneous i.e., τ_c equals zero. Chemical equilibrium may be a good approximation if τ_c is negligible compared to τ_f. In reality, chemical reactions do not take place instantaneously and τ_c may be of the same order of magnitude as τ_f. In this case, the flow is in chemical nonequilibrium. Table 6-2 provides a summary of the criteria for the distinction of the chemical states.

$\tau_f \ll \tau_c$	Frozen flow
$\tau_f \approx \tau_c$	Nonequilibrium flow
$\tau_f \gg \tau_c$	Equilibrium flow

Table 6-2. Chemical states criteria.

These concepts are graphically illustrated in the Figure 6-1. For the sake of simplicity, consider the following reaction of dissociation of chemical species AB into species A and species B.

$$AB \xrightarrow{\ K\ } A + B$$

where K is chemical rate constant.

Chemically frozen flow :
No dissociation of species AB

Chemical nonequilibrium :
Partial dissociation of species AB

Chemical equilibrium :
Full dissociation of species AB

Fluid particle
upstream of shock wave
(low - temperature environment)

Same particle
right downstream of shock wave
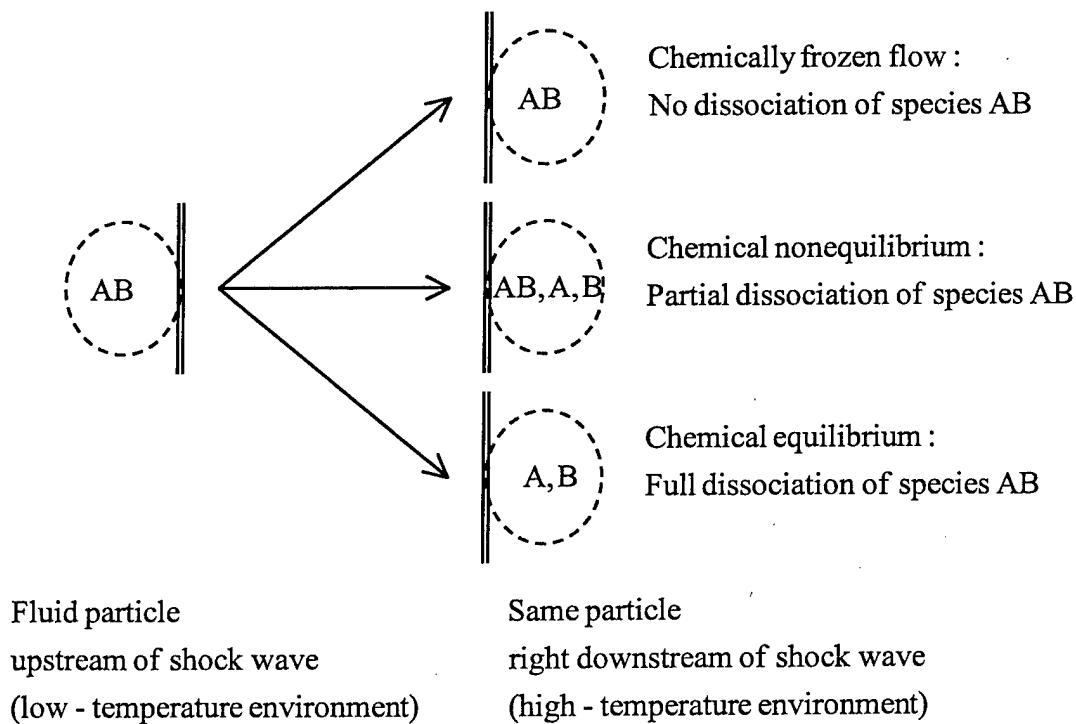(high - temperature environment)

Figure 6-1. Illustration of the chemical states.

For the purpose of illustration, consider a fluid particle crossing a normal shock wave at hypersonic regime. Upstream of the shock wave, freestream conditions and low temperature are assumed. In contrast, the downstream of the shock wave is a high-temperature region. Recall that the chemical reactions considered in the present case are enhanced as the temperature is increased (chemical rate constant K increases with temperature). Thus, the upstream region is not favorable to chemical reactions unlike the downstream region. Now, to determine whether or not chemical reactions have a significant effect on the flow composition, it is necessary to compare the chemical time scale τ_c and the flow time scale τ_f. In other words, how long does the fluid particle take to cross the shock wave and how much time does the chemical reaction take to complete? If the particle crosses the shock wave in a too brief time compared to the reaction time, its chemical composition is unchanged: this is the frozen state. On the contrary, if the reaction is instantaneous, species AB has the time to dissociate completely into A and B: this is chemical equilibrium. An intermediate state is chemical nonequilibrium for which the dissociation of AB in the immediate postshock region is partial.

Note. In the case of a chemical nonequilibrium steady-state solution, there is no local time rate of change in any property. In other words, at a given location downstream of the shock wave, the field chemical composition is invariant with time. However, the composition of a fluid particle, as it moves further downstream, changes. For instance, the fluid particle may have a nonequilibrium chemical composition (AB, A and B) in the vicinity of the shock wave, and an equilibrium composition (A and B) at another location farther downstream, if the reaction has time to complete.

6.2. Thermochemical Models

Various thermochemical models to simulate high-temperature effects using CFD techniques have been proposed by several investigators [94, 95]. Modeling chemical equilibrium can be accomplished by incorporating tables and curve fits of thermodynamic properties [96]. On the other hand, computing chemical and possible thermal nonequilibrium is far more complex due to the abundance of the species present in the medium and the various energy levels that must be taken into account. Moreover, it requires the solution of species conservation equations. Extension of CFD algorithms to nonequilibrium chemistry has been accomplished by several investigators [97-99].

In magnetogasdynamics, literature generally contains studies about nonequilibrium calculations involving noble gases and possibly nitrogen [100]. However, only a few MGD computations with nonequilibrium air have been reported [86, 101]. In order to simulate the flight environment of hypersonic vehicles in the atmosphere, it is necessary to use air as the working medium instead of a plasma of given species.

In the present research, air thermochemical properties are computed by a five-species, seventeen-reaction nonequilibrium chemical model, associated with a one-

temperature model, based on a scheme employed by Chiang [102]. The temperature model is modified to account for the magnetic field energy.

Physically, fluid motion and chemical reactions are intrinsically coupled. Thus, solving both simultaneously is a logical procedure called the "coupled method". If such an approach were selected, a modification of the flux vectors and the flux Jacobian matrices would be required to account for the mass conservation of the chemical species. This would result in a large system of equations. The system eigenstructure (used in the TVD scheme) would have to be determined again. A simpler approach, known as "loosely coupled method" or "chemistry-split" is to solve the MGD equations and chemistry equations separately in an iterative fashion. The gas constant R and the ratio of specific heats γ are considered as functions of both time and space. The chemical reactions affect the fluid motion in two ways, namely via pressure and temperature. The change in pressure Δp and the change in temperature ΔT are expressed as the sum of those due to the ideal gas and those due to the chemical reactions.

In chemically reacting flows at high temperatures, nonequilibrium vibrational temperature becomes important. Disregarding the nonequilibrium vibrational temperature certainly degrades the accuracy of the numerical predictions, but reduces the complexity of the numerical scheme and the computational effort. Conscious of this issue, the author prefers developing the chemistry model using a one-temperature model, while not excluding the implementation of multitemperature model, in future studies. For example, a two-temperature model [95] may be selected for its comprehensive and concise treatment of vibrational and electronic energies, and due to its computational efficiency compared to higher-order multitemperature models.

In the following sections, nonequilibrium and equilibrium models are described.

6.3. Procedure For Chemical Nonequilibrium

6.3.1. Thermochemical Equations

- **Chemical model**
  The proposed model is based on the following reactions:
  - thermal dissociation of air molecules:

$$O_2+M \rightleftharpoons 2O+M \qquad (6\text{-}1)$$

$$N_2+M \rightleftharpoons 2N+M \qquad (6\text{-}2)$$

$$NO+M \rightleftharpoons N+O+M \qquad (6\text{-}3)$$

  - exchange reactions involving NO:

$$NO+O \rightleftharpoons N+O_2 \qquad (6\text{-}4)$$

$$O+N_2 \rightleftharpoons N+NO \tag{6-5}$$

where M represents a third body, which can be either O_2, N_2, NO, O or N. Thus, seventeen reactions involving five chemical species are considered.

- **Thermodynamic model**

The specific internal energy for a species s is expressed as

$$e_s = e_{t,s} + e_{e,s} + e_{0,s} \quad \text{for an atom,} \tag{6-6a}$$

$$e_s = e_{t,s} + e_{r,s} + e_{v,s} + e_{e,s} + e_{0,s} \quad \text{for a molecule.} \tag{6-6b}$$

where $e_{t,s}$, $e_{r,s}$, $e_{v,s}$, $e_{e,s}$ and $e_{0,s}$ represent the translational, rotational, vibrational electronic and zero-point specific energies, respectively. Statistical thermodynamics, for chemical species assumed perfect gas, leads to the following expressions.

$$e_{t,s} = \frac{3}{2}R_s T \quad (6\text{-}7a) \qquad e_{r,s} = R_s T \quad (6\text{-}7b) \qquad e_{v,s} = \frac{\theta_{v,s}/T}{e^{\theta_{v,s}/T}-1}R_s T \quad (6\text{-}7c)$$

where T is the system temperature[*].

$R_s = \Re/M_s$ defines the specific gas constant of chemical species s.

$\theta_{v,s}$ denotes the characteristic vibrational temperature for polyatomic species s.

In this model, the electronic energy is neglected. For air, neglecting this energy is a reasonable assumption, which induces an error less than 1% [97]. The zero-point energy is replaced by the heat of formation $h_{0,s}$. Thus, the internal specific energy is rewritten as

$$e_s = \frac{3}{2}R_s T + h_{0,s} \quad \text{for an atom,} \tag{6-8a}$$

$$e_s = \frac{3}{2}R_s T + R_s T + \frac{R_s \theta_{v,s}}{e^{\theta_{v,s}/T}-1} + h_{0,s} \quad \text{for a diatomic molecule.} \tag{6-8b}$$

Chemical properties (molar masses, heats of formation and characteristic vibrational temperatures) for species O_2, N_2, NO, O or N are provided in Appendix E.

- **Chemical governing equations**

The nonequilibrium species continuity equation for a three-dimensional inviscid flow is expressed in a flux-vector form as

$$\frac{\partial \boldsymbol{Q}_c}{\partial t_c} + \frac{\partial \boldsymbol{E}_c}{\partial x} + \frac{\partial \boldsymbol{F}_c}{\partial y} + \frac{\partial \boldsymbol{G}_c}{\partial z} = \dot{\boldsymbol{W}}_c \tag{6-9}$$

where

---

[*] In a one-temperature model, the system temperature is associated to the translational temperature.

$$
Q_c = \left\{ \begin{array}{c} \rho c_1 \\ \rho c_2 \\ \rho c_3 \\ \vdots \\ \rho c_s \\ \vdots \\ \rho c_{SM} \end{array} \right\}, \quad
E_c = \left\{ \begin{array}{c} \rho u c_1 \\ \rho u c_2 \\ \rho u c_3 \\ \vdots \\ \rho u c_s \\ \vdots \\ \rho u c_{SM} \end{array} \right\}, \quad
F_c = \left\{ \begin{array}{c} \rho v c_1 \\ \rho v c_2 \\ \rho v c_3 \\ \vdots \\ \rho v c_s \\ \vdots \\ \rho v c_{SM} \end{array} \right\}, \quad
G_c = \left\{ \begin{array}{c} \rho w c_1 \\ \rho w c_2 \\ \rho w c_3 \\ \vdots \\ \rho w c_s \\ \vdots \\ \rho w c_{SM} \end{array} \right\}, \quad
\dot{W}_c = \left\{ \begin{array}{c} \dot{w}_1 \\ \dot{w}_2 \\ \dot{w}_3 \\ \vdots \\ \dot{w}_s \\ \vdots \\ \dot{w}_{SM} \end{array} \right\}
$$

(6-10a)   (6-10b)   (6-10c)   (6-10d)   (6-10e)

ρ is the mixture density, u, v and w are the fluid velocity components.

Index $s \in \{1, 2, 3, \cdots, SM\}$ denotes the chemical species s. $SM = 5$ is the number of chemical species.

c_s is the mass fraction of species s.

$\dot{w}_s$ represents the mass change rate of species s.

$$
\dot{w}_s = M_s \frac{d[A_s]}{dt} \tag{6-11}
$$

A_s is the symbol for species s i.e., O_2, N_2, NO, O or N.

$[A_s]$ is the concentration of species s (mole per unit volume).

$$
[A_s] = \frac{\rho c_s}{M_s} \tag{6-12}
$$

At chemical equilibrium, $\left. \dfrac{d[A_s]}{dt} \right|_{net} = 0$.

- **Chemical kinetics**

Given a reacting mixture of SM species undergoing the general elementary reaction

$$
\sum_{s=1}^{SM} v_s^R A_s \underset{K_b}{\overset{K_f}{\rightleftharpoons}} \sum_{s=1}^{SM} v_s^P A_s \tag{6-13}
$$

where K_f and K_b are the forward rate constant and backward rate constant, respectively. v_s^R and v_s^P are the stoichiometric coefficients of reactants and products, respectively. The reaction rates are expressed as follows.

Forward rate:
$$
\left. \frac{d[A_s]}{dt} \right|_f = \left(v_s^P - v_s^R \right) K_f \prod_{s=1}^{SM} [A_s]^{v_s^R} \tag{6-14}
$$

Backward (or reverse) rate:
$$
\left. \frac{d[A_s]}{dt} \right|_b = \left(v_s^R - v_s^P \right) K_b \prod_{s=1}^{SM} [A_s]^{v_s^P} \tag{6-15}
$$

Net rate of formation:
$$
\left. \frac{d[A_s]}{dt} \right|_{net} = \left. \frac{d[A_s]}{dt} \right|_f + \left. \frac{d[A_s]}{dt} \right|_b \tag{6-16}
$$

The net rate of formation of A_s can be rewritten as

$$\frac{d[A_s]}{dt}\bigg|_{net} = \left(v_s^P - v_s^R\right)\left(K_f \prod_{s=1}^{SM}[A_s]^{v_s^R} - K_b \prod_{s=1}^{SM}[A_s]^{v_s^P}\right) \tag{6-17}$$

Expanded expressions of Equation (6-17) for each of the five chemical species are provided in Appendix F.

K_f is obtained empirically using the modified Arrhenius equation expressed as

$$K_f(T) = CT^\alpha\, e^{-e_a/kT} \tag{6-18}$$

where e_a is the activation energy, k is the Boltzmann constant, C and α are constants provided in Appendix E.

In a scheme presented by Park [103], K_b is evaluated as

$$K_b = \frac{K_f}{K_e} \tag{6-19}$$

K_e is the equilibrium constant, which is expressed in a functional form as

$$K_e(T) = \exp\left(A_1 + A_2 \ln Z + A_3 Z + A_4 Z^2 + A_5 Z^3\right) \tag{6-20}$$

where $Z = 10,000/T[K]$ and coefficients A_1 through A_5 are provided in Appendix E.

The numerical data contained in Appendix E are dimensional, therefore, a nondimensionalization consistent with that presented in Section 2.1.2 is required.

- **Generalized coordinates**

  Equation (6-9) in the physical space is expressed in the computational space as

$$\frac{\partial \overline{Q}_c}{\partial t_c} + \frac{\partial \overline{E}_c}{\partial \xi} + \frac{\partial \overline{F}_c}{\partial \eta} + \frac{\partial \overline{G}_c}{\partial \zeta} = \overline{W}_c \tag{6-21}$$

where

$$\overline{Q}_c = \frac{Q_c}{J} \tag{6-22a}$$

$$\overline{E}_c = \frac{1}{J}\left(\xi_x E_c + \xi_y F_c + \xi_z G_c\right) \tag{6-22b}$$

$$\overline{F}_c = \frac{1}{J}\left(\eta_x E_c + \eta_y F_c + \eta_z G_c\right) \tag{6-22c}$$

$$\overline{G}_c = \frac{1}{J}\left(\zeta_x E_c + \zeta_y F_c + \zeta_z G_c\right) \tag{6-22d}$$

$$\overline{W}_c = \frac{W_c}{J} \tag{6-22e}$$

The chemical flux Jacobian matrices are defined as follows.

$$\overline{A}_c = \frac{\partial \overline{E}_c}{\partial \overline{Q}_c} = \xi_x A_c + \xi_y B_c + \xi_z C_c \tag{6-23a}$$

$$\overline{B}_c = \frac{\partial \overline{F}_c}{\partial \overline{Q}_c} = \eta_x A_c + \eta_y B_c + \eta_z C_c \tag{6-23b}$$

61

$$\overline{C}_c = \frac{\partial \overline{G}_c}{\partial \overline{Q}_c} = \zeta_x A_c + \zeta_y B_c + \zeta_z C_c \qquad (6\text{-}23c)$$

$$\overline{D}_c = \frac{\partial \overline{\dot{W}}}{\partial \overline{Q}_c} = \frac{\partial \dot{W}}{\partial Q_c} \qquad (6\text{-}23d)$$

where

$$A_c = \frac{\partial E_c}{\partial Q_c} = u\mathbf{I} \qquad (6\text{-}24a)$$

$$B_c = \frac{\partial F_c}{\partial Q_c} = v\mathbf{I} \qquad (6\text{-}24b)$$

$$C_c = \frac{\partial C_c}{\partial Q_c} = w\mathbf{I} \qquad (6\text{-}24c)$$

That is to say,

$$\overline{A}_c = \overline{U}\mathbf{I} \qquad (6\text{-}25a)$$

$$\overline{B}_c = \overline{V}\mathbf{I} \qquad (6\text{-}25b)$$

$$\overline{C}_c = \overline{W}\mathbf{I} \qquad (6\text{-}25c)$$

where $\overline{U}$, $\overline{V}$ and $\overline{W}$ represent the contravariant velocities and $\mathbf{I}$ is the $SM \times SM$ identity matrix. Chemical Jacobian matrix $\overline{D}_c$ is provided in Appendix G.

- **Boundary conditions**

Boundary conditions for the conservative variable $\overline{Q}_c$ are required for the solution of Equation (6-21). They involve, in general, a surface chemistry interaction with the gas at the wall and they depend on the wall catalyticity. The catalyticity is the property of a substance to enable a chemical reaction to proceed at a usually faster rate or under different conditions than otherwise possible. A fully catalytic wall is a wall at which chemical reactions are catalyzed at an infinite rate. In other words, the mass fractions at the wall are their local equilibrium values at the local pressure and temperature at the wall. A partially catalytic wall is a wall at which chemical reactions are catalyzed at a finite rate. A noncatalytic wall is a wall at which no chemical reaction takes place. Depending on the case considered, the boundary conditions on c_s are summarized in the Table 6-3.

$\left(\dot{w}_c\right)_w = 0 \Leftrightarrow \left(\vec{\nabla} c_s \cdot \vec{n}\right)_w = 0$	Noncatalytic wall
$\left(\dot{w}_c\right)_w = \rho D_s \left(\vec{\nabla} c_s \cdot \vec{n}\right)_w$	Partially catalytic wall
$\left(c_s\right)_w = \left(c_s\right)_{equilibrium}$	Fully catalytic wall

Table 6-3. Boundary conditions on c_s and wall catalyticity.

In the present chemical model, diffusion phenomena are not represented (the flow is assumed inviscid), and boundary conditions at the wall are specified assuming noncatalytic wall.

6.3.2. Numerical Method

Due to the good stability characteristic of implicit methods, an implicit flux-vector splitting is selected to solve Equation (6-21). The flux-vector splitting method for the two-dimensional case is described in Appendix H.

Figure 6-2 contains a flow chart of the computational scheme for nonequilibrium flow simulations. The integration of the loosely coupled scheme is performed according to the steps listed below.

(i) MGD equations are solved for the conservative variable $\overline{Q}$ by the four-stage modified Runge-Kutta scheme, as described in Chapter 3. This intermediate solution (before chemistry adjustment) is denoted by a prime.

$$\overline{Q}' = \overline{Q}^n + \Delta\overline{Q} \qquad (6\text{-}26)$$

Primitive variables such as pressure, p', temperature, T', etc. can be evaluated using conservative variables. At this step, the mass fractions, c_s^n, the ratio of specific heats, γ^n and the gas constant of the mixture, R^n are held to their previous values.

(ii) The mass change rate $\dot{w}_s$ is evaluated according to Equations (6-11) and (6-17), using T', c_s^n and ρ'. Subsequently, unknowns $\Delta(\rho c_s)$ in the chemistry equations can be evaluated using c_s^n, ρ', $(\rho u)'$, $(\rho v)'$, $(\rho w)'$ and $\dot{w}_s$. Intermediate partial densities are computed as

$$(\rho c_s)' = \rho' c_s^n + \Delta(\rho c_s) \qquad (6\text{-}27)$$

The species mass fractions are updated by

$$c_s^{n+1} = \frac{(\rho c_s)'}{\sum\limits_{s=1}^{SM} (\rho c_s)'} \qquad (6\text{-}28)$$

and the mixture gas constant is evaluated as

$$R^{n+1} = \sum\limits_{s=1}^{SM} \frac{c_s^{n+1} \Re}{M_s} \qquad (6\text{-}29)$$

(iii) Translational temperature is computed assuming that pressure p', momentum components, $(\rho u)'$, $(\rho v)'$, $(\rho w)'$, magnetic field components, B_x', B_y', B_z', and total enthalpy, h_t' are invariant during the chemistry step (ii). That is to say,

$$p^{n+1} = p' \quad \text{(6-30a)} \qquad (\rho u)^{n+1} = (\rho u)' \quad \text{(6-30b)} \qquad (\rho v)^{n+1} = (\rho v)' \quad \text{(6-30c)}$$

$$(\rho w)^{n+1} = (\rho w)' \quad \text{(6-30d)} \qquad B_x^{n+1} = B_x' \quad \text{(6-30e)} \qquad B_y^{n+1} = B_y' \quad \text{(6-30f)}$$

$$B_z^{n+1} = B_z' \quad \text{(6-30g)} \qquad h_t^{n+1} = h_t' \quad \text{(6-30h)}$$

By definition of the total enthalpy,

$$h_t^{n+1} = e_t^{n+1} + \frac{p^{n+1}}{\rho^{n+1}} \tag{6-31}$$

where

$$e_t^{n+1} = e^{n+1} + \frac{1}{2\rho^{n+1}} \left\{ \left[(\rho u)^{n+1} \right]^2 + \left[(\rho v)^{n+1} \right]^2 + \left[(\rho w)^{n+1} \right]^2 + \frac{1}{\mu_{e0}} \left[\left(B_x^{n+1} \right)^2 + \left(B_y^{n+1} \right)^2 + \left(B_z^{n+1} \right)^2 \right] \right\} \tag{6-32}$$

with

$$\rho^{n+1} = \frac{p^{n+1}}{R^{n+1} T^{n+1}} = \frac{p'}{R^{n+1} T^{n+1}} \tag{6-33}$$

$$e^{n+1} = \sum_{s=1}^{SM} c_s^{n+1} e_s \tag{6-34}$$

Substitution of Equations (6-32) through (6-34) into Equation (6-31) yields

$$h_t^{n+1} = h_t' = \sum_{s=1}^{SM} c_s^{n+1} e_s + R^{n+1} T^{n+1}$$

$$+ \frac{1}{2} \left\{ \left[(\rho u)' \right]^2 + \left[(\rho v)' \right]^2 + \left[(\rho w)' \right]^2 + \frac{1}{\mu_{e0}} \left[(B_x')^2 + (B_y')^2 + (B_z')^2 \right] \right\} \frac{\left(R^{n+1} \right)^2 \left(T^{n+1} \right)^2}{(p')^2} \tag{6-35}$$

where the internal specific energy e_s is expressed by Equations (6-8a) and (6-8b).

The unknown in this equation is the translational temperature T^{n+1}, which is determined using the Newton-Raphson method.

(iv) Once the translational temperature is known, all the properties can be updated as follows.

$$\rho^{n+1} = \frac{p'}{R^{n+1} T^{n+1}} \tag{6-36a}$$

$$u^{n+1} = \frac{(\rho u)'}{\rho^{n+1}} \tag{6-36b}$$

$$v^{n+1} = \frac{(\rho v)'}{\rho^{n+1}} \tag{6-36c}$$

$$w^{n+1} = \frac{(\rho w)'}{\rho^{n+1}} \tag{6-36d}$$

$$B_x^{n+1} = B_x' \tag{6-36e}$$

64

$$B_y^{n+1} = B_y' \tag{6-36f}$$

$$B_z^{n+1} = B_z' \tag{6-36g}$$

$$\left(\rho e_t\right)^{n+1} = \rho^{n+1} h_t' - p' \tag{6-36h}$$

$$\left(\rho e\right)^{n+1} = \left(\rho e_t\right)^{n+1}$$
$$-\frac{1}{2}\rho^{n+1}\left[\left(u^{n+1}\right)^2 + \left(v^{n+1}\right)^2 + \left(w^{n+1}\right)^2\right] - \frac{1}{2\mu_{e0}}\left[\left(B_x^{n+1}\right)^2 + \left(B_y^{n+1}\right)^2 + \left(B_z^{n+1}\right)^2\right] \tag{6-36i}$$

$$\gamma^{n+1} = \frac{p'}{\left(\rho e\right)^{n+1}} + 1 \tag{6-36j}$$

The steps (i) through (iv) are repeated until a convergence criterion is satisfied. The criterion is usually expressed as

$$\sum_{i=1}^{IM}\sum_{j=1}^{JM}\sum_{k=1}^{KM}\left|\frac{f_{i,j,k}^{n+1} - f_{i,j,k}^n}{f_{i,j,k}^n}\right| < \varepsilon_f$$

where f is a property such as temperature, or species mass fraction, and ε_f is a prescribed value for this property.
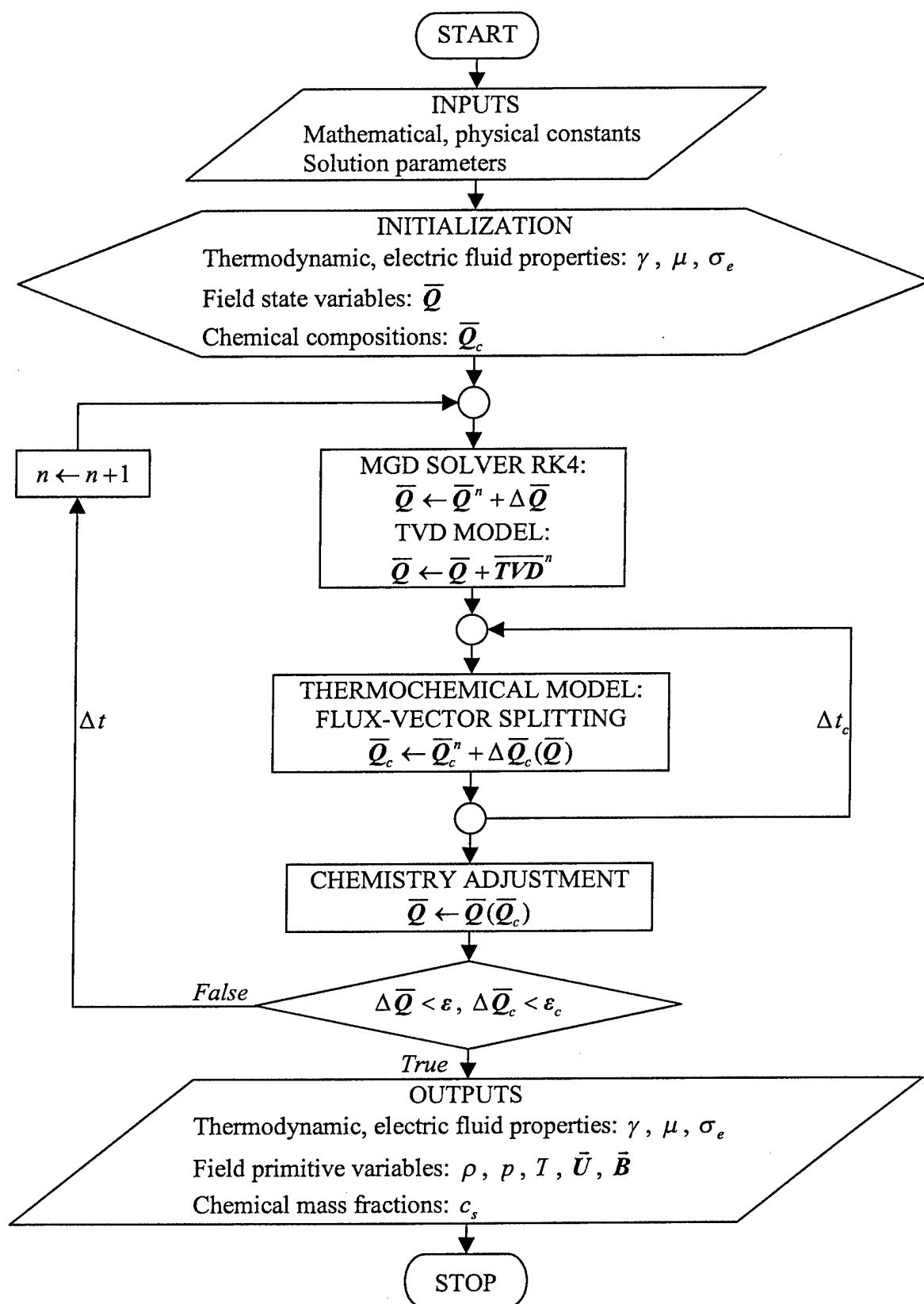
Figure 6-2. Program flow chart for nonequilibrium computations.

6.3.3. Numerical Issues And Model Limitations

The coupling of thermochemical equations and MGD equations generally leads to a set of stiff partial differential equations. The stiffness is due to the disparity between the rates of some chemical reactions and the rate of bulk flow properties. More specifically, stiffness is associated with high reaction rates. In order to overcome the intrinsic difficulty, an implicit time marching solution technique has been chosen over an explicit method. Moreover, as shown in Figure 6-2, two loops are considered, namely an outer loop with a computational time step Δt for the solution of the MGD equations, and an inner loop for the chemistry model with a time step Δt_c, which is in general different from Δt by several orders of magnitude. The computational time steps can be determined using the von Neumann stability analysis, as reported in Reference [104].

In theory, for a chemical system of SM species, only $SM-1$ species conservation equations have to be added to the frozen MGD equations, which include the global continuity equation. One of the species variables can be expressed as a combination of the others, via the continuity equation. However, in practical computations, redundancy in the conservation equations (SM species equations instead of $SM-1$) is preferable. Indeed, if one of the species, say A, is expressed as a combination of others, numerical error on each of the species variables is compounding on the A value. If the A species is dominant and the A value is large, then the error may be negligible. However, in strongly reacting flow, no such dominant species exists. If the A value becomes small, the compounded error may be a large fraction of the true value of A. The consequence of retaining the redundant species equation is that the numerical error now causes the sum of species concentrations to deviate from the overall mass.

Another source of stiffness is due to the nonlinearity of the mass production rate terms. The equations associated with the kinetics of chemical reactions, e.g. Equation (6-17), are nonlinear in species concentrations. The exponents are the stoichiometric coefficients. The nonlinearity worsens stiffness when negative concentrations occur as a consequence of numerical errors (round-off and truncation). In many intances, a small negative concentration value amplifies into a large negative value. Moreover, a negative value in one species concentration leads to negative concentration values for other species. In order to prevent system degeneration, negative concentrations are overwritten, but this violates the conservation of mass. To overcome the problem of mass conservation violation, the species mass fractions are renormalized after each integrating step, so that after modification, their sum equals unity.

As mentioned previously, a one-temperature model is selected for the sake of simplicity and for minimization of the computation time. However, several issues are associated with the use of a one-temperature model. The question of solution accuracy has been already discussed. Another issue is the sensitivity of computation to numerical errors and the stiffness of the chemical reactions behind a shock wave. Indeed, in a one-temperature model, the temperature at the first node point behind a shock wave is very high, and therefore, the chemical reaction rates and their associated Jacobian elements become very large. A small numerical error in the postshock conditions results in a large

error in the rate of dissociation at that point. In contrast, with a two-temperature model, the vibrational temperature is very low behind the shock, and so chemical reaction rates are nearly zero there. Chemical reaction rates become large only after a few node points downstream of the shock.

The current thermochemical model is designed to simulate seventeen chemical reactions involving five chemical species. Ionization is not considered. As indicated in Table 6-1, ionization begins at about 9,000 K, a temperature reached only in high hypersonic regime. The accuracy of the solution can be considered a posteriori by checking the maximum temperature in the flow field. In most of the simulations in the current investigation, the onset temperature of ionization should not be reached. Though ionization is not included, the gas is still assumed to possess some level of electrical conductivity (for magnetic interaction).

Finally, the model presented does not include the diffusion terms. It cannot be applied to simulations of viscous flows.

6.4. Procedure For Chemical Equilibrium

The chemical composition of air for many applications is not required, in which case only thermodynamic properties need to be computed, using a curve-fit procedure. The thermodynamic properties are obtained using the following correlations.

(i) $\tilde{\gamma} = \tilde{\gamma}(\rho, e)$ where $\tilde{\gamma} = h/e$

from which pressure is evaluated as $p = \rho e(\tilde{\gamma} - 1)$

(ii) $T = T(\rho, e)$

(iii) $\tilde{\gamma} = \tilde{\gamma}(\rho, p)$

and enthalpy is calculated as $h = \dfrac{p}{\rho} \dfrac{\tilde{\gamma}}{\tilde{\gamma} - 1}$

(iv) $T = T(\rho, p)$

The procedure developed by Tannehill et al. [96] is summarized in Reference [105].

Chapter 7
Results and Discussions

The results of computations, comparisons of the results to experimental data or other solutions, and subsequent discussions are presented in this chapter. The first stage of this investigation was the implementation of turbulence models. Their performances are first compared with experimental data for a supersonic flow over a compression corner, in Section 7.1. Although this test case represents by itself a challenging application, it addresses the accuracy and limitations of turbulence models based on the Reynolds Averaged Navier-Stokes formulation. Next, the MHD solver is examined for simple but fundamental MHD problems in Section 7.2. The MHD Rayleigh problem is numerically solved and compared to the existing analytical solution. The supersonic flow over a blunt body is also investigated and the shock standoff distance compared to analytical solution. Subsequently, the turbulent MHD Hartmann flow is used to calibrate the proposed modifications of the turbulence models to account for the presence of a magnetic field (Section 7.3). The key-feature of this type of flow is the relaminarization process that has been experimentally observed. Once the turbulence models have been calibrated, they are applied for the turbulent supersonic flow over a flat plate in Section 7.4. Here, the effect of the magnetic field on the skin friction is investigated. Finally, the turbulent flow over a cone is investigated to assess the possible reduction of the heat transfer by application of a magnetic field (Section 7.5). The performance of the algorithm in the simulation of hypersonic flows over blunt bodies is explored for the case of a hemisphere and a cylinder-wedge, for which hypersonic chemistry modeling is also included (Sections 7.6 to 7.8).

7.1. Supersonic Flow over a Compression Corner

The accuracy of the turbulence models is investigated in this section. The results are compared to the experimental data obtained by Settles [106, 107] for a Mach 2.85 flow over a 24 degrees compression corner, without magnetic field. The flow is fully turbulent and the incoming boundary layer thickness is $\delta_0 = 0.83\,in$. The following freestream conditions have been implemented (Table 7-1):

Quantity	Value
Mach number	$M_\infty = 2.85$
Freestream velocity	$u_\infty = 1875\,ft/sec$
Freestream density	$\rho_\infty = 1.4944 \times 10^{-3}\,slug/ft^3$
Freestream pressure	$p_\infty = 461.6\,lbf/ft^2$
Freestream Temperature	$T_\infty = 180\,°R$

Table 7-1. Freestream quantities for the turbulent flow over a compression corner.

The Reynolds number based on the inflow boundary layer thickness is $1.33 \cdot 10^6$. A constant wall temperature of 498 $^\circ R$ was specified along the surface. The inflow profiles of all quantities have been generated by executing the code over a flat plate until the velocity profile, skin friction coefficient, and boundary layer matched the experimental data upstream of the corner. These inlet profiles have been used to start the solution over the compression corner.

An algebraic grid has been generated to represent the geometry of the problem. The domain of solution for the compression corner is shown in Figure 7-1. The grid size is 100 by 80 in the x- and y-directions respectively. Clustering near the surface and at the corner has been implemented. After an initial computation, the values of y^+ have been recalculated and the grid has been refined. Additional computations have been performed until the first y^+ away from the wall was less than one from the inflow to the outflow.
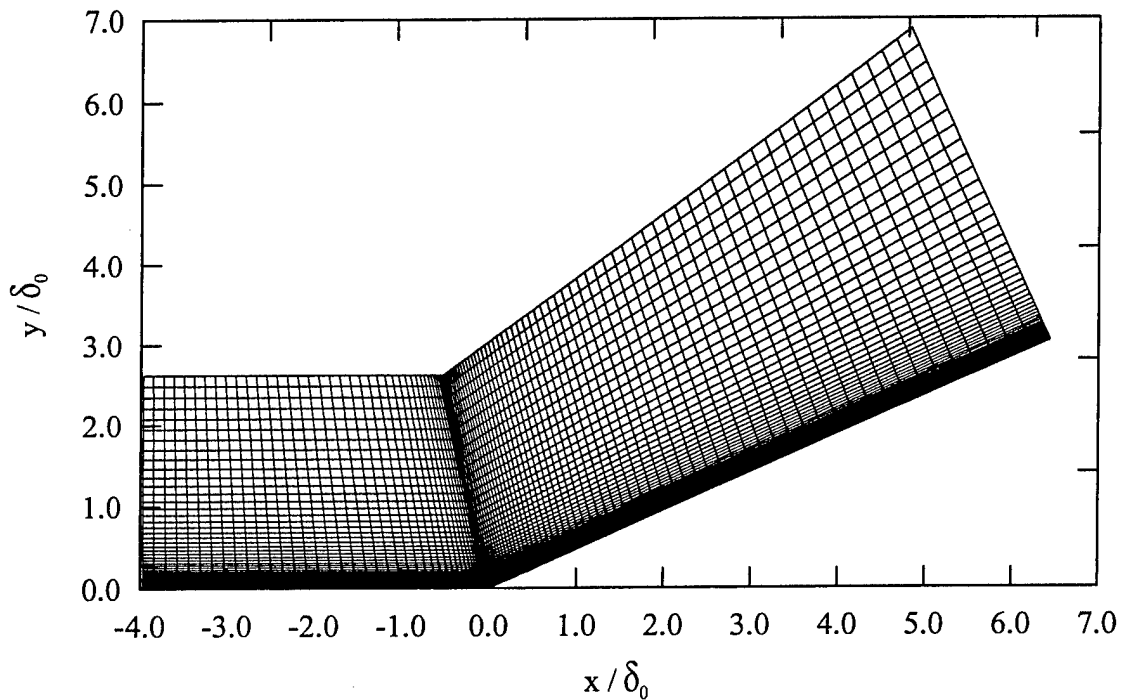
Figure 7-1. The grid system for the supersonic flow

over a 24-degree compression corner (100×80 grid points).

The incoming turbulent boundary layer separates upstream of the compression corner due to the adverse pressure gradient and reattaches downstream, forming a recirculation region. The interaction between the boundary layer and the shock wave at the corner is highly unsteady and the size and position of the separation bubble vary in time. However, due to the Reynolds Averaged approach considered for this investigation,

it is not possible to capture these oscillations and a steady state solution is sought. A typical flow field is shown in Figure 7-2.
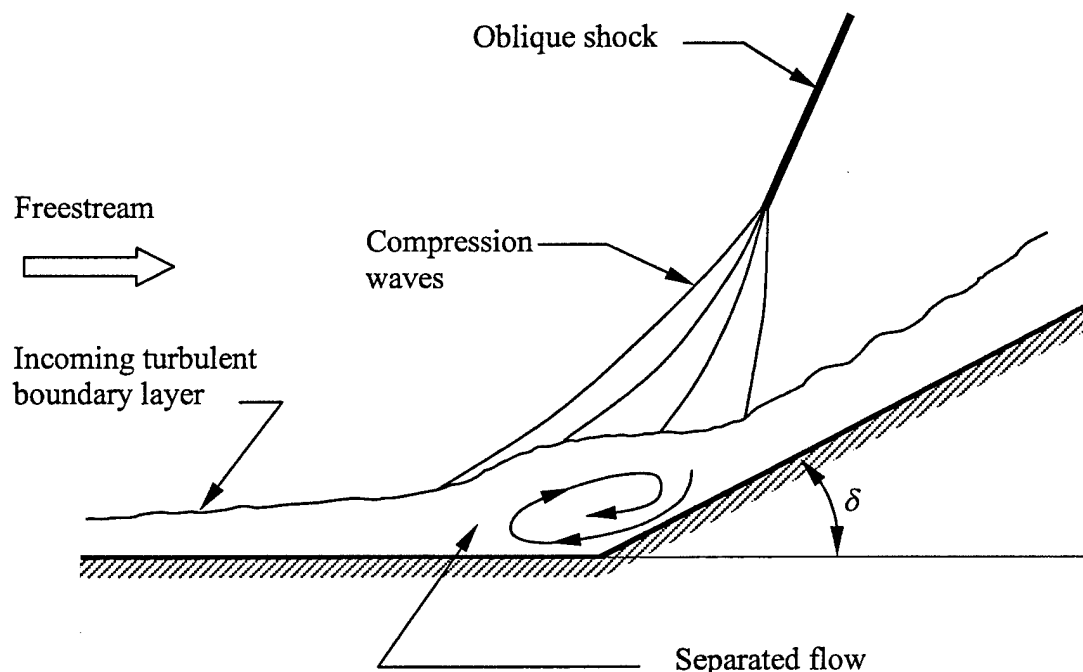
Figure 7-2. Illustration of a supersonic flow over a compression corner.

The available experimental data include the surface pressure, skin friction and velocity profiles at several locations. For each of the turbulence model investigated, the following results are given: skin friction coefficient, surface pressure and velocity profiles at the corner and at a location further downstream. In the following description of the results obtained by various turbulence models, the separation region has been identified as the region where the skin friction becomes negative.

The turbulence models have been investigated with and without compressibility correction terms. Appendix C summarizes the available options for these terms. No converged solution could be obtained with the Baldwin-Lomax model, since this turbulence model is not designed for separated flows. For the Baldwin-Barth turbulence model, no solution could be obtained without compressibility correction terms due to the instability mentioned in Section 4.3. Results obtained with compressibility correction terms (Figure 7-3), where a new calculation of y^+ is introduced show that the separation region is over predicted, as well as the upstream surface pressure (Figure 7-4). The upstream skin friction shows good agreement with the experimental data, whereas the downstream skin friction is higher than the experimental one.

71

The Spalart-Allmaras turbulence model, with and without compressibility correction terms are unable to accurately predict the skin friction (Figure 7-5). When compressibility correction terms are turned on, the model provides a larger separation region. The surface pressure is in good agreement with the experiment, especially downstream of the corner (Figure 7-6).

The $k-\epsilon$ model provides an accurate downstream skin friction with compressibility correction terms and an accurate upstream skin friction without compressibility correction terms (Figure 7-7). In both cases, the surface pressure is over predicted (Figure 7-8).

The Baseline model shows good agreement in the skin friction prediction with and without compressibility correction terms (Figure 7-9), although slightly under predicted downstream. The pressure is very similar for both models and is higher than the experimental data (Figure 7-10).

The SST model, which is designed to provide a larger separation bubble, over predicts the size of the recirculation region. Similar results for the skin friction are obtained whether the compressibility correction terms are included or not. The skin friction is under predicted (Figure 7-11) and the pressure is over predicted upstream (Figure 7-12).

The velocity profiles have been extracted at two locations referred to as Station 22 (at the corner) and Station 47 (at $x = 4.0$ in, downstream of the corner), which correspond to the experimental results of Settles. The velocities are nondimensionalized by the local velocity at the edge of the boundary layer, which has a different value upstream and downstream of the shock. The y-coordinate represents the normal distance from the wall. Some models show similar results for the prediction of the velocity profiles. The Baldwin-Barth (Figure 7-13), $k-\epsilon$ (Figure 7-15), and Baseline models without compressibility correction terms (Figure 7-16) show a higher acceleration of the flow at the corner. On the other hand, the Spalart-Allmaras (Figure 7-14) and SST models (Figure 7-17) predict a lower acceleration. The velocity profiles obtained at the corner with the $k-\epsilon$ and Baseline models (with compressibility correction terms) are in good agreement with the experimental data. No model is able to accurately predict the downstream velocity profile (Figures 7-18 to 7-22). They all indicate lower accelerations.

The pressure contours are shown for the Baseline model in Figure 7-23, which illustrates how the compression waves merge to form the oblique shock wave. The streamline patterns at the corner (Figure 7-24) shows the recirculation region. The turbulent viscosity contours (Figure 7-25) show that most of the turbulent viscosity is created downstream the oblique shock.

The ability to accurately represent all features of the flow varies from one turbulence model to another, as expected. In some cases, the introduction of compressibility correction terms provides a more accurate solution. It should be noted that the supersonic flow over a compression corner is an unsteady problem, and the interaction between the oblique shock wave and the boundary layer causes it to be a very challenging problem. The Reynolds Averaged approach provides a solution that is averaged in time, which can explain some of the discrepancies between the numerical and experimental results.
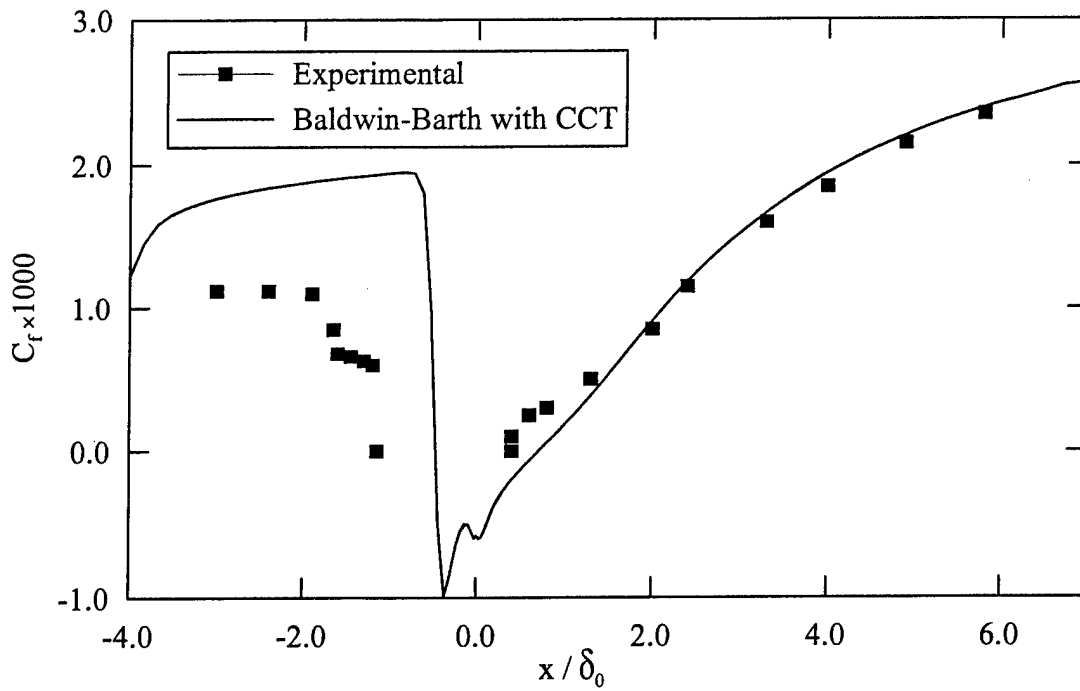
Figure 7-3. Skin friction coefficient (Baldwin-Barth model).
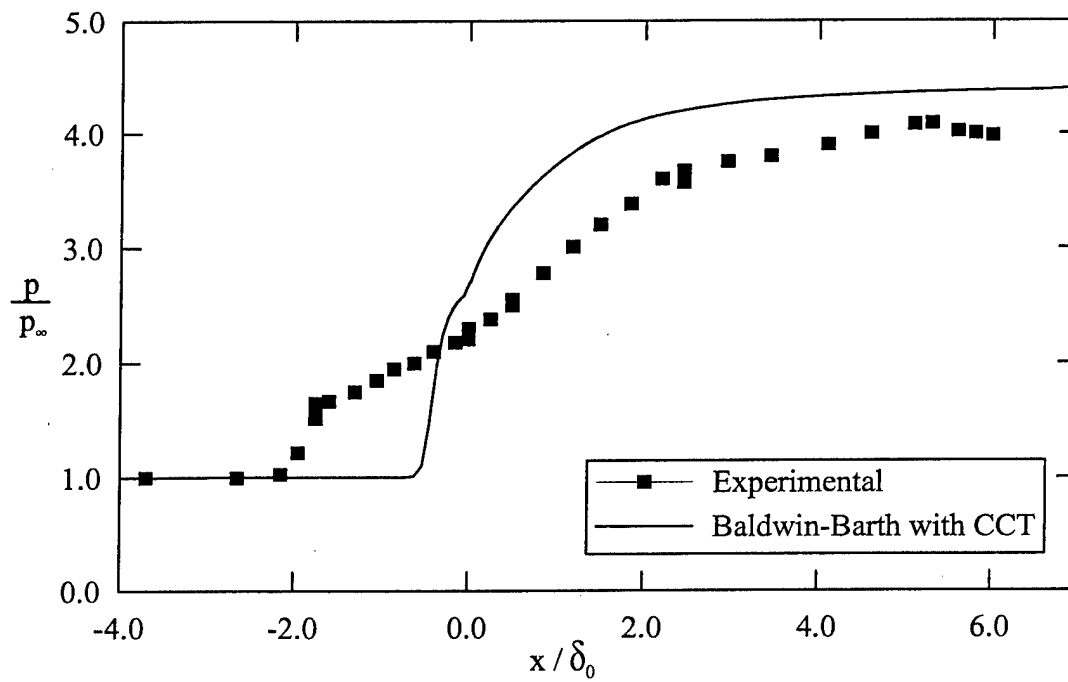
Figure 7-4. Surface pressure (Baldwin-Barth model).
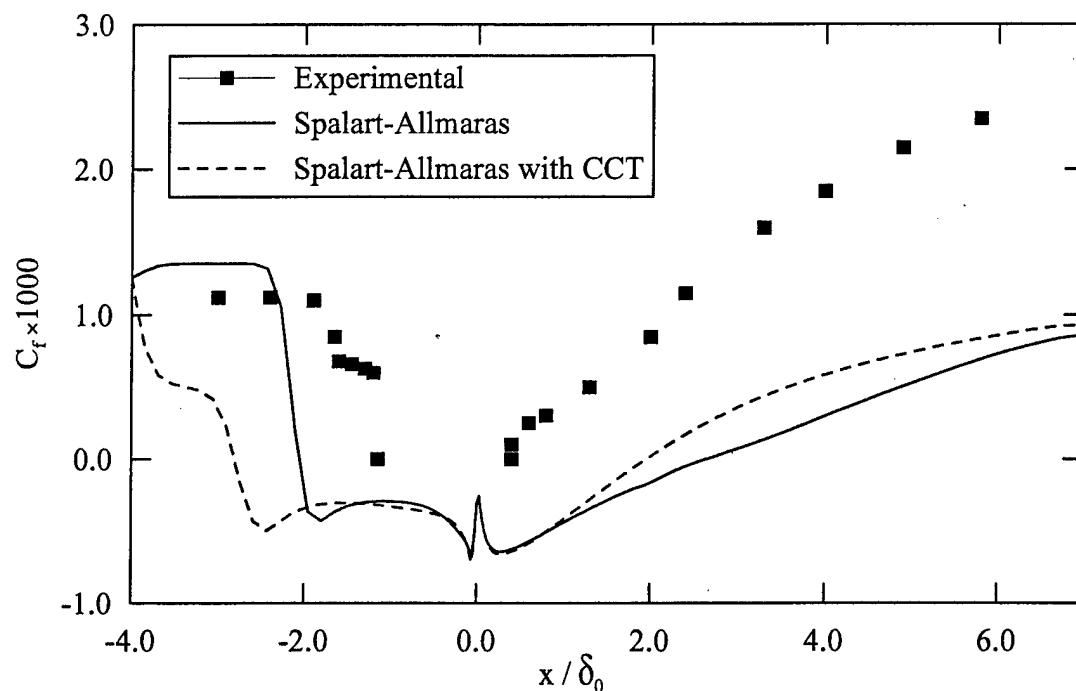
Figure 7-5. Skin friction coefficient (Spalart-Allmaras model).
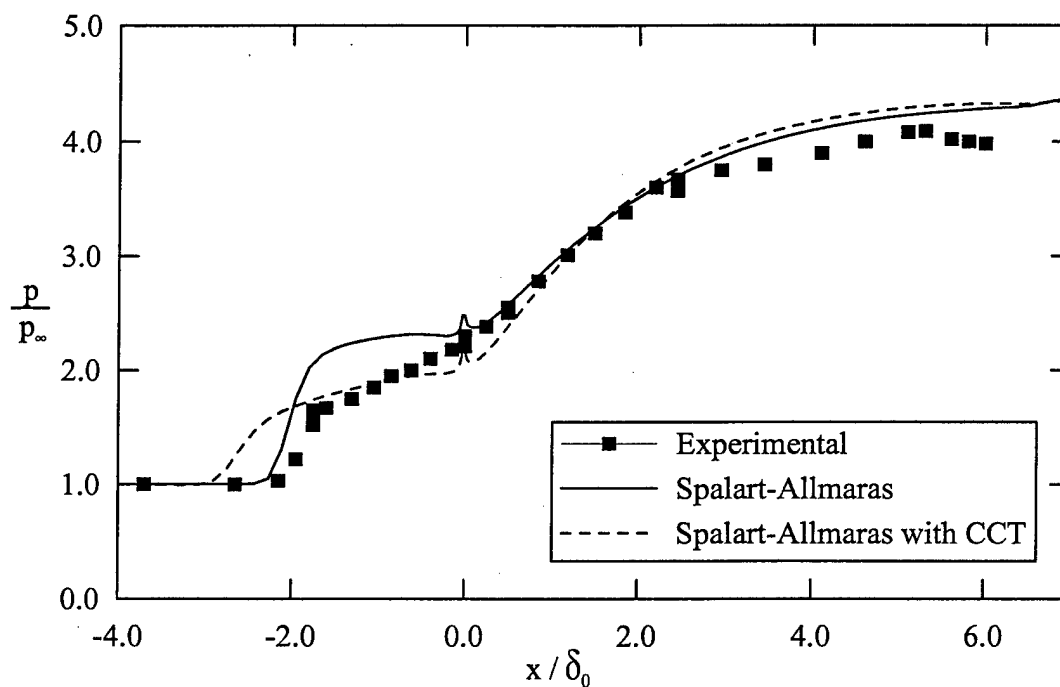
Figure 7-6. Surface pressure (Spalart-Allmaras model).
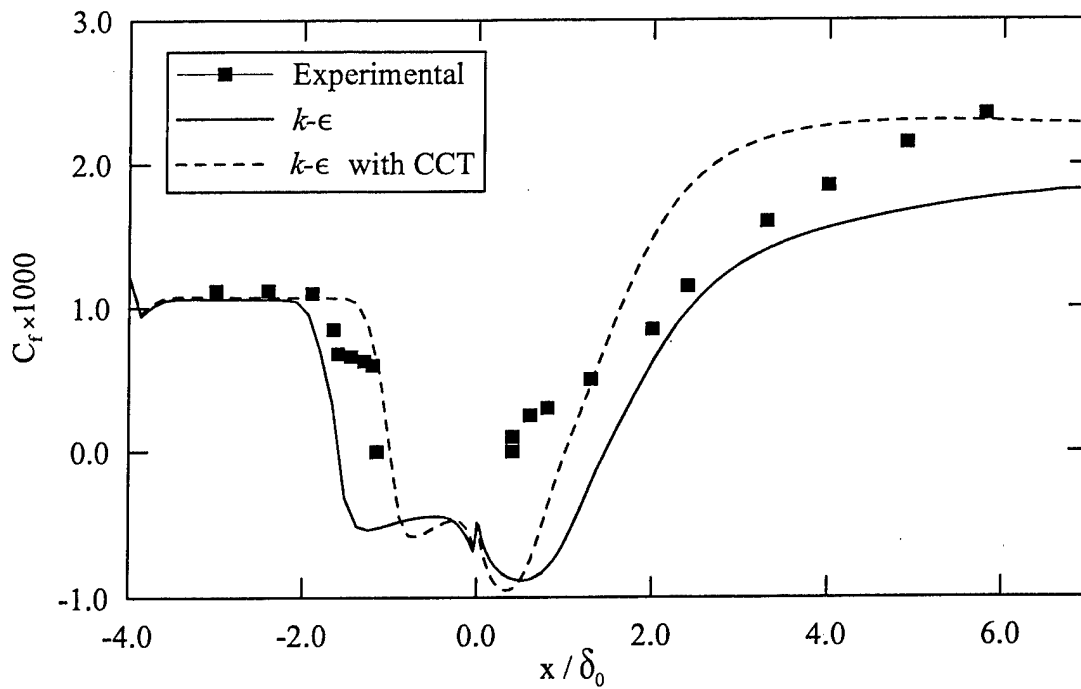
Figure 7-7. Skin friction coefficient ($k - \epsilon$ model).
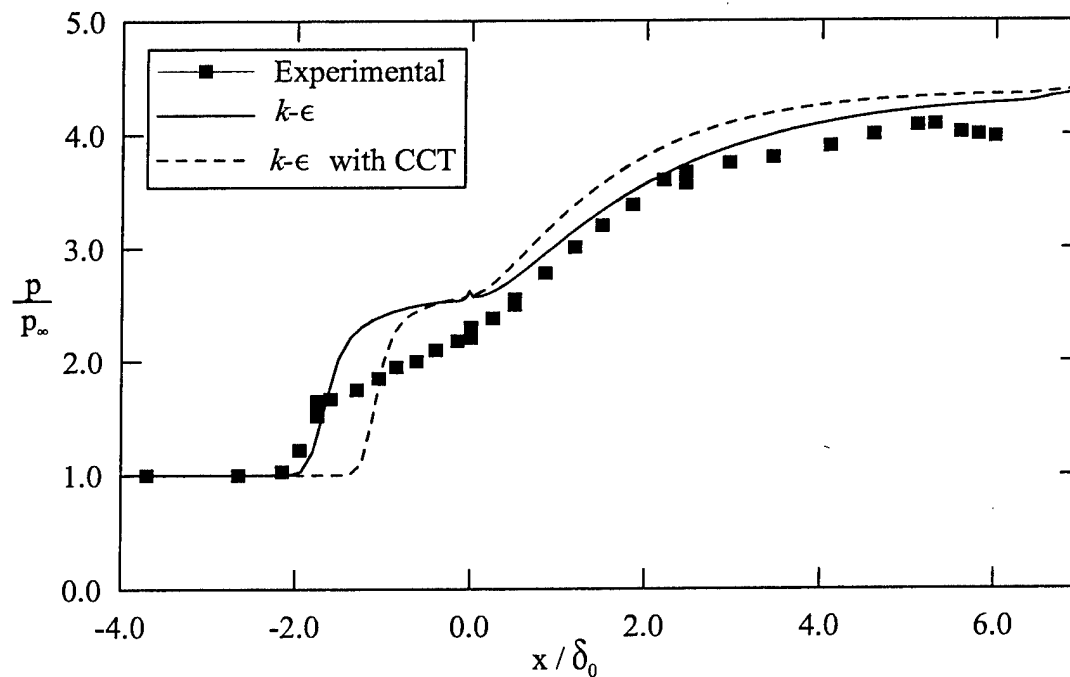
Figure 7-8. Surface pressure ($k - \epsilon$ model).
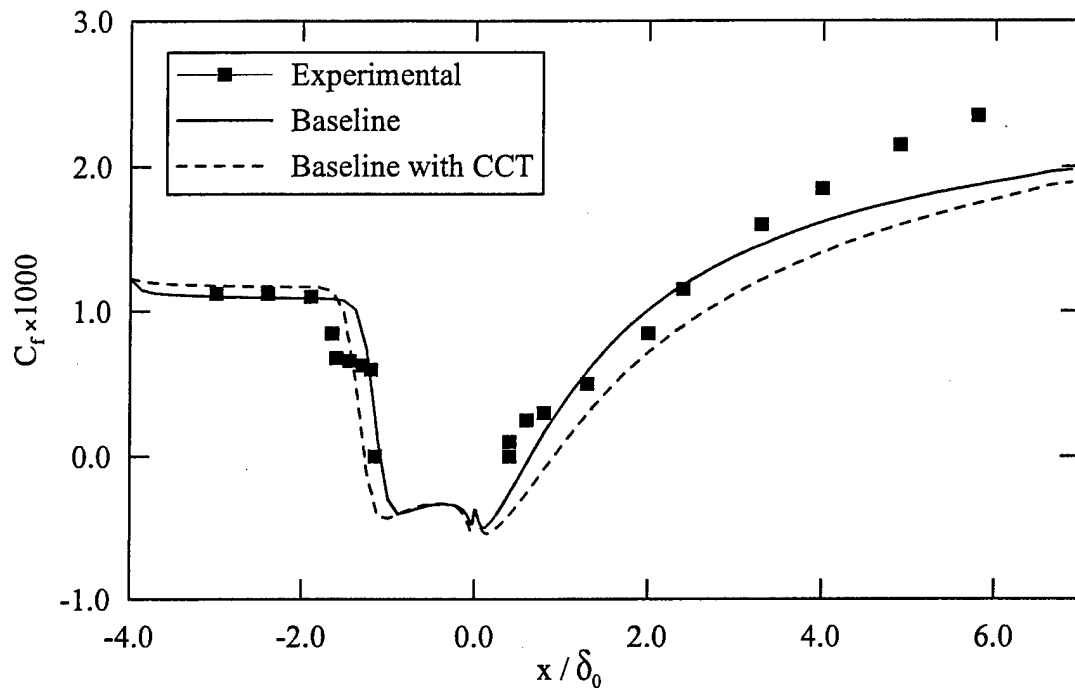
Figure 7-9. Skin friction coefficient (Baseline model).
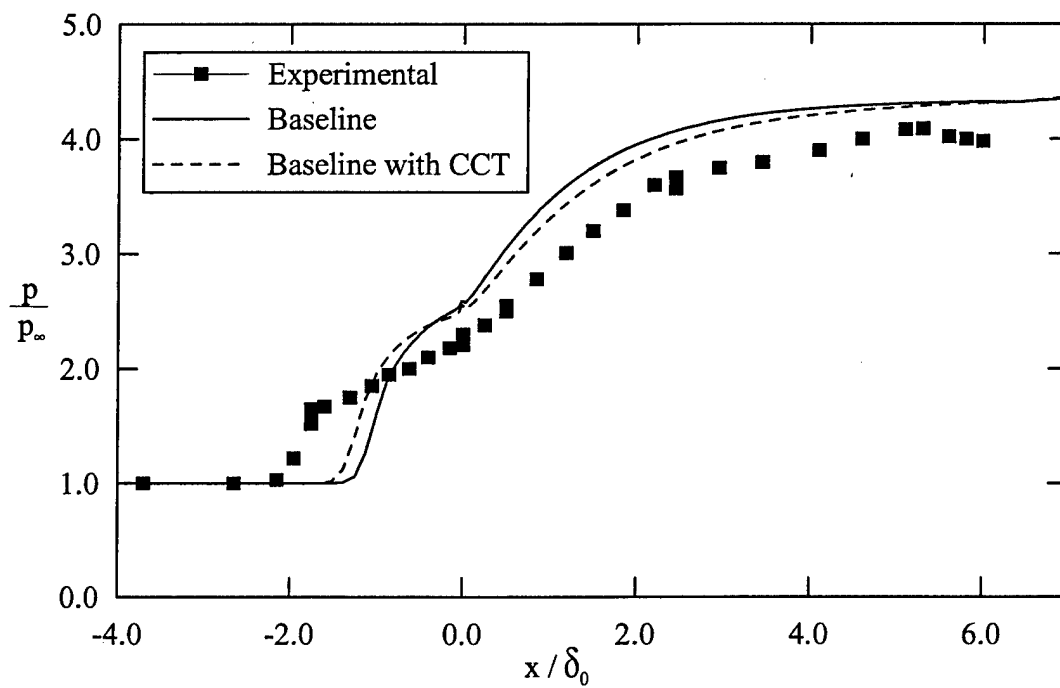
Figure 7-10. Surface pressure (Baseline model).
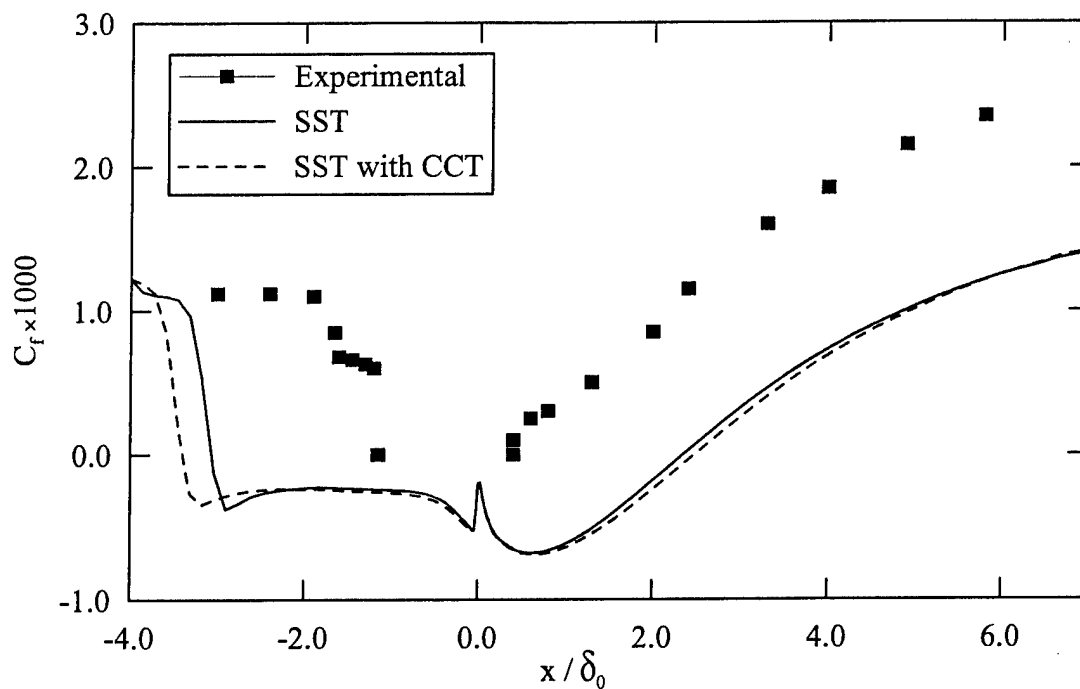
Figure 7-11. Skin friction coefficient (SST model).
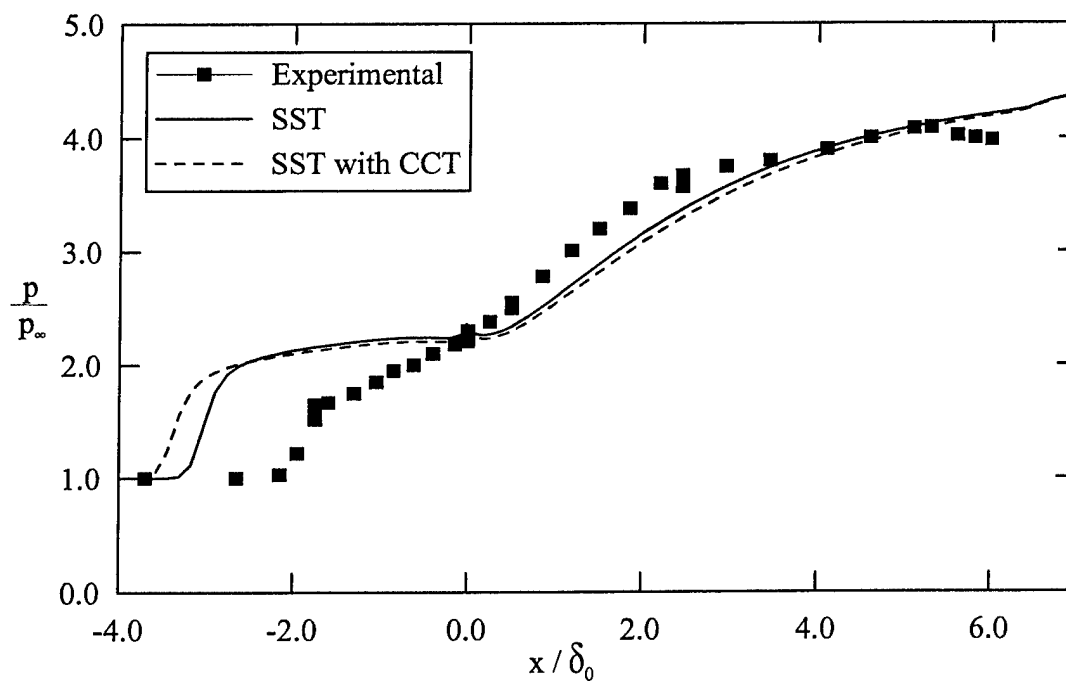
Figure 7-12. Surface pressure (SST model).

78
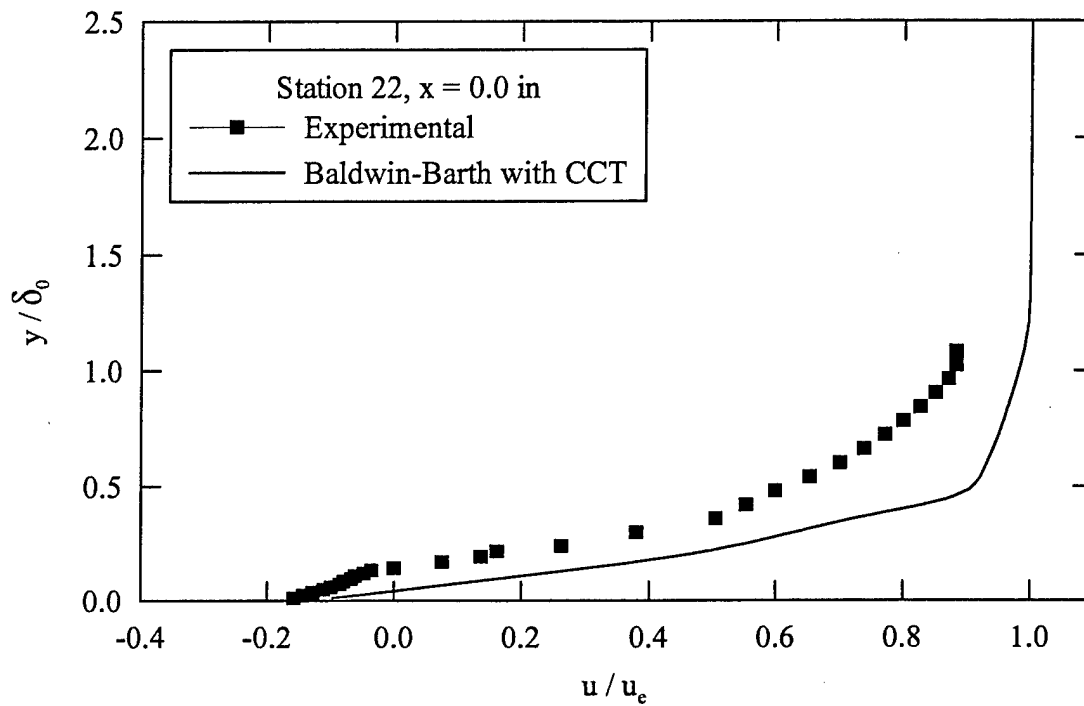
Figure 7-13. Corner velocity profile (Baldwin-Barth model).
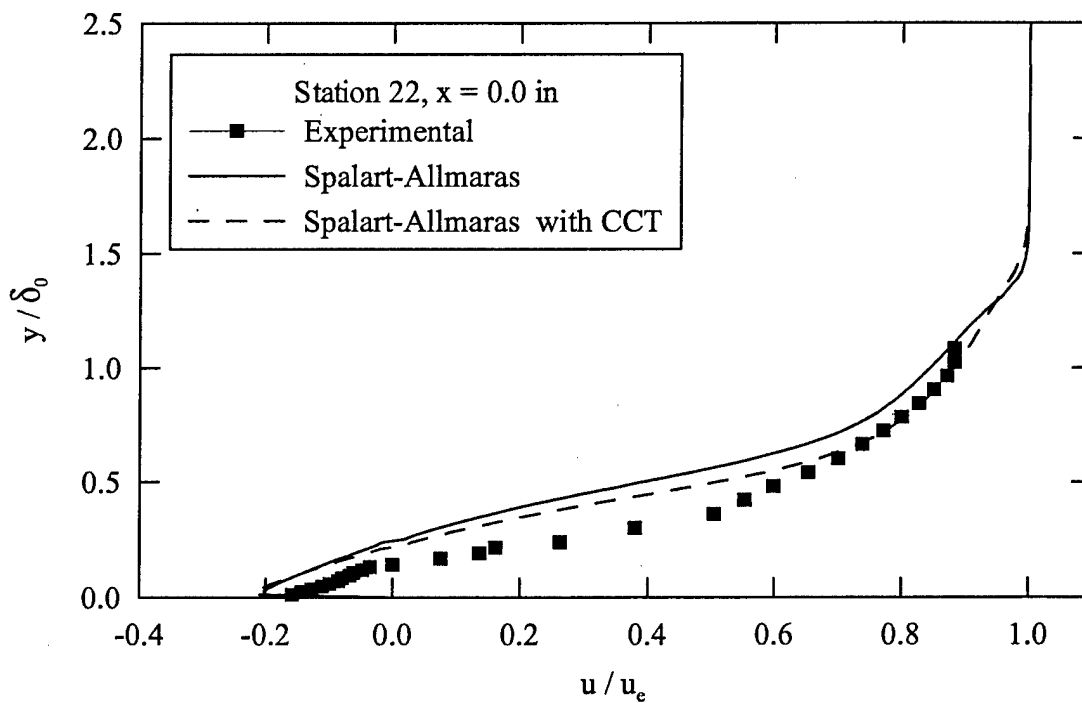
Figure 7-14. Corner velocity profile (Spalart-Allmaras model).
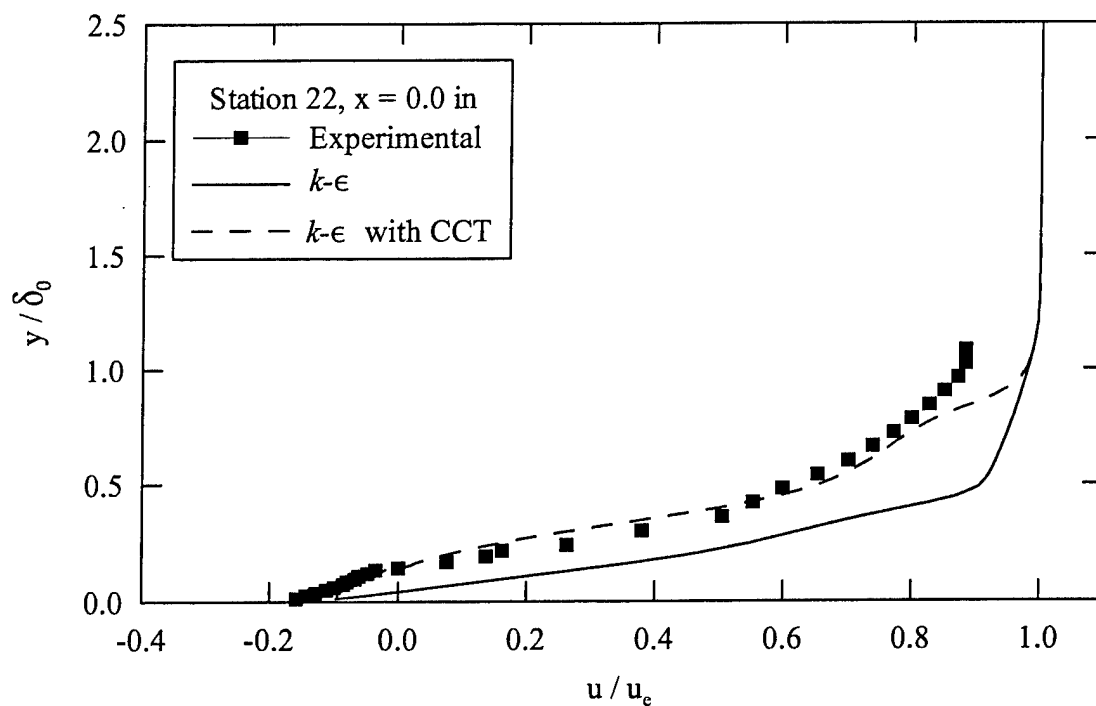
Figure 7-15. Corner velocity profile ($k - \epsilon$ model).
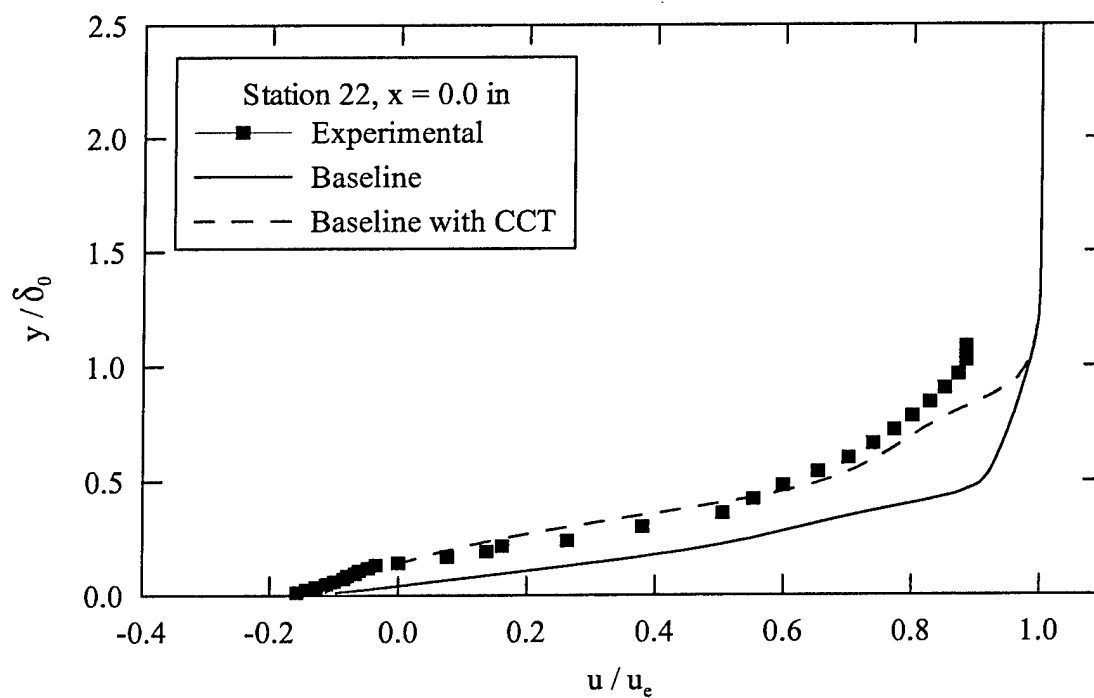
Figure 7-16. Corner velocity profile (Baseline model).
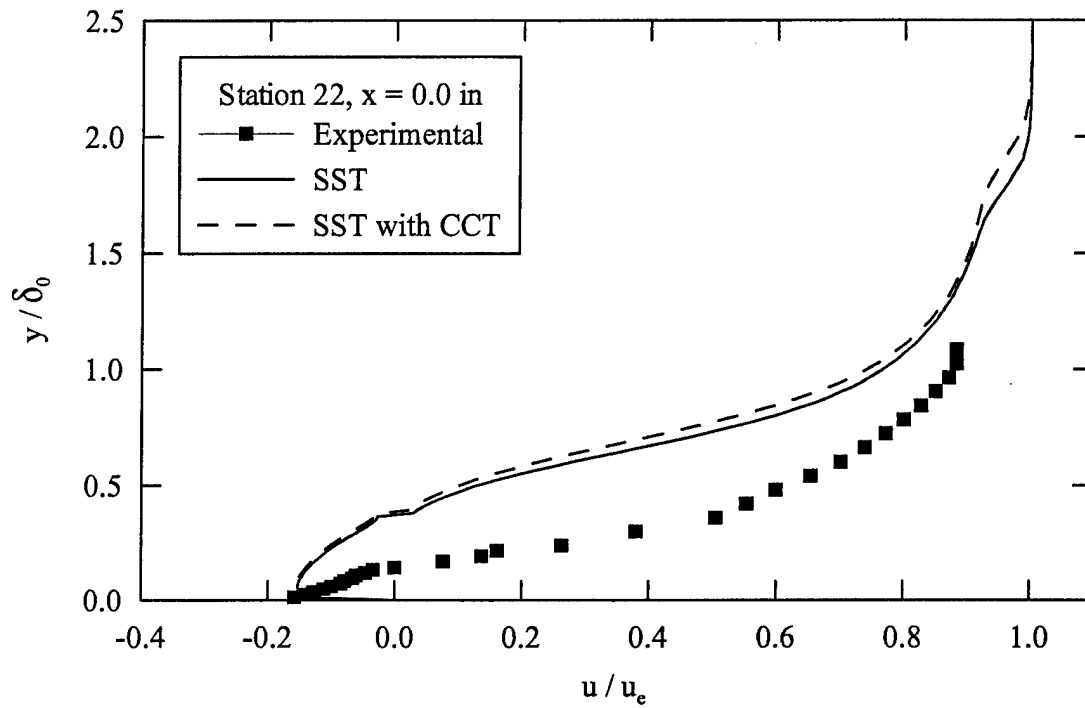
Figure 7-17. Corner velocity profile (SST model).
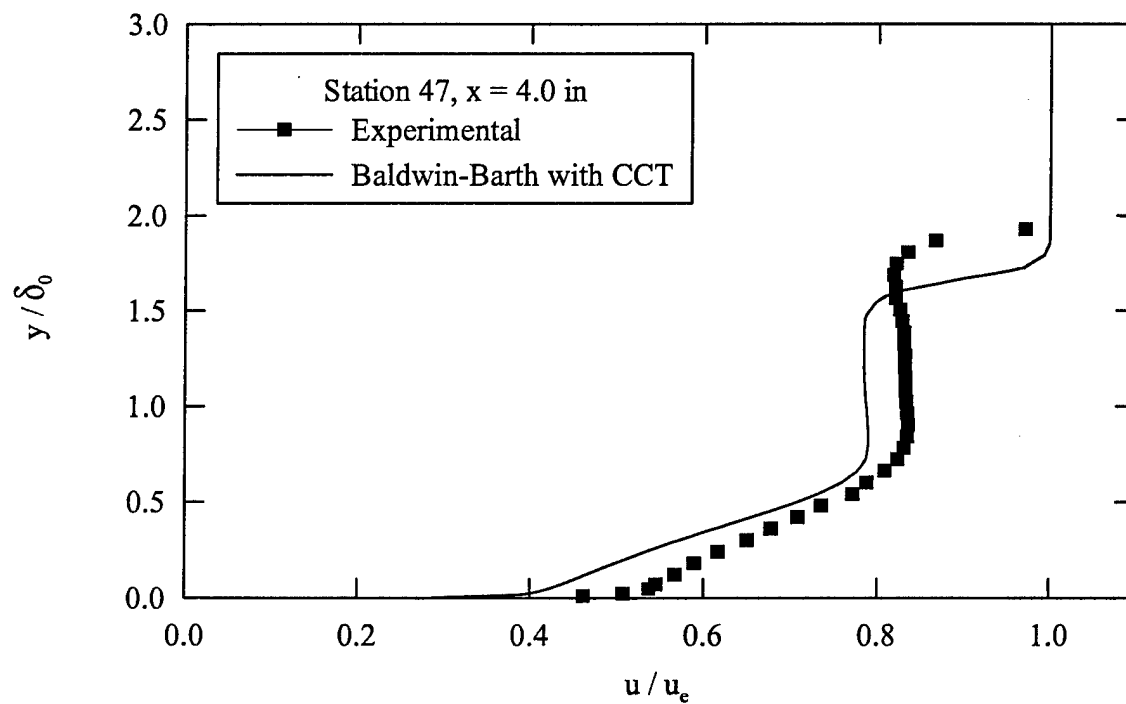
Figure 7-18. Downstream velocity profile (Baldwin-Barth model).
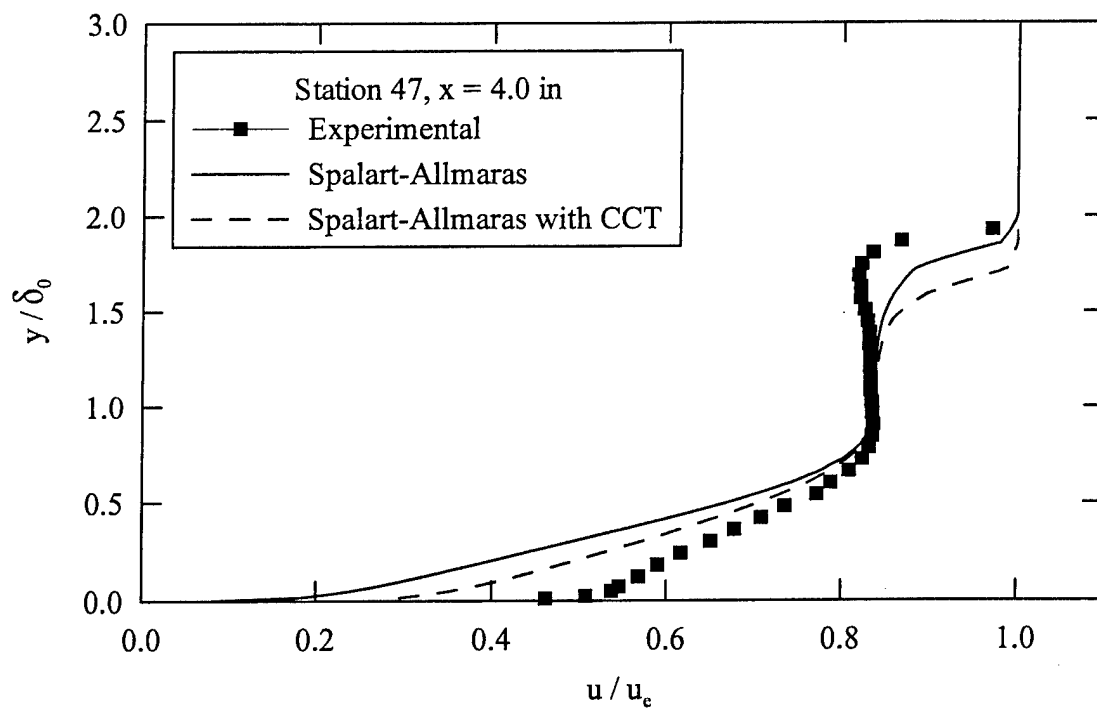
Figure 7-19. Downstream velocity profile (Spalart-Allmaras model).
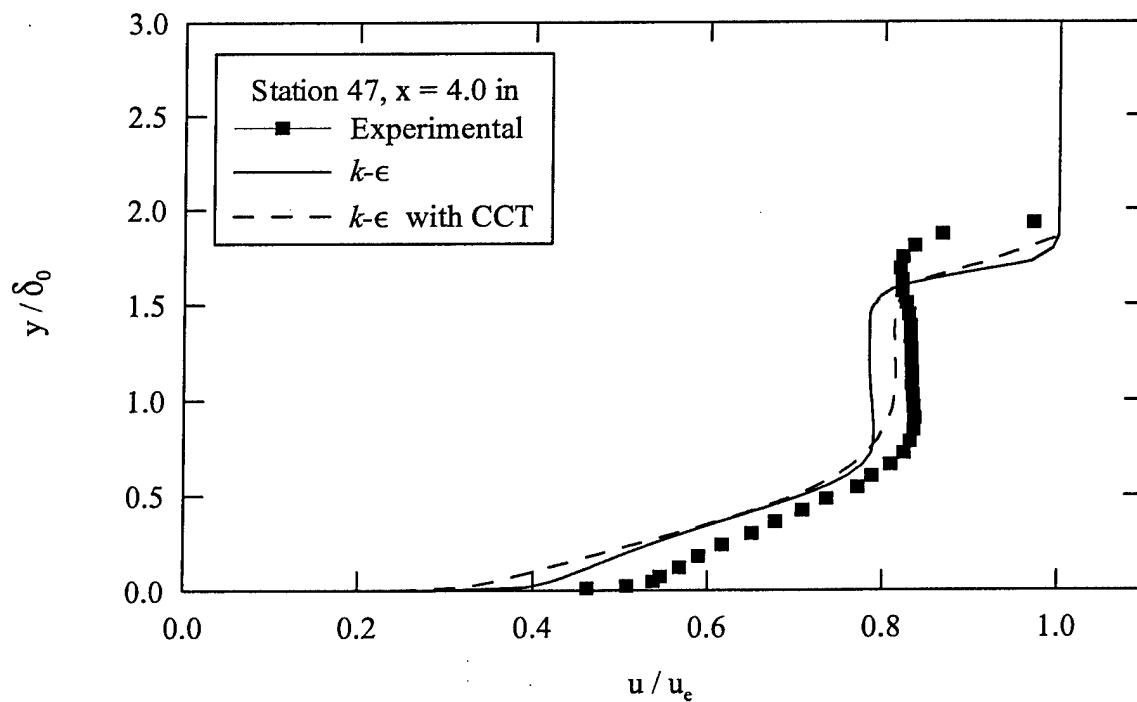
Figure 7-20. Downstream velocity profile ($k - \epsilon$ model).
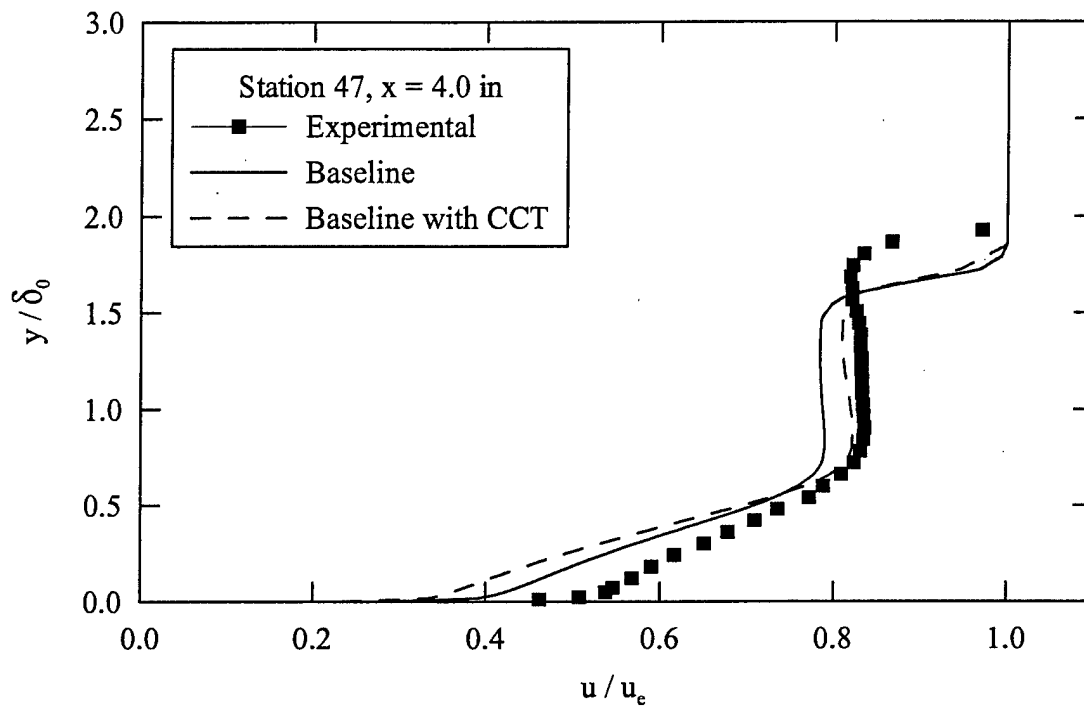
Figure 7-21. Downstream velocity profile (Baseline model).
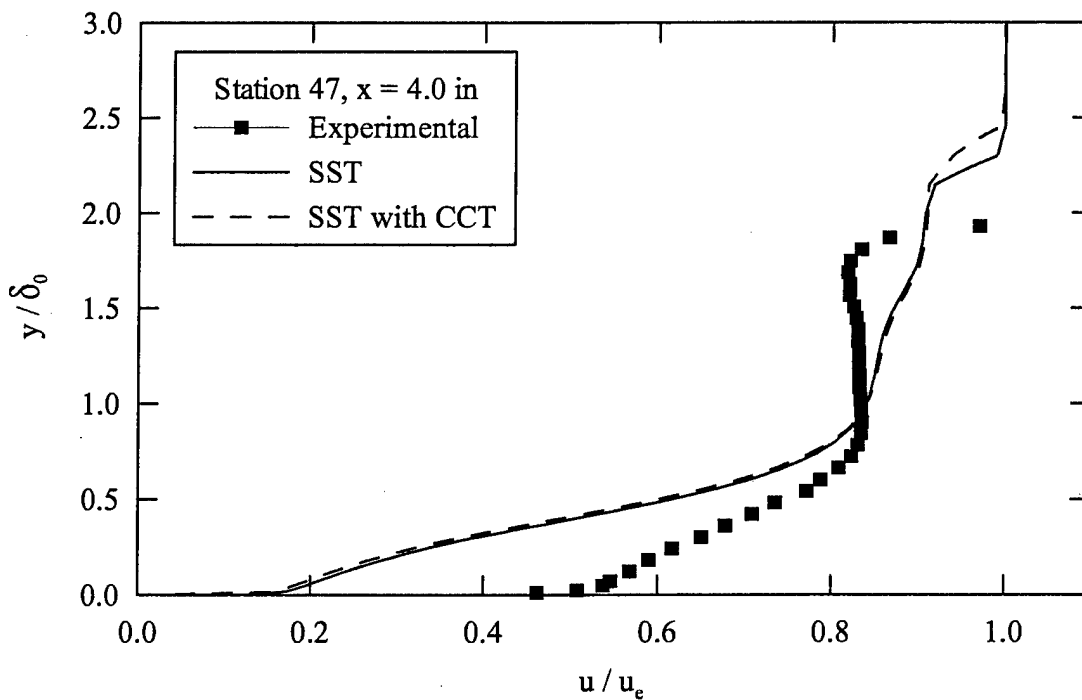
Figure 7-22. Downstream velocity profile (SST model).
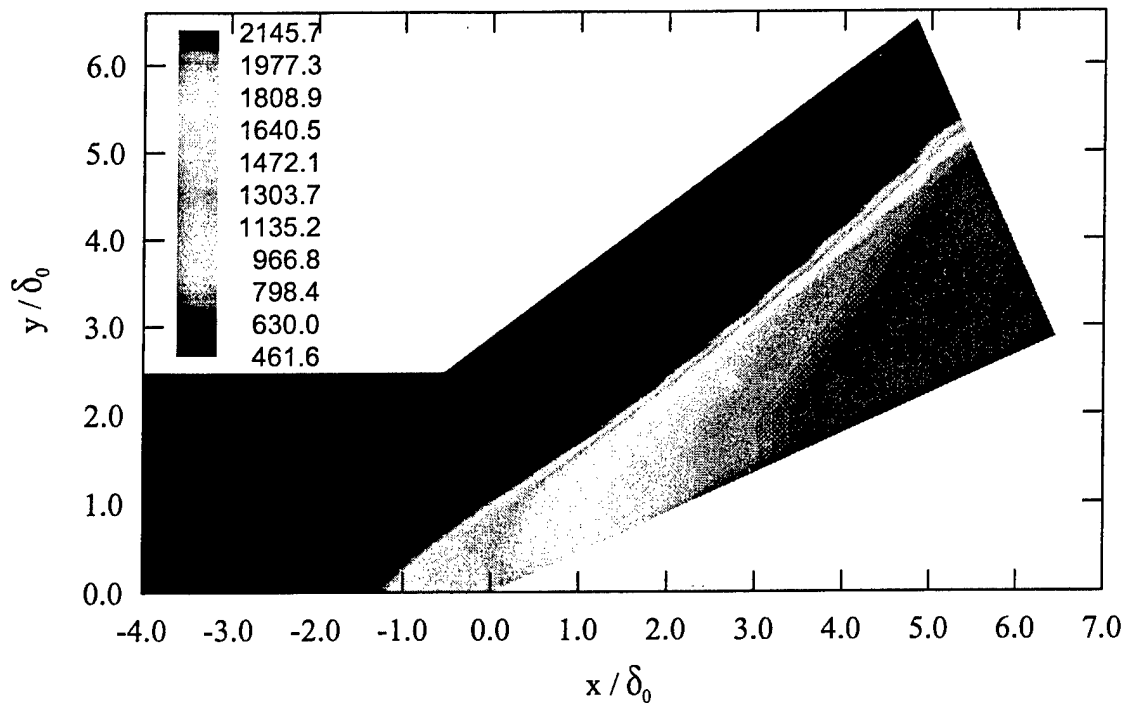
Figure 7-23. Pressure contours (Baseline model).
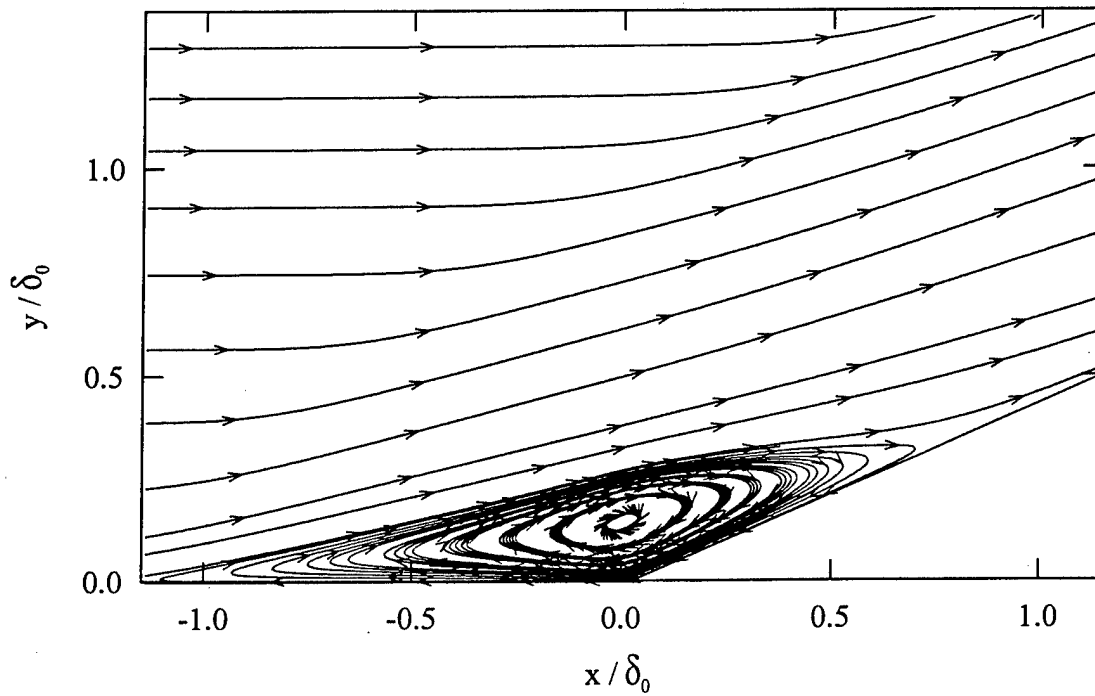
Figure 7-24. Streamline patterns at the corner (Baseline model).

84
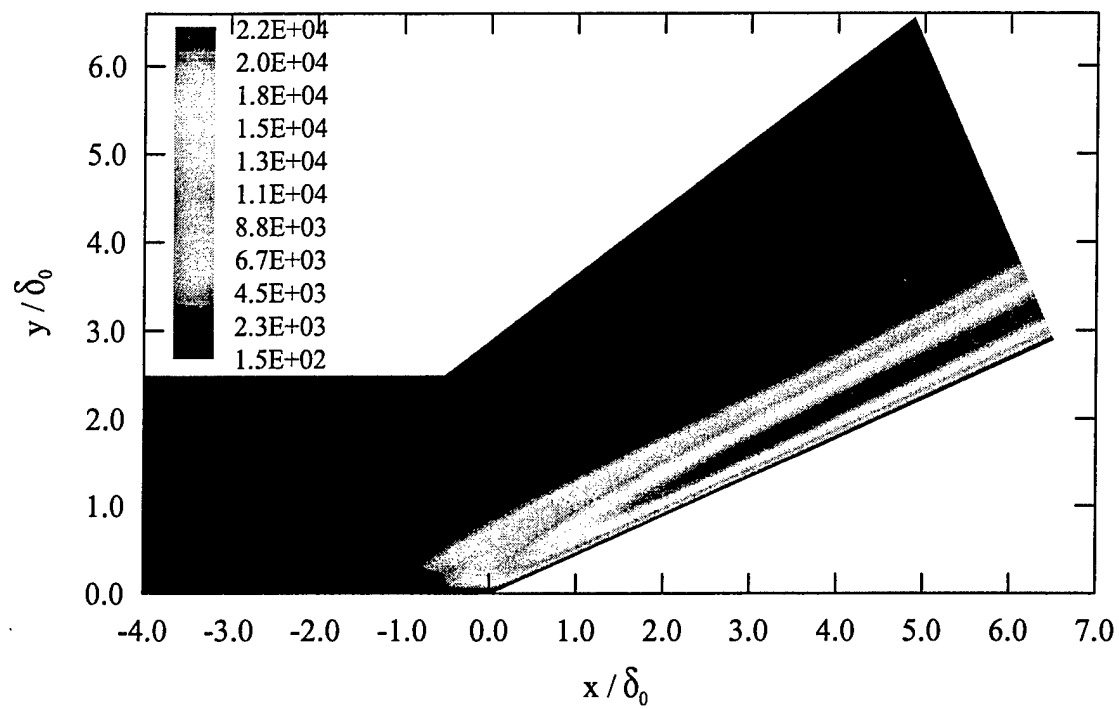
Figure 7-25. Turbulent viscosity $\dfrac{\mu_t}{\mu_\infty}$ contours (Baseline model).

7.2. Validation of the MHD Solver

7.2.1. The MHD Rayleigh Problem

The MHD Rayleigh problem is a key benchmark problem for MHD flows. It is a time accurate problem that involves molecular viscosity, magnetic diffusivity and wave propagation. This test case is used to validate the ability of the numerical code to accurately compute boundary layer type of flows. Consider an infinite flat plate at rest in a motionless electrically conducting fluid. A constant magnetic field B_0 is applied in the y-direction, i.e., perpendicularly to the plate. At time $t = 0.0$, the plate is suddenly set into motion in the x-direction (i.e., in the direction of the plate) at a constant speed of U_0. Figure 7-26 illustrates a typical velocity profile obtained for the MHD Rayleigh flow. The motion of the plate drives the fluid close to the plate and the motion propagates within the fluid as time increases. The wave front separates the region where the fluid is at rest (ahead of the wave front) and the region where the fluid is accelerating (close to the wall). The latter is referred to as the Hartmann layer and has a thickness of $\delta_H = \sqrt{\rho v / \sigma_e} / B_0$. The velocity field induces a magnetic field that propagates in the y-direction as a plane wave, which is called the Alfvèn wave. It travels at the constant speed $A_0 = B_0 / \sqrt{\mu_{e0} \rho}$ (Alfvèn speed). In the case where the magnetic Prandtl number equals unity (i.e., the kinematic viscosity and the magnetic diffusivity are equal), there exists an analytical solution [108, 109]. The velocity and induced magnetic field are given by Equations (7.1) through (7.5) for an electrically insulating wall and by Equations (7.6) and (7.7) for a perfectly conducting wall.

Electrically insulating wall:

$$\frac{u}{U_0} = \frac{1}{4}\left[2.0 - \left(erf(\lambda_+) + erf(\lambda_-)\right) + e^{\frac{-A_0 y}{d}} erfc(\lambda_-) + e^{\frac{A_0 y}{d}} erfc(\lambda_+) \right] \tag{7.1}$$

$$\frac{B_x}{B_{ref}} = \frac{1}{4}\left[\left(erf(\lambda_-) - erf(\lambda_+)\right) + e^{\frac{-A_0 y}{d}} erfc(\lambda_-) - e^{\frac{A_0 y}{d}} erfc(\lambda_+) \right] \tag{7.2}$$

$$B_{ref} = U_0 \sqrt{\mu_{e0} \rho} \tag{7.3}$$

$$d = v = \eta \tag{7.4}$$

$$\lambda_{\pm} = \frac{y \pm A_0 t}{2\sqrt{dt}} \tag{7.5}$$

Perfectly conducting wall:

$$\frac{u}{U_0} = \frac{1}{2}\left[2.0 - \left(erf(\lambda_-) + erf(\lambda_+)\right)\right] \qquad (7.6)$$

$$\frac{B_x}{B_{ref}} = \frac{1}{2}\left[\left(erf(\lambda_-) - erf(\lambda_+)\right)\right] \qquad (7.7)$$

Where u is the $x-$ component of the velocity field and B_x is the $x-$ component of the induced magnetic field. The error function and the complementary error function are denoted by erf and $erfc$, respectively.
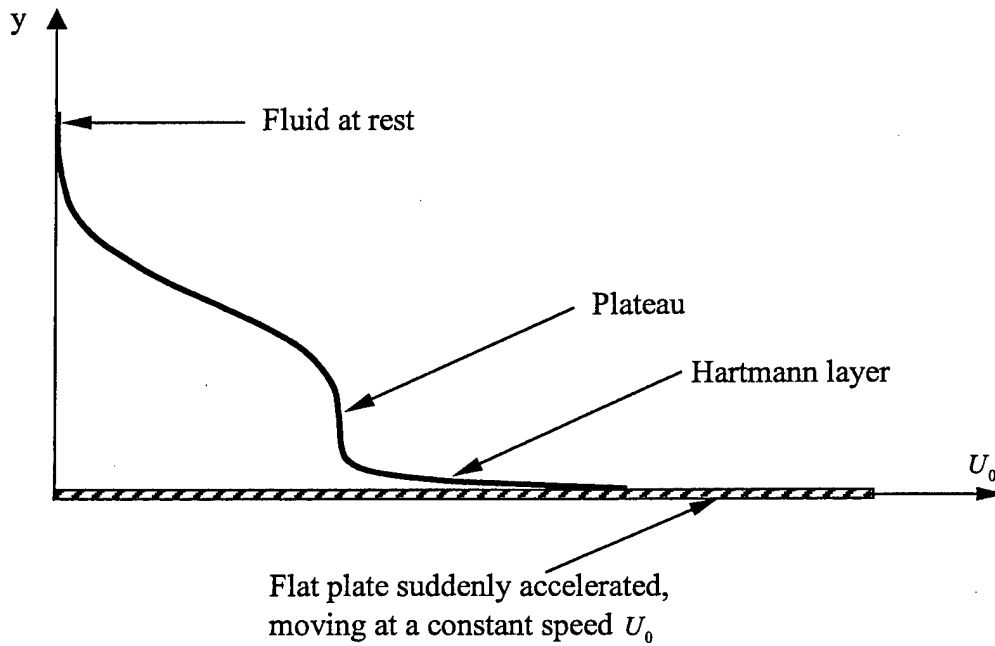

Figure 7-26. Schematic of the MHD Rayleigh flow.

The MHD Rayleigh flow has been computed and compared with the analytical solution for the following case (Table 7-2):

Property	Value
Electrical conductivity	$\sigma_e = 10^7/4\pi \; mho/m$
Fluid density	$\rho = 0.4 \times 10^{-4} \; kg/m^3$
Applied magnetic field	$B_0 = 1.449 \times 10^{-4} \, T$
Vertical range of the domain	$0 \le y \le 2.5 \, m$
Time interval	$0 \le t \le 0.06 \; sec$

Table 7-2. Summary of the MHD Rayleigh problem parameters.

The magnetic Reynolds number based on the height of the domain is $Re_m = 2.5$, and therefore, the full MHD equations are solved. The temperature of the flow has been adjusted such that the kinematic viscosity, calculated from the Sutherland's law, equals the magnetic diffusivity. Figure 7-27 and 7-28 show the velocity profiles and induced magnetic fields obtained for $t \le 0.06$ sec in the case of an electrically insulating wall. The numerical solutions show good agreement with the analytical solutions. All the features of Figure 7-26 are represented. Figure 7-29 and Figure 7-30 show the velocity profiles and induced magnetic fields in the case of a perfectly conducting wall. In this case, the Hartmann layer is not present.
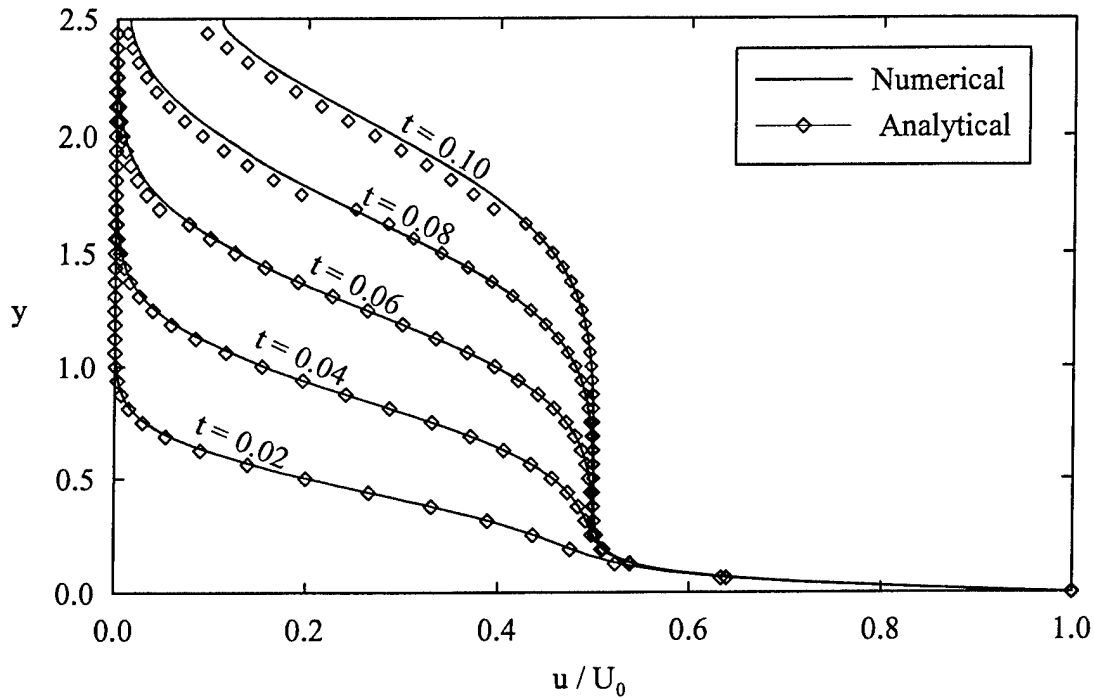
Figure 7-27. Velocity profiles for the MHD Rayleigh problem

(electrically insulating wall).
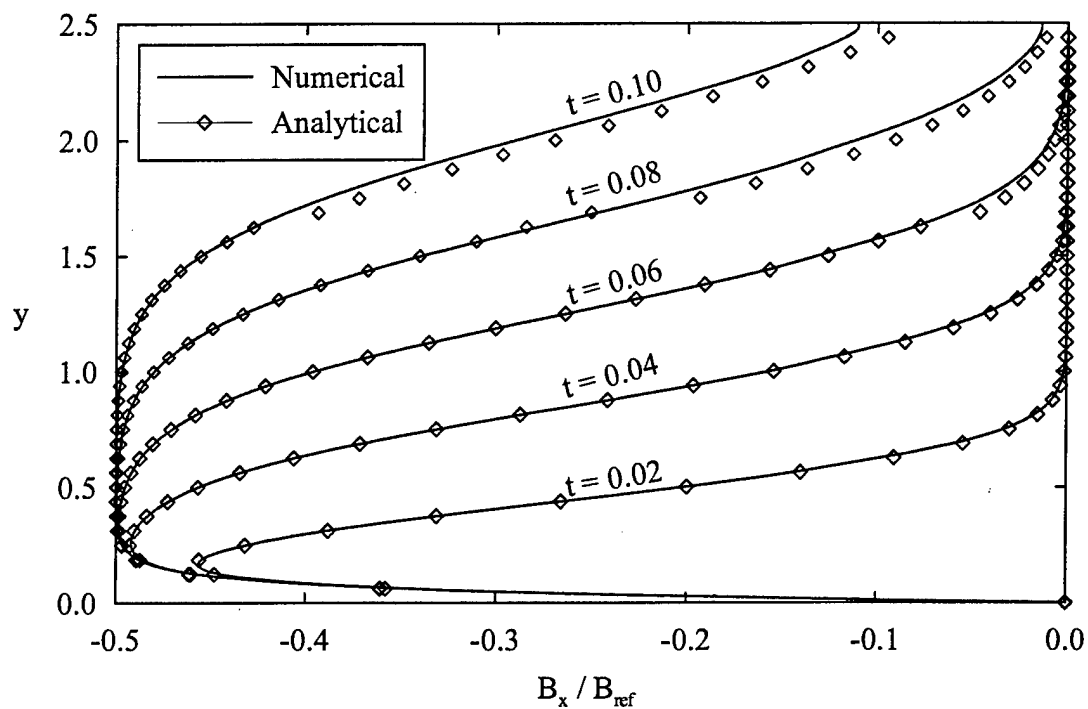
Figure 7-28. Induced magnetic field profiles for the MHD Rayleigh problem
(electrically insulating wall).
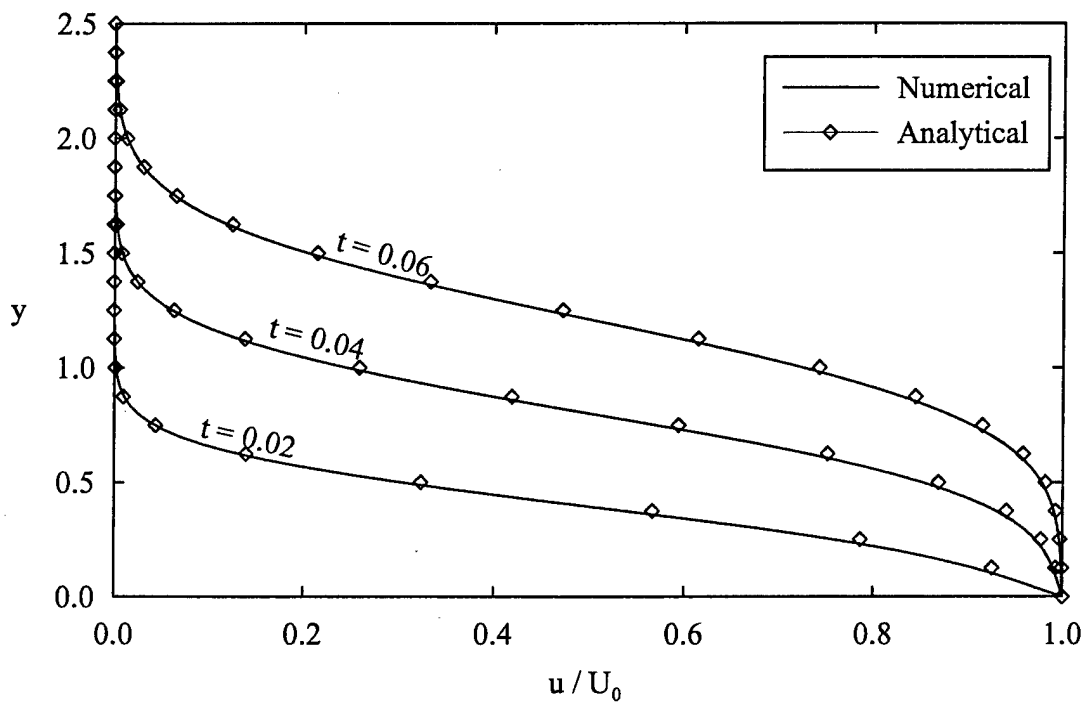
Figure 7-29. Velocity profiles for the MHD Rayleigh problem
(perfectly conducting wall).
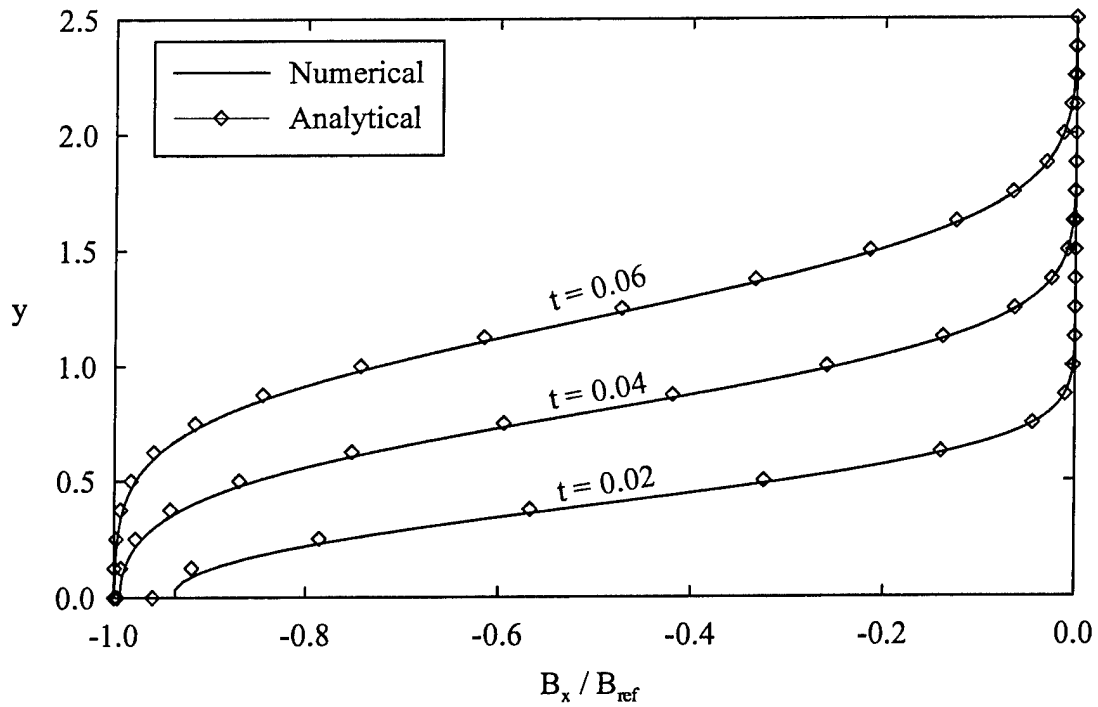
Figure 7-30. Induced magnetic field profiles for the MHD Rayleigh problem
(perfectly conducting wall).

7.2.2. Supersonic MHD Flow over a Blunt Body

In this section, the supersonic flow over a blunt body is computed and the shock standoff distance is compared to the analytical solution proposed by Lykoudis [3]. Details of the analytical solution are given in Appendix D. The inflow conditions are:

Flow property	Value
Mach number	$M_\infty = 2.97$
Freestream velocity	$u_\infty = 3625 \, m/sec$
Freestream density	$\rho_\infty = 3.035 \times 10^{-5} \, kg/m^3$
Freestream pressure	$p_\infty = 32.3 \, Pa$
Freestream Temperature	$T_\infty = 3708 \, K$

Table 7-3. Flow properties of the supersonic flow over a blunt body.

The blunt body radius of curvature is $r_b = 0.025 \, m$. The grid system is shown in Figure 7-31. The magnetic field is initially oriented in the y-direction, and the conductivity is assumed to be constant ($\sigma_e = 800 \, mho/m$) for all the computations.

90

The shock standoff distance moves away from the body as the magnetic field is increased (Figure 7-32). When the magnetic field is oriented in the y-direction, the body force created by the magnetic field is acting in the opposite direction of the incoming velocity, which slows down the flow. Since the velocity is decreased in the region between the blunt body and the shock wave, a wider area is required for the fluid passage and therefore, the shock standoff distance has to increase. In the analytical solution proposed by Lykoudis [3], the shock standoff distance ratio between the MHD and no-magnetic case is a function of the density ratio across the shock and the interaction parameter S (see Appendix D). The standoff distances have been non-dimensionalized by the radius of curvature of the shock. However, the analytical solution assumes that the shock wave and the body are concentric. In reality, the shock wave can be approximated by a circle having a different center from the blunt body center (Figure 7-33). Therefore, when the shock and body are considered concentric, the radius of curvature of the shock r is smaller than the actual radius r_s. The numerical results are compared with the analytical solution in Figure 7-34. The location of the shock has been achieved by locating a point in the centerline where the pressure was the average between the extreme values of the pressure across the shock. The calculation of the non-dimensional shock standoff ratio between the non-magnetic and magnetic case has been performed with r and r_s. The prediction of the shock standoff distance is more accurate when the actual shock radius of curvature is considered for non-dimensionalization. When the shock and body are considered concentric, the difference between the numerical and analytical solution increases with the magnitude of the magnetic field. This can be explained by the fact that the assumptions made to derive the analytical solutions are less valid for higher magnetic fields. The assumption that the pressure at the stagnation region is not disturbed by a magnetic field is not satisfied since the presence of a magnetic field tends to decrease the stagnation pressure.
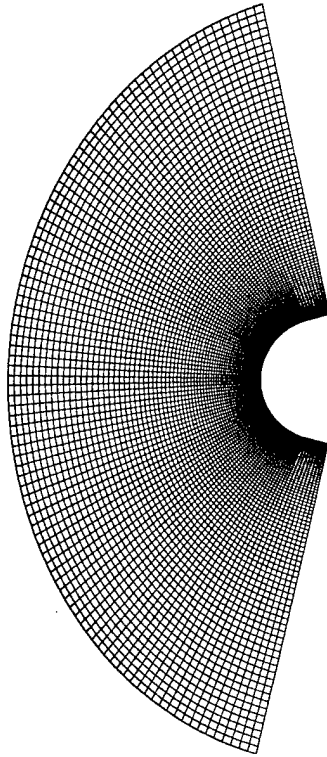
Figure 7-31. The grid configuration for the blunt body (100×80 grid points).

By=0.0 T By=0.02 T By=0.025 T By=0.030 T By=0.035 T
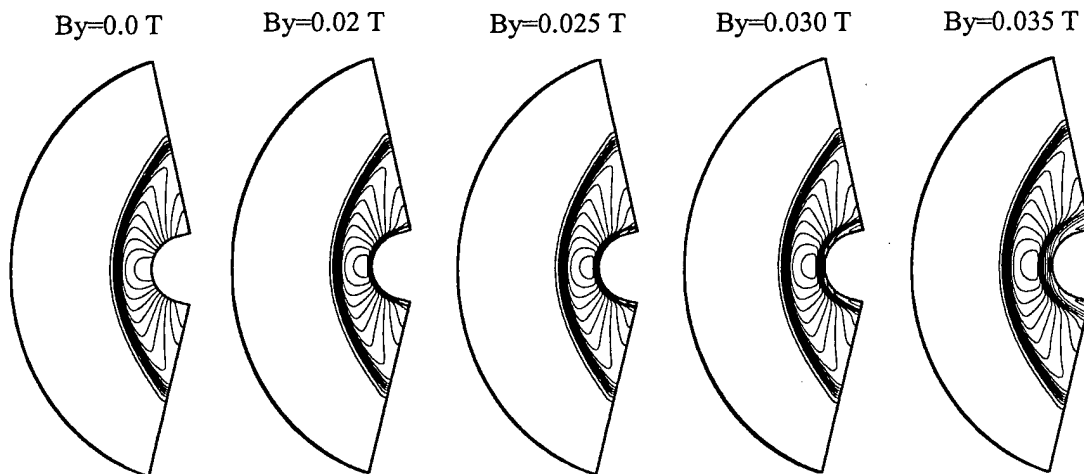
Figure 7-32. Pressure contours for various magnetic field intensities.
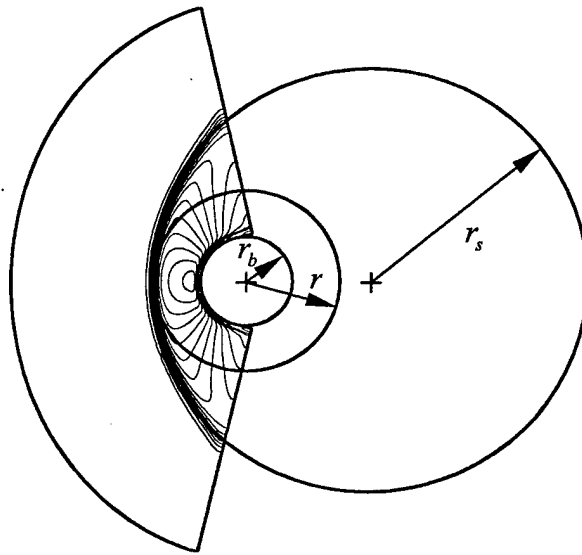
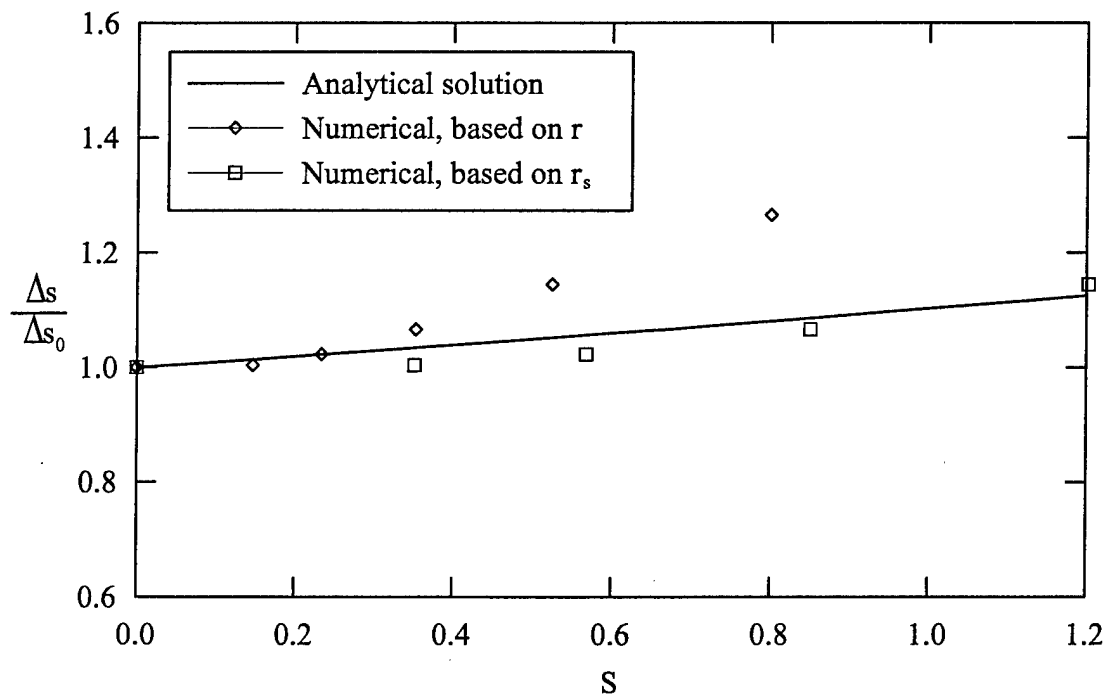Figure 7-33. Two approaches in evaluating the shock wave radius of curvature.

Figure 7-34. Shock standoff distance for the supersonic flow over a blunt body.

7.3. The MHD Hartmann Flow

The fully developed flow between two parallel plates under a transverse magnetic field is investigated under the influence of a magnetic field. It is the equivalent of the Couette flow in ordinary fluid mechanics. The term fully developed refers to the velocity profile being independent of the axial coordinate. A pressure gradient exists in the longitudinal coordinate, which drives the fluid into motion and balances the viscous and magnetic friction. This type of flow is the simplest magnetohydrodynamic channel flow and was first investigated by Hartmann in 1930. The presence of a magnetic field alone can only slow down the flow and a larger pressure gradient is required to maintain the same mass flow rate. The Hartmann flow has been extended to the case where both a magnetic and electric fields are present. In this case, it is possible to decelerate or accelerate the flow by a suitable combination of the electric and magnetic fields. Here, both laminar and turbulent flows are considered and compared with analytical or experimental results. This test case serves as a basis for the calibration of the modified turbulence models.

Consider an incompressible fluid, with constant viscosity and constant electrical conductivity flowing between two infinite parallel flat plates (Figure 7-35). A constant magnetic field is applied in the transverse direction (i.e., the y-direction). All variables are functions of y only, except the pressure. The walls are located at $y = \pm h$.
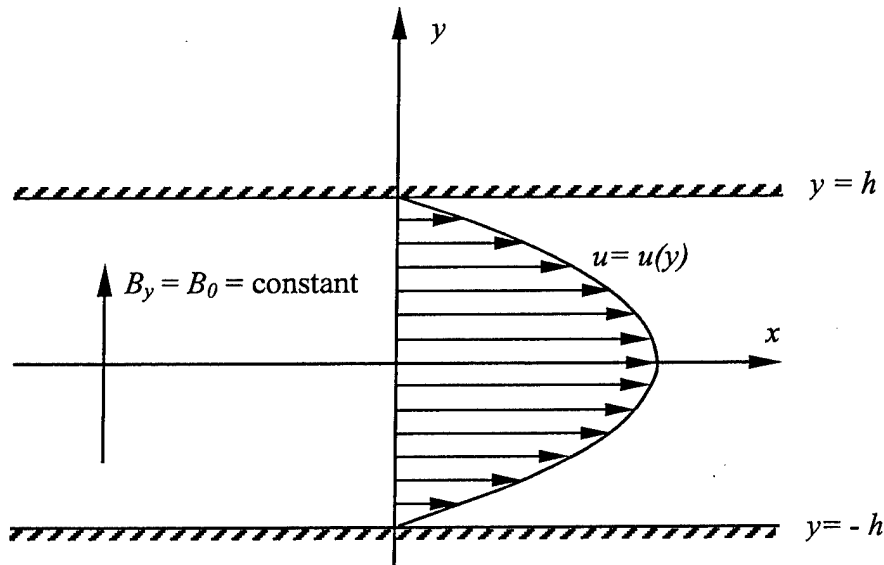
Figure 7-35. Schematic of the Hartmann flow.

94

Laminar and turbulent flows are investigated under the following conditions:

Property	Value
Density	$\rho = 1.225 \; kg/m^3$
Electrical conductivity	$\sigma_e = 800 \; mho/m$
Viscosity	$\mu = 1.8 \times 10^{-5} \; kg/(m \cdot sec)$
Distance between the plates	$h = 0.005 \; m$

Table 7-4. Properties of the MHD Hartmann flow.

The Reynolds number based on the half-height h between the two plates and the average velocity, ranges from 5,000 to 50,000. The magnetic Reynolds number corresponding to these conditions is $Re_m = 1.51 \times 10^{-4}$. Therefore, the induced magnetic field can be considered negligible compared to the applied magnetic field. In fact, the value of the induced magnetic field can be analytically evaluated in the general case and is given by

$$\frac{b_x}{B_0} = \frac{\mu \sigma_e V h}{Ha} \frac{\sinh(Ha\eta)}{\cosh(Ha)} \tag{7.8}$$

where V and η are provided in Equations (7.11) and (7.12). Figure 7-36 illustrates the relative magnitude of the induced magnetic field b_x compared to the applied field B_0 (theoretical distribution). It can be observed that for a given Hartmann number, the induced field is maximum at the wall and zero at the centerline. The ratio b_x/B_0 decreases as the Hartmann number increases. In all cases, the induced magnetic field is negligible compared to the applied field. In fact, the largest value of the induced field is more than 2,000 times smaller than the applied field. Therefore, the low magnetic Reynolds number approximation can be considered valid for this application.
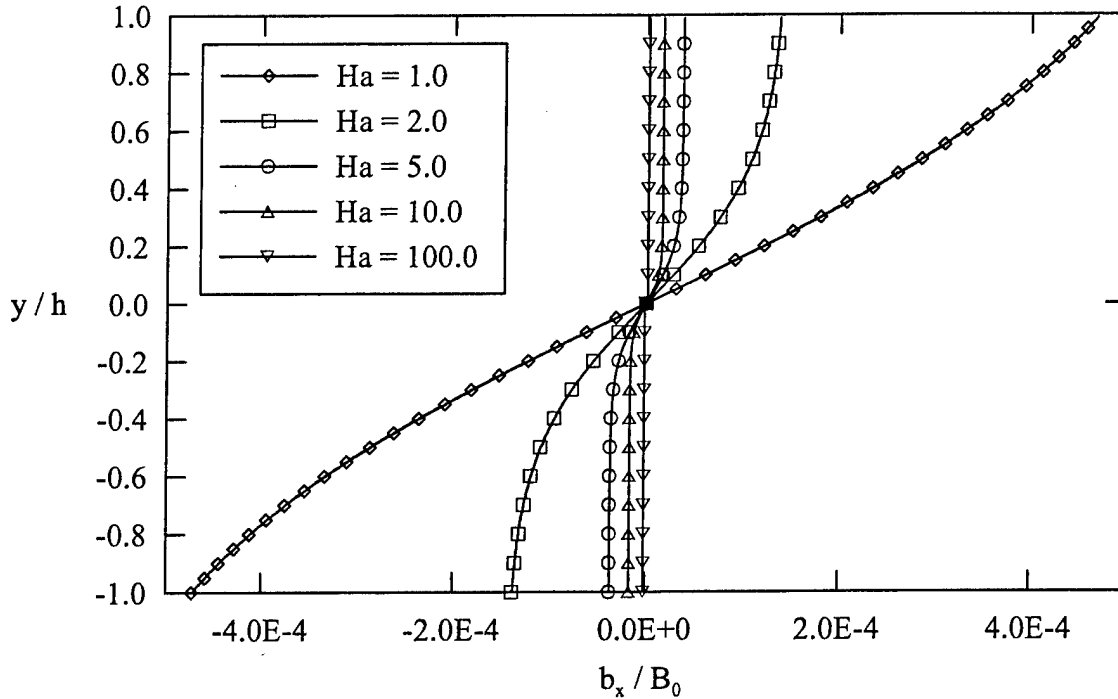
Figure 7-36. Analytical distribution of the induced magnetic field.

The influence of the induced magnetic field is much less than that of the applied magnetic field. It is therefore sufficient to consider only the applied field in the flow analysis, and it is appropriate to solve this MHD Hartmann problem by the low magnetic Reynolds number formulation.

The computation is performed on a two dimensional domain. In order to obtain a fully developed flow, the length of the numerical domain should be much larger than its height. This requires a large number of grid points in the x-direction and results in a prohibitive computational time for such a simple case. However, it is possible to accelerate the convergence of the code, by having a small computational domain and modifying the boundary conditions. The ratio between the length and the height of the domain is $L/2h = 10$ and the number of grid points is 10 in the x-direction with uniform grid spacing. There are 150 grid points in the y-direction and grid clustering is implemented near the two solid walls to resolve the velocity gradients. The velocity is extrapolated at the inlet and outlet to obtain a fully developed flow in a short computational time. The pressure gradient in the x-direction is adjusted to provide the same mass flow rate regardless of the strength of the magnetic field.

In the case of a laminar flow, an analytical solution exists [110]. It can be simplified further since the magnetic Reynolds number is small. The pressure gradient is denoted by

$$\frac{\partial p}{\partial x} = -\rho G \qquad (7.9)$$

where G is the force per unit mass that maintains motion of the fluid. It balances the Lorentz force induced by the interaction between the magnetic field and velocity field. The x-component of the velocity is a function of y only and is given by

$$\frac{u(y)}{V} = 1 - \frac{\cosh(Ha\eta)}{\cosh(Ha)} \qquad (7.10)$$

where
$$V = \frac{\rho G}{\sigma_e B_0^{\;2}} \qquad (7.11)$$

$$\eta = \frac{y}{h} \qquad (7.12)$$

$$Ha = B_0 h \sqrt{\frac{\sigma_e}{\mu}} \qquad (7.13)$$

Here, B_0 is the constant value of the magnetic field that is applied in the positive y-direction. The Hartmann number Ha is a nondimensional parameter which its square represents a measure of the ratio of the electromagnetic to viscous forces. It is important to note that the reference length associated with the Hartmann number should represent a characteristic length of the variation of $u(y)$.

The skin friction coefficient can be analytically calculated according to Equation (7-14),

$$C_f = \frac{\mu \dfrac{du}{dy}\Big|_{y=h}}{\dfrac{1}{2}\rho U^2} = 2\frac{Ha^2}{Re} \cdot \frac{1}{\dfrac{Ha}{\tanh(Ha)} - 1} \qquad (7.14)$$

where U is the average velocity between the plates.

$$U = \frac{1}{h}\int_0^h u\,dy = V\left[1 - \frac{\tanh(Ha)}{Ha}\right] \qquad (7.15)$$

In the case of a turbulent flow, it has been experimentally shown by Lykoudis [93] that a relaminarization process should occur when the magnetic field is sufficiently strong. The criterion for the relaminarization process is expressed by the ratio of the Hartmann number to the Reynolds number. The advantage of expressing the relaminarization criterion with this ratio is that it becomes independent of the reference length. Lykoudis found that when the critical value of $Ha/Re = 1/225$ is reached, the flow should return to a laminar state. The goal of this investigation is to verify this experimental conclusion.

Figure 7-37 shows the fully developed velocity profile for different values of the Hartmann number in the laminar case, for which a comparison with the analytical solution is possible. The velocities are normalized with the maximum velocity obtained in the non-magnetic laminar case. When $Ha = 0.0$, the well known parabolic profile corresponding to the Couette flow in fluid dynamic is obtained. As the Hartmann number is increased, the velocity profiles are flattened, the maximum velocity (at the centerline) decreasing. For Hartmann numbers greater than 10.0, the velocity remains almost constant on a large portion between the two flat plates. It can be qualitatively observed by inspecting the velocity slopes at the walls that the skin friction increases with the Hartmann number. In all cases, the computed solutions are in excellent agreement with the analytical theory.
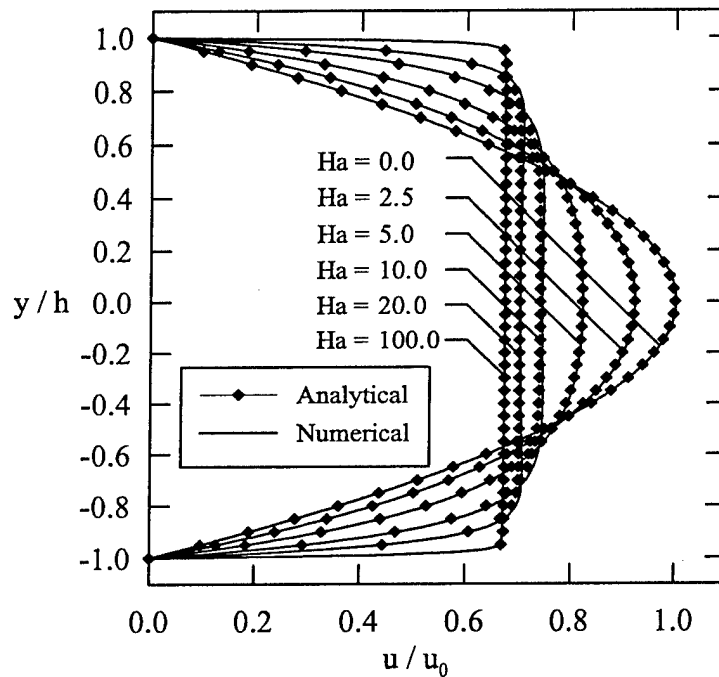
Figure 7-37. Laminar velocity profiles for the Hartmann flow.

7.3.1. Baldwin-Lomax Model

The skin friction coefficient is plotted versus the ratio Ha / Re in Figure 7-38 for a Reynolds number of 10,000. In the case of the laminar flow, the computed values compare well with the analytical solution. Note that for large values of the Hartmann number, the skin friction coefficient can be approximated by the straight line $2\,Ha / Re$. In the case of the turbulent flow, the skin friction obtained with the original model do not show any relaminarization process, the turbulent skin friction always remains greater than the laminar one. When the damping terms are implemented to provide the modified Baldwin-Lomax model, the relaminarization process takes place at the expected location ($Ha / Re \approx 1 / 225$). As expected, both original and modified models provide the same skin friction in the non-magnetic case. The turbulent velocity profiles are shown in Figure

7-39 for the original model and Figure 7-40 for the modified model. The velocities are normalized with the maximum velocity obtained in the non-magnetic turbulent case. When $Ha = 0.0$, the velocity profile is flatter than in the laminar case, as expected. However, the effect of the magnetic field is less important for small values of Ha than it was for the laminar case. In fact, the velocity profiles remain almost identical until the Hartmann number approaches a value of 10.0 (not shown). For values of Ha greater than 10.0, the velocity flattening becomes noticeable. For large values of the Hartmann number, the shape of the velocity profile is identical to the laminar profile, suggesting that a relaminarization process has occurred. No significant difference in velocity profiles is noticeable between the two versions of the Baldwin-Lomax model.

Figure 7-41 shows the distributions of the turbulent viscosity obtained with the original model. At low Hartmann numbers, the profiles exhibit sharp corners, with a relative minimum at the centerline. As the Hartmann number increases, the amount of turbulent viscosity is decreases and the profiles become more round in shape. The sharp profiles are most likely due to the nature of the algebraic model turbulence model, and the definition of the mixing length on which the model is based. The modified model provides similar turbulent viscosity profiles (Figure 7-42). For low Hartmann numbers, the turbulent viscosity begins to slightly increase, followed by a rapid decrease, which is faster than when the original model was employed. For example, there is almost no turbulent viscosity produced by the modified model when $Ha = 30.0$, whereas the original model provided more turbulent viscosity. When the maximum turbulent viscosity is plotted versus Ha/Re (Figure 7-43), it can be seen that at the relaminarization point, the original model still provides a substantial amount of turbulent viscosity, whereas the damping terms in the modified version bring the turbulent viscosity to such a low level that the flow can be considered laminar. Figure 7-44 shows the maximum velocity (at the centerline) versus Ha/Re. The velocity is nondimensionalized by the non-magnetic maximum velocity. The effect of the magnetic field is to flatten the velocity profiles. In the case of a laminar flow, the flattening is large for low Hartmann numbers and remains almost constant for large Hartmann numbers. It is more than 30% for the largest magnetic field investigated. In the case of turbulent flow, the relative flattening is less than the one obtained for a laminar flow, because the turbulent profiles are already flatter than the laminar one. The maximum flattening is less than 10%. Figure 7-45 shows the pressure gradient required to maintain a constant mass flow rate between the two flat plates. Since the effect of the magnetic field is to slow down the flow (the Lorentz force is acting in the opposite direction of the flow field), a larger pressure gradient must be provided to maintain the same flow rate. A larger pressure gradient is required for the turbulent flow at low Hartmann numbers since the friction forces are greater than for the laminar flow. As the magnetic field is increased, the turbulent and laminar skin friction become similar, meaning that the friction forces are comparable. Subsequently, the pressure gradients required to maintain a constant flow rate become identical.

Similar results are obtained in terms of skin friction, as observed in Figure 7-46 (for a lower Reynolds number of 5,000), and in Figure 7-47 (for a higher Reynolds number of 50,000). In all cases, the original model does not yield any relaminarization

99

process whereas the modified version shows that the flow becomes laminar at about the same ratio of $Ha/Re \approx 1/225$. Figure 7-48 shows a summary of the skin frictions obtained by the modified model at different Reynolds numbers. As the Reynolds number is increased, the non-magnetic skin friction is decreased, and the turbulent skin friction coincide with the laminar one after the relaminarization is achieved.
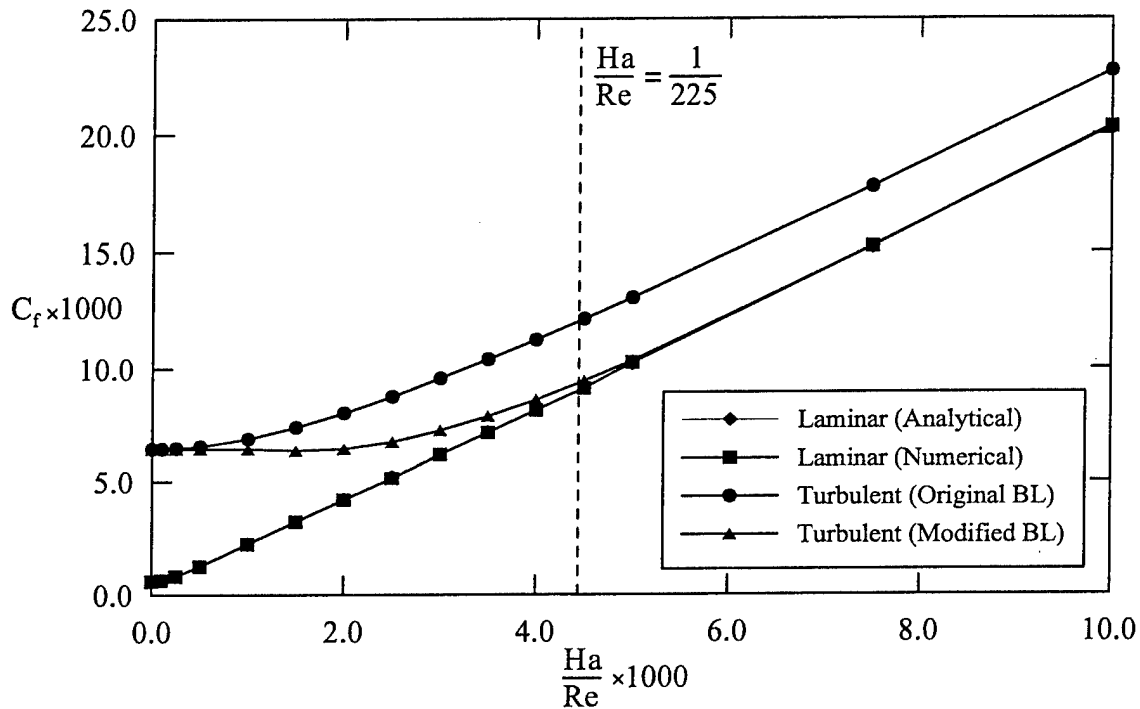
Figure 7-38. Skin friction coefficient for the Hartmann flow at $Re = 1.0 \times 10^4$

(Baldwin-Lomax model).
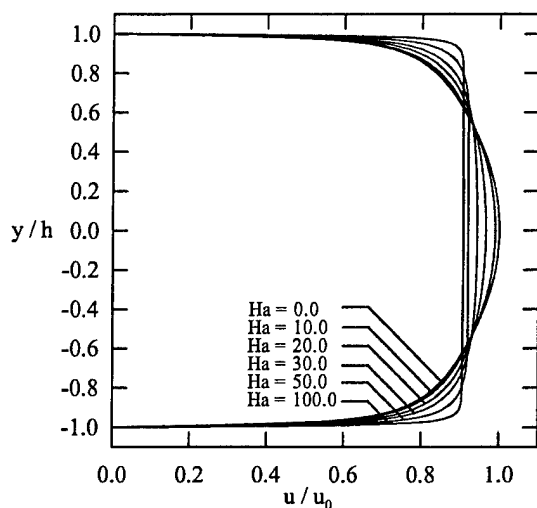
Figure 7-39. Turbulent velocity profiles
(original Baldwin-Lomax model).
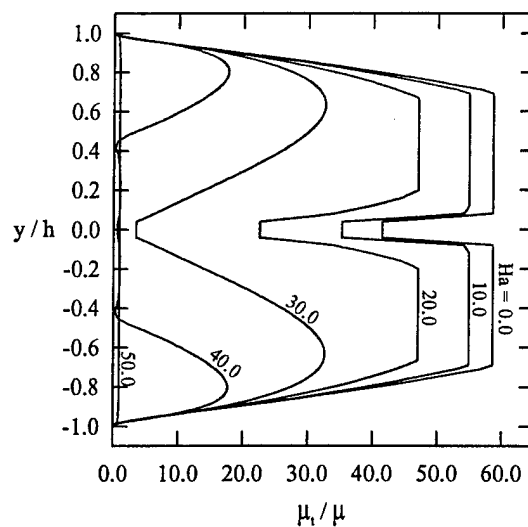
Figure 7-41. Turbulent viscosity profiles
(original Baldwin-Lomax model).
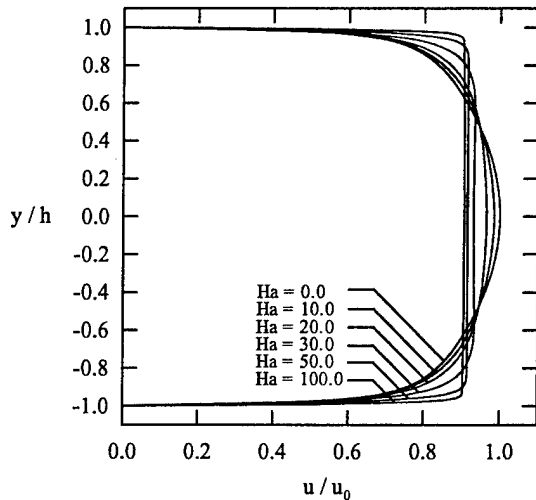
Figure 7-40. Turbulent velocity profiles
(modified Baldwin-Lomax model).
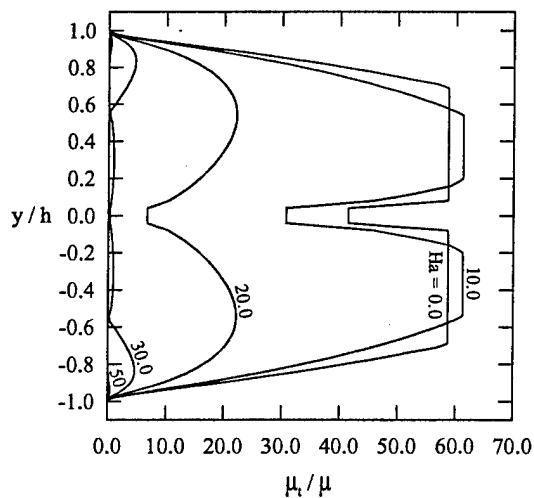
Figure 7-42. Turbulent viscosity profiles
(modified Baldwin-Lomax model).
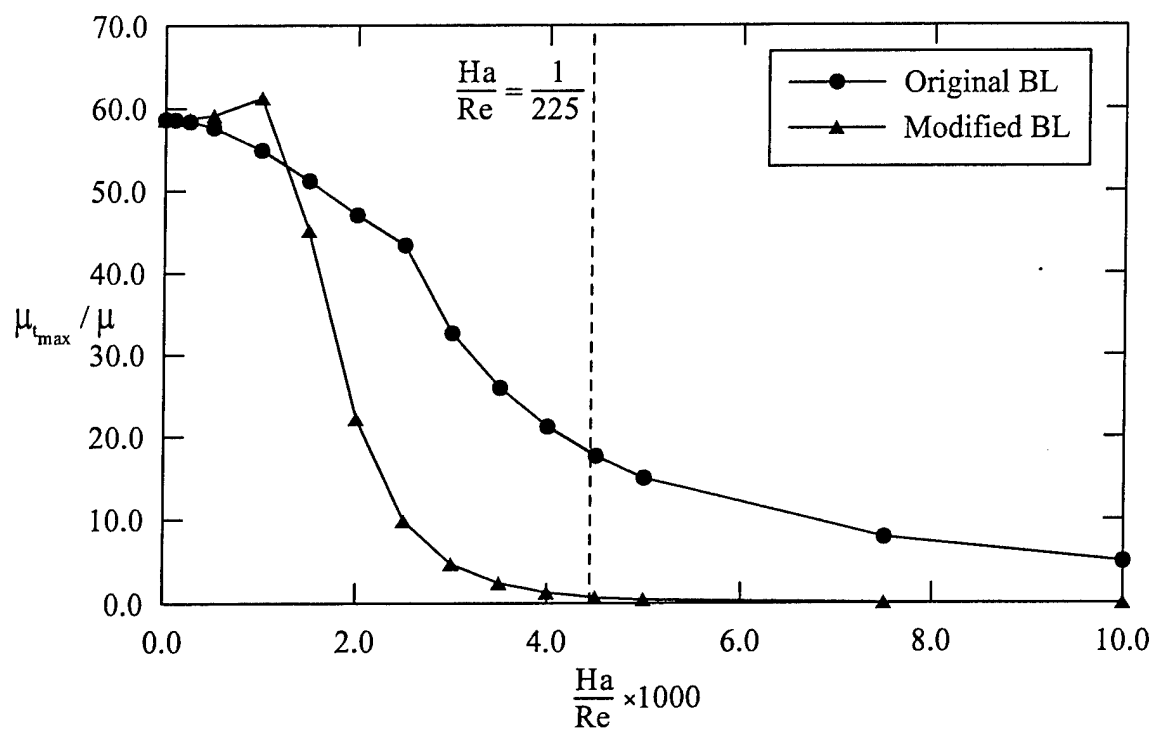
Figure 7-43. Maximum turbulent viscosity (Baldwin-Lomax model).
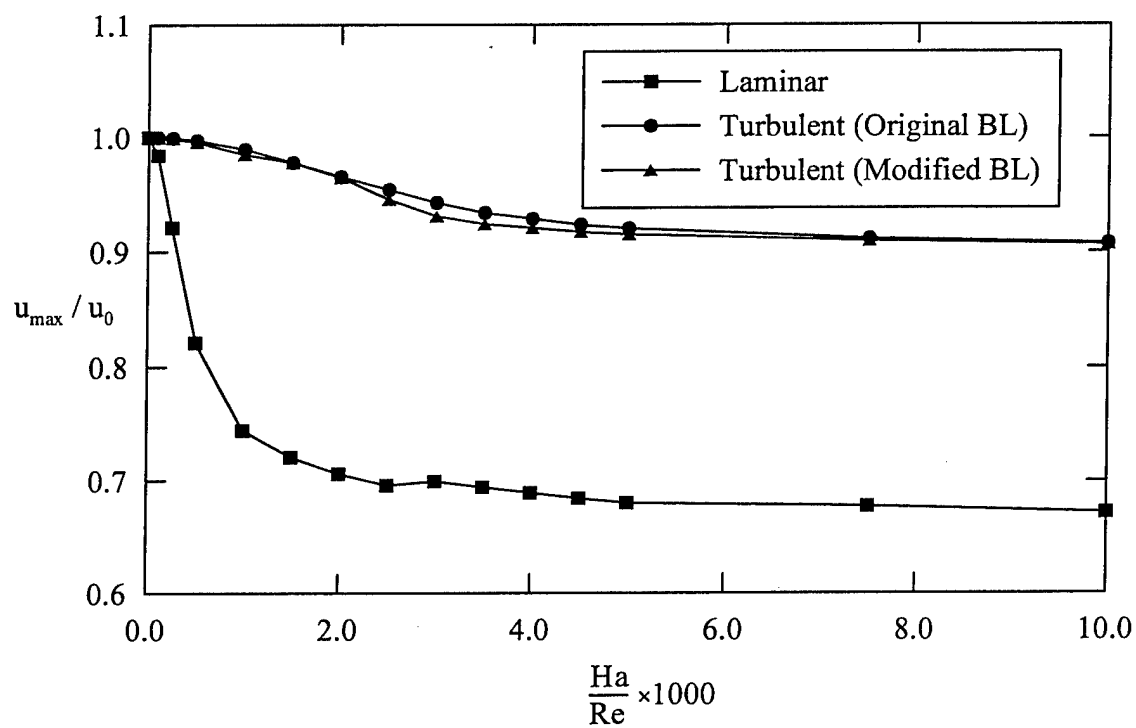
Figure 7-44. Maximum velocity (Baldwin-Lomax model).

102
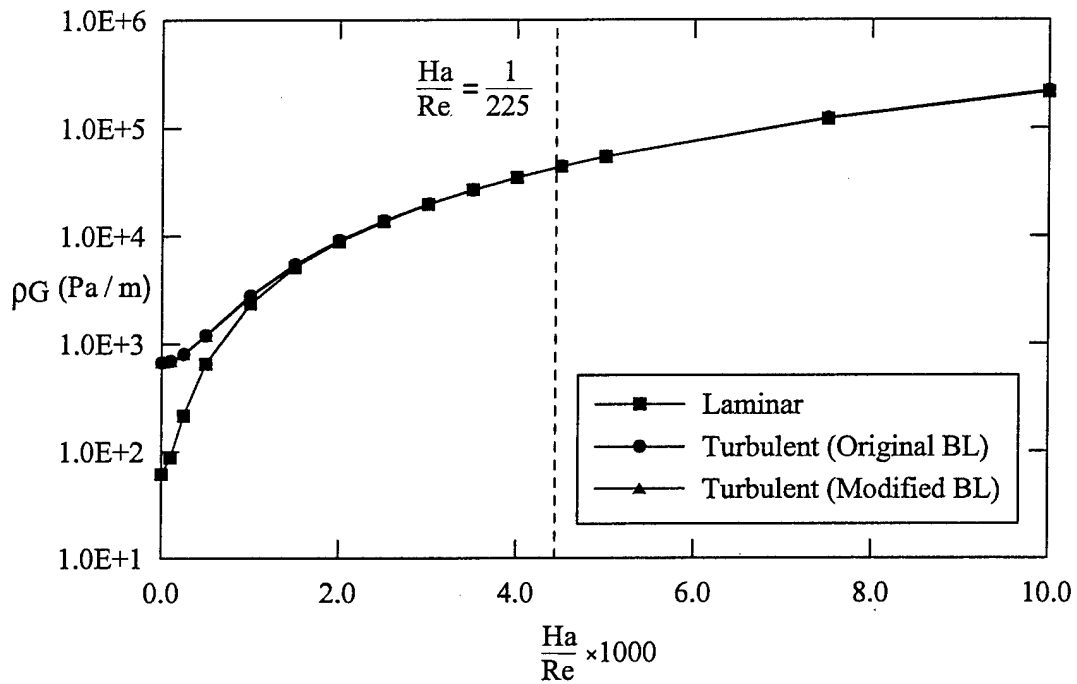
Figure 7-45. Pressure gradient (Baldwin-Lomax model).
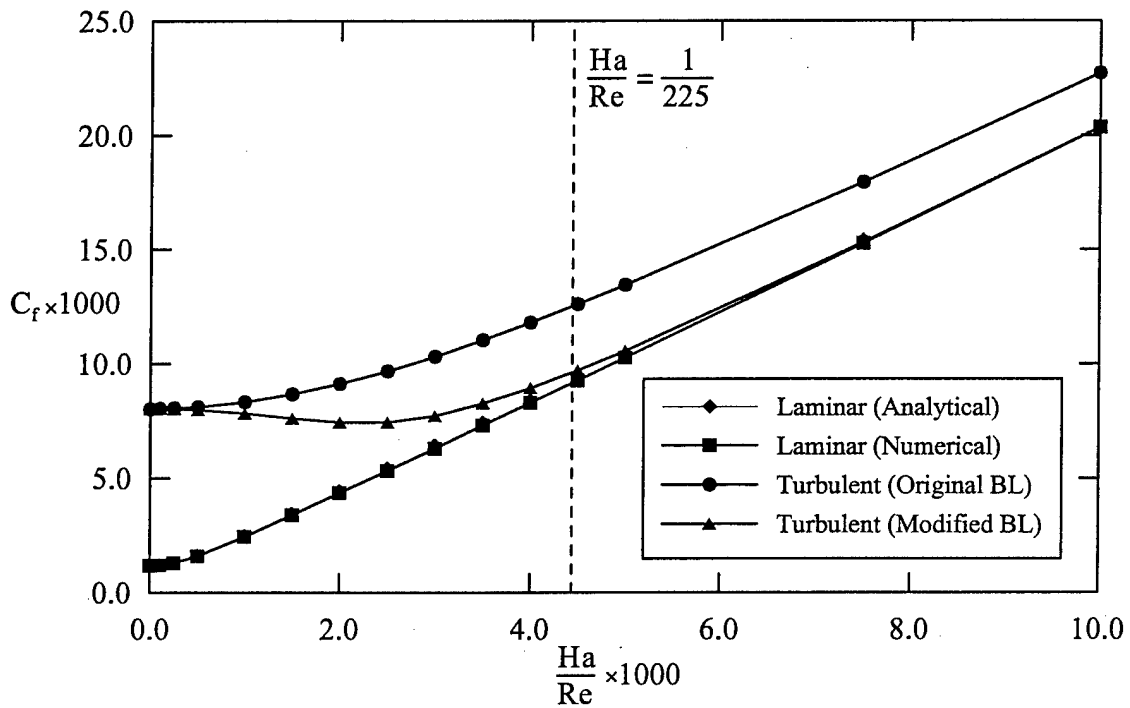
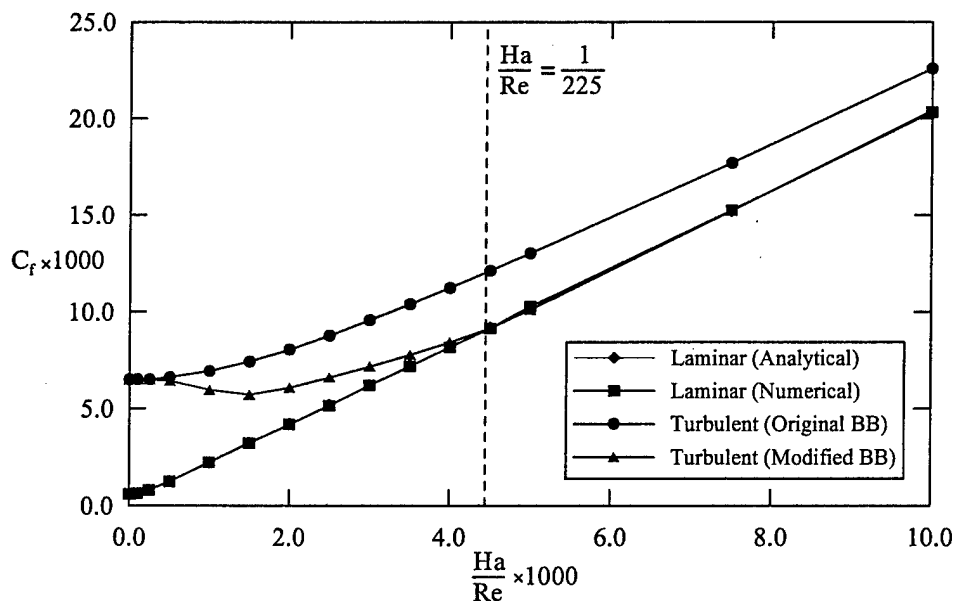Figure 7-46. Skin friction coefficient for the Hartmann flow at $Re = 5.0 \times 10^3$

(Baldwin-Lomax model).
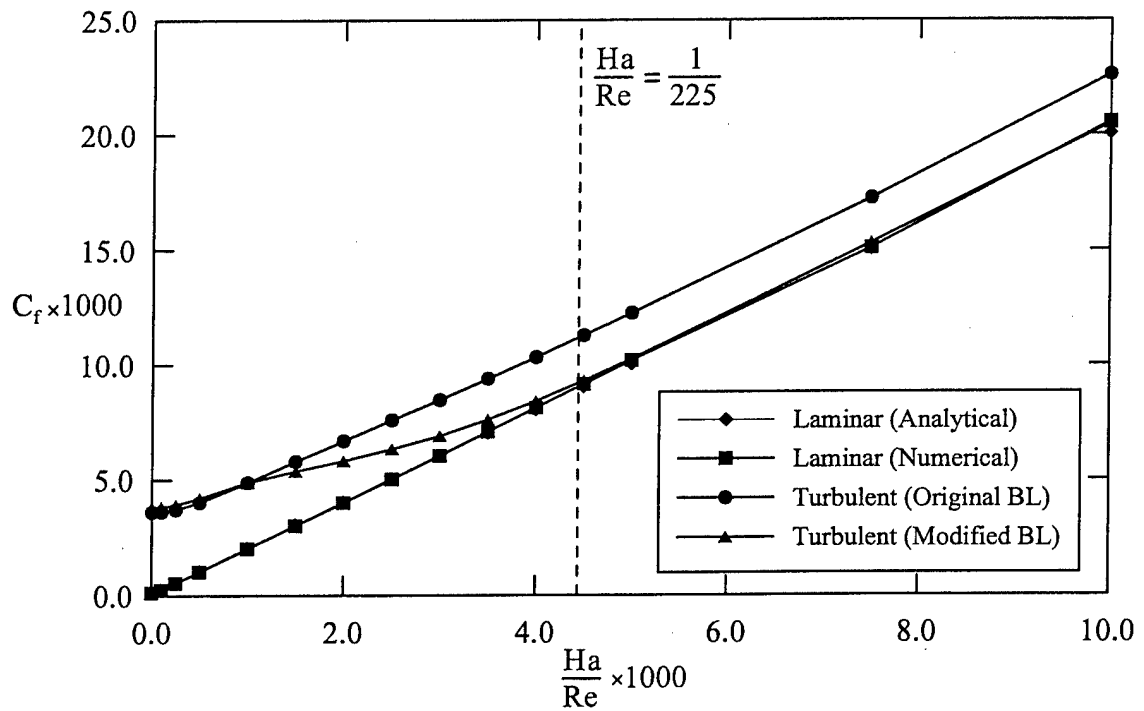
Figure 7-47. Skin friction coefficient for the Hartmann flow at $Re = 5.0 \times 10^4$

(Baldwin-Lomax model).
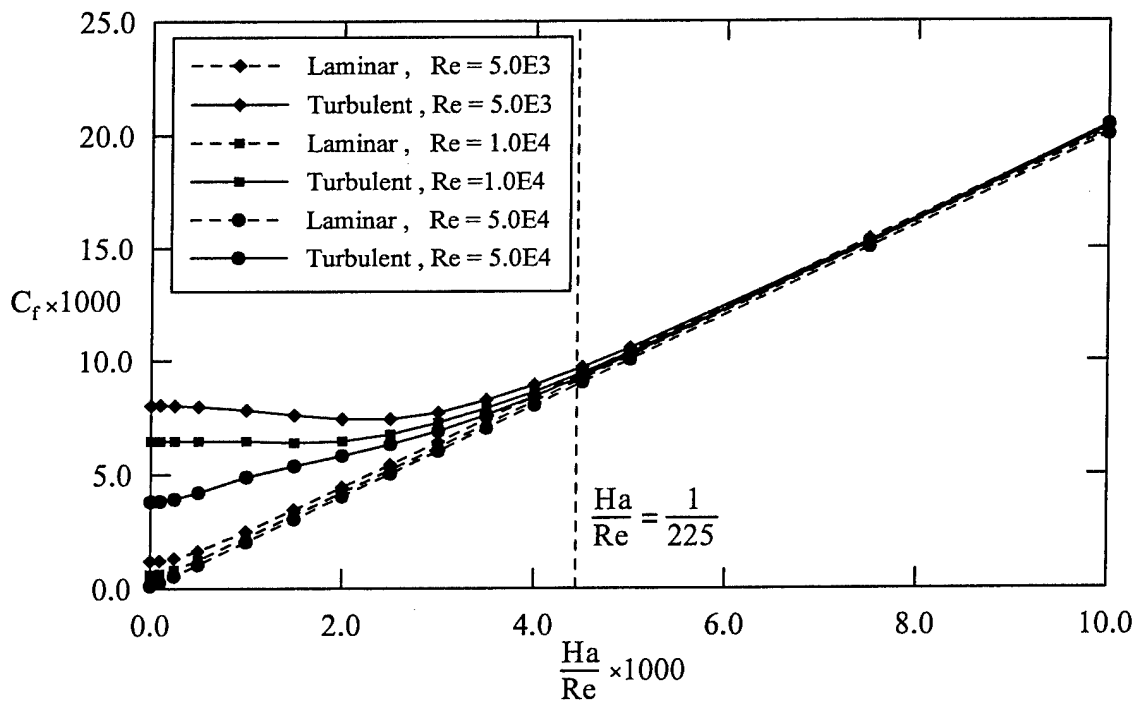
Figure 7-48. Summary of skin friction coefficient for the Hartmann flow

(Baldwin-Lomax model).

7.3.2. Baldwin-Barth Model

The same set of plots is provided for the results concerning the Baldwin-Barth model. Figure 7-49 shows the skin friction versus Ha/Re at $Re = 10,000$. As for the Baldwin-Lomax model, the original model does not yield a relaminarization process, whereas the modified version provides a relaminarization process at the exact point, matching the experimental results of Lykoudis. The closure constant C_{Re_T} appearing in the magnetic terms of the modified model has been calibrated to provide this result ($C_{Re_T} = 6.0$). Figures 7-50 and 7-51 illustrate the velocity profiles for the original and modified model, respectively. For moderate Hartmann number, there is an increase in the maximum velocity when the modified model is used, whereas the original model always provided a flattening of the profiles as the Hartmann number is increased. The turbulent viscosity decreases as the Hartmann number is increased (original model, Figure 7-52), and some turbulent viscosity is still present in the flow at high Hartmann numbers, which does not enable the flow to become laminar again. The modified version decreases the turbulent viscosity more substantially, especially in the center region of the flow (Figure 7-53). It can be observed that at $Ha/Re = 1/225$, the maximum turbulent viscosity is decreased to the point that it becomes negligible in the case of the modified model (Figure 7-54), whereas the flow remains turbulent even at very large Hartmann numbers for the original model.

The Baldwin-Barth model behaves similarly for $Re = 5,000$, (Figure 7-55), and $Re = 50,000$, (Figure 7-56). The original model is not able to predict the relaminarization, whereas the modified version does. Figure 7-57 summarizes the skin frictions at various Reynolds numbers.

Figure 7-49. Skin friction coefficient for the Hartmann flow at $Re = 1.0 \times 10^4$
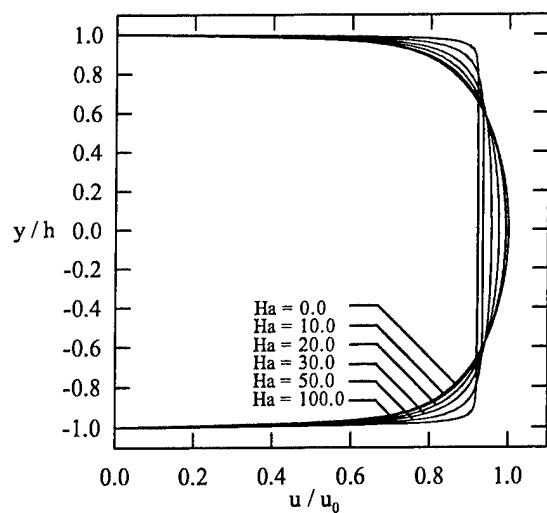
(Baldwin-Barth model).

Figure 7-50. Turbulent velocity profiles
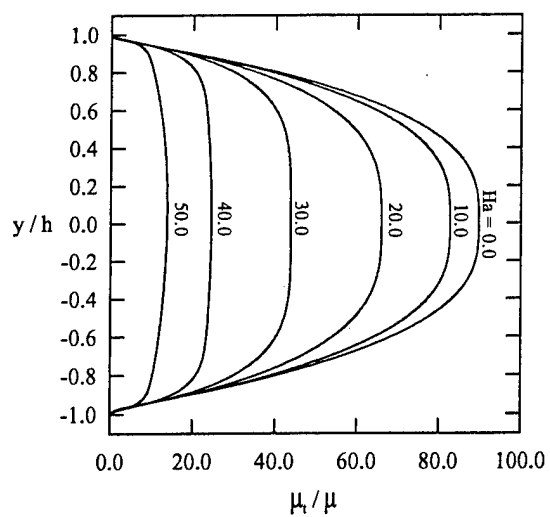(original Baldwin-Barth model).

Figure 7-52. Turbulent viscosity profiles
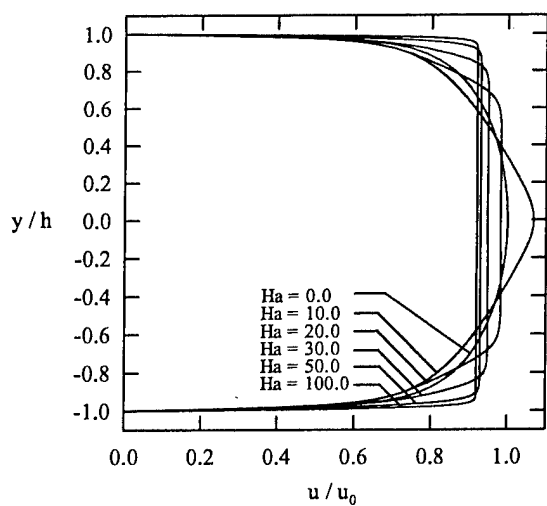(original Baldwin-Barth model).

Figure 7-51. Turbulent velocity profiles
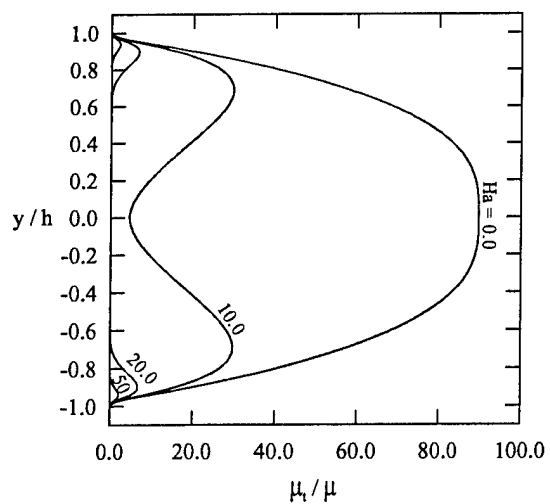(modified Baldwin-Barth model).

Figure 7-53. Turbulent viscosity profiles
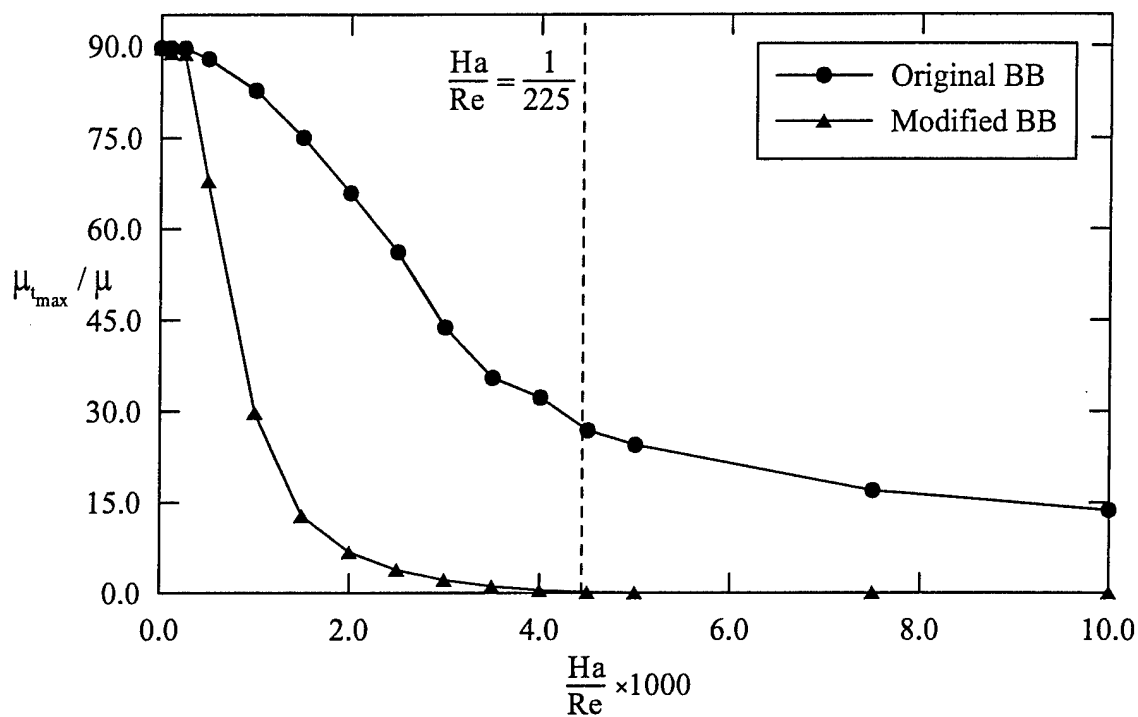(modified Baldwin-Barth model).

106

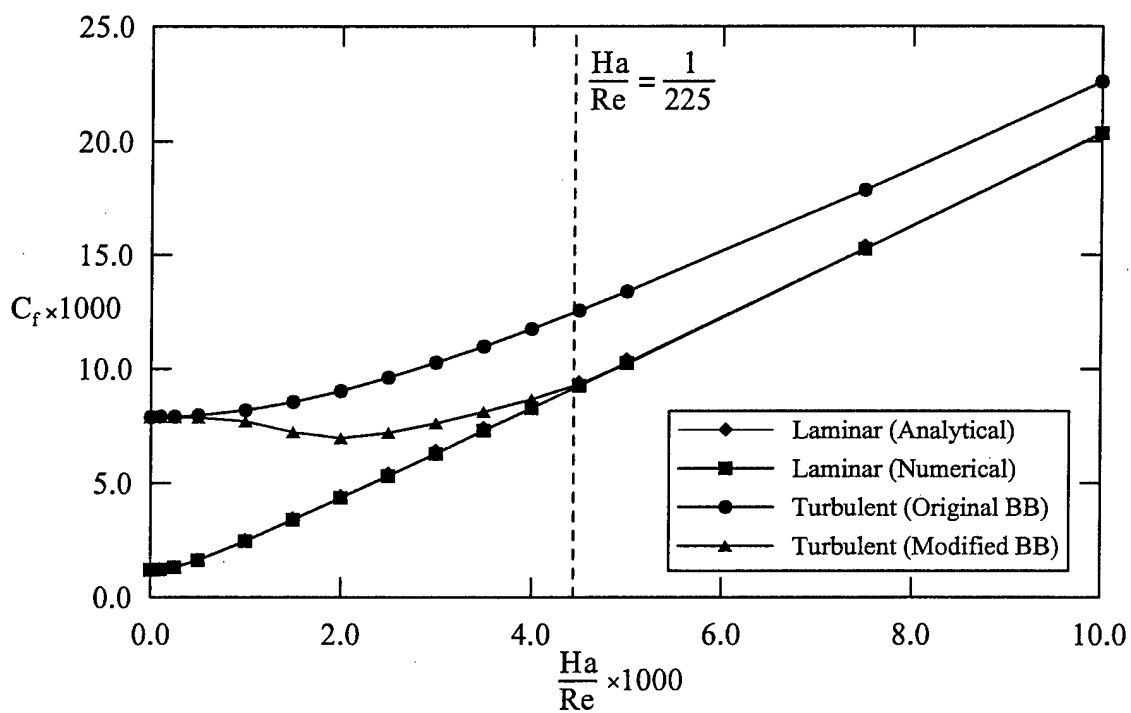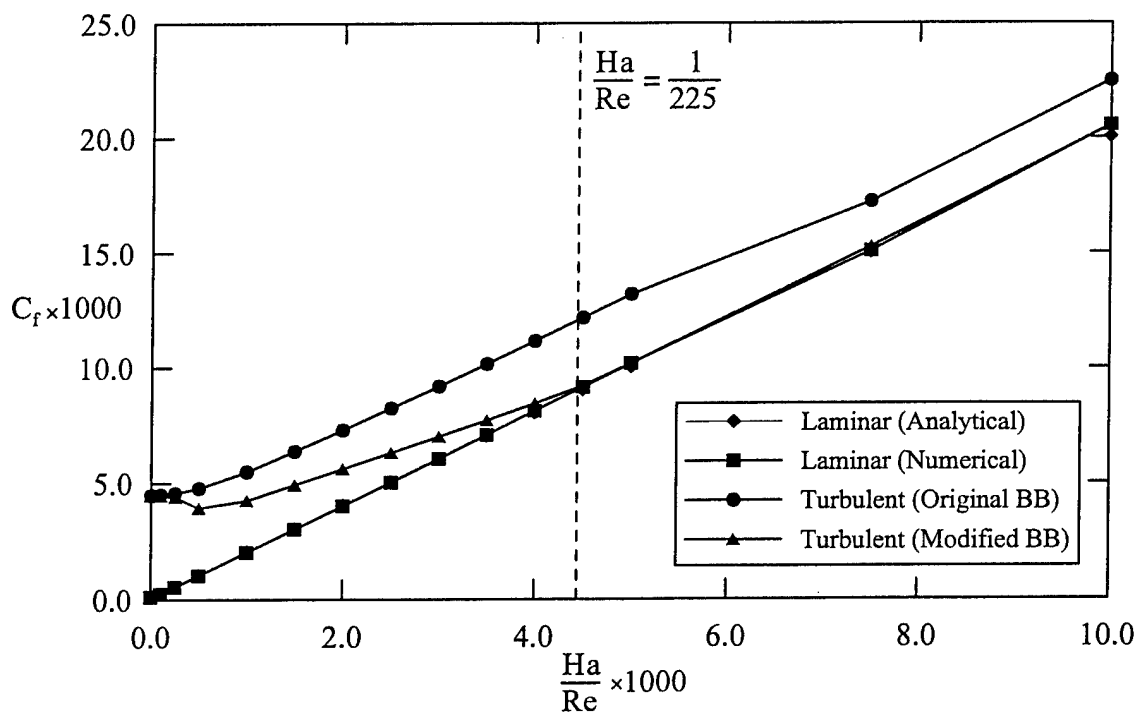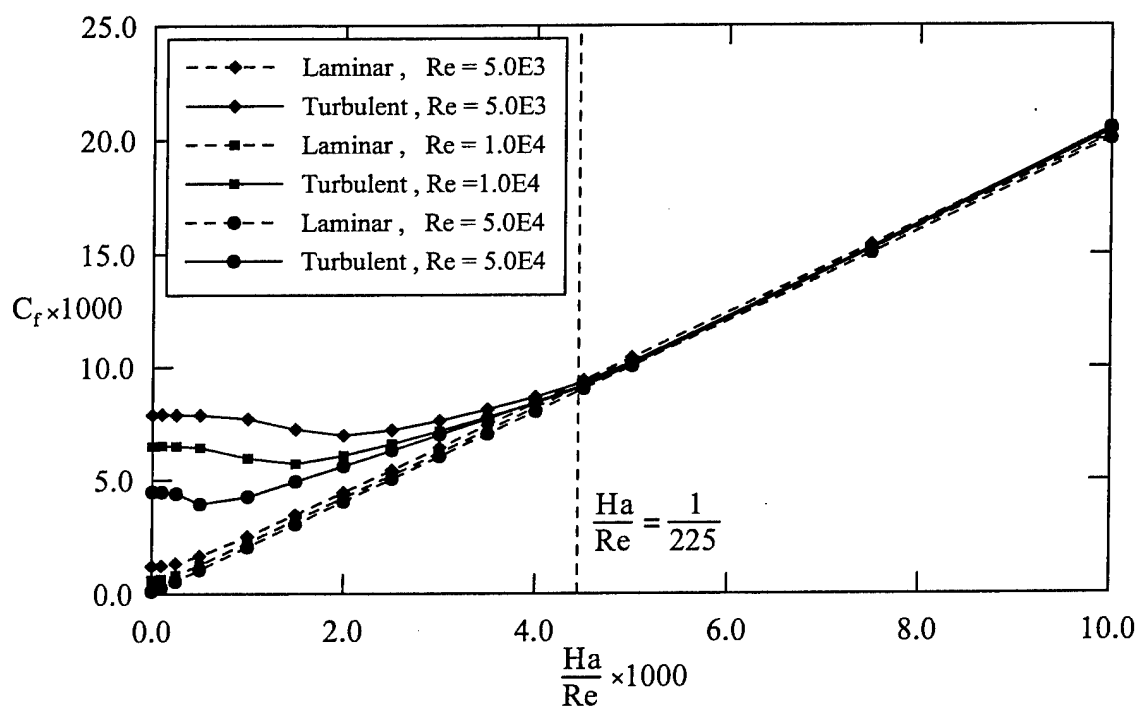Figure 7-54. Maximum turbulent viscosity (Baldwin-Barth model).

Figure 7-55. Skin friction coefficient for the Hartmann flow at $Re = 5.0 \times 10^3$

(Baldwin-Barth model).

Figure 7-56. Skin friction coefficient for the Hartmann flow at $Re = 5.0 \times 10^4$

(Baldwin-Barth model).

Figure 7-57. Summary of skin friction coefficient for the Hartmann flow

(Baldwin-Barth model).

108

7.3.3. Spalart-Allmaras Model

The skin friction obtained with the Spalart-Allmaras model at $Re = 10,000$ is shown in Figure 7-58. With the original model, the turbulent skin friction almost recovers the laminar skin friction values when $Ha/Re \approx 6 \times 10^{-3}$, which is greater than the experimental prediction of Lykoudis, as shown by the vertical dashed line. However, it always remains slightly greater than its laminar counterpart. In order to match the experimental result illustrating the relaminarization process, a modification of the Spalart-Allmaras closure coefficient C_{v1} is proposed. This closure coefficient influences the production term in the turbulence model and the evaluation of the turbulent viscosity from the turbulent quantity $\overline{v}$. An increase of this coefficient decreases the production of turbulent viscosity. When the closure coefficient C_{v1} is made dependent on the Hartmann number, it is possible to verify the relaminarization criterion of $Ha/Re = 1/225$. This modification does not significantly modify the velocity profiles compared to those obtained with the original Spalart-Allmaras model (Figures 7-59 and 7-60).

The turbulent viscosity profiles are illustrated in Figures 7-61 and 7-62 for the original and modified model, respectively. The general shape of the profile shows that the turbulent viscosity first increases away from the wall and then exhibits a local minimum at the centerline. As Ha is increased, the amount of turbulent viscosity is naturally decreased until it is sufficiently small to initiate the relaminarization process. For the original Spalart-Allmaras model, the turbulent viscosity becomes negligible when Ha reaches a value of 50.0. The turbulent viscosity profiles obtained by the modified Spalart-Allmaras model are very similar to those obtained by the original model. The difference between the two models becomes noticeable for Ha greater than 20.0, where the amount of turbulent viscosity is further reduced by the higher values of C_{v1} in the modified model. The turbulent viscosity becomes negligible when Ha reaches a value of 40, when the relaminarization process is about to occur.

Figure 7-63 illustrates the dependence of the closure coefficient C_{v1} on the Hartmann number. The proposed relation between C_{v1} and Ha/Re is provided by Equation (7.16). A substantial increase in the coefficient C_{v1} is required in the relaminarization region in order to obtain the anticipated effect.

$$C_{v1} = 7.1\min\left[2.6 + 1.6\tanh\left(4.43\frac{Ha}{Re} - 19.345\right) + 0.022\frac{Ha}{Re}, 4.225\right] \quad (7.16)$$

Another illustration of the differences between the original and modified Spalart-Allmaras models is shown in Figure 7-64, where, the maximum values of the turbulent viscosity are plotted versus Ha/Re. For small values of Ha/Re, no noticeable change is observed and both models provide identical turbulent viscosities. It is followed by a

rapid decrease in the maximum turbulent viscosity when the magnetic field is increased. At the relaminarization point, the modified Spalart-Allmaras model provides a sufficiently small turbulent viscosity, whereas the original model is not adapted to exactly meet the relaminarization criterion, providing a too large turbulent viscosity, the relaminarization process being reached for larger values of the Hartmann number.

Figures 7-65 through 7-67 show that the Reynolds number has no influence on the relaminarization point.

$$\frac{Ha}{Re} = \frac{1}{225}$$

Legend:
- Laminar (Analytical)
- Laminar (Numerical)
- Turbulent (Original SA)
- Turbulent (Modified SA)

y-axis: $C_f \times 1000$

x-axis: $\frac{Ha}{Re} \times 1000$
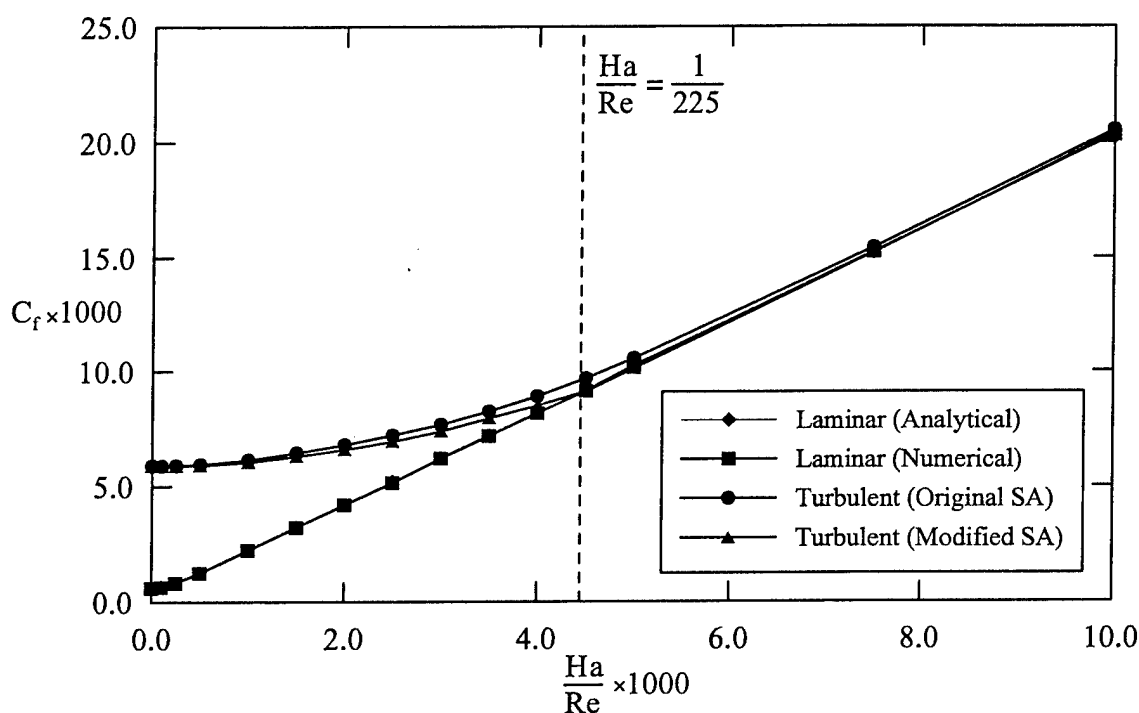
Figure 7-58. Skin friction coefficient for the Hartmann flow at $Re = 1.0 \times 10^4$

(Spalart-Allmaras model).

110
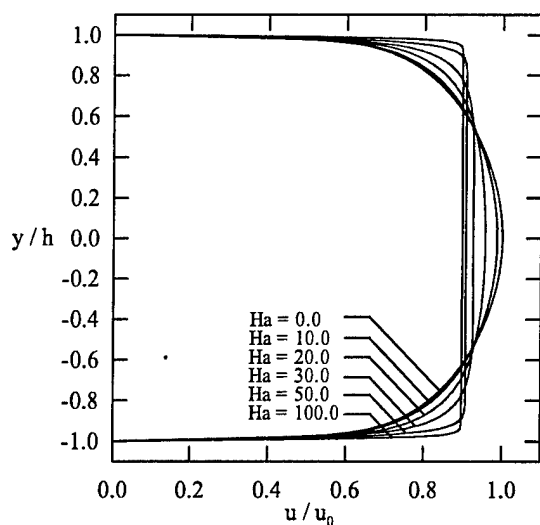
Figure 7-59. Turbulent velocity profiles
(original Spalart-Allmaras model).
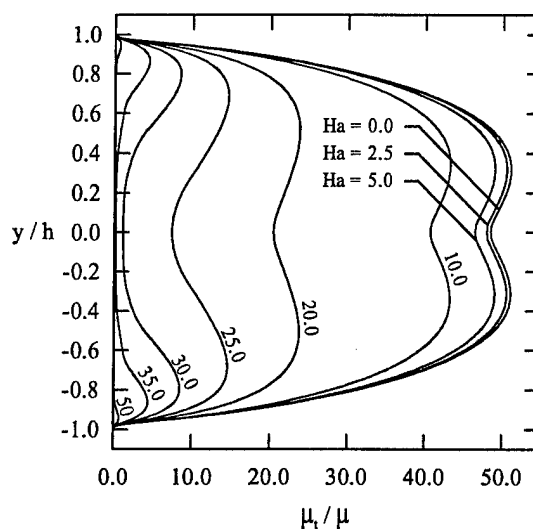
Figure 7-61. Turbulent viscosity profiles
(original Spalart-Allmaras model).
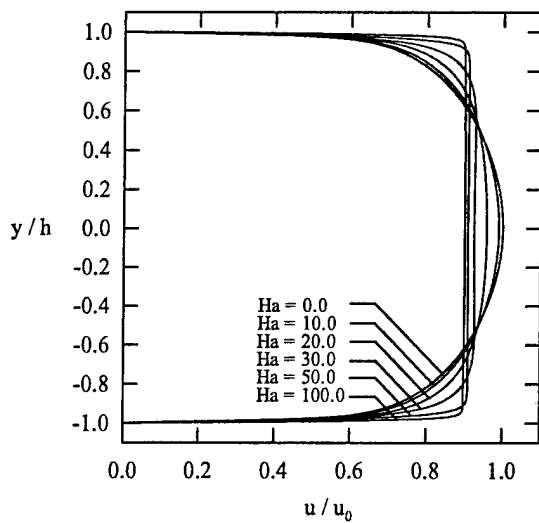
Figure 7-60. Turbulent velocity profiles
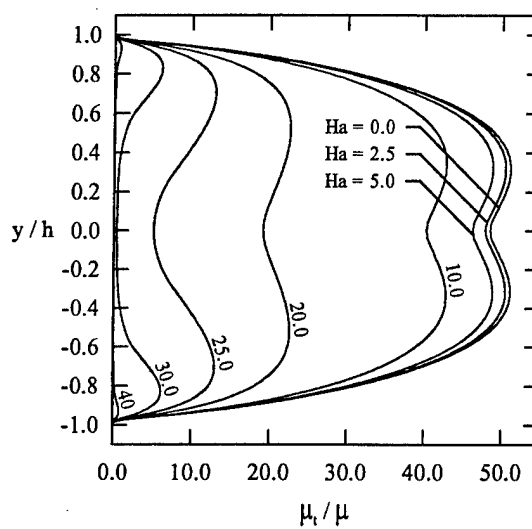(modified Spalart-Allmaras model).

Figure 7-62. Turbulent viscosity profiles
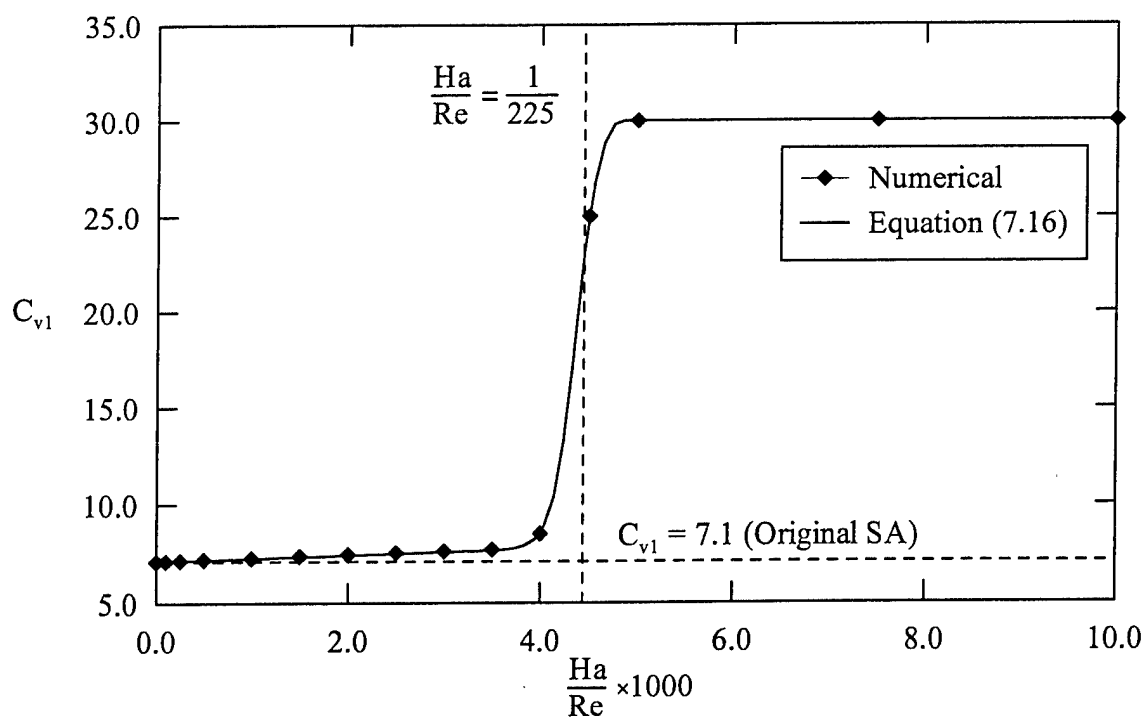(modified Spalart-Allmaras model).

111

Figure 7-63. Closure coefficient C_{v1} for the modified Spalart-Allmaras model.
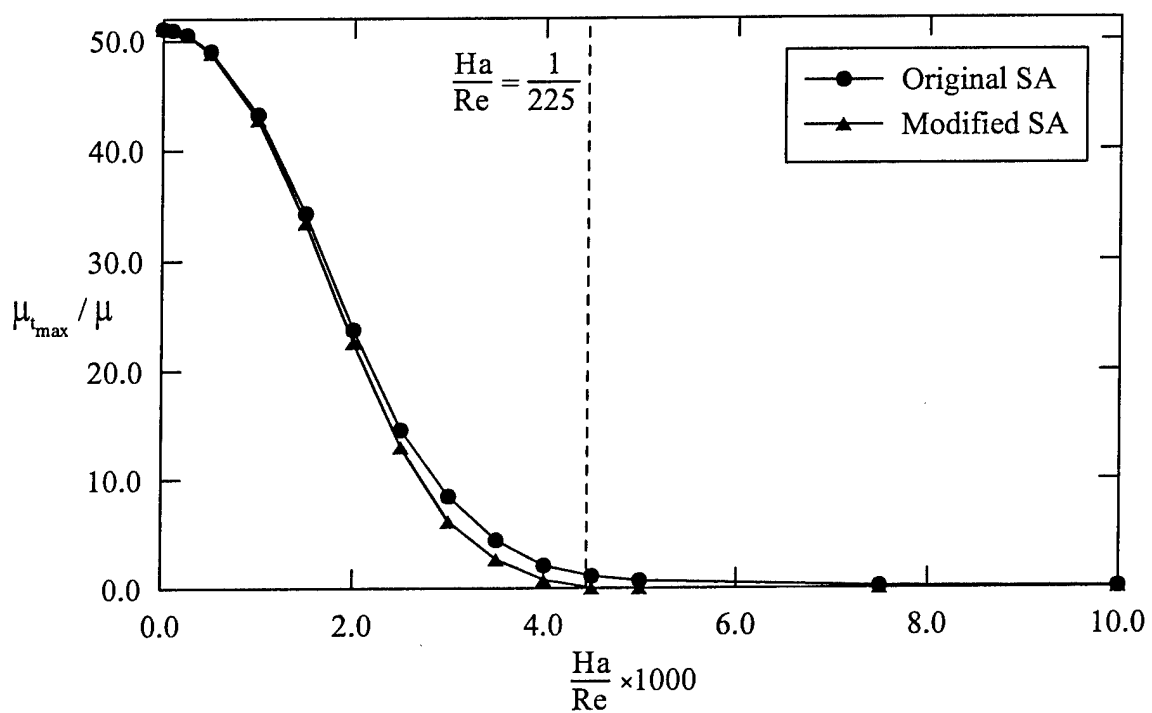

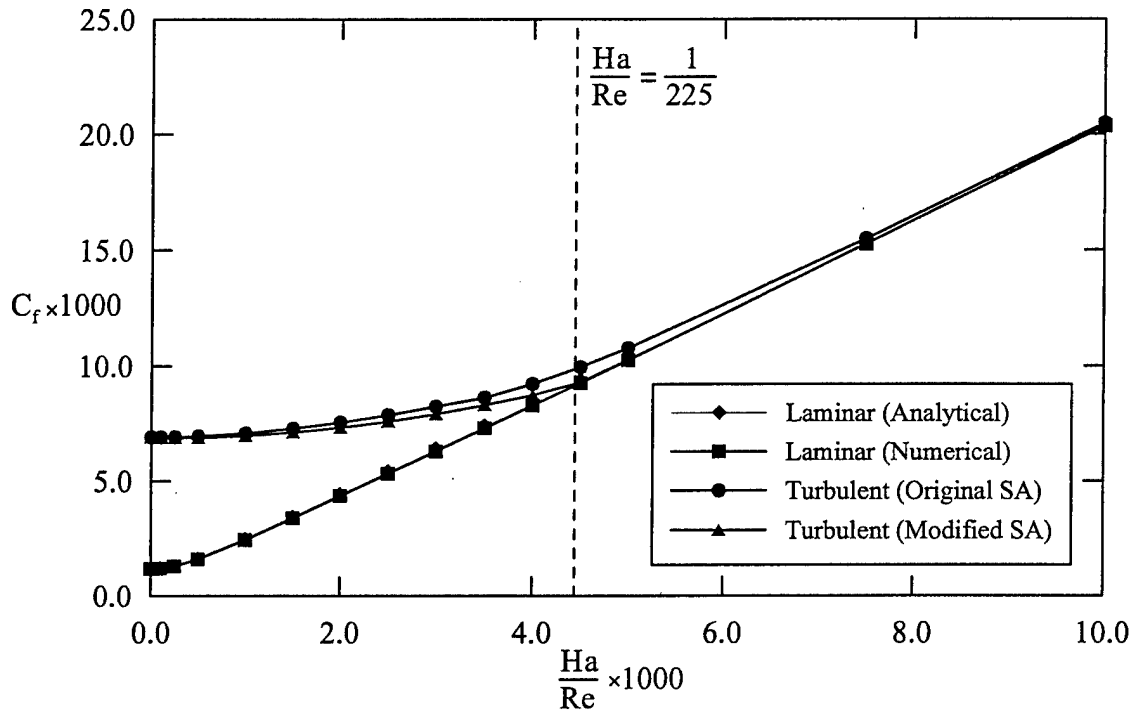Figure 7-64. Maximum turbulent viscosity (Spalart-Allmaras model).

112

Figure 7-65. Skin friction coefficient for the Hartmann flow at $Re = 5.0 \times 10^3$ (Spalart-Allmaras model).
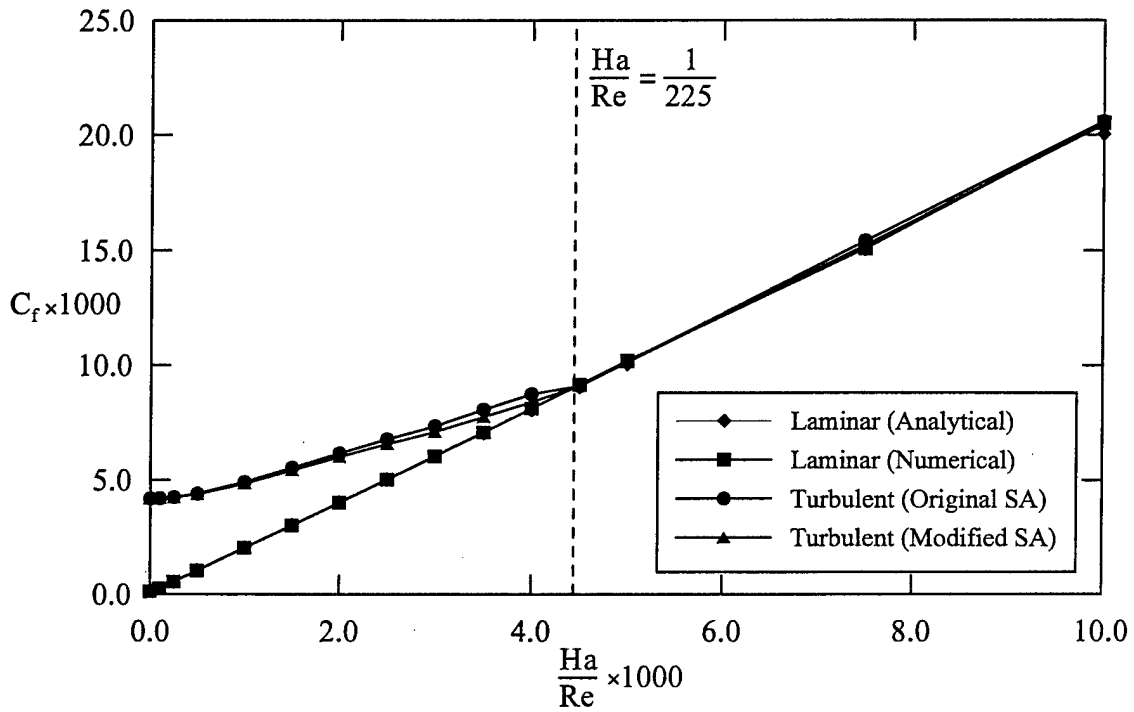

Figure 7-66. Skin friction coefficient for the Hartmann flow at $Re = 5.0 \times 10^4$ (Spalart-Allmaras model).
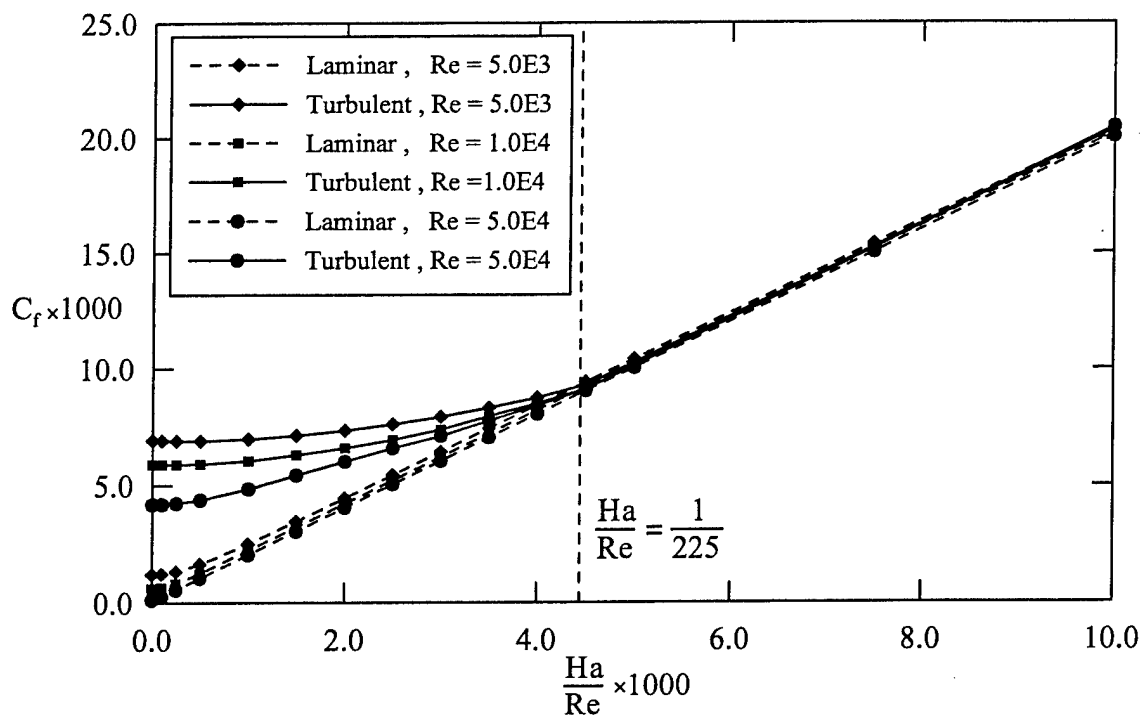
Figure 7-67. Summary of skin friction coefficient for the Hartmann flow (Spalart-Allmaras model).

7.3.4. k-ε Model

Figure 7-68 shows the skin friction distribution at $Re = 10,000$ obtained with the $k-\epsilon$ model. The original $k-\epsilon$ model is not able to predict the relaminarization process at $Ha/Re = 1/225$. Contrary to other original turbulence models that tend to over predict the relaminarization process, the original $k-\epsilon$ turbulence model predicts that the relaminarization occurs at $Ha/Re = 1/330$. The modified version of the $k-\epsilon$, in which additional magnetic terms have been included, has been calibrated to provide a relaminarization at the appropriate Hartmann number. The closure constant associated with the magnetic terms are $C'_{kN1} = -0.5$ and $C'_{\epsilon N1} = -1.0$. Figures 7-69 and 7-70 show the turbulent velocity profiles obtained with the original and modified models, respectively.

Figure 7-71 shows the turbulent viscosity profile obtained by the original $k-\epsilon$ model. First, observe that the $k-\epsilon$ model does not provide a hollow profile at the centerline, as opposed to other turbulence models. Second, the amount of turbulent viscosity decreases too rapidly as the Hartmann number is increased. In fact, when $Ha = 25.0$, there is almost no turbulent viscosity left in the domain, and the flow is about to become laminar. This particular behavior of the $k-\epsilon$ model was a source of difficulty in the calibration process. Since the original model does not generate enough turbulent viscosity, the modified version must provide a mechanism to increase the turbulent viscosity. In order to increase the turbulent viscosity, one can either increase the turbulent kinetic energy, or decrease the dissipation rate, or a combination of both. However, since the magnetic field must also be responsible for dissipating some turbulent kinetic energy, it is not suitable to decrease the dissipation of turbulent kinetic energy. Therefore, the model has been calibrated to generate an increase in turbulent kinetic energy up to a Hartmann number of $Ha = 40.0$. It can be seen in Figure 7-72 that the resulting turbulent viscosity profiles obtained by the modified turbulence model present a different shape than the one obtained by other models. For small Hartmann numbers, there is an augmentation of turbulent viscosity at the center. For moderate Hartmann number ($Ha = 20.0$ to 30.0) the turbulent viscosity starts to decrease until Ha reaches a value of 40.0, at which point there is no turbulent viscosity at the center. This precedes the relaminarization of the flow.

Figures 7-73 and 7-74 show the turbulent kinetic energy profiles for the original and modified $k-\epsilon$ models, respectively. The original model provides a too low turbulent kinetic energy close to the solid wall, which accelerates the relaminarization process. The modified version provides sufficient turbulent kinetic energy at moderates Hartmann numbers. However, the additional turbulent kinetic energy close to the solid surfaces also increases its value at the center. For example, at $Ha = 20.0$, there is no turbulent kinetic energy at the center when the original model is used whereas there is still a measurable amount of it when the modified version is implemented. This explains why the turbulent viscosity profiles present a large increase at the center. Figures 7-75 and 7-76 show the distribution of dissipation rate for both versions of the model. No significant difference can be observed. It should be noted that the dissipation rate should be increasing as the magnetic field increases, since it also dissipates some energy. However, due to the

115

behavior of the original model, a calibration of the modified version resulting in an increase of dissipation rate would further decrease the turbulent viscosity, accelerate the relaminarization process, and have the opposite effect as what is sought.

Figure 7-77 shows the maximum turbulent viscosity as a function of the Hartmann number. When the original model is used, there is no turbulent viscosity when $Ha = 20.0$, which leads to an early relaminarization. The modified model shows first an increase and then a rapid decrease before the relaminarization occurs. Figure 7-78 shows the maximum turbulent kinetic energy as a function of the Hartmann number. The original model provides too little turbulent kinetic energy whereas the modified model generates the appropriate amount. Figure 7-79 shows that the minimum dissipation rate remains almost identical for both versions of the model. Figures 7-80 through 7-82 show the effect of the Reynolds number on the skin friction distribution. The original model under predicts the relaminarization process in all cases. The modified version is able to correctly predict the value of the Hartmann number at which the relaminarization process occurs.
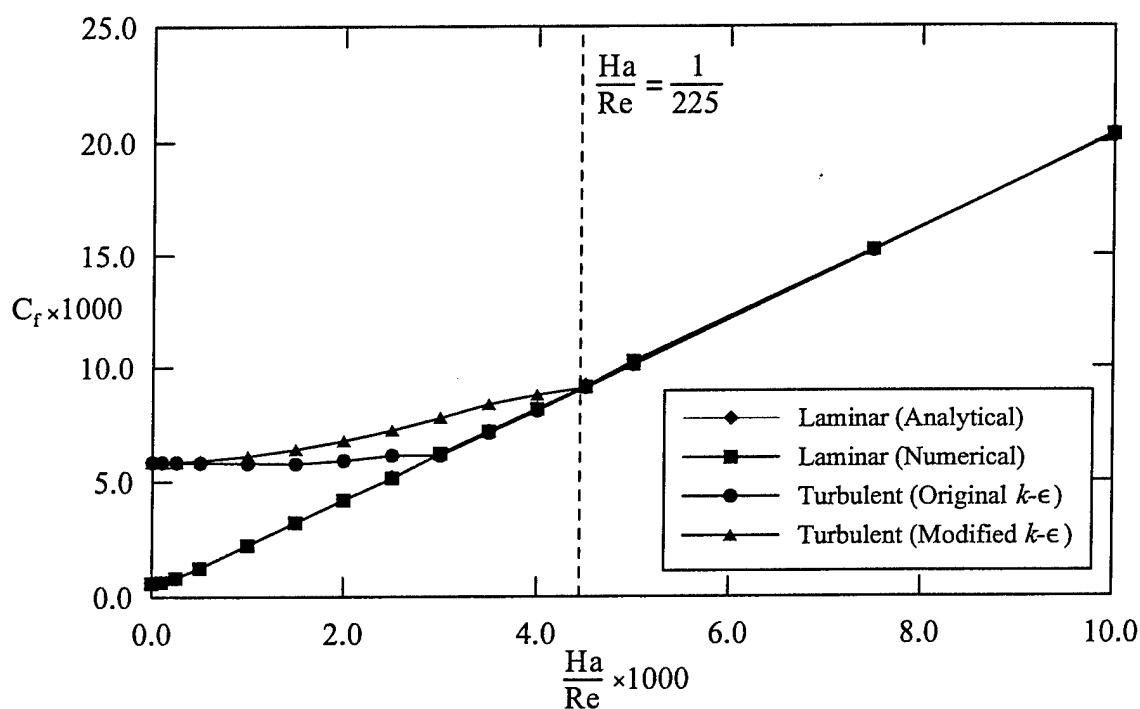

Figure 7-68. Skin Friction coefficient for the Hartmann flow at $Re = 1.0 \times 10^4$
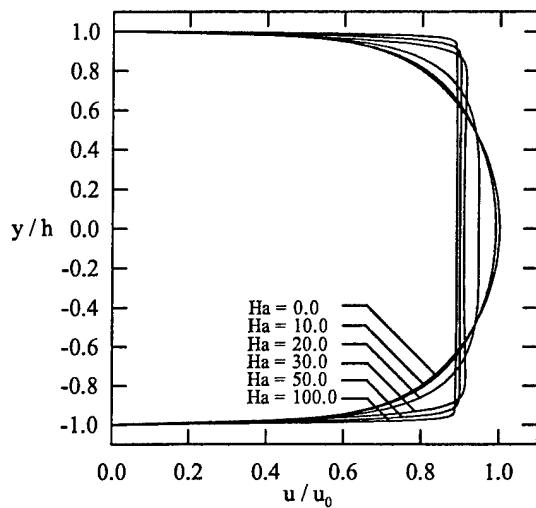
($k - \epsilon$ model).

116

Figure 7-69. Turbulent velocity profiles (original $k - \epsilon$ model).
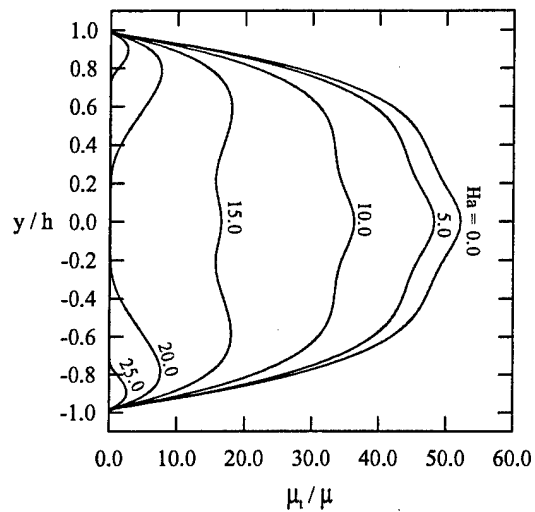

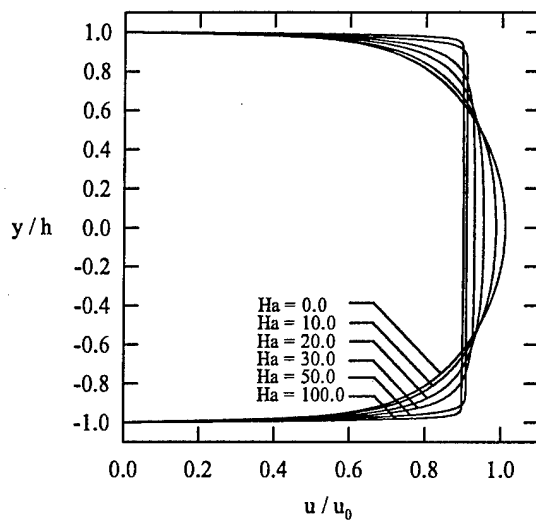Figure 7-71. Turbulent viscosity profiles (original $k - \epsilon$ model).

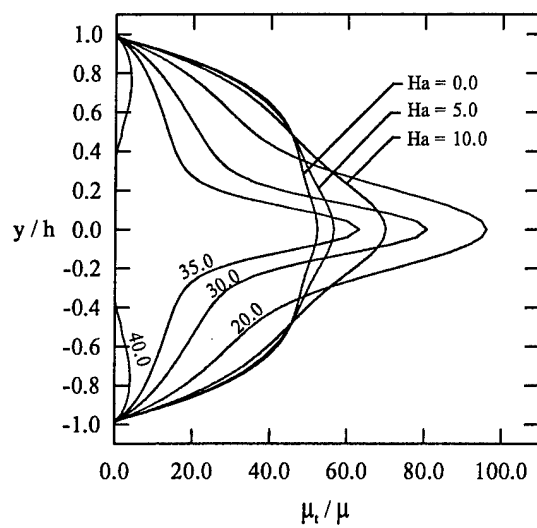Figure 7-70. Turbulent velocity profiles (modified $k - \epsilon$ model).

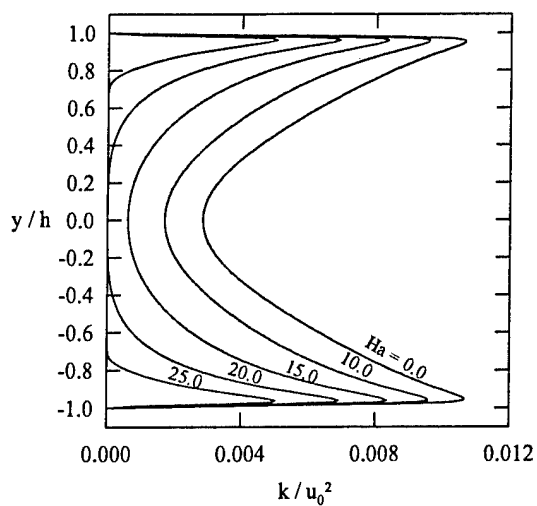Figure 7-72. Turbulent viscosity profiles (modified $k - \epsilon$ model).

117

Figure 7-73. Turbulent kinetic energy
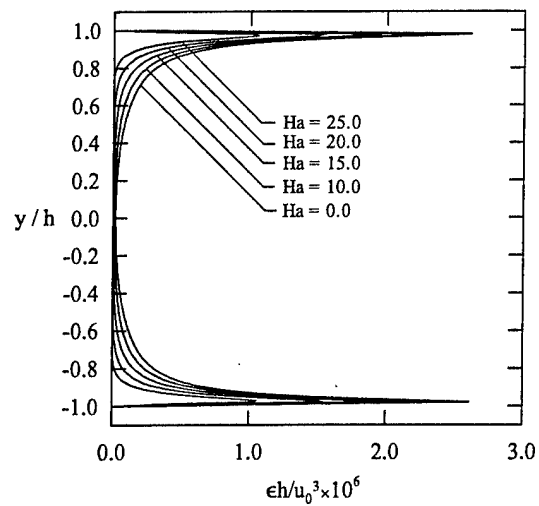profiles (original $k - \epsilon$ model).

Figure 7-75. Turbulent dissipation
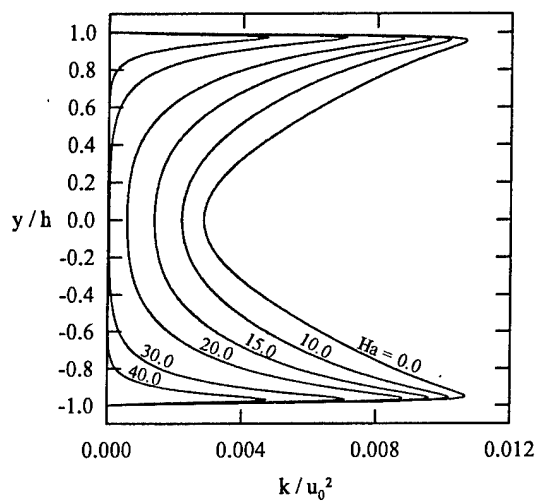profiles (original $k - \epsilon$ model).

Figure 7-74. Turbulent kinetic energy
profiles (modified $k - \epsilon$ model).
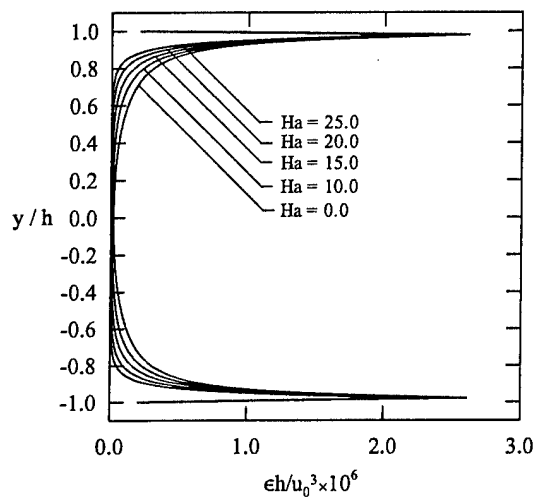

Figure 7-76. Turbulent dissipation
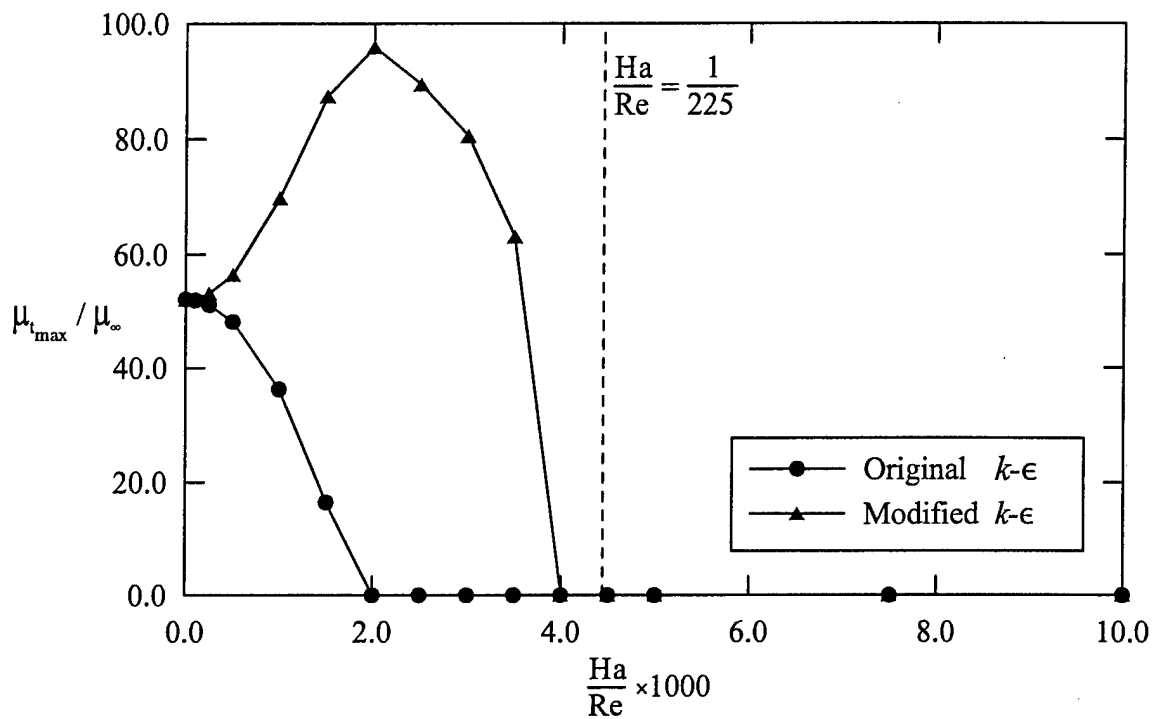profiles (modified $k - \epsilon$ model).

118

Figure 7-77. Maximum turbulent viscosity ($k - \epsilon$ model).
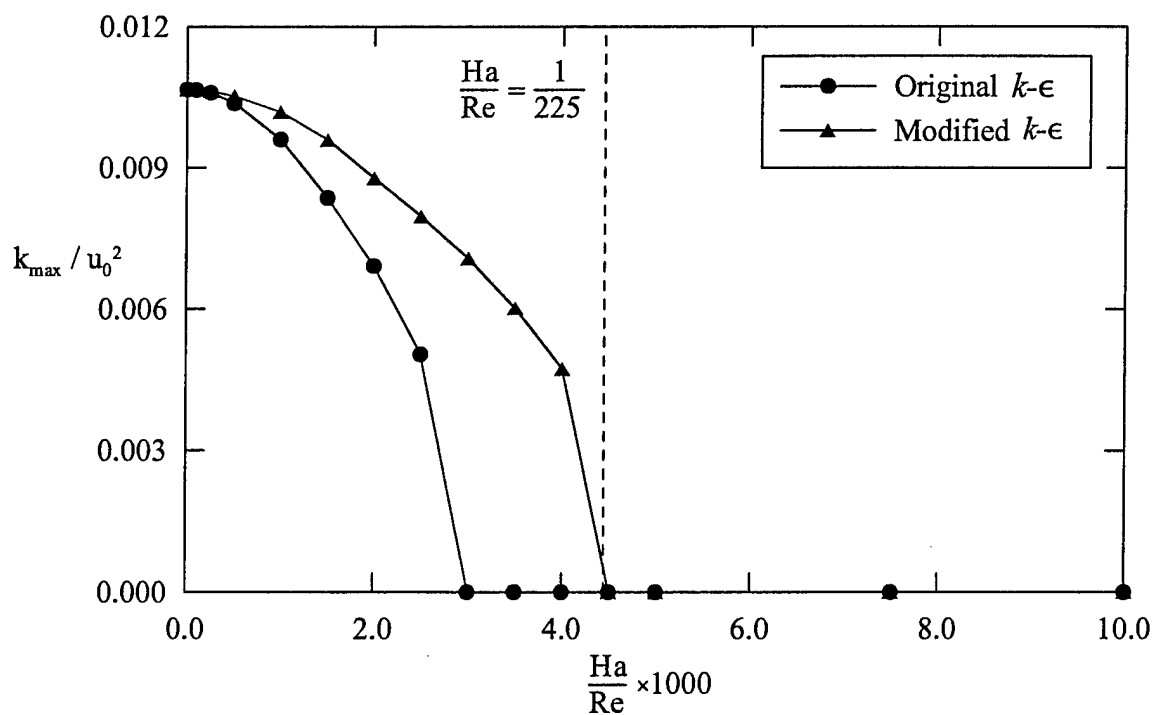
Figure 7-78. Maximum turbulent kinetic energy ($k - \epsilon$ model).

119
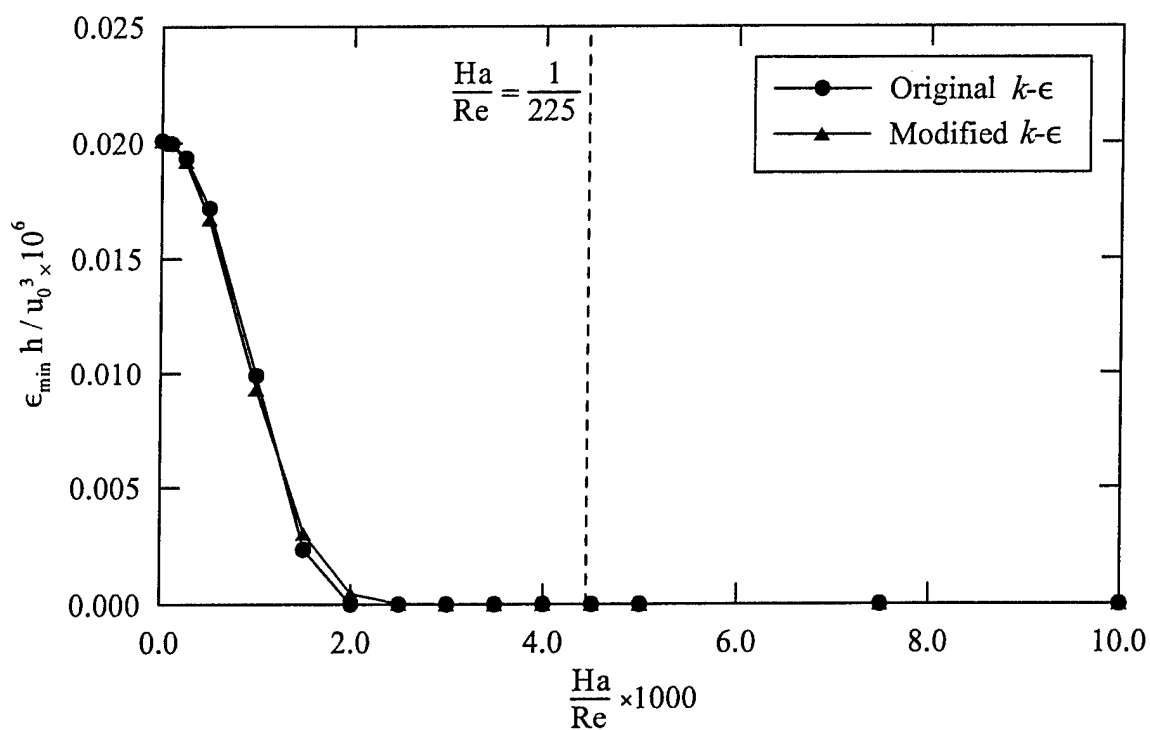
Figure 7-79. Minimum turbulent dissipation ($k-\epsilon$ model).
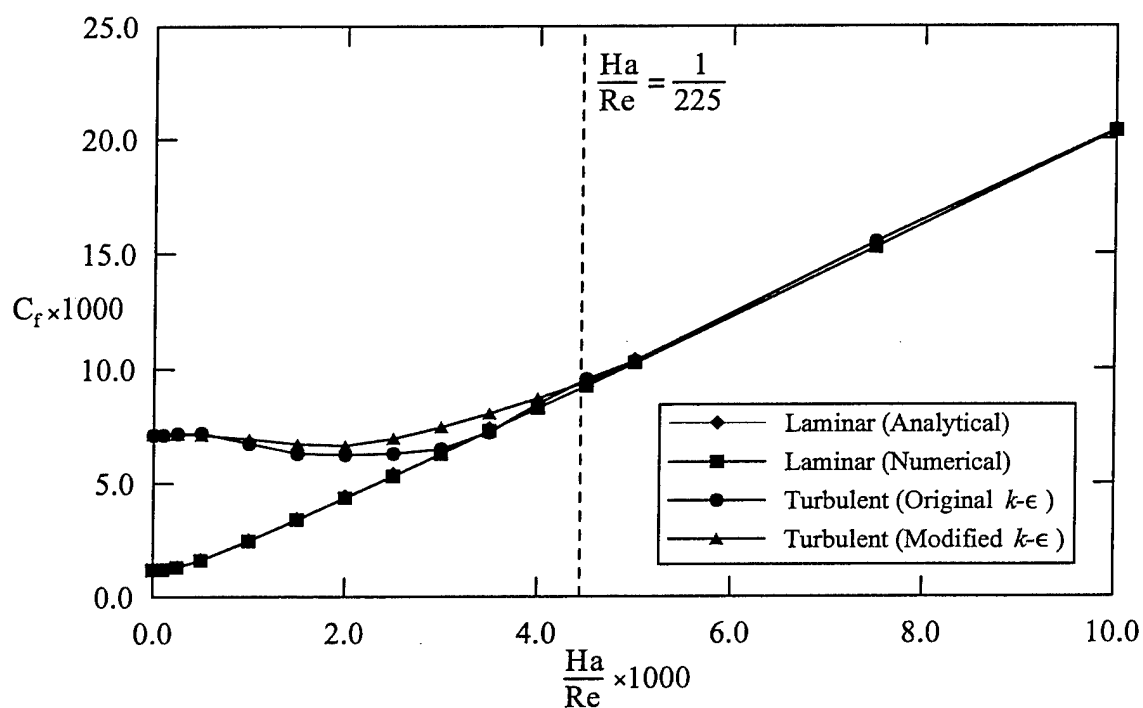
Figure 7-80. Skin friction coefficient for the Hartmann flow at $Re = 5.0 \times 10^3$

($k-\epsilon$ model).

120
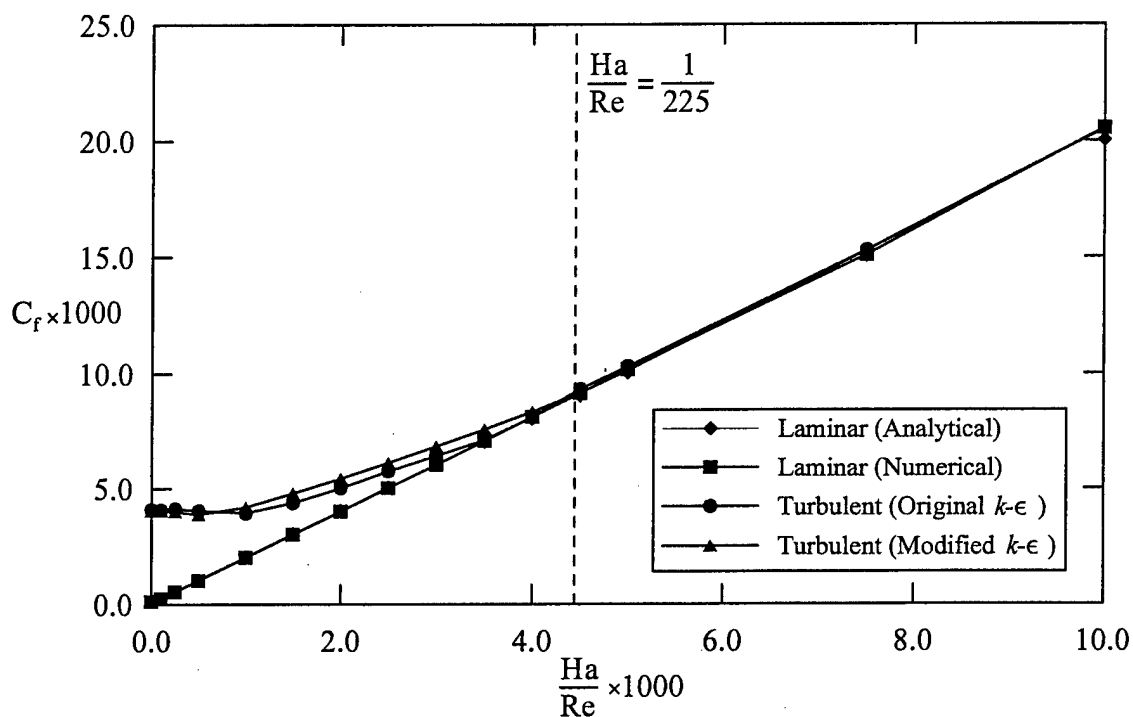
Figure 7-81. Skin friction coefficient for the Hartmann flow at $Re = 5.0 \times 10^4$

($k - \epsilon$ model).
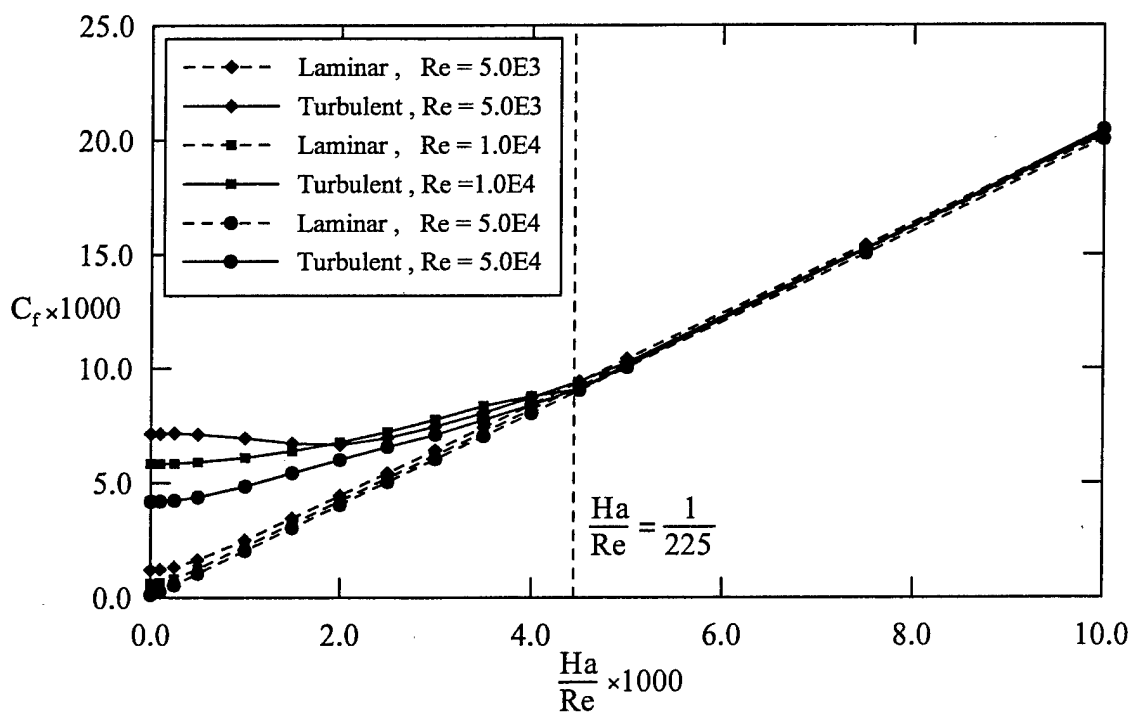
Figure 7-82. Summary of skin friction coefficient for the Hartmann flow

($k - \epsilon$ model).

7.3.5. Baseline Model

Figure 7-83 shows that the original Baseline model is not able to predict the relaminarization process at $Re = 10,000$. The closure constants in the modified version have been calibrated to result in a relaminarization process at $Ha / Re = 1 / 225$. The two constant are $C'_{KN1} = 3.0$ and $C'_{\omega N1} = -1.5$. Figures 7-84 and 7-85 show the turbulent velocity profiles for the original and modified models, respectively. The modified model provides an increase in the velocity at the centerline for moderate Hartmann number ($Ha = 10.0$). The turbulent viscosity is further reduced in the case of the modified model (Figure 7-87) compared with the original one (Figure 7-86), especially at the centerline. The Baseline model involves the computation of the turbulent kinetic energy k, and the turbulent dissipation rate ω. It is thus interesting to display their distributions between the flat pates. Figures 7-88 and 7-89 show the turbulent kinetic energy profiles for the original and modified models, respectively. In both cases, the maximum turbulent kinetic energy is obtained close to the walls, and is minimum at the center. The amount of turbulent kinetic energy is decreased as the Hartmann number is increased. The modified model yields a faster decrease of the turbulent kinetic energy compared to the original model, resulting in a faster relaminarization process. In terms of turbulent dissipation rate, a noteworthy observation can be made. In the case of the original model (Figure 7-90), the dissipation rate decreases as the magnetic field is increased. The modified version provides the opposite effect: the turbulent dissipation rate increases when the Hartmann number increases, which is more representative of the physics of the problem (Figure 7-91), since some energy has to be dissipated by viscous as well as magnetic action. Figure 7-92 illustrates how the turbulent viscosity is decreased as the Hartmann number increases. The reduction is faster in the case of the modified model. Figure 7-93 shows the maximum turbulent kinetic energy as a function of Ha / Re. The level of turbulent kinetic energy is negligible at the relaminarization point for the modified model whereas a substantial amount remains in the flow when the original model is employed. Figure 7-94 shows the minimum of the turbulent dissipation rate (since the maximum is constant at the wall, based on the applied boundary conditions). In the case of the original model, the dissipation rate is small and decreases as the Hartmann number is increased. In the case of the modified model, it is an increasing function of the Hartmann number, illustrating that the presence of the magnetic field results in a greater dissipation of the turbulent kinetic energy. Figures 7-95 through 7-97 show that the relaminarization process is not affected by the Reynolds number.

Figure 7-83. Skin friction coefficient for the Hartmann flow at $Re = 1.0 \times 10^4$
(Baseline model).
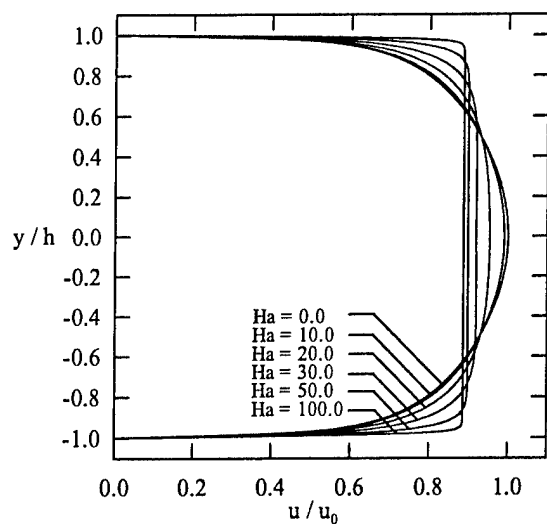
Figure 7-84. Turbulent velocity profiles
(original Baseline model).

Figure 7-86. Turbulent viscosity profiles
(original Baseline model).

Figure 7-85. Turbulent velocity profiles
(modified Baseline model).

Figure 7-87. Turbulent viscosity profiles
(modified Baseline model).

Figure 7-88. Turbulent kinetic energy
profiles (original Baseline model).

Figure 7-90. Turbulent dissipation rate
profiles (original Baseline model).

Figure 7-89. Turbulent kinetic energy
profiles (modified Baseline model).
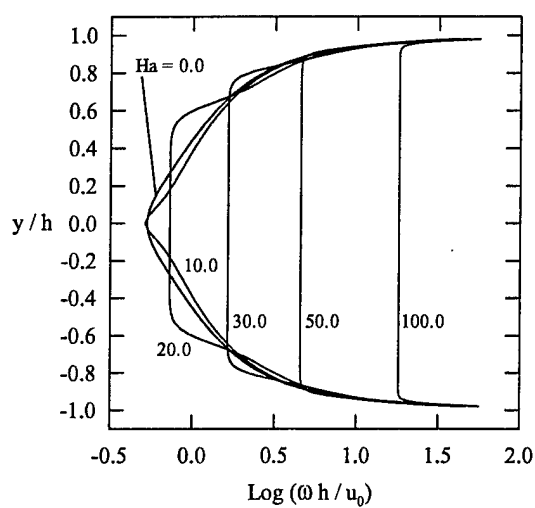
Figure 7-91. Turbulent dissipation rate
profiles (modified Baseline model).

125
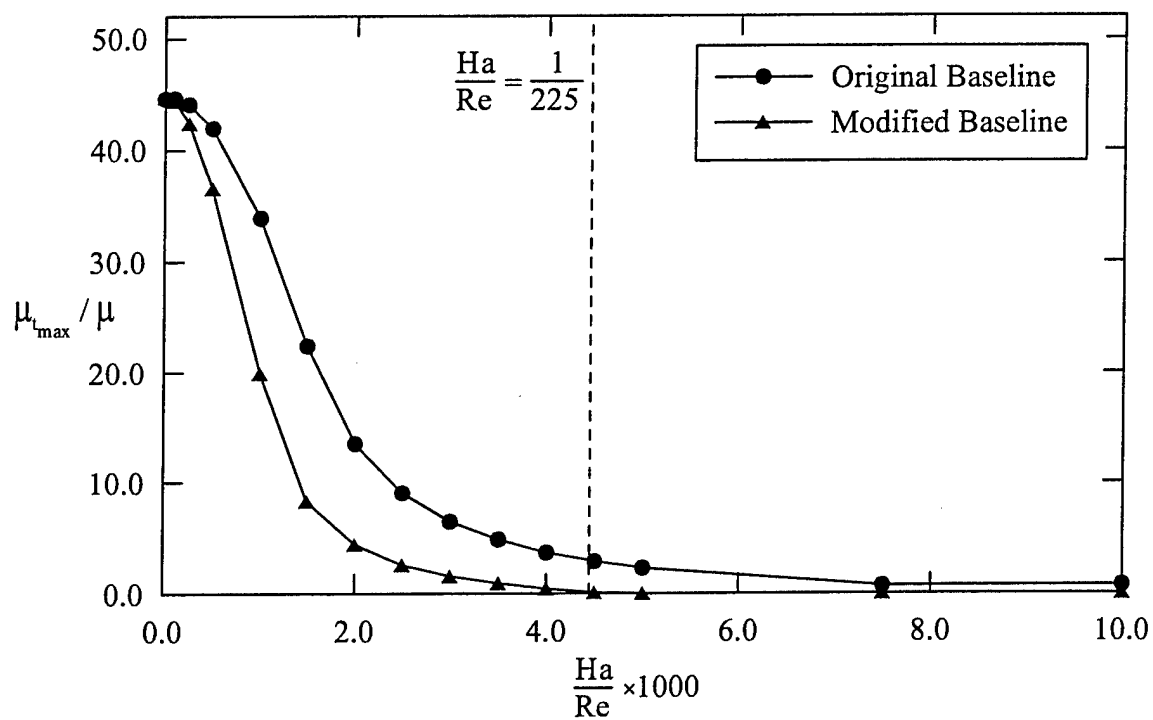
Figure 7-92. Maximum turbulent viscosity (Baseline model).
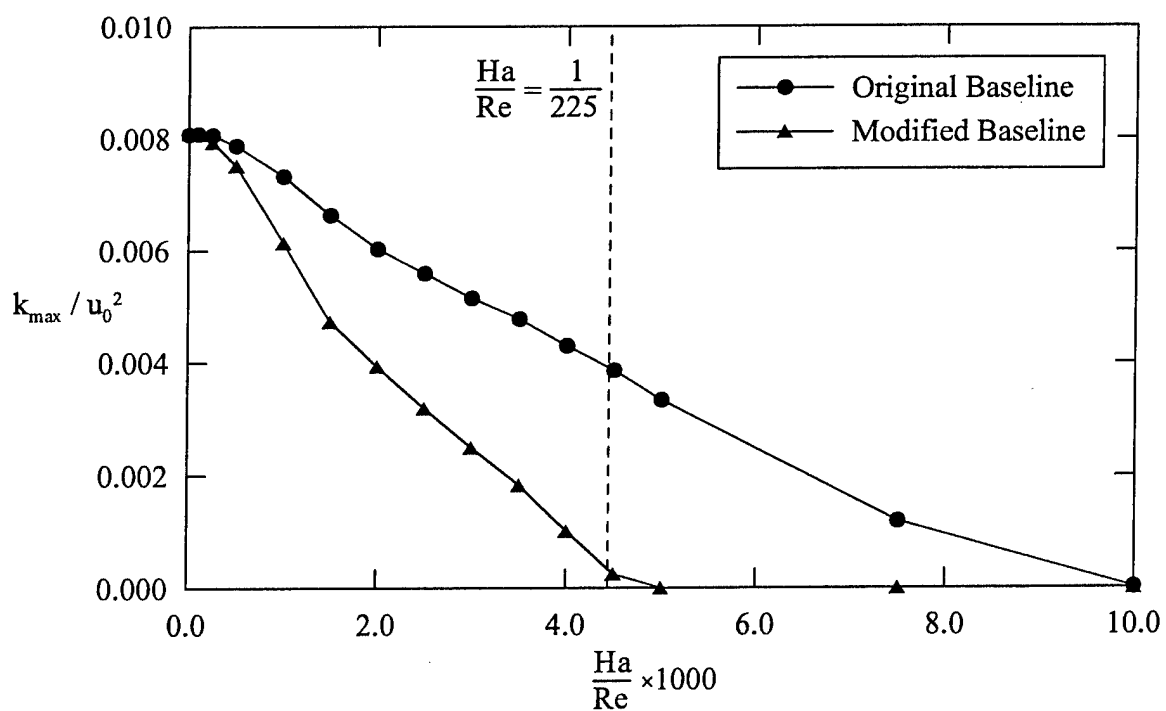
Figure 7-93. Maximum turbulent kinetic energy (Baseline model).

126

Figure 7-94. Minimum turbulent dissipation rate (Baseline model).
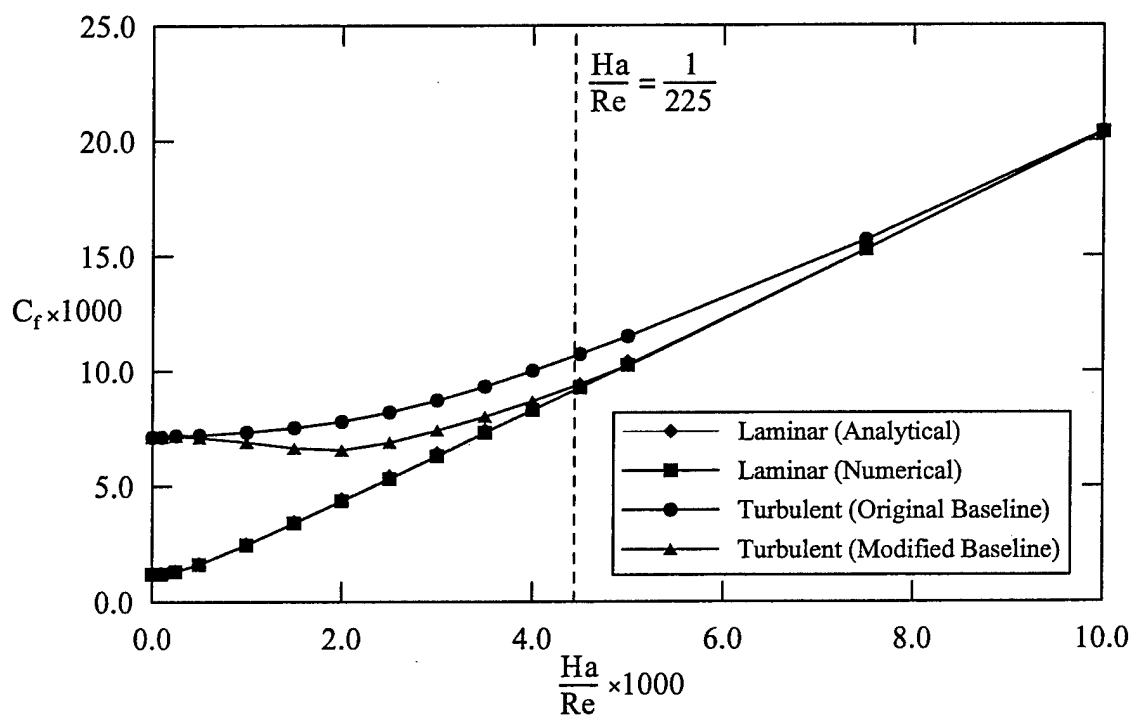
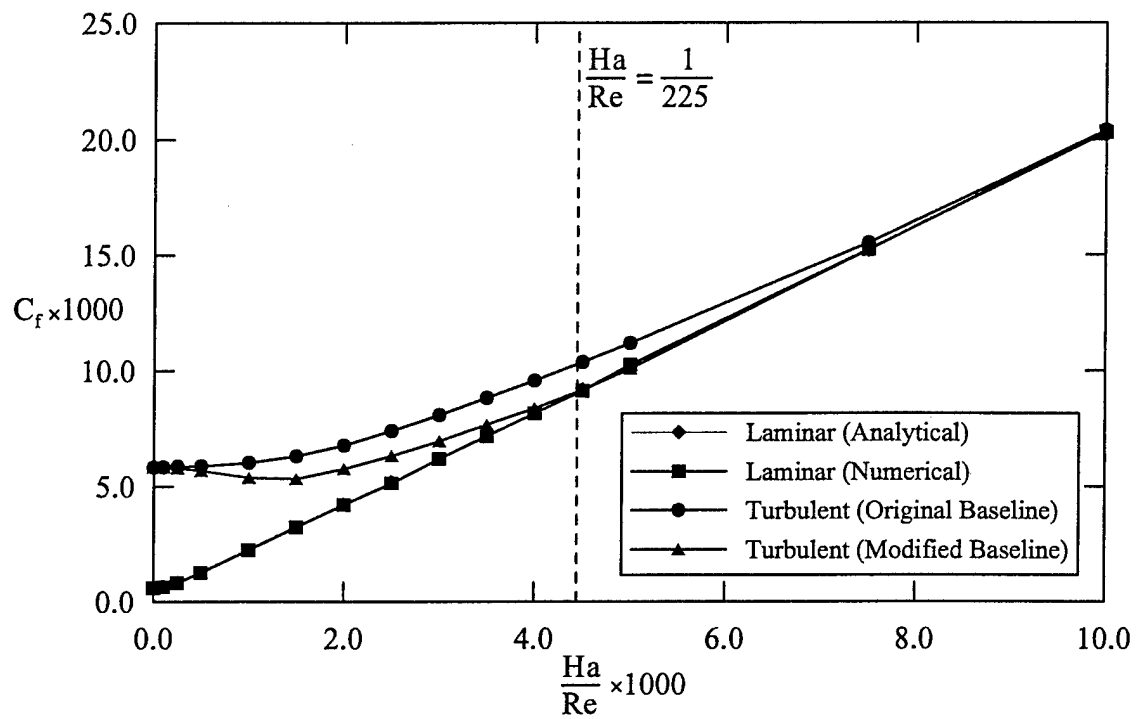Figure 7-95. Skin friction coefficient for the Hartmann flow at $Re = 5.0 \times 10^3$

(Baseline model).

Figure 7-96. Skin friction coefficient for the Hartmann flow at $Re = 5.0 \times 10^4$

(Baseline model).

Figure 7-97. Summary of skin friction coefficient for the Hartmann flow

(Baseline model).

128

7.6.3. Shear Stress Transport Model

The SST model provides very similar results as the Baseline model. The main difference between these two models lies in the determination of the two closure constants associated with the magnetic terms. Here the values of the constants are $C'_{KN1} = 1.0$ and $C'_{\omega N1} = -0.5$ compared to $C'_{KN1} = 3.0$ and $C'_{\omega N1} = -1.5$ for the Baseline model. Figure 7-98 shows that the modified version performs better than the original one at $Re = 10,000$. Figures 7-99 and 7-100 show that the turbulent velocity profiles are similar for both models. Figures 7-101 and 7-102 illustrate the turbulent viscosity profiles for the original and modified models, respectively. The original model does not exhibit a relative minimum at the centerline, whereas the modified version does. The modified model is able to sufficiently reduce the turbulent viscosity as the Hartmann number is increased to provide the correct relaminarization process. Figures 7-103 and 7-104 show the turbulent kinetic energy profiles for the original and modified models, respectively. Similar to the Baseline model, the modified SST model results in a faster decrease of the turbulent kinetic energy as the Hartmann number is increased. The original model shows a decrease in the dissipation rate as the magnetic field increases (Figure 7-105), whereas the modified model shows an increase (Figure 7-106), representing more accurately the physics of the problem. Figures 7-107 through 7-109 show the maximum turbulent viscosity, maximum turbulent kinetic energy and minimum dissipation rate as functions of Ha / Re. The effect of the modified model is to further decrease the turbulent viscosity and turbulent kinetic energy compared to the original model. The dissipation rate tends to decrease with the original model whereas it significantly increases with the modified version. Figures 7-110 through 7-112 show the effect of the Reynolds number on the skin friction, which is similar to what was obtained with all turbulence models.
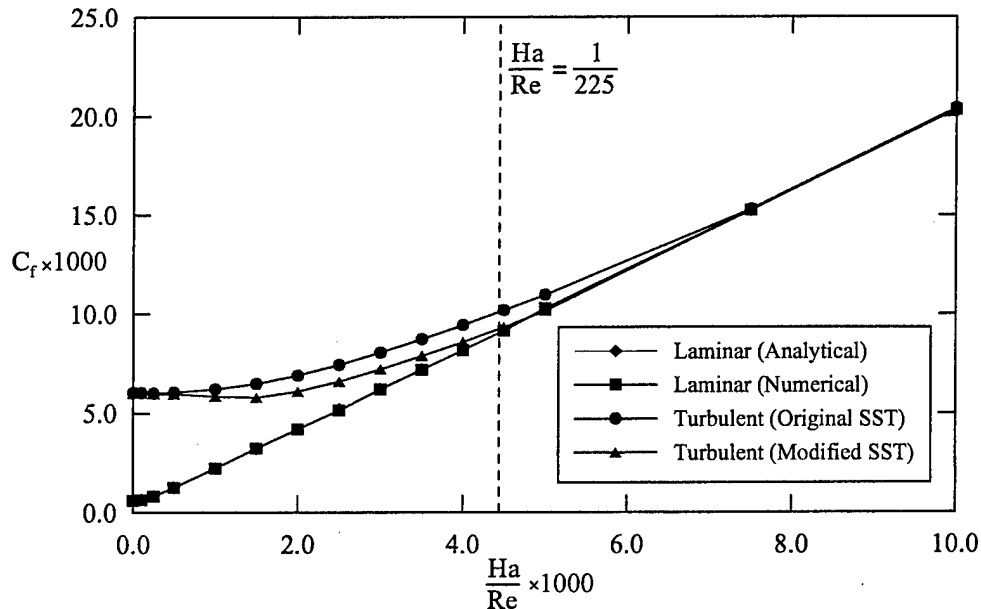
Figure 7-98. Skin friction coefficient for the Hartmann flow at $Re = 1.0 \times 10^4$

(SST model).
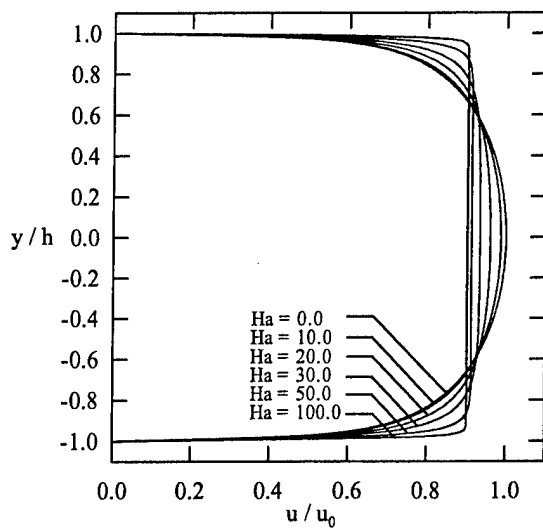
Figure 7-99. Turbulent velocity profiles (original SST model).
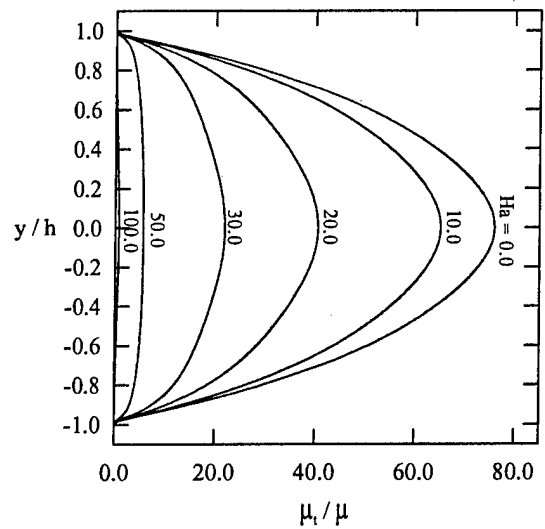
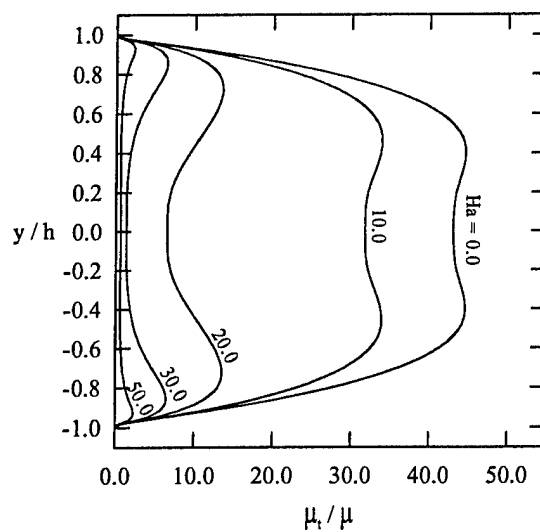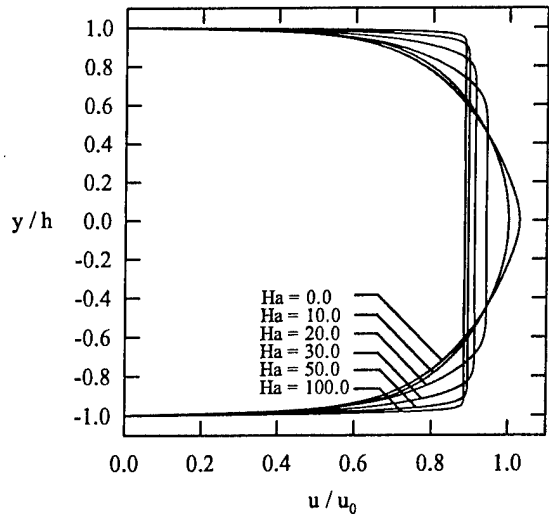Figure 7-101. Turbulent viscosity profiles (original SST model).
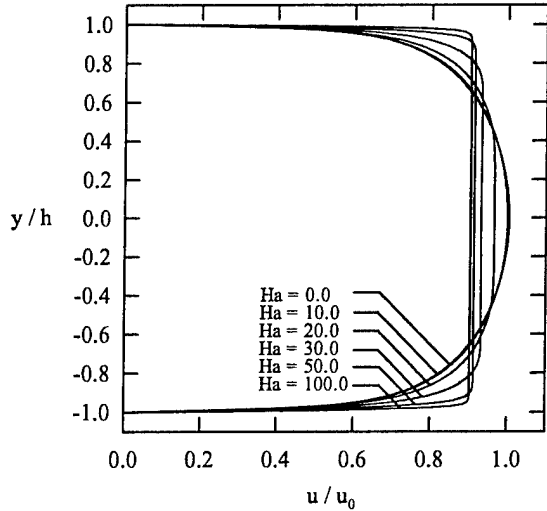
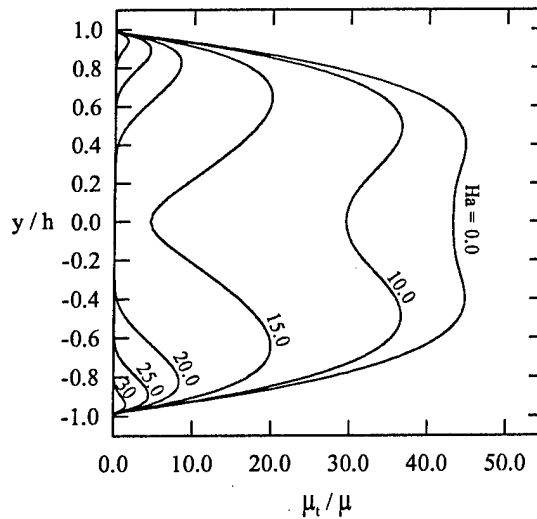Figure 7-100. Turbulent velocity profiles (modified SST model).
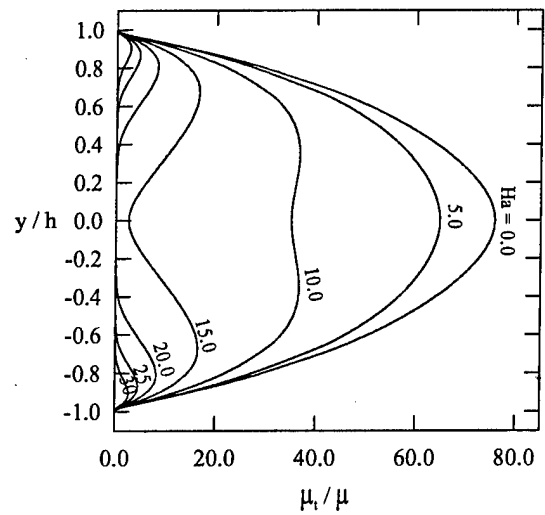
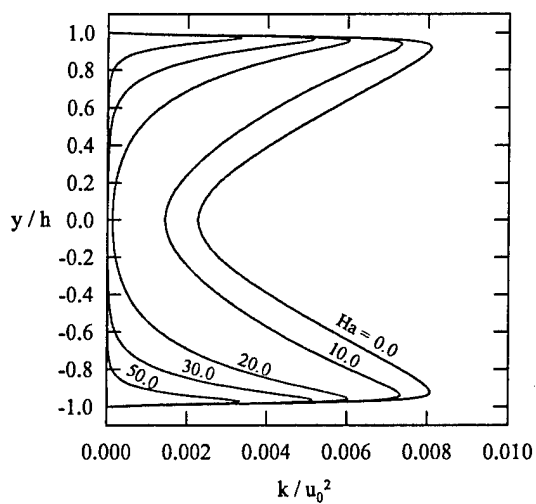Figure 7-102. Turbulent viscosity profiles (modified SST model).

130
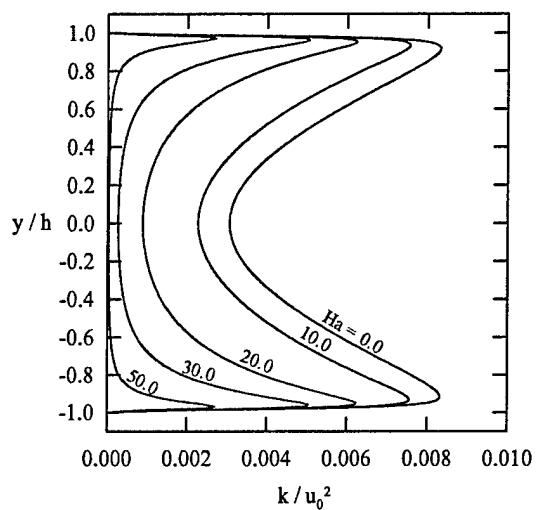
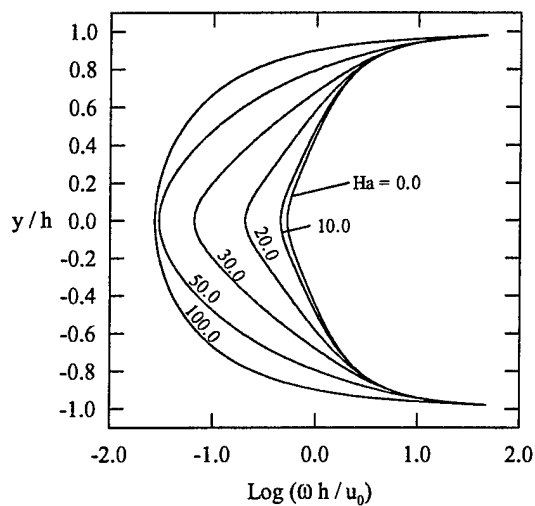Figure 7-103. Turbulent kinetic energy
profiles (original SST model).
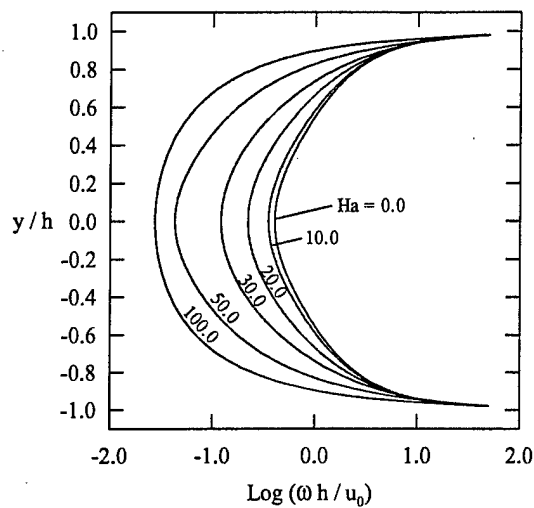
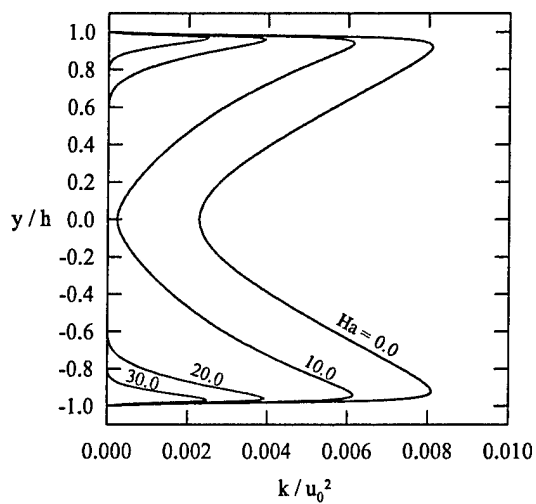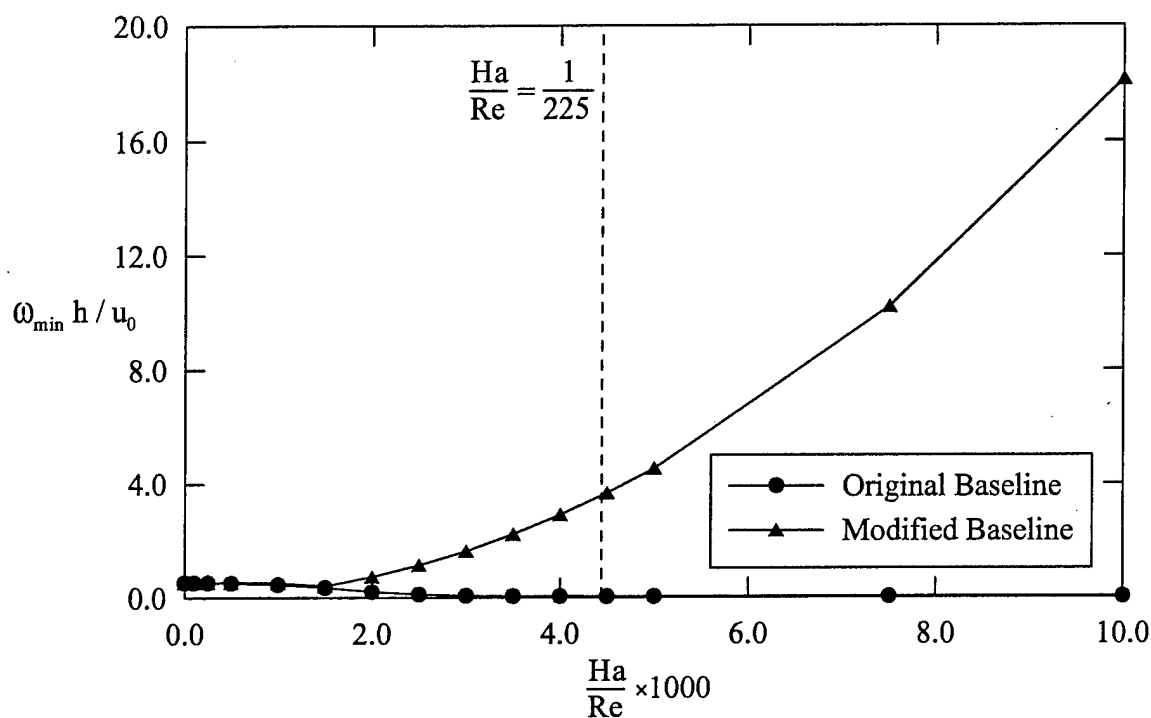Figure 7-105. Turbulent dissipation rate
profiles (original SST model).
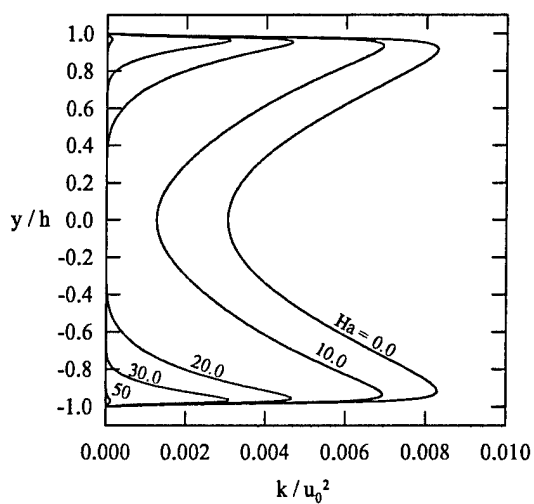
Figure 7-104. Turbulent kinetic energy
profiles (modified SST model).
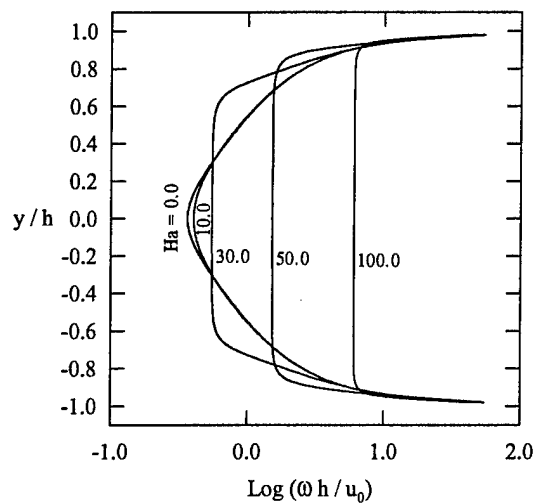
Figure 7-106. Turbulent dissipation rate
profiles (modified SST model).

131
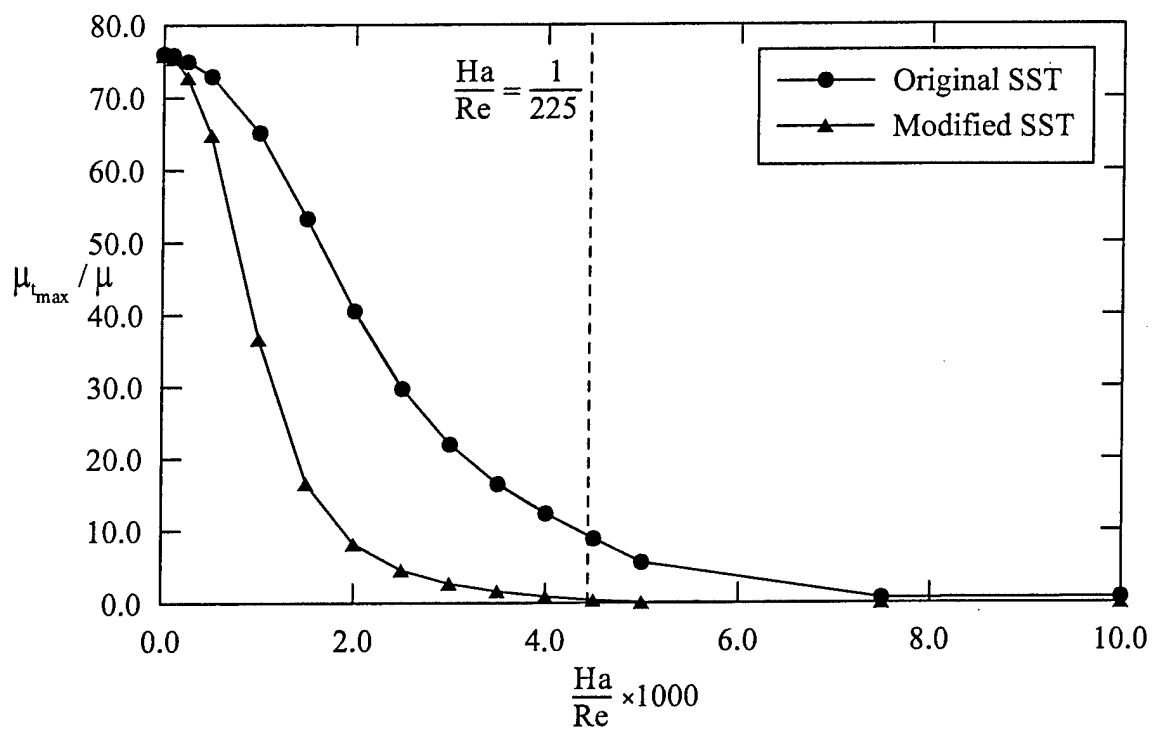
Figure 7-107. Maximum turbulent viscosity (SST model).
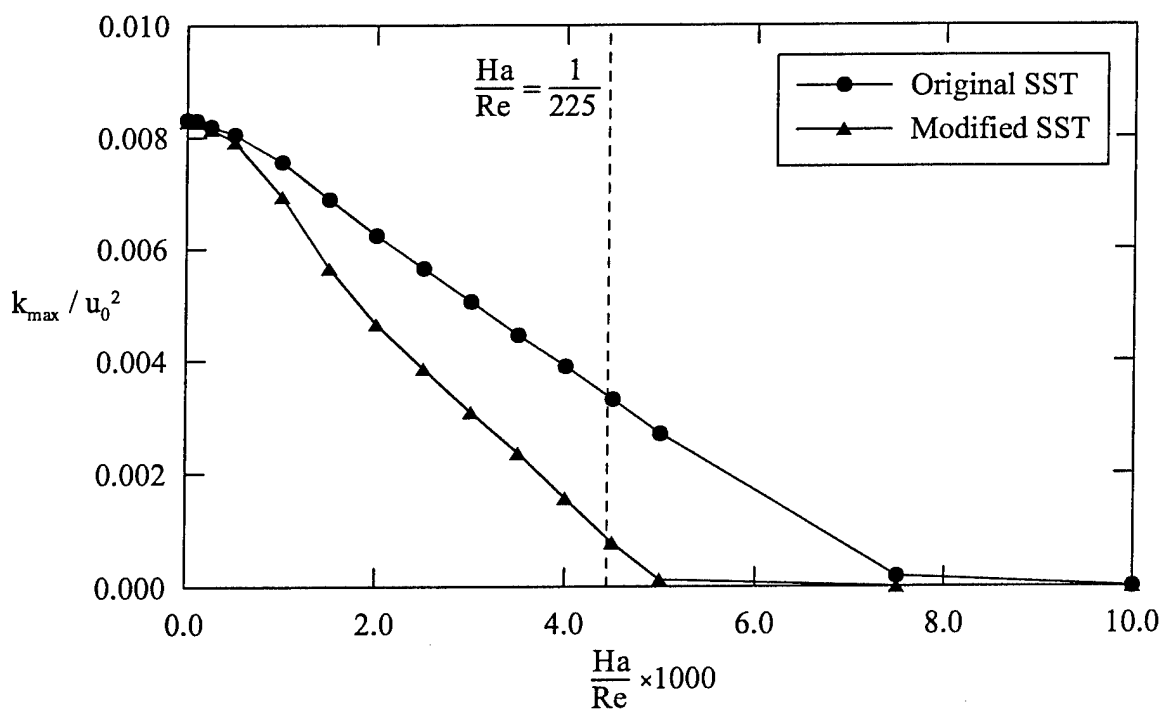
Figure 7-108. Maximum turbulent kinetic energy (SST model).

132
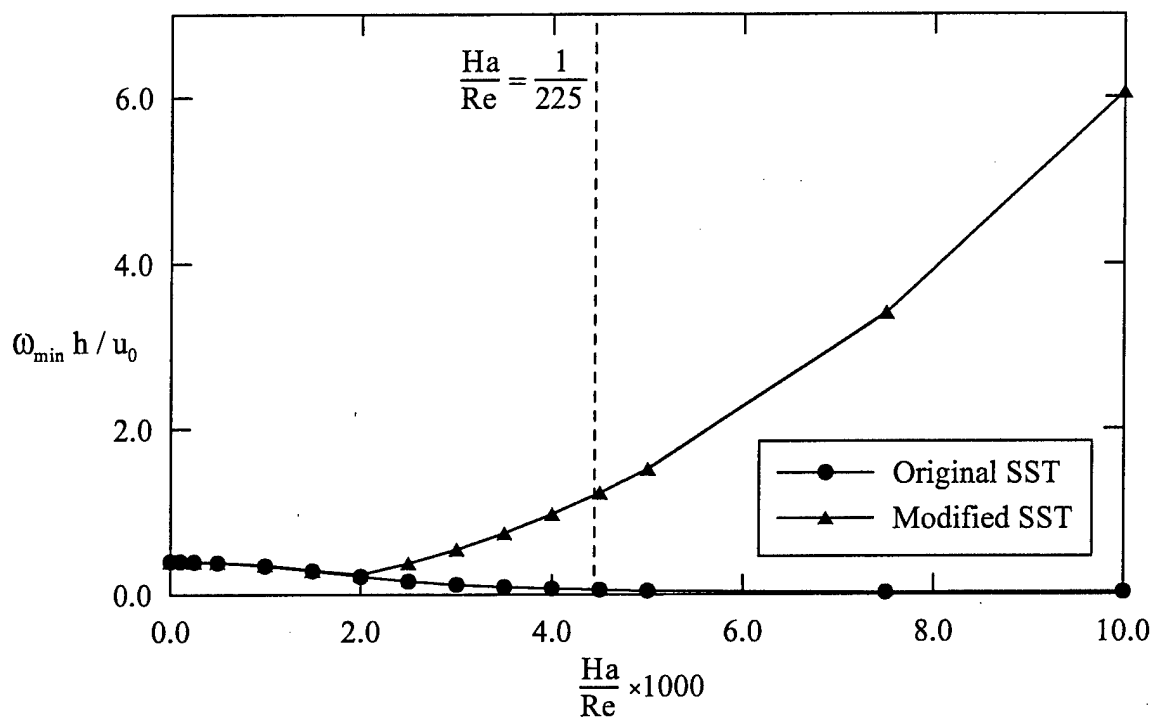
Figure 7-109. Minimum turbulent dissipation rate (SST model).
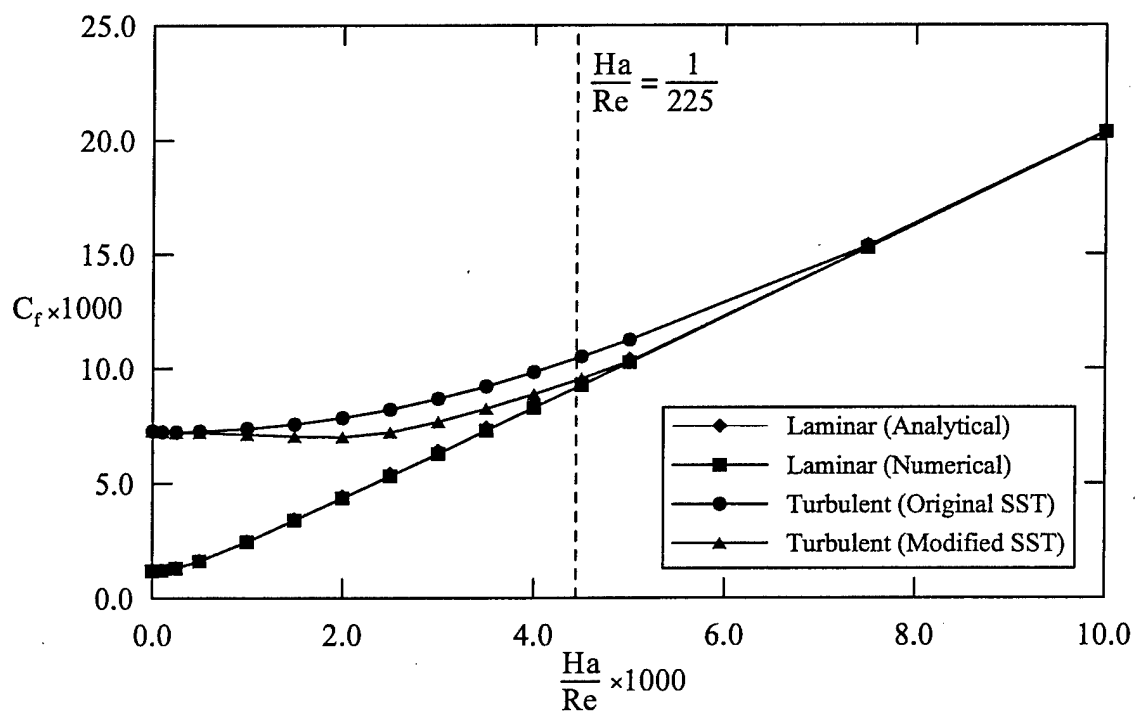
Figure 7-110. Skin friction coefficient for the Hartmann flow at $Re = 5.0 \times 10^3$
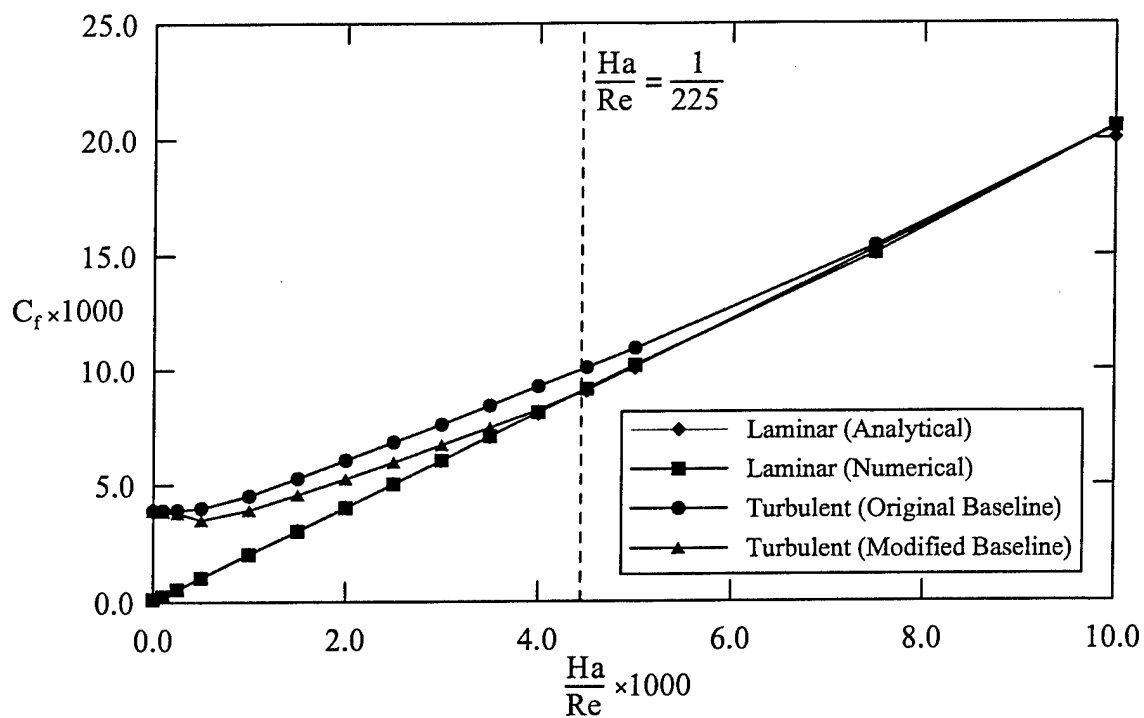
(SST model).

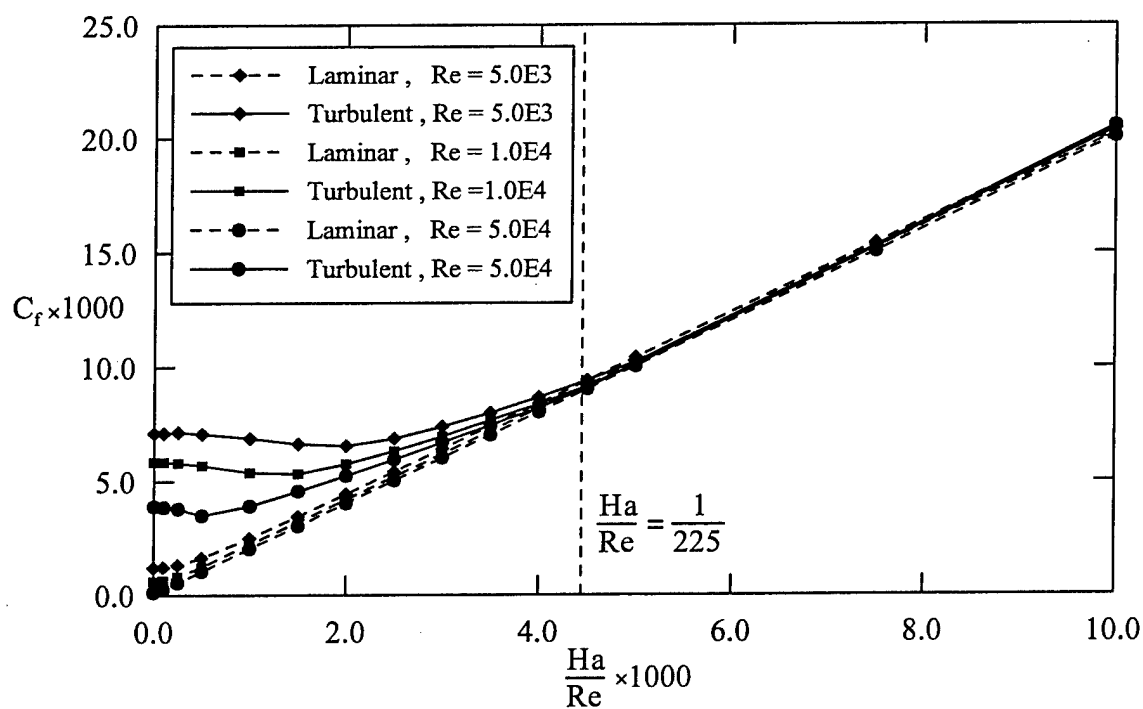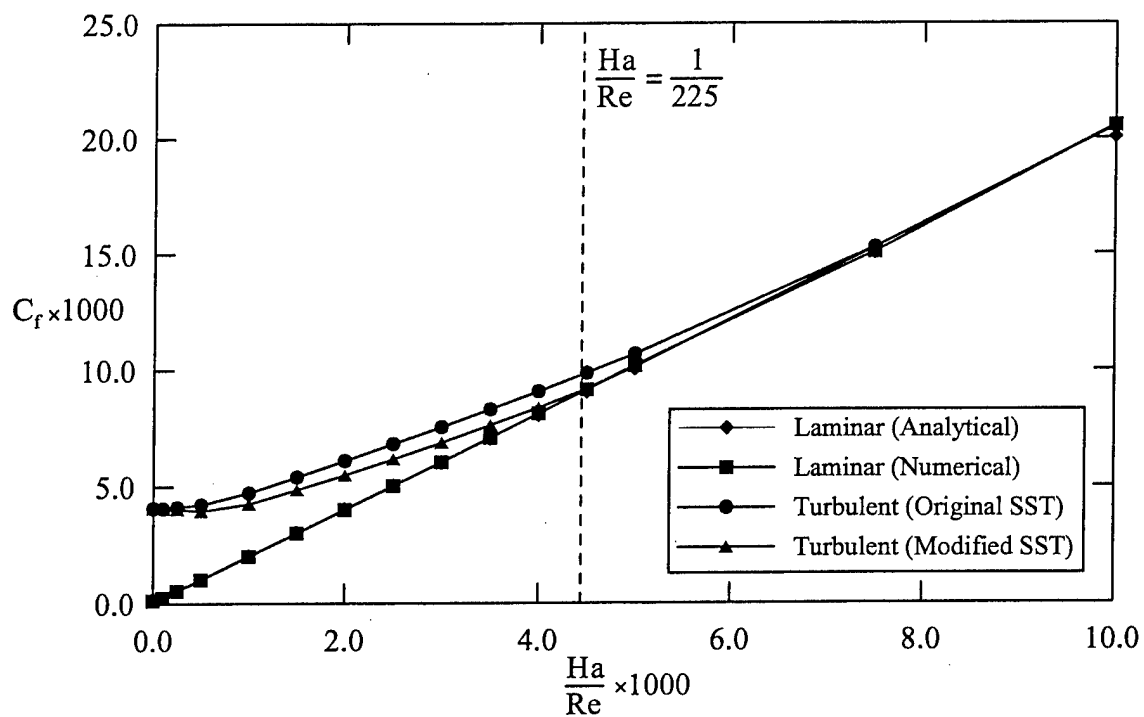Figure 7-111. Skin friction coefficient for the Hartmann flow at $Re = 5.0 \times 10^4$

(SST model).
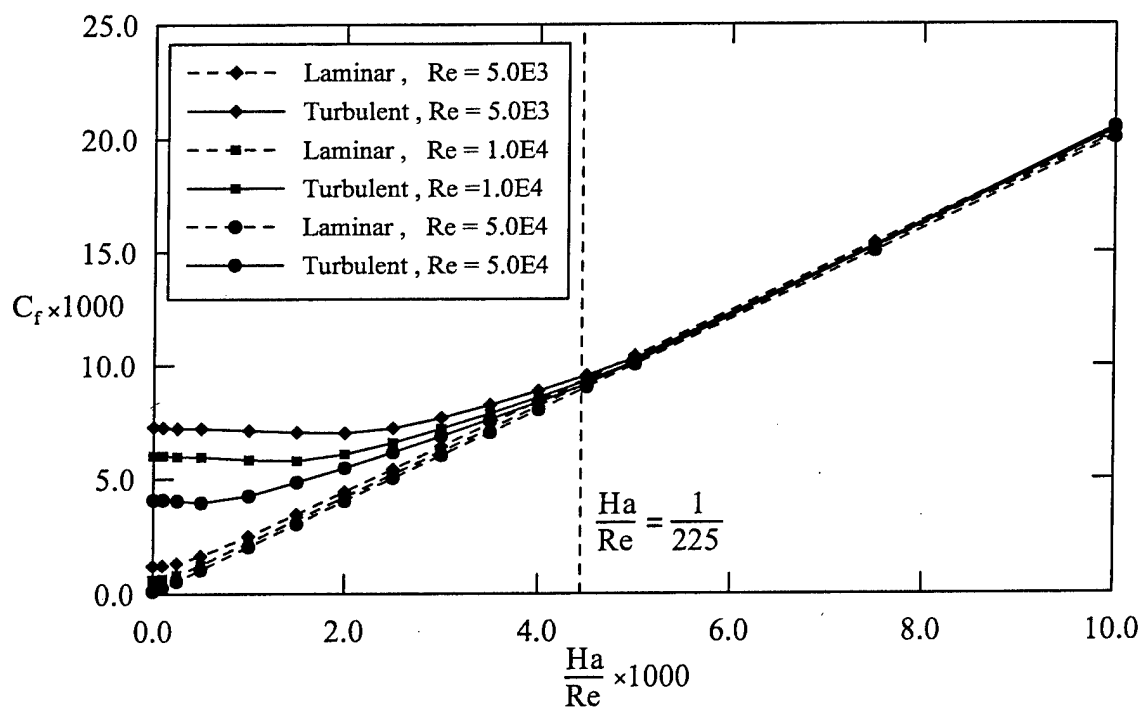
Figure 7-112. Summary of skin friction coefficient for the Hartmann flow (SST model).

134

7.3.7. Comparison of All Turbulence Models

All turbulence models can be compared to the experimental data when the Reynolds number is $Re = 50,000$. Figure 7-113 shows the skin friction coefficient for the original turbulence models. Most models over predict the skin friction and therefore, are not able to accurately predict the relaminarization process. The $k-\epsilon$ under predicts the skin friction, leading to an early relaminarization process. The original Spalart-Allmaras model is the only one that can accurately predict that the relaminarization process occurs at $Ha/Re = 1/225$. On the other hand, all modified models provide a more accurate results and the relaminarization process is well predicted (Figure 7-114). It is concluded that the calibration of the modified versions of the turbulence models results in a better representation of the turbulent MHD Hartman flow.
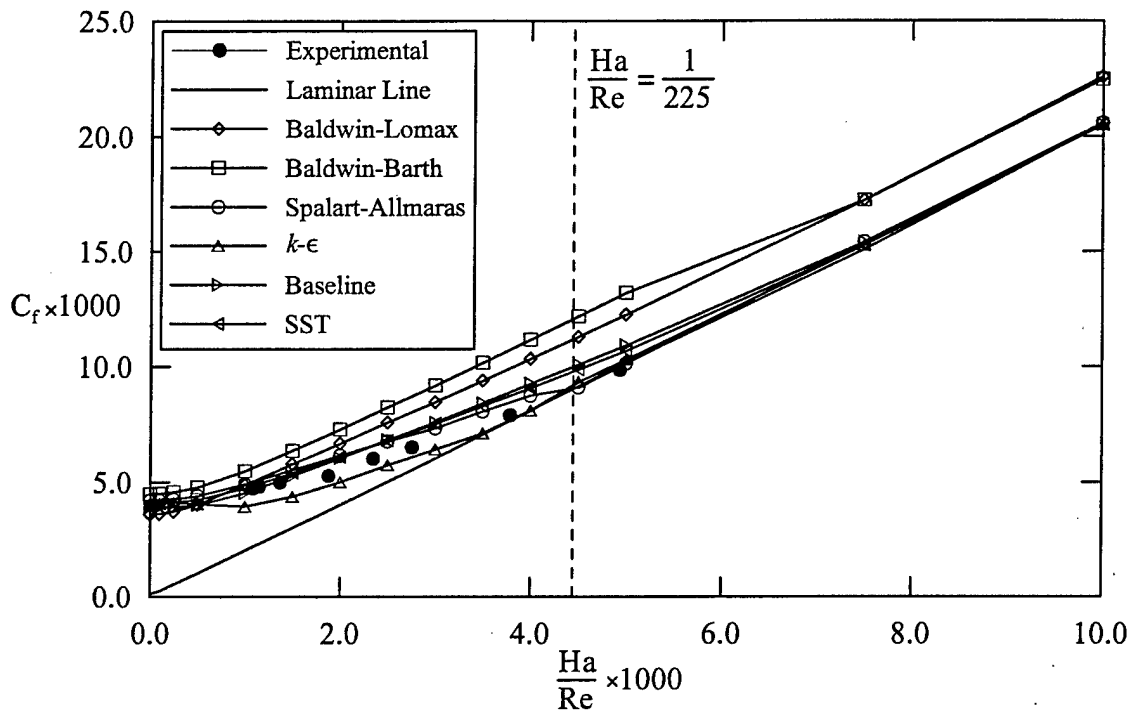
Figure 7-113. Comparison of all original turbulence models at $Re = 5.0 \times 10^4$.
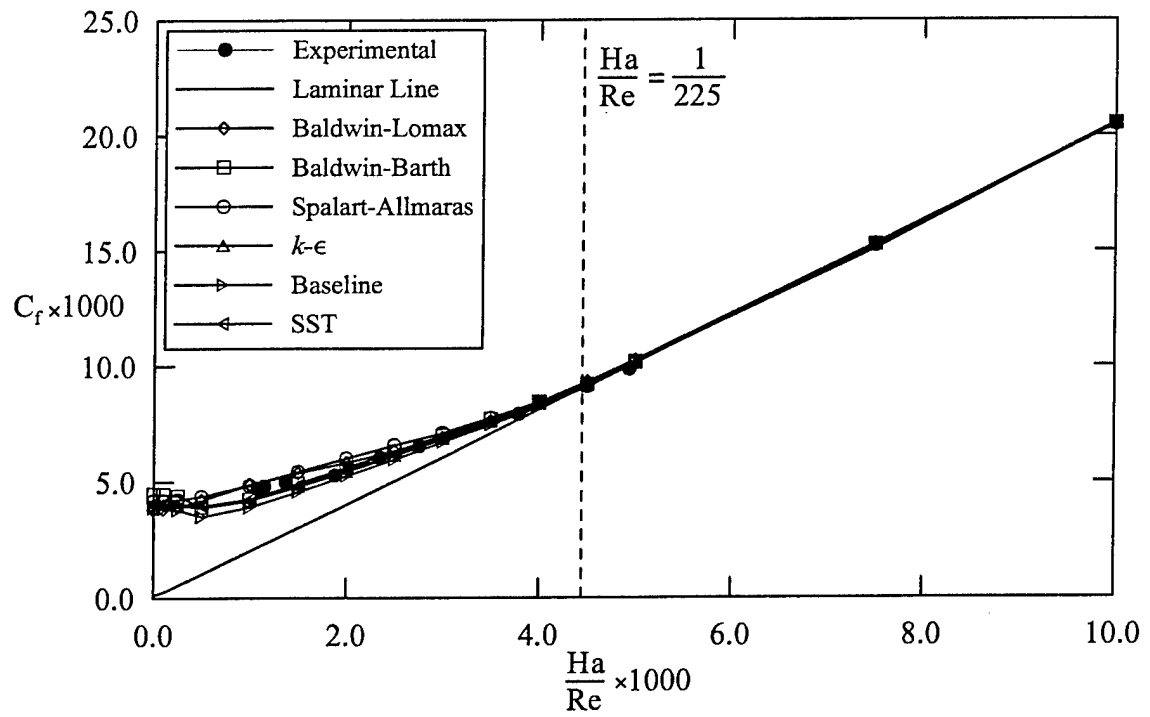
Figure 7-114. Comparison of all modified turbulence models at $Re = 5.0 \times 10^4$.

7.4. Supersonic Flow over a Flat Plate

7.4.1. Low Magnetic Reynolds Number Formulation

The objective of this section is to investigate the effect of the magnetic field on the skin friction for a supersonic turbulent flow over a flat plate. The freestream conditions are summarized in Table 7-5. The length of the flat plate is $0.08\,m$ and the transition is triggered at $x = 0.04\,m$. The magnetic Reynolds number based on the length of the flat plate is $Re_m = 0.058$, which can be considered negligible compared to one. Therefore, the MHD equations will be solved by the low magnetic Reynolds number formulation. A schematic of a typical flow is illustrated in Figure 7-115.

Property	Symbol	Value
Mach number	M_∞	2.0
Pressure	p_∞	1.0 atm
Temperature	T_∞	$300.0\,K$
Reynolds number	Re_∞	3.75×10^6
Electrical conductivity	$\sigma_{e\infty}$	$800\,mho\,/\,m$

Table 7-5. Freestream conditions over the flat plate.

The grid system consists of 100 grid points in the x – direction and 50 in the y – direction. Grid point clustering has been implemented near the leading edge to capture the weak leading edge shock-wave and near the solid surface to resolve the laminar and turbulent boundary layers. The grid system is shown in Figure 7-116. The plate is considered to be an adiabatic wall.
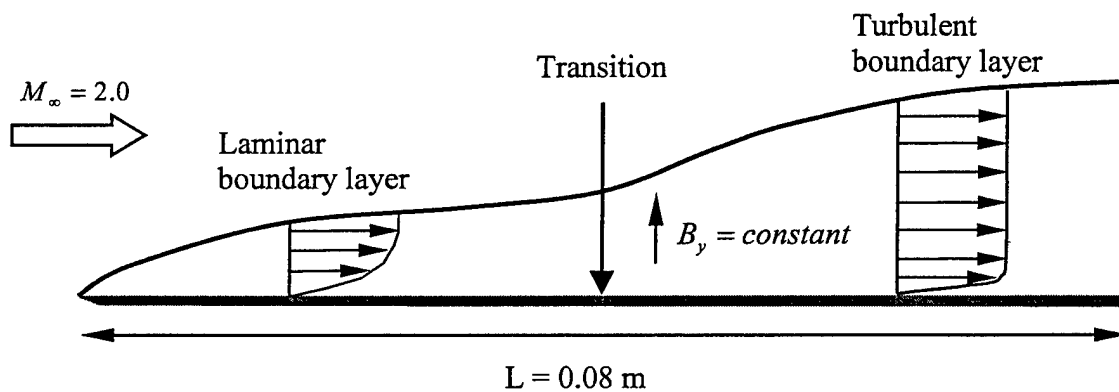
Figure 7-115. Schematic of the flow over a flat plate.
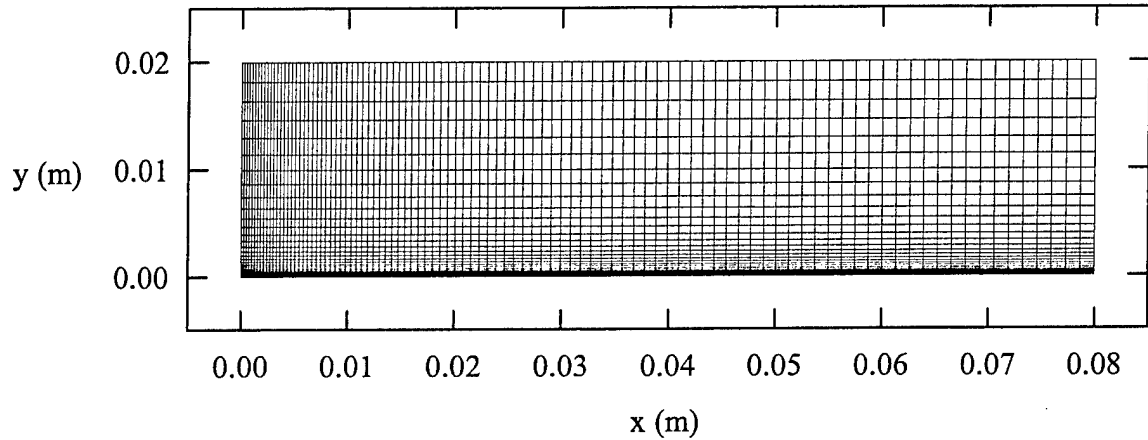
Figure 7-116. Grid system (100× 50 grid points).

The magnetic field is applied in the y – direction, ranging from zero to $1.4\,T$. The strength of the magnetic field can be represented either by the magnitude of the applied magnetic field B_y, or by the parameter m. The relation between B_y and m is provided in Equation (7.17).

$$m = \frac{\sigma_{e\infty} B_y^2}{\rho_\infty U_\infty}$$ (7.17)

First, all the turbulence models are compared in the non-magnetic case. Figure 7-117 illustrates the skin friction coefficient along the flat plate. Since the transition from laminar to turbulent flow is triggered at $x = 0.04\,m$, the laminar skin friction, from the leading edge to the transition point does not depend on the turbulence model. In the turbulent region, all turbulence models provide a skin friction coefficient that falls between the analytical solution or the pseudo empirical method of Spalding and Chi [111]. However, each model behaves slightly differently along the transition region.
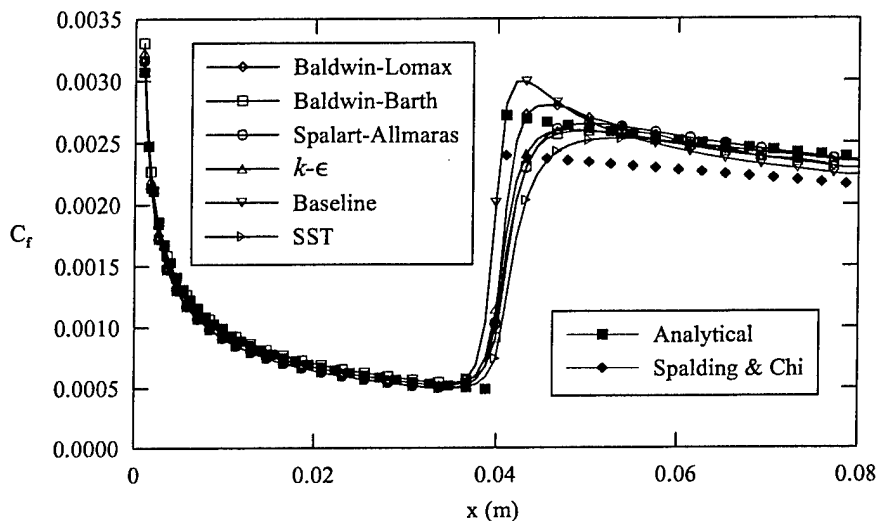
Figure 7-117. Comparison of all turbulence models in the non-magnetic case.

138

Next, the magnetic field is turned on in the y – direction. Figure 7-118 shows the skin friction coefficient obtained by the original Baldwin-Lomax model for different values of the magnetic field. The skin friction is decreased in the laminar region as the magnetic field is increased. The same effect can be observed in the turbulent region. However, no relaminarization process is achieved, since the skin friction does not reach a sufficiently low value. The modified Baldwin-Lomax model provides similar skin friction distributions (Figure 7-119), the turbulent skin frictions being slightly lower than those obtained by the original model.
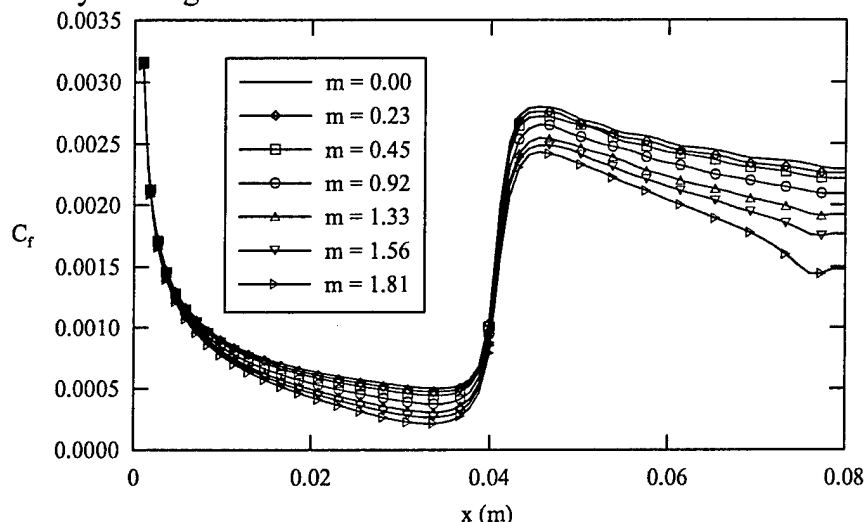
Figure 7-118. Skin friction coefficients (original Baldwin-Lomax model).
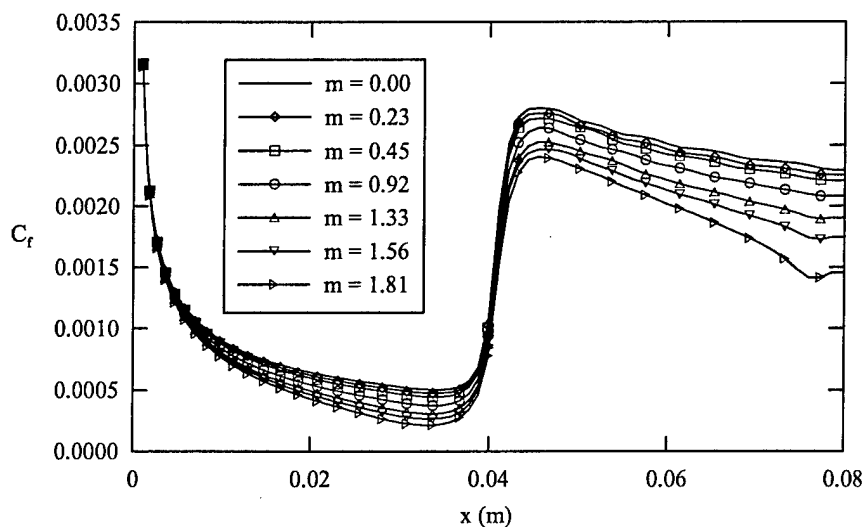
Figure 7-119. Skin friction coefficients (modified Baldwin-Lomax model).

In order to understand why the full relaminarization process does not occur, the velocity profiles are examined. First, the laminar velocity profiles are plotted at $x = 0.06\,m$ (Figure 7-120). These profiles were obtained by considering a fully laminar flow along the flat plate. The effect of the magnetic field is to generate a Lorentz force acting in the opposite direction of the incoming flow. Therefore, the flow is decelerated as the magnetic field is increased. For a sufficiently large value of the magnetic field, it

139

leads to a separation of the flow, at $m = 1.33$. The freestream velocity is also reduced as the magnetic field increases, because the magnetic field remains constant within the entire domain. Once the flow is separated, it is not possible to obtained a converged solution, because a large subsonic region develops, which reaches the boundaries of the computational domain. The boundary conditions, based on a supersonic inflow and outflow are not adapted to such a flow.
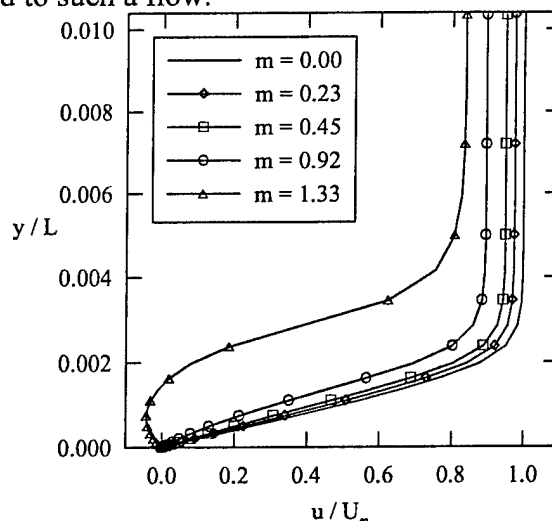
Figure 7-120. Laminar velocity profiles at $x = 0.06\,m$.

Figure 7-121 illustrates the turbulent velocity profile obtained by the original Baldwin Lomax turbulence model, at $x = 0.06\,m$. In the turbulent case, it is possible to increase the magnetic field up to $m = 1.81$, after which a massive separation occurs. The separation occurs later than for the laminar case because the turbulent layer can sustain stronger Lorentz force. This is similar to the comparison between laminar and turbulent boundary layers subject to adverse pressure gradient. The separation is delayed when the boundary layer is turbulent.
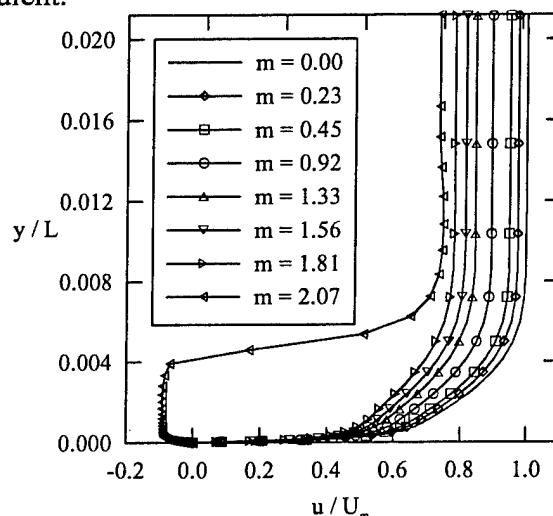
Figure 7-121. Turbulent velocity profiles at $x = 0.06\,m$
(original Baldwin-Lomax model).

140

The temperature profiles are illustrated in Figure 7-122 for the laminar case and Figure 7-123 for the turbulent case. The effect of the magnetic field is to increase the surface temperature as well as the freestream temperature, due to the Joule's effect. The thermal boundary layer is also larger in the turbulent case.
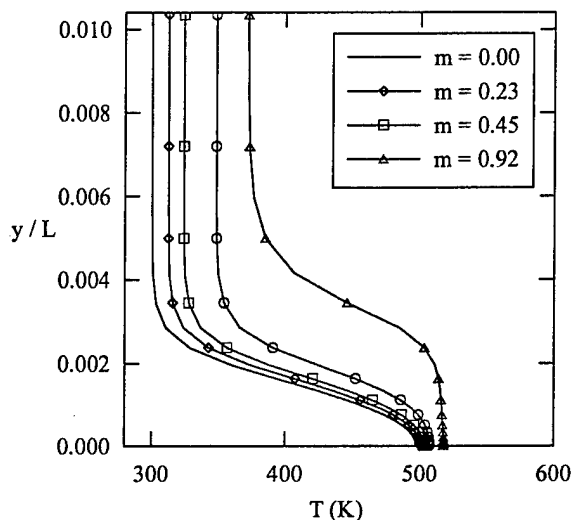
Figure 7-122. Laminar temperature profiles at $x = 0.06\,m$.
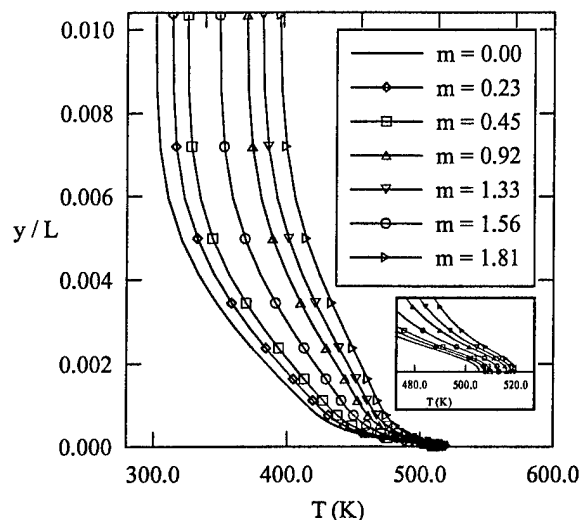
Figure 7-123. Turbulent temperature profiles at $x = 0.06\,m$ (original Baldwin-Lomax model).

Similar results are obtained with the other turbulence models. Figures 7-124 through 7-133 illustrate how the skin friction coefficient decreases as the magnetic field increases. Results are shown for the original and modified versions of the Baldwin-Barth, Spalart-Allmaras, $k - \epsilon$, Baseline and SST models. For all models, the modified version provides a slightly lower skin friction than the original version, but no relaminarization process occurs. For all turbulence models, a separation consistently occurred when m was greater than 1.81.
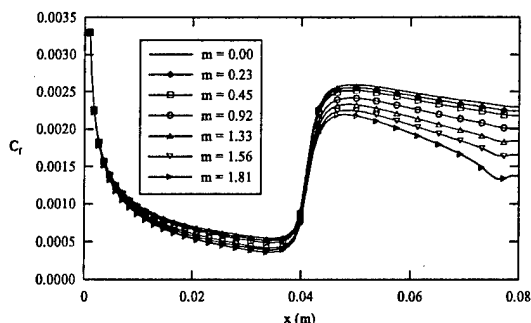
Figure 7-124. Skin friction coefficients (original Baldwin-Barth).
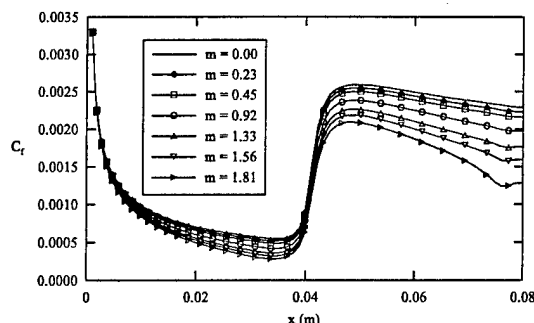
Figure 7-125. Skin friction coefficients (modified Baldwin-Barth).

141
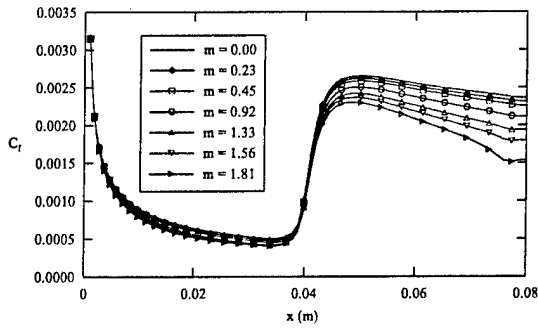
Figure 7-126. Skin friction coefficients (original Spalart-Allmaras).
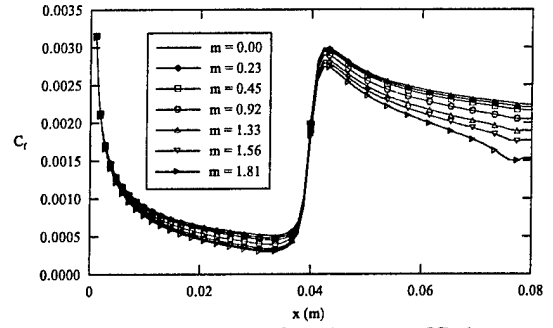
Figure 7-130. Skin friction coefficients (original Baseline).
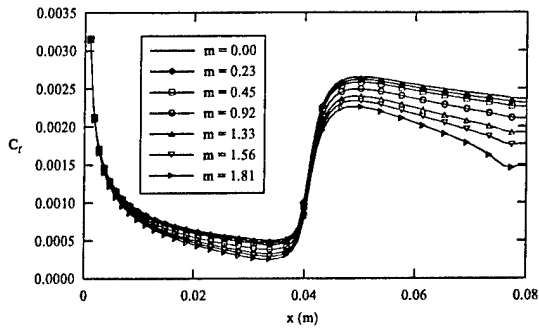
Figure 7-127. Skin friction coefficients (modified Spalart-Allmaras).
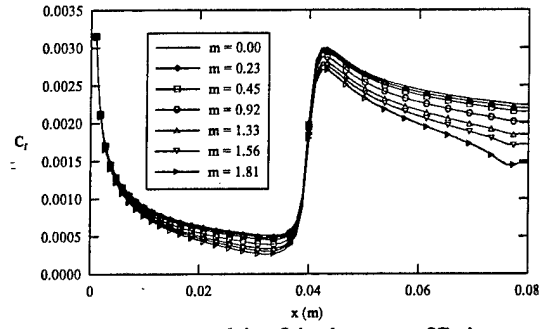
Figure 7-131. Skin friction coefficients (modified Baseline).
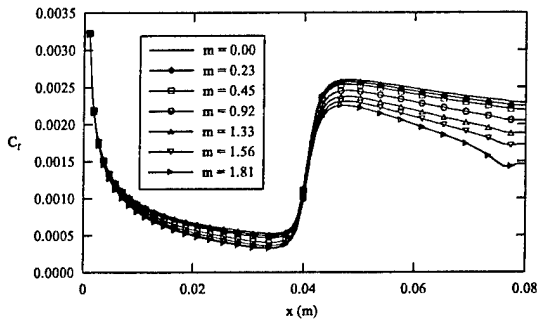
Figure 7-128. Skin friction coefficients (original $k-\epsilon$).
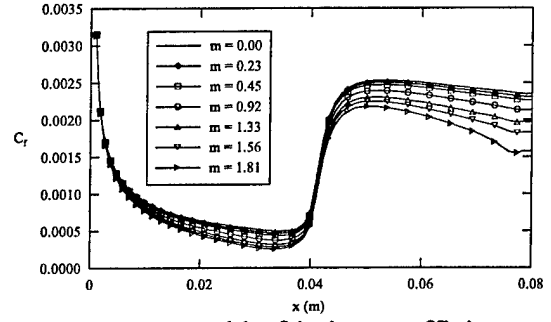
Figure 7-132. Skin friction coefficients (original SST).
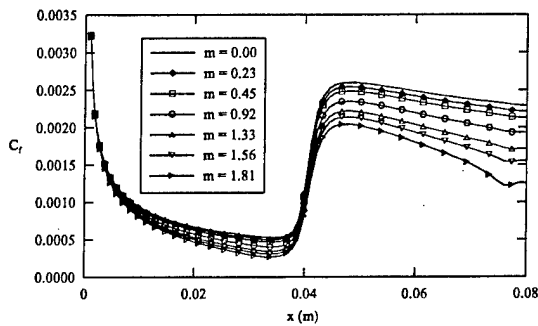
Figure 7-129. Skin friction coefficients (modified $k-\epsilon$).
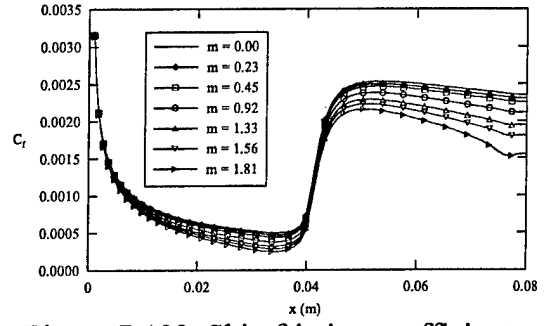
Figure 7-133. Skin friction coefficients (modified SST).

142

Figure 7-134 illustrates the turbulent velocity profiles obtained by all turbulence models in the non-magnetic case. A good consistency between the turbulence models can be observed. For a magnetic field corresponding to $m = 1.33$ (Figure 7-135), all turbulence models provide similar velocity profiles. It should be noted that the freestream velocity is reduced by about 12% when the magnetic field is turned on.
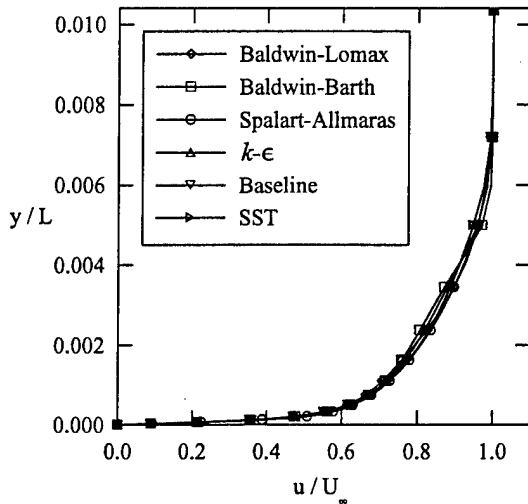
Figure 7-134. Comparison of turbulent velocity profiles at $m = 0.00$.
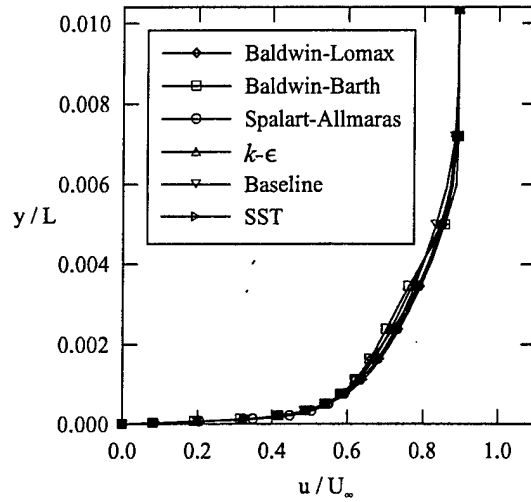
Figure 7-135. Comparison of turbulent velocity profiles at $m = 1.33$.

Figure 7-136 presents a comparison of all original turbulence models at $m = 1.33$. The models are consistent with each other, except in the transition region. Figure 7-137 illustrates the skin friction coefficient obtained by all modified turbulence models. The skin frictions obtained by the modified models are less consistent with each other than when the original models were implemented. Figure 7-138 shows the relative skin friction at a given location ($x = 0.06\,m$), when it is normalized with its non-magnetic counterpart. In the laminar case, the relative reduction of the skin friction is more important than in the turbulent case. A substantial reduction is achieved, which leads to the separation of the flow (negative value of the skin friction). In the turbulent case, a reduction of up to about 20% is achieved with all turbulence models, at the highest value of magnetic field. When the same quantities are plotted for the modified versions of the turbulence models (Figure 7-139), the reduction in the skin friction is less homogeneous, ranging from 20% for the Baldwin-Lomax and Baseline models to 30% for the $k - \epsilon$ model. A complete relaminarization of the flow cannot be achieved because the effect of the magnetic field on the mean flow is more important than the effect on the small scales of motion. A flow separation occurs before the relaminarization of the flow is achieved.
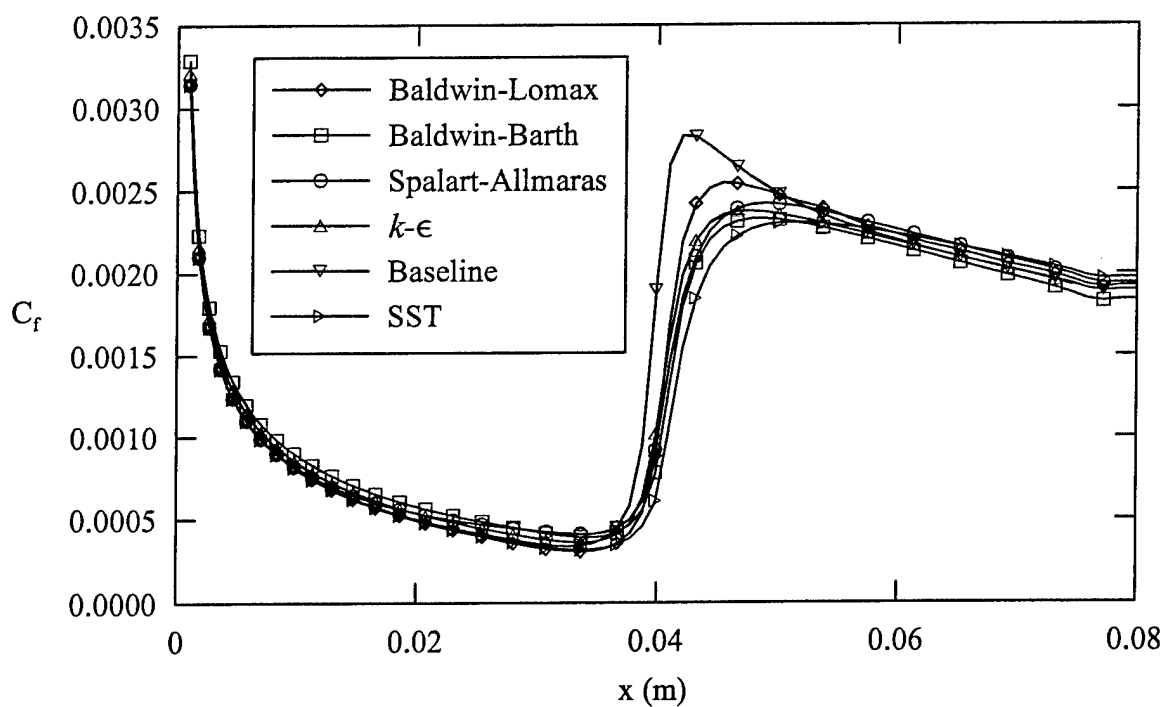
Figure 7-136. Comparison of all original turbulence models at $m = 1.33$.
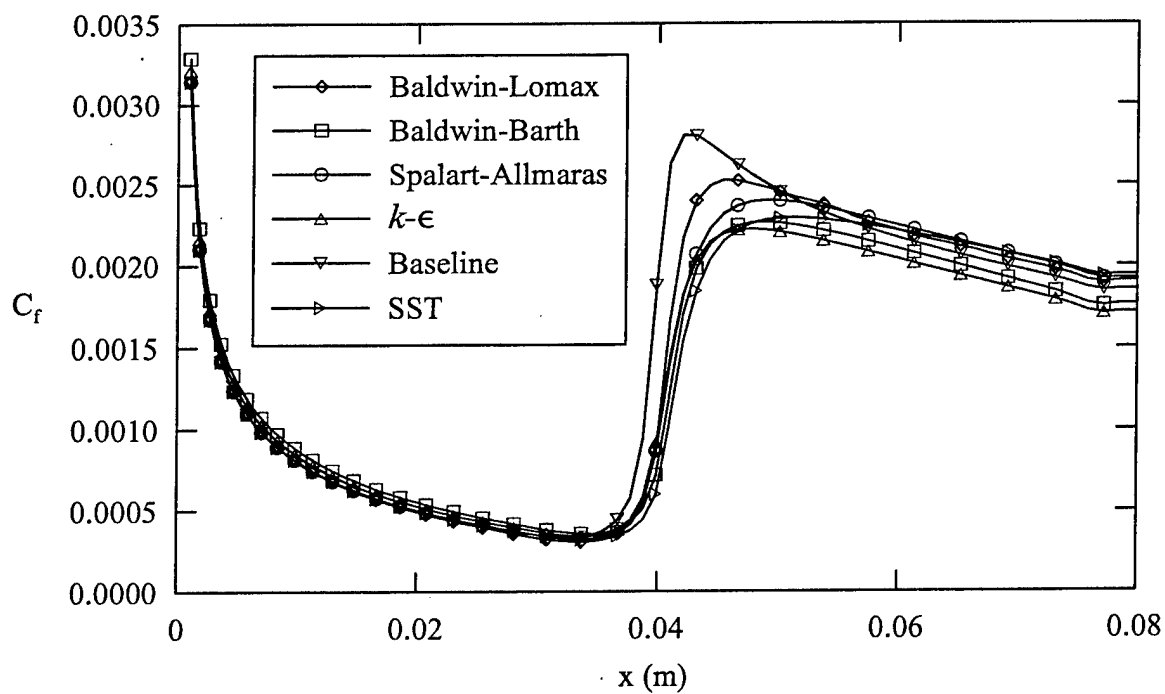
Figure 7-137. Comparison of all modified turbulence models at $m = 1.33$.

144
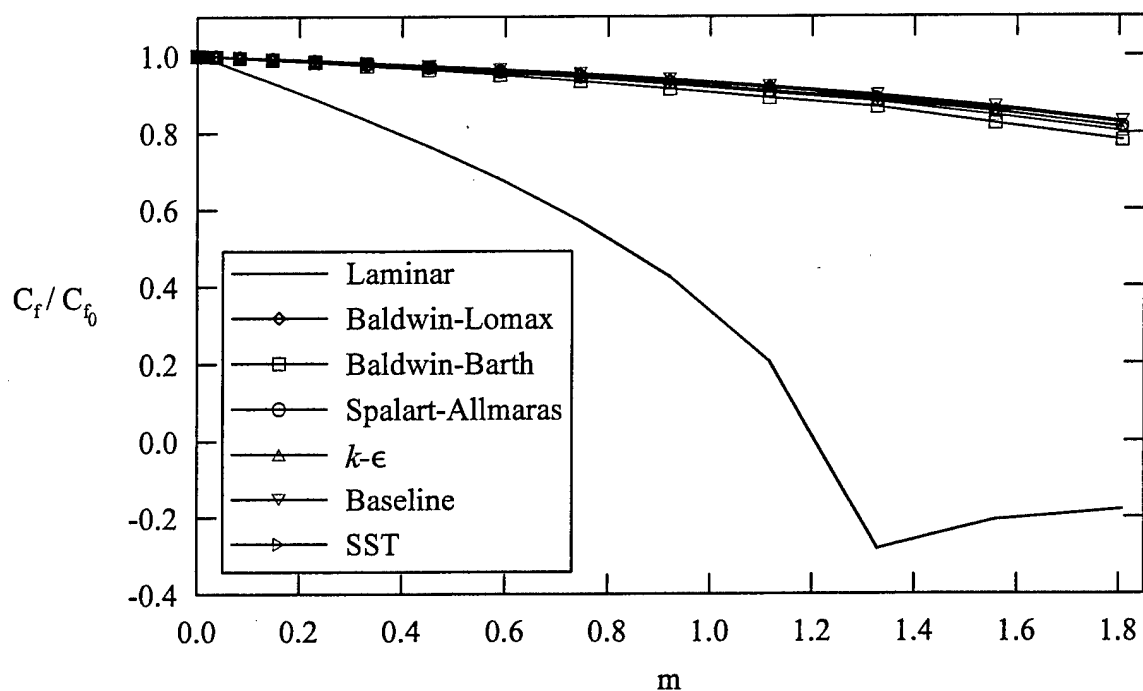
Figure 7-138. Skin friction coefficient ratio obtained by all original models.
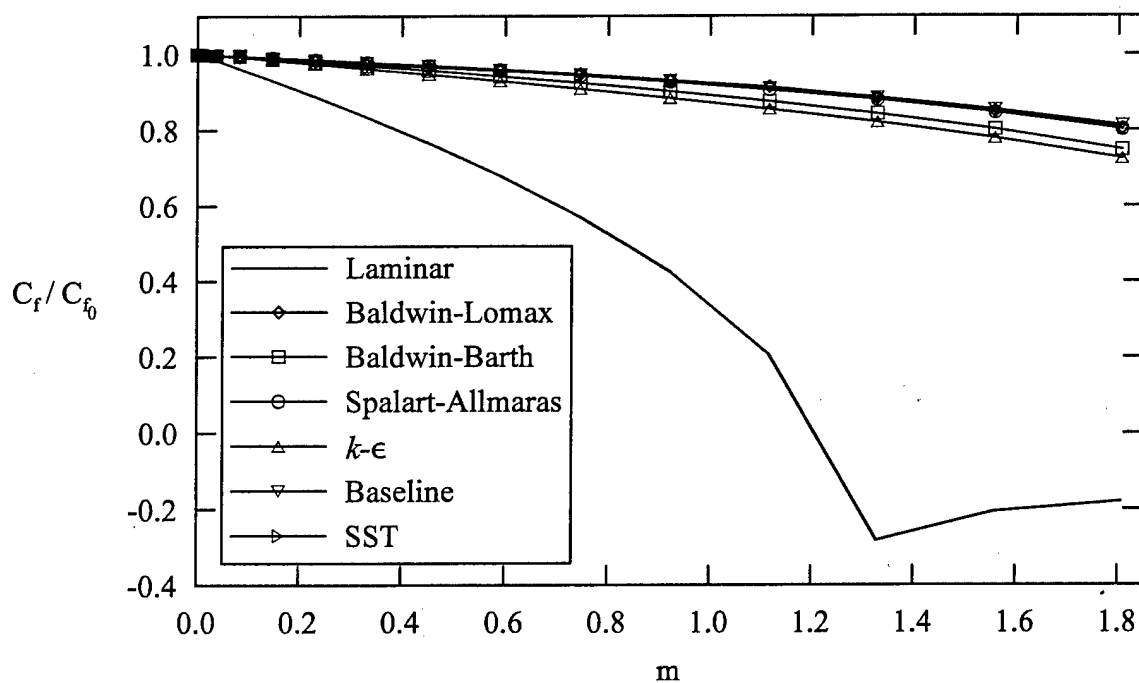
Figure 7-139. Skin friction coefficient ratio obtained by all modified models.

145

An expression for the skin friction coefficient obtained for an incompressible MHD flow over a flat plate can be found in the literature [112, 113]. This is the equivalent of the Blasius solution in fluid mechanics. The application of a magnetic field tends to decrease the skin friction. The effect of the magnetic field is introduced through the parameter m. Equation (7.18) is valid for small values of the product mx. Note that Equation (7.18) reduces to the Blasius solution when no magnetic field is present (i.e., $m = 0.0$).

$$C_f = \frac{0.664 - 1.789mx}{\sqrt{Re_x}} \tag{7.18}$$

For the laminar but compressible case, it is assumed that Equation (7.18) can be modified by the introduction of compressibility correction factors. Therefore, the following approximation for the skin friction over a flat plate is proposed:

$$C_{f_l} = \frac{C_{0l} \cdot 0.664 - C_{ml} \cdot 1.789 \cdot mx}{\sqrt{Re_x}} \tag{7.19}$$

The coefficients C_{0l} and C_{ml} are compressibility correction coefficients. They are determined from numerical results obtained for a fully laminar flow over a flat plate, at different Mach numbers. Figure 7-140 shows the dependence of C_{0l} and C_{ml} on the Mach number. Figure 7-141 shows a comparison of Equation (7.19) with the numerical results. The skin friction is extracted at $x = 0.06m$. The expression given by Equation (7.19) is valid for values of m up to 0.75, where the product mx equals 0.045. As the Mach number increases, the skin friction tends to decrease. At Mach 2.0, the magnetic field reduces the skin friction until a separation occurs. For larger Mach numbers, the slope of the curve increases, and no separation of the flow occurs.

For a turbulent flow, the following expression for the skin friction is proposed:

$$C_{f_t} = \frac{C_{0t} \cdot 0.0577 - C_{mt} \cdot 1.789 \cdot mx}{Re_x^{1/5}} \tag{7.20}$$

It also reduces to the expression for the skin friction of a turbulent incompressible flow over a flat plate, when no magnetic field is present. The compressibility correction factors C_{0t} and C_{mt} are determined from numerical results obtained of a fully turbulent flow over a flat plate at different Mach numbers. They both decrease when the Mach number increases (Figure 7-142). Figure 7-143 shows the good agreement between the numerical results and Equation (7.20). Here, increasing magnetic field and Mach number tend to decrease the skin friction.

146
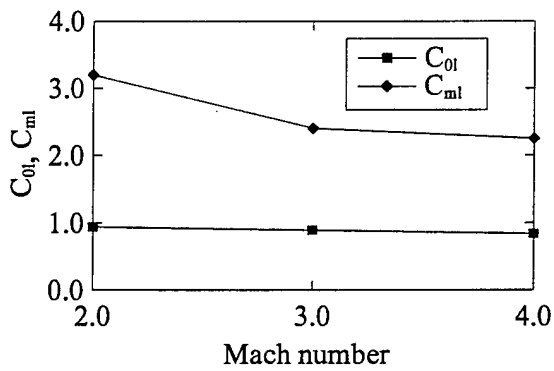
Figure 7-140. Coefficients C_{0l} and C_{ml} as a function of the Mach number.
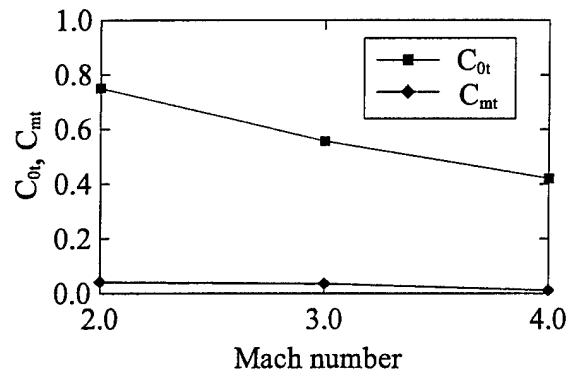
Figure 7-142. Coefficients C_{0t} and C_{mt} as a function of the Mach number.
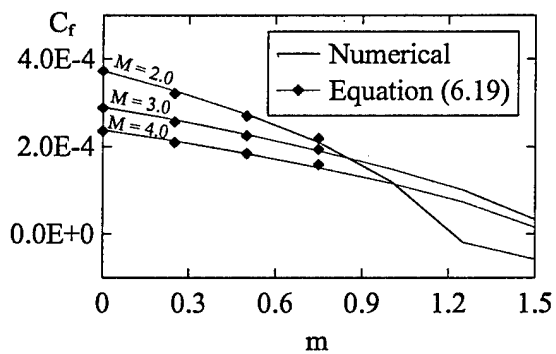
Figure 7-141. Effect of the Mach number on the laminar skin friction coefficient.
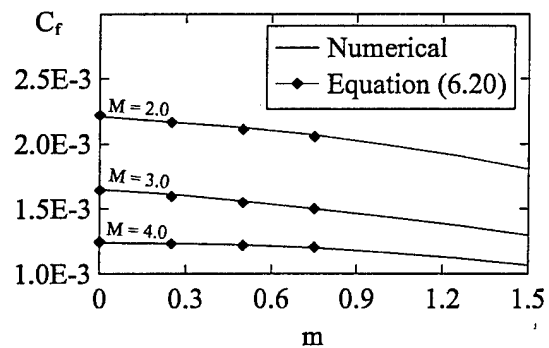
Figure 7-143. Effect of the Mach number on the turbulent skin friction coefficient.

147

7.4.2. Full MHD Equations

7.4.2.1. Effect of the Magnitude of the Applied Magnetic Field

In this section, the flow over a supersonic flat plate is investigated when the full MHD equations are solved. For numerical stability considerations, the electrical conductivity is considered to be almost infinite ($\sigma_{e\infty} = 10^{10}\,mho/m$). All other flow conditions are similar as described in Section 7.4.1. The magnetic field is applied in the y – direction, but its magnitude is sufficiently small to provide a finite value for the parameter m.

Figure 7-144 shows the laminar velocity profiles at $x = 0.06\,m$. As the magnetic field is increased, the flow is decelerated within the boundary layer and the boundary layer thickness is increased. The freestream velocity is not affected by the magnetic field. The turbulent velocity profiles obtained by the original Baldwin-Lomax turbulent model are shown in Figure 7-145. No measurable effect of the magnetic field can be observed in the vicinity of the wall. However, the boundary layer becomes thicker as the magnetic field is increased. When the modified version of the Baldwin-Lomax model is implemented, the magnetic field has a larger influence on the velocity profiles (Figure 7-146). The deceleration of the flow is greater than with the original model. For a large value of the applied magnetic field, corresponding to $m = 3.69$, the velocity profile is similar to the laminar profile obtained at the same value of m. Therefore, it can be anticipated that a relaminarization process has occurred. Figure 7-147 illustrates the turbulent viscosity profiles when $m = 0.92$. The original Baldwin-Lomax model produces turbulent viscosity neat the wall, whereas the damping terms in the modified version destroy the turbulent viscosity near the wall. The maximum amount of turbulent viscosity is also reduced when the modified Baldwin-Lomax model is used. For a larger value of the magnetic field ($m = 3.69$), a large quantity of turbulent viscosity is destroyed near the wall (Figure 7-148), which results in a relaminarization of the flow.

Figure 7-149 shows the magnitude of the magnetic field at $x = 0.06m$, when it is normalized with the magnitude of the applied magnetic field. In the region near the wall, the magnetic field is about 500 times larger than the applied magnetic field. In this case, the induced magnetic field is much larger than the applied field within the boundary layer. Outside the boundary layer, no induced field is generated.

Figure 7-150 shows the skin friction obtained with various turbulence models. No converged solution could be obtained with the modified Baldwin-Barth and the $k-\epsilon$ models. The value of the skin friction has been extracted at $x = 0.06\,m$. The solid line represents the laminar skin friction. As the magnetic field increases, the laminar skin friction is reduced. The non-magnetic turbulent skin friction is more than five times larger than the laminar one. None of the original turbulence models predicts a complete relaminarization of the flow, even though a substantial reduction is achieved (up to 80%, when $m = 3.69$). The modified versions of the turbulence models exhibit a faster reduction of the skin friction, leading to a complete relaminarization of the flow. At $m = 1.0$, it can be considered that the flow returns to a laminar state when the modified

Baldwin-Lomax, Baseline and SST models are implemented. The modified Spalart-Allmaras predicts that the relaminarization process occurs for $m = 3.69$.
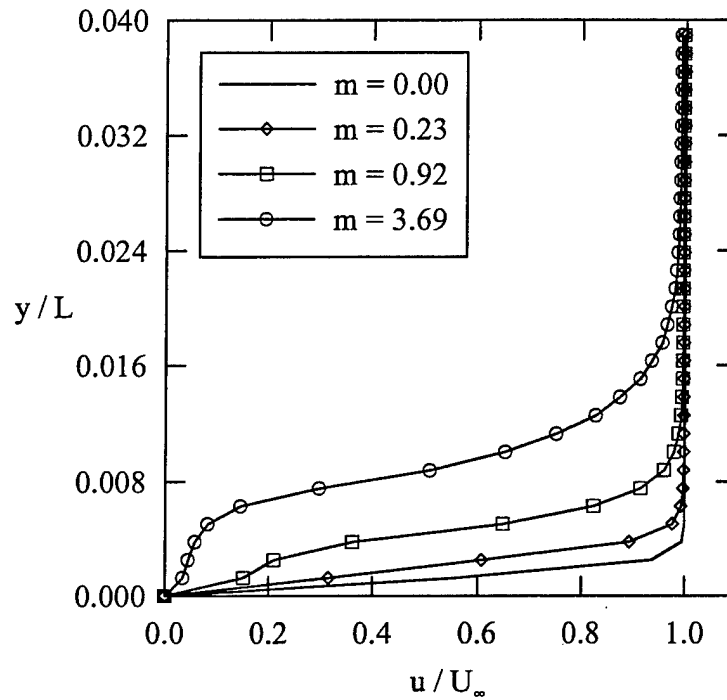
Figure 7-144. Laminar velocity profiles.
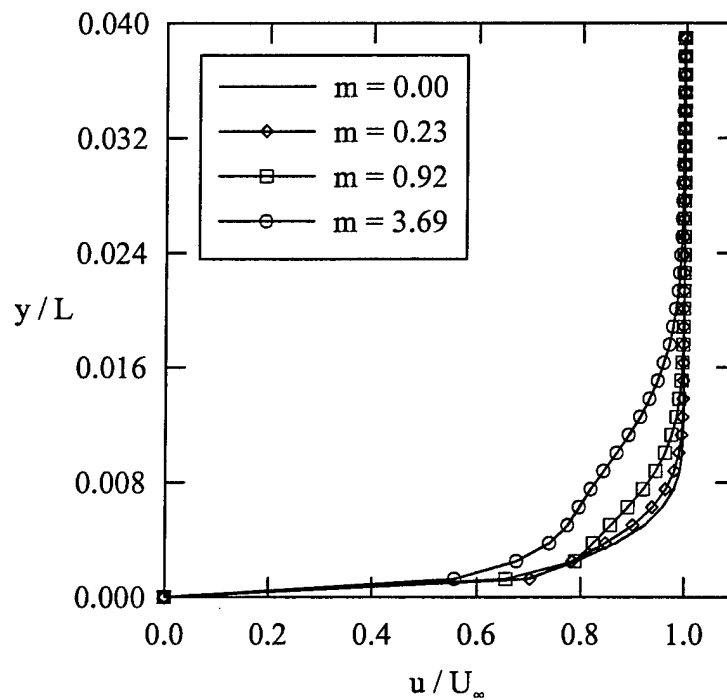
Figure 7-145. Turbulent velocity profiles
(original Baldwin-Lomax model).
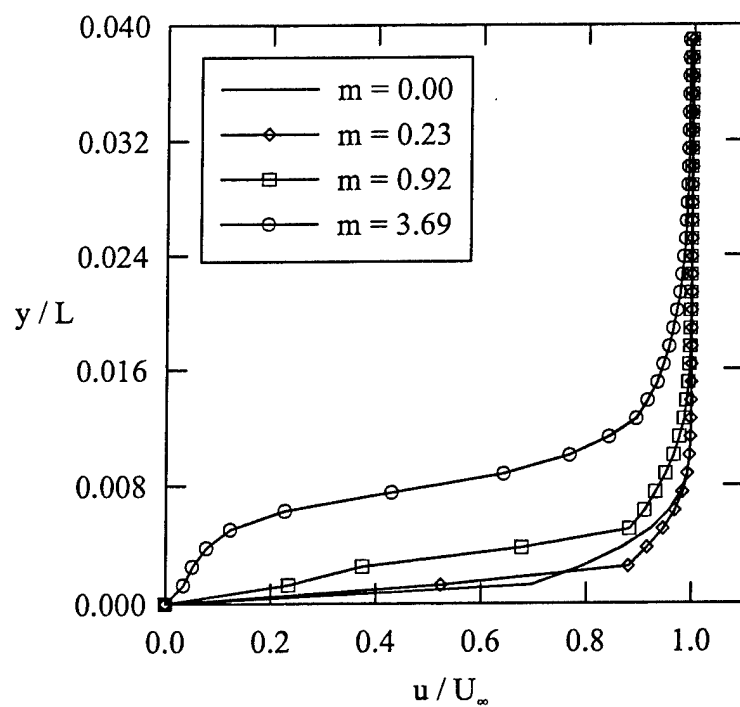
Figure 7-146. Turbulent velocity profiles
(modified Baldwin-Lomax model).
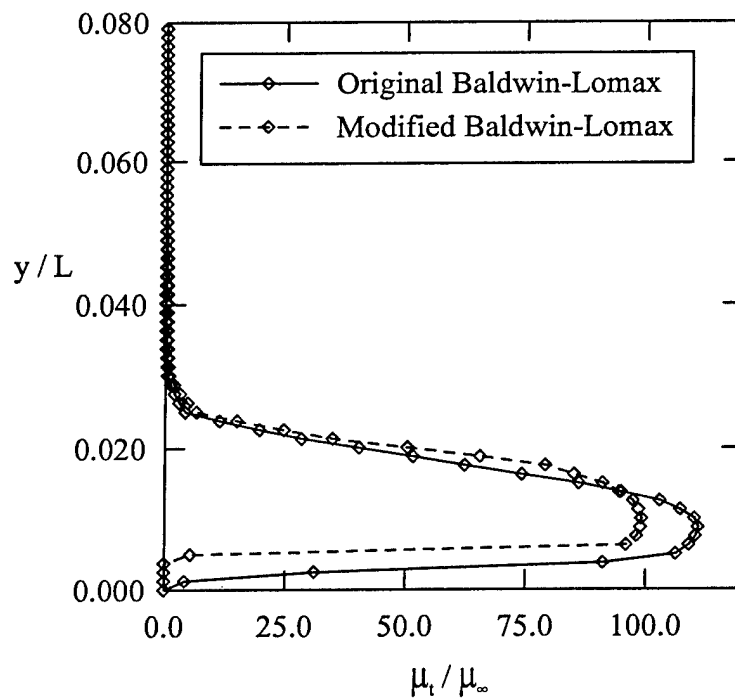
Figure 7-147. Turbulent viscosity profiles at $m = 0.92$
(Baldwin-Lomax model).

150
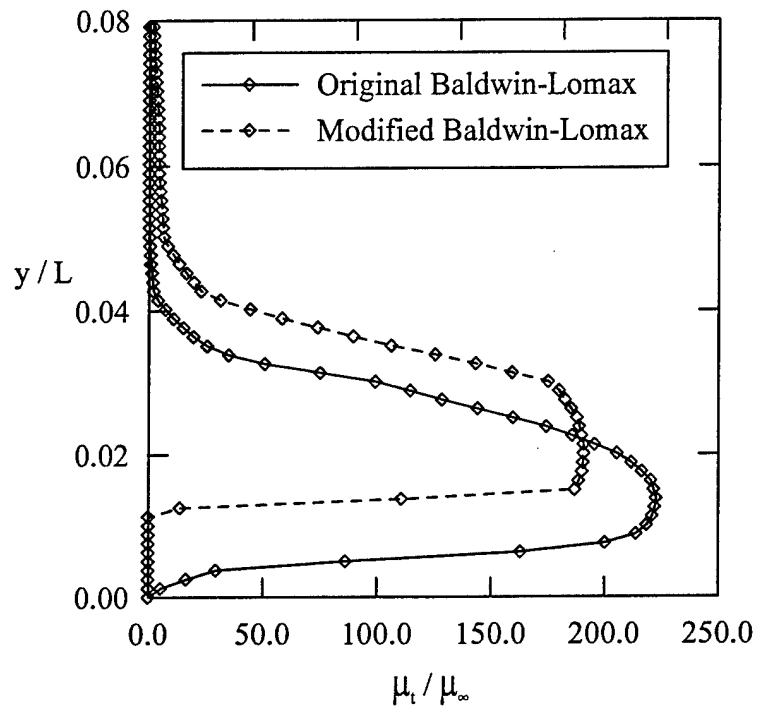
Figure 7-148. Turbulent viscosity profiles at $m = 3.69$
(Baldwin-Lomax model).
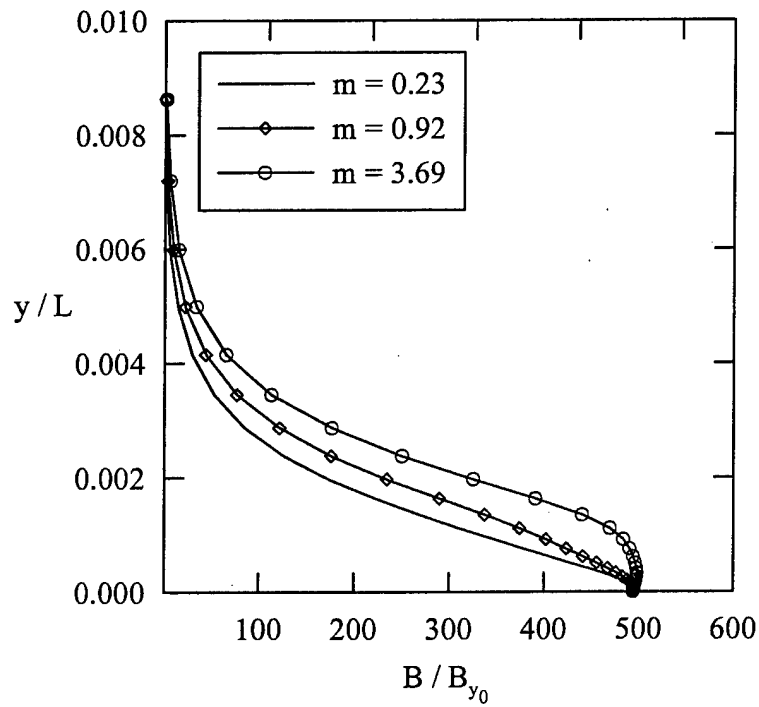
Figure 7-149. Magnitude of the magnetic field across the boundary layer.

151
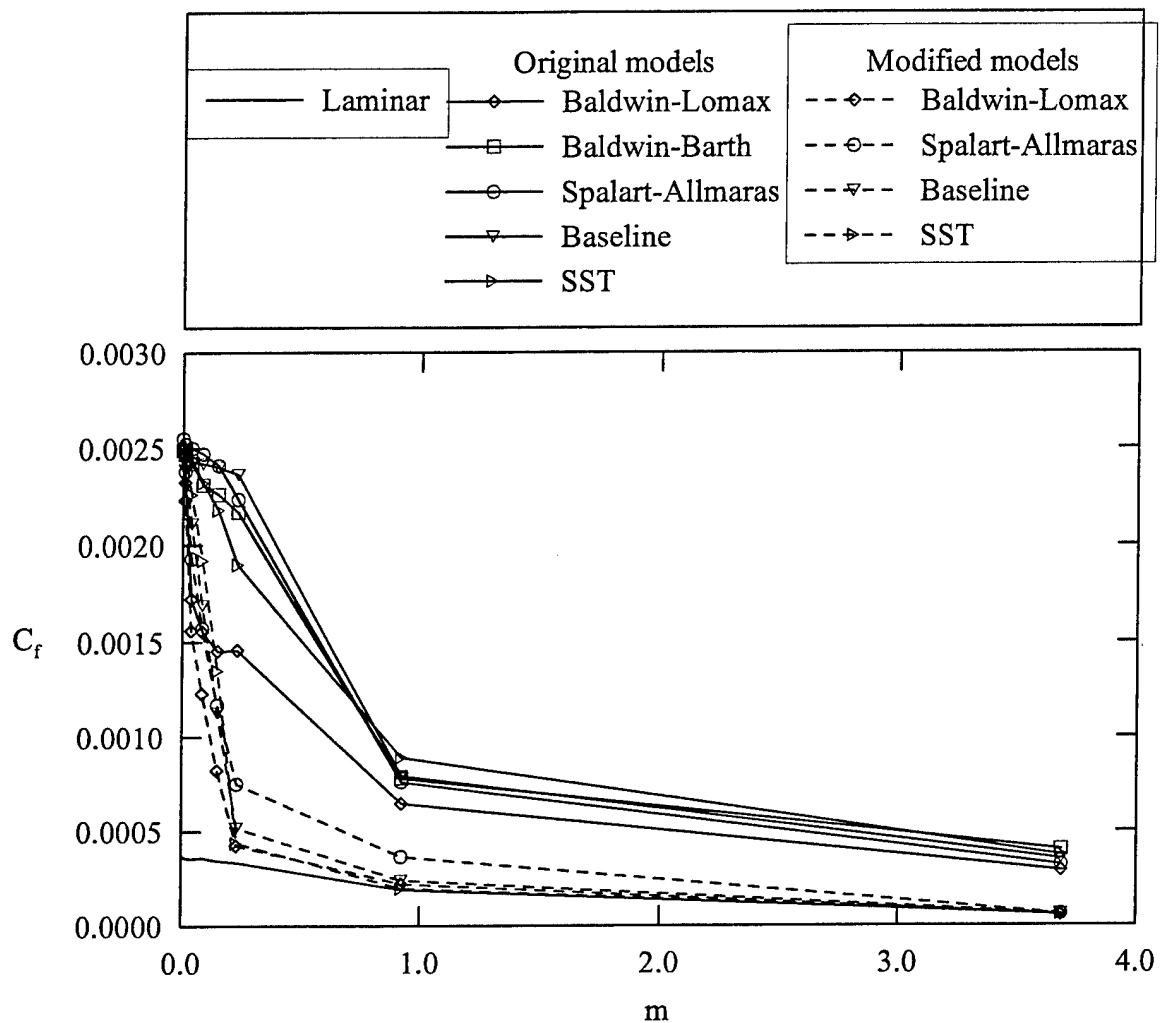
Figure 7-150. Skin friction coefficients
(original and modified turbulence models).

7.4.2.2. Effect of the Orientation of the Applied Magnetic Field

The interaction between the magnetic field and the flow field generates an induced electric field $\bar{U} \times \bar{B}$ which creates a body force $\sigma_e \left(\bar{U} \times \bar{B} \right) \times \bar{B}$ in the absence of an externally applied electric field, which is the case considered here. Therefore, the relative orientation of the applied magnetic field with respect to the velocity field has a great impact on the solution [114]. Figure 7-151 shows the skin friction obtained at $x = 0.06\,\mathrm{m}$ when the angle θ between the applied magnetic field and velocity field varies from zero degree (i.e. $\bar{U}$ and $\bar{B}$ are aligned and pointing in the same direction) to 180 degrees (i.e. $\bar{U}$ and $\bar{B}$ are aligned and pointing in opposite directions). The skin frictions are normalized by the skin friction obtained at $\theta = 0°$. The flow is turbulent and the solution is obtained with the Baldwin-Lomax model. The reduction in the skin friction is maximal when the magnetic field and velocity fields are perpendicular. A substantial reduction of about 80% in the skin friction is achieved at $\theta = 90°$, compared to the case where the magnetic field and velocity fields are aligned. Furthermore, the symmetry of the curve suggests that the same effect is obtained whether the magnetic field and velocity field are pointing in the same direction or not.
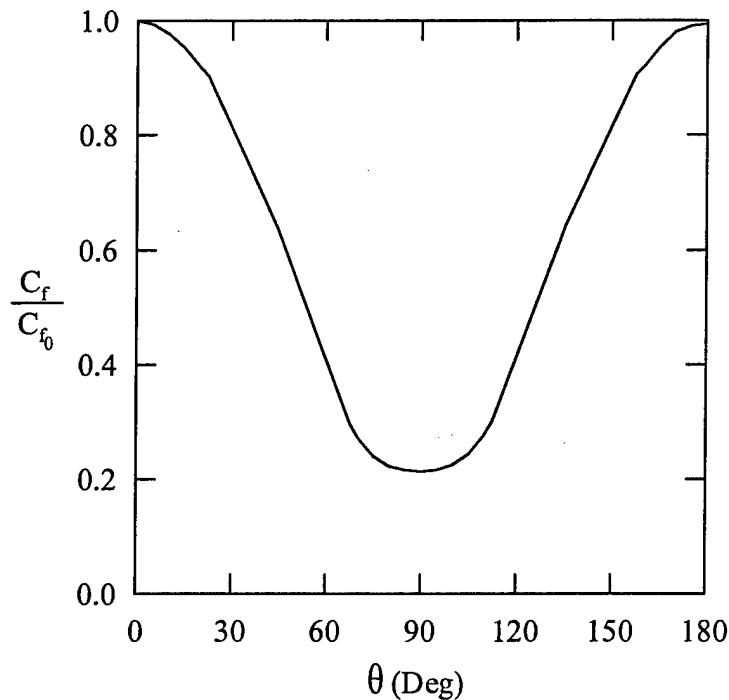
Figure 7-151. Effect of the orientation of the applied magnetic field.

7.5. Flow over a Cone at Mach 6.86

The objective of this section is to investigate the effect of the magnetic field on the heat transfer rate for a hypersonic turbulent flow. It has been stated in the literature that the application of a magnetic field should result in a decrease in the skin friction and a decrease in the heat transfer. It has been seen in Section 7.4 that the presence of a magnetic field does indeed reduce the skin friction. The proper evaluation of the heat transfer rate is a key-element that influences the design of hypersonic vehicles. The possibility of reducing it by an appropriate usage of magnetic field is a promising application of MHD to high-speed vehicles design.

In order to assess the accuracy of the results, the non-magnetic case will be compared to the experimental results obtained by Fischer [115]. He investigated the boundary layer transition on a 10-degree half-angle cone at hypersonic speed. The configuration for the non-magnetic case (i.e., the experimental conditions) is summarized in Table 7-6. Under these conditions, the transition begins at $s = 0.168\,m$ and the flow becomes fully turbulent at $s = 0.269\,m$, where s represents the curvilinear abscissa from the tip of the cone. Suzen and Hoffmann [116] were able to numerically compute the turbulent heat rate transfer by solving the Reynolds Averaged Navier-Stokes equations with a flux vector splitting scheme. They found that the Baseline model would provide more accurate results than the Baldwin-Barth, Spalart-Allmaras and SST models.

Property	Symbol	Value
Inflow Mach number	M_∞	6.86
Total pressure	p_t	$377 \times 10^4\ N/m^2$
Total temperature	T_t	$594.0\,K$
Wall temperature	T_w/T_t	0.52
Reynolds number	Re_∞	17.48×10^6 per meter

Table 7-6. Configuration of flow over a cone.

First, the MHD equations have been solved in the laminar case in order to determine a suitable range for the magnitude of the applied magnetic field. Since the tip of the cone is in reality blunt, a detached shock wave develops upstream of the cone and it behaves like a blunt body. The application of a magnetic field will increase the shock standoff distance. From a numerical point of view, the domain of solution cannot be extended too far away from the cone, which would prevent the computation of a converged solution in a realistic computational time, especially in the turbulent cases. Therefore, the range of the applied magnetic field has been selected such that the shock wave always remains within the boundaries of the domain and it has a measurable effect on the skin friction and heat transfer rate. The grid spacing near the wall has a great impact on the calculation of the heat transfer rate [117]. The grid has been refined until the solution exhibited grid independence. The grid system, composed of 124 by 80 grid

points is illustrated in Figure 7-152. To minimize the computational time required to reach a converged solution, only half of the cone is modeled, and symmetry boundary conditions are implemented to represent the entire body.
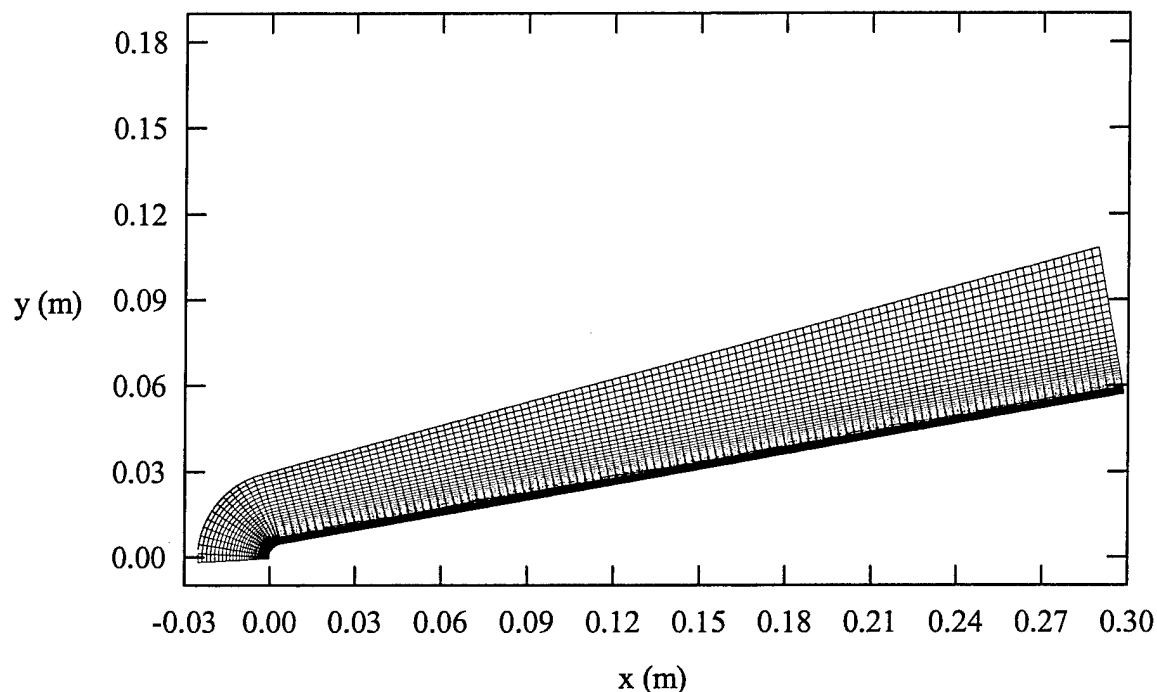
Figure 7-152. Grid system (124× 80 grid points).

The strength of the magnetic field can be represented either by the magnitude of the applied magnetic field B_y, or by the parameter m. Table 7-7 shows the relation between B_y and m. The magnetic Reynolds number based on the cone tip radius is $Re_m = 0.052$, which is much less than unity. Therefore, the problem will be solved by the low magnetic Reynolds number formulation.

B_y (T)	m
0.0	0.00
0.1	0.12
0.2	0.49
0.3	1.10
0.4	1.95
0.5	3.05
0.6	4.39

Table 7-7. Conversion table between the applied magnetic field and m.

Figure 7-153 illustrates the shock wave pattern near the tip of the cone. As the magnetic field increases, the shock wave moves away from the body. Figure 7-154 shows the pressure distribution along the stagnation streamline. The shock standoff distance increases and the stagnation pressure decreases with an increasing magnetic field.

155

| m = 0.00 | m = 0.12 | m = 0.49 | m = 1.10 |
| m = 1.95 | m = 3.05 | m = 4.39 | |
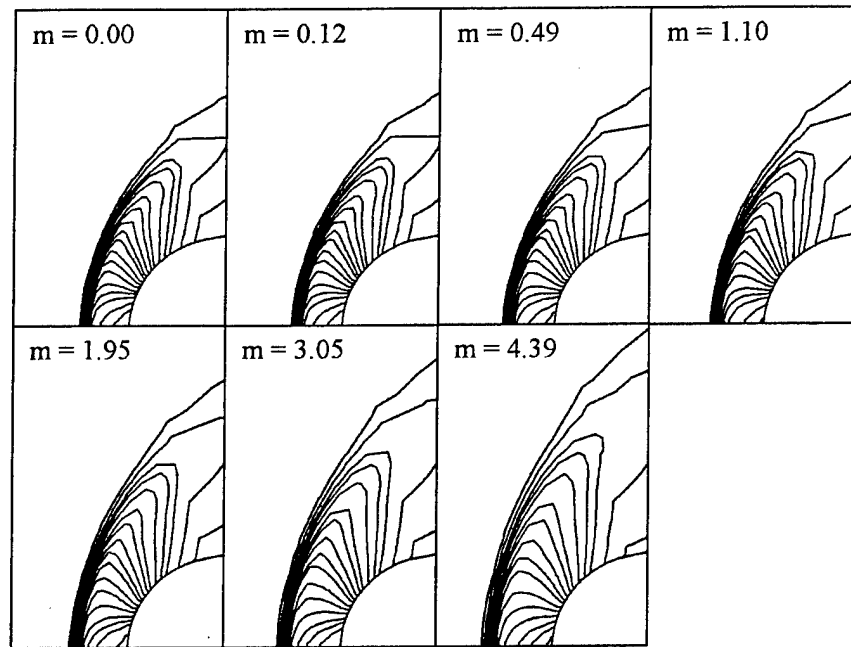
Figure 7-153. Shock wave pattern.

The accurate computation of heat transfer rate is a very challenging task, especially for turbulent flows. It is therefore not in the scope of this investigation to calibrate all turbulence models for this particular application. The wide choice of turbulence models provided in the computational code will allow the selection of the turbulence models that perform the best in the non-magnetic case, based on the comparison with existing experimental data. Only those that perform well in the non-magnetic case will be used when the magnetic field is turned on.
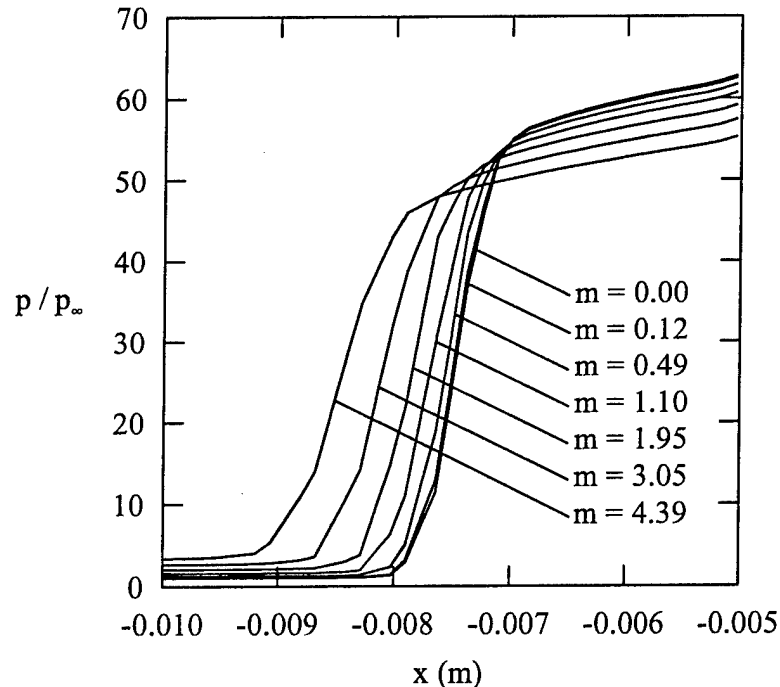
Figure 7-154. Pressure distribution along the stagnation streamline.

All available turbulence models are tested in the non-magnetic case. The transition has been triggered at $s = 0.20\,m$ to reproduce the experimental transition behavior of the boundary layer. The heat transfer rate is shown in Figure 7-155. The laminar heat transfer rate is well predicted by the main solver. As expected, comparison between the numerical and experimental results shows that some turbulence models perform better than others. The Spalart-Allmaras model under-estimates the most the heat transfer rate in the turbulent region. The Baldwin-Barth, $k - \epsilon$ and SST model perform better, but are still under-predicting the turbulent heat transfer rate by about 30%. The Baldwin-Lomax and Baseline model are able to accurately predict the heat transfer in the turbulent region. Therefore, only the Baldwin-Lomax and Baseline models will be used when computations are carried out with the magnetic field turned on.

Next, the magnetic field is applied in the y – direction and remains constant within the entire domain. Both original and modified versions of the Baldwin-Lomax and Baseline models are investigated. Figure 7-156 shows the heat rate transfer obtained by the original Baldwin-Lomax model. It is difficult to extract a general trend from this plot. The application of a magnetic field seems to provide a higher heat rate transfer in the laminar region, when compared to the non-magnetic case. In the turbulent region, the heat rate first increases for small values of the magnetic field, and then decreases as m is increased, until it reaches its laminar value. However, the distribution of the heat rate transfer remains very irregular. Figure 7-157 shows the heat rate transfer obtained by the modified Baldwin-Lomax model, i.e., when damping terms are added in the computation of the turbulent viscosity. In this case, a more general trend can be observed. The heat rate transfer decreases as the magnetic field increases until it reaches its laminar value. Some hollows can still be observed for intermediate values of the magnetic field.

Figures 7-158 and 7-159 illustrate the skin friction distribution obtained with the original and modified Baldwin-Lomax models, respectively. For both versions, the skin friction distribution is smooth. The skin friction is noticeably reduced as the magnetic field increases in both the laminar and turbulent regions. When the magnetic field is sufficiently large, the skin friction shows the characteristics of a laminar flow along the entire domain.

Figures 7-160 and 7-161 show the heat rate transfer obtained by the original and modified Baseline models, respectively. The modified Baseline model contains additional magnetic terms in the turbulent equations. The same trend can be observed for both models. The heat rate transfer distribution is smoother that the one obtained by the Baldwin-Lomax model, which is probably due to the different nature of the models. The Baseline model contains a convection and a diffusion term that makes the turbulent viscosity more smoothly distributed. For both versions of the model, the heat rate transfer decreases as m is increased until the laminar value is reached for a large magnitude of the magnetic field. However, the relaminarization occurs earlier with the modified Baseline model than with the original version.

The same observation can be made about the skin friction coefficient. Figures 7-162 and 7-163 show the skin friction distributions for the original and modified Baseline

models, respectively. The relaminarization process occurs for both versions and is faster in the case of the modified model.

In order to compare the turbulence models, the heat rate transfer and skin friction are plotted versus the strength of the magnetic field, at the location $s = 0.28\,m$ and normalized with their non-magnetic counterparts. Figure 7-164 shows the heat rate transfer as a function of m. In the case where the original models were used, the relaminarization occurs at $m = 2.0$ for the Baldwin-Lomax model and $m = 1.8$ for the Baseline model. When the modified versions of the turbulence models are used, the relaminarization occurs earlier, at $m = 1.05$ for the Baldwin-Lomax, and $m = 1.2$ for the Baseline model. Overall, a reduction of about 70% is achieved by the application of a strong magnetic field. Figure 7-165 shows the skin friction coefficient as a function of m. Here again, all models illustrate the relaminarization process. It occurs earlier in the case of the modified models, at about $m = 1.05$ for both the Baldwin-Lomax and $m = 1.2$ for the Baseline models. The original models provide a relaminarization at $m = 2.0$ for the Baldwin-Lomax and $m = 1.8$ for the Baseline model. The maximum reduction in skin friction is about 90%. Note that the values of the magnetic strength for which the skin friction reaches its lower values are consistent with those associated with the heat rate transfer.

It is concluded that the application of a magnetic field leads to a substantial reduction in the skin friction coefficient (90%) and heat rate transfer (70%), primarily due to the relaminarization of the flow. A relaminarization process occurs between $m = 1.8$ and $m = 2.0$ with the implementation of the original turbulence models, whereas it occurs between $m = 1.05$ and $m = 1.20$ with the implementation of the modified turbulence models.
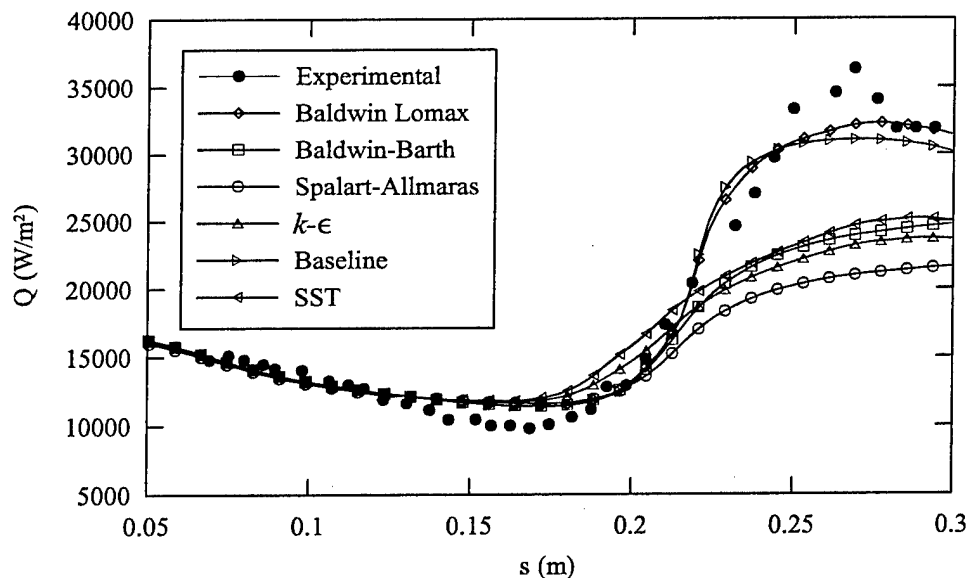
Figure 7-155. Comparison of the turbulence models in the non-magnetic case.

158
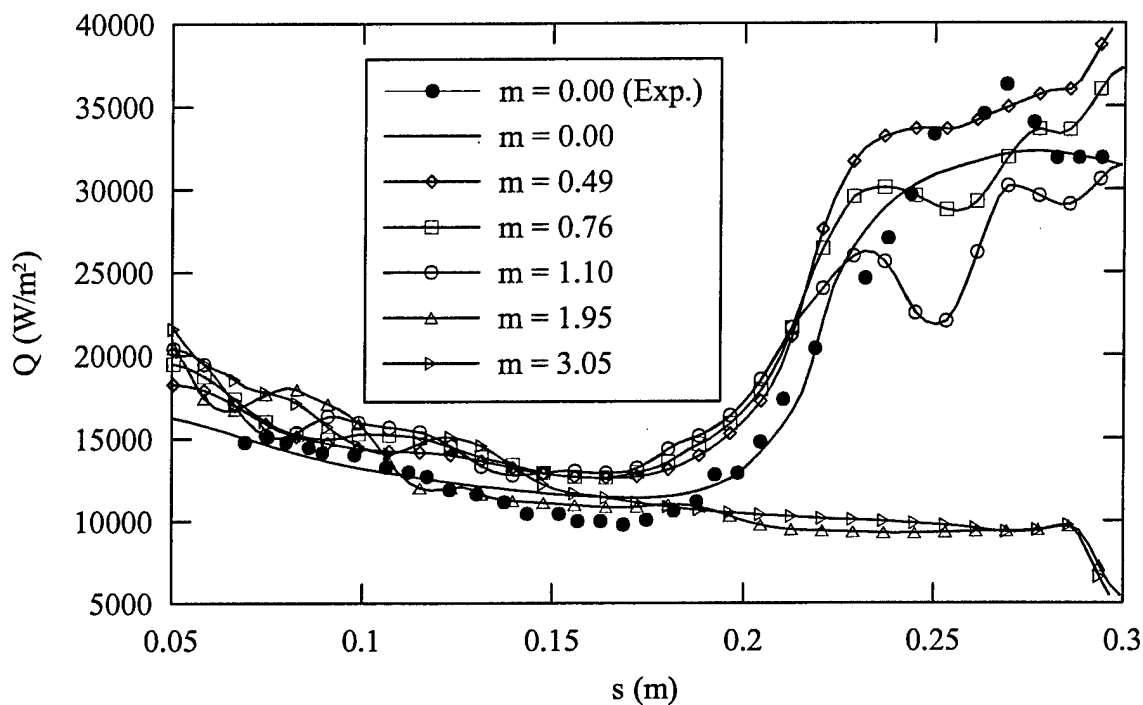
Figure 7-156. Heat rate transfer (original Baldwin-Lomax model).
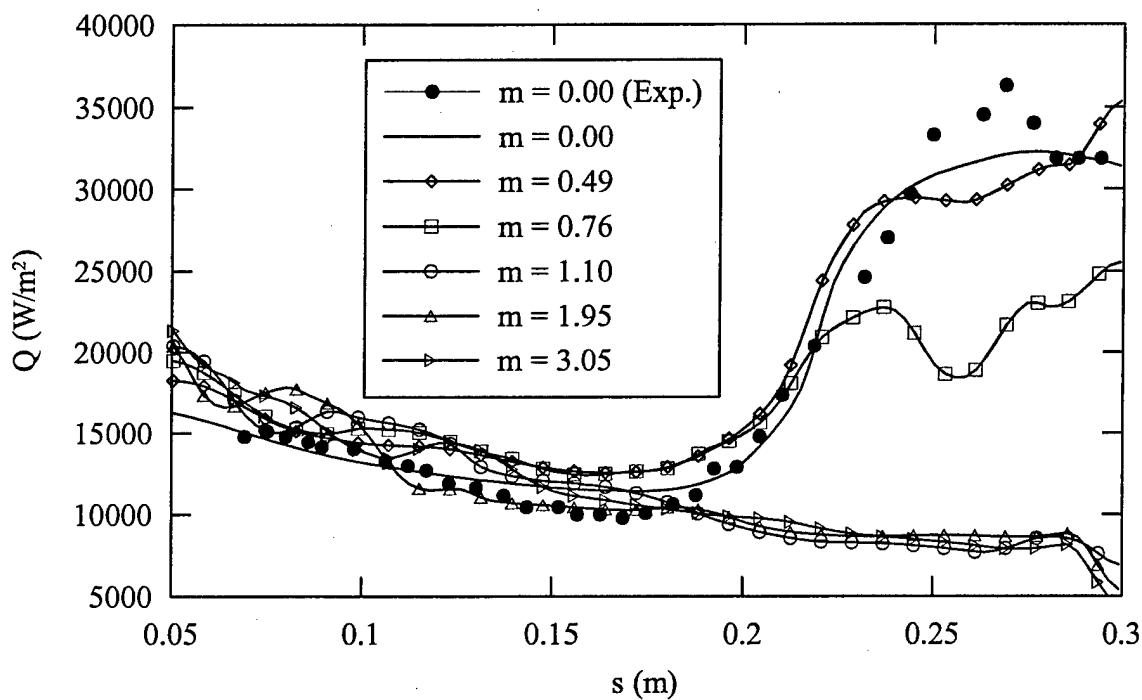
Figure 7-157. Heat rate transfer (modified Baldwin-Lomax model).
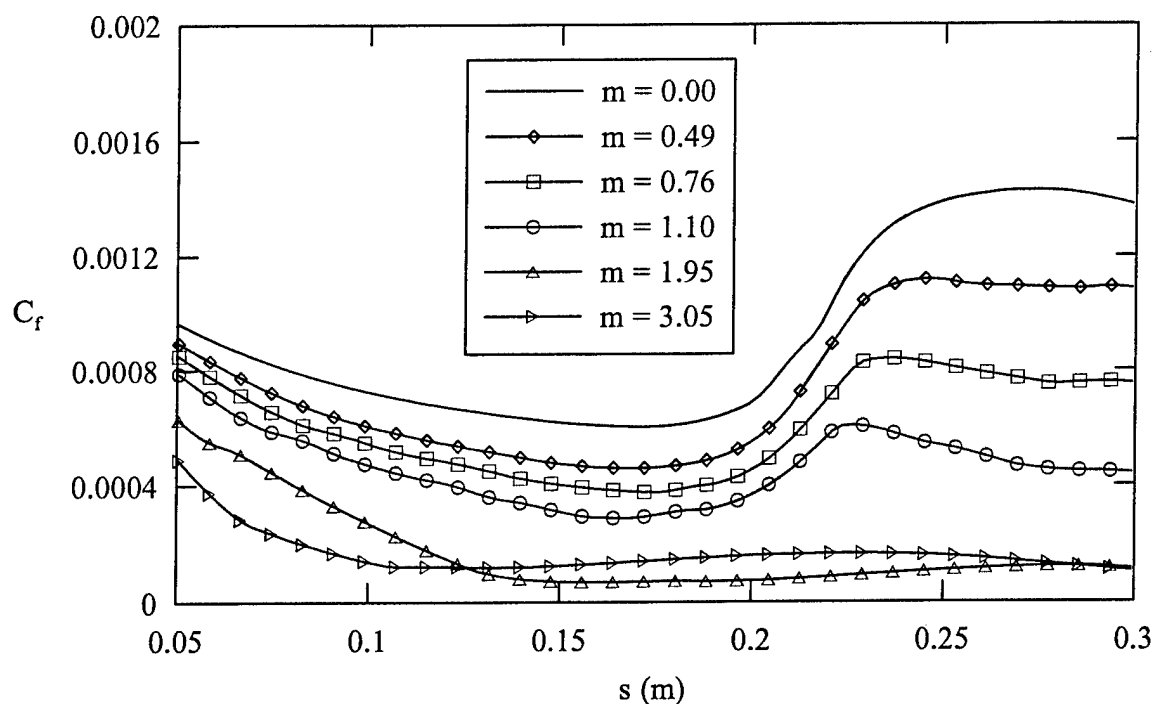
Figure 7-158. Skin friction coefficient (original Baldwin-Lomax model).
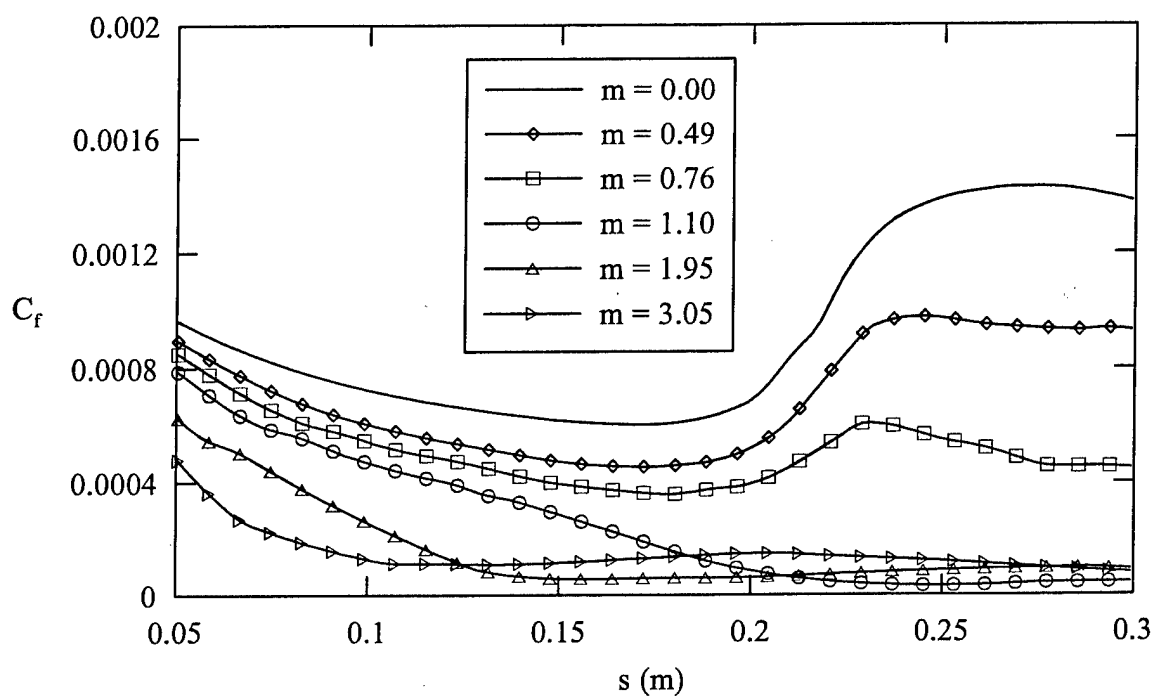
Figure 7-159. Skin friction coefficient (modified Baldwin-Lomax model).
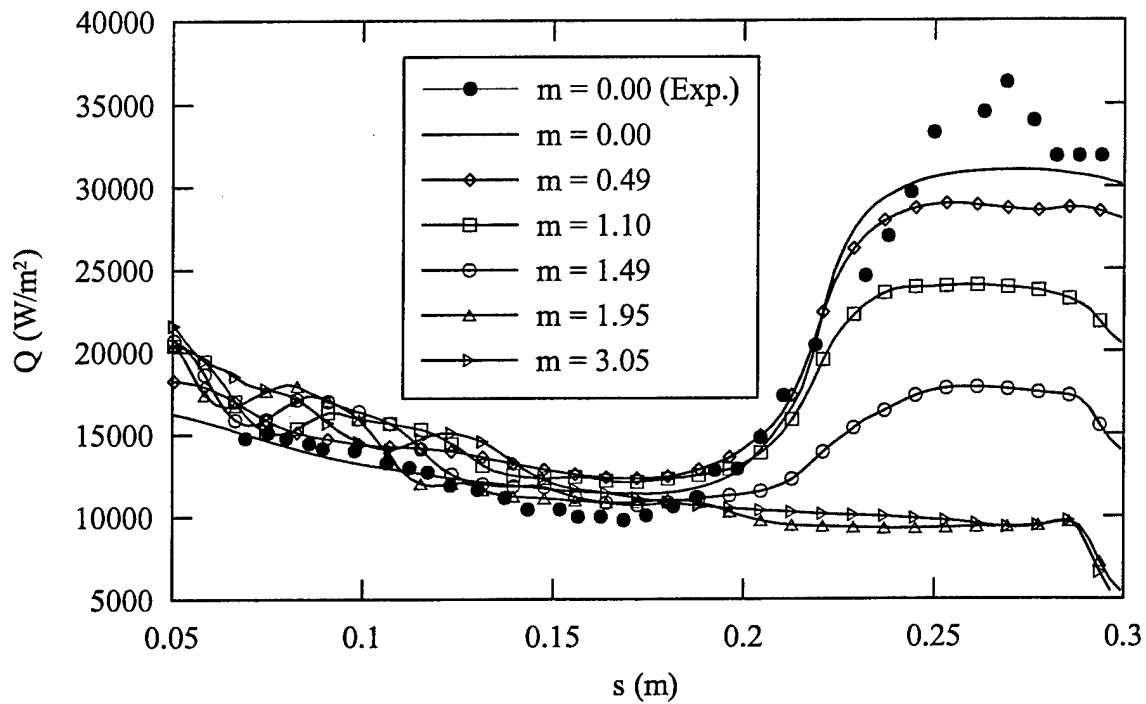
Figure 7-160. Heat rate transfer (original Baseline model).
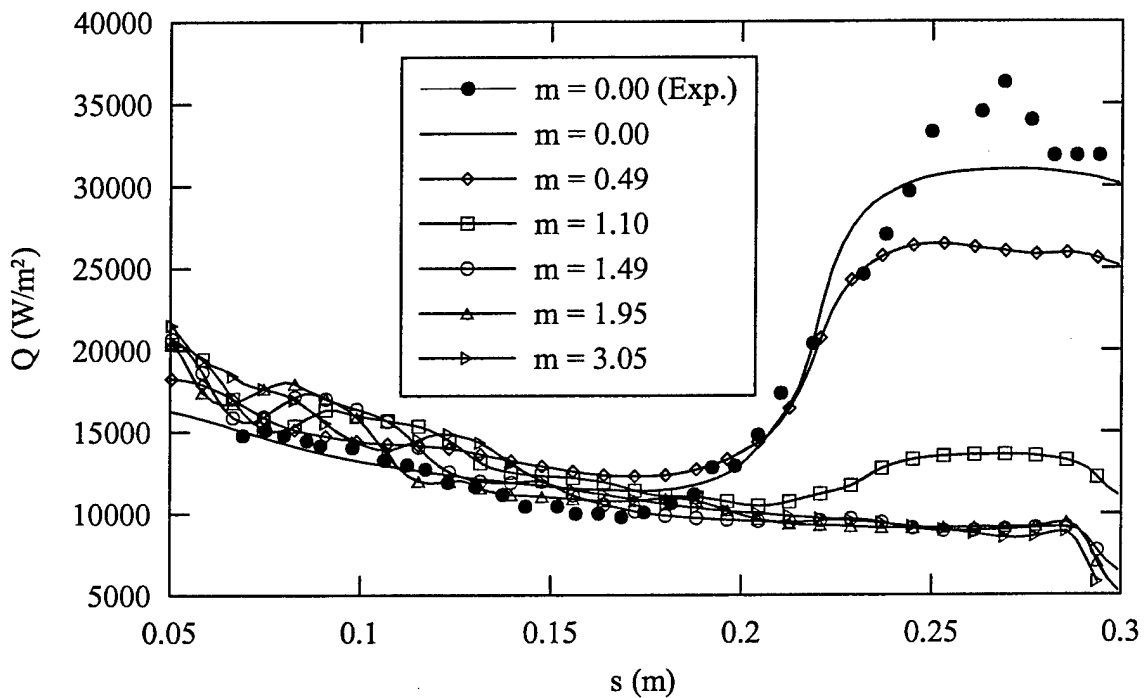
Figure 7-161. Heat rate transfer (modified Baseline model).

161
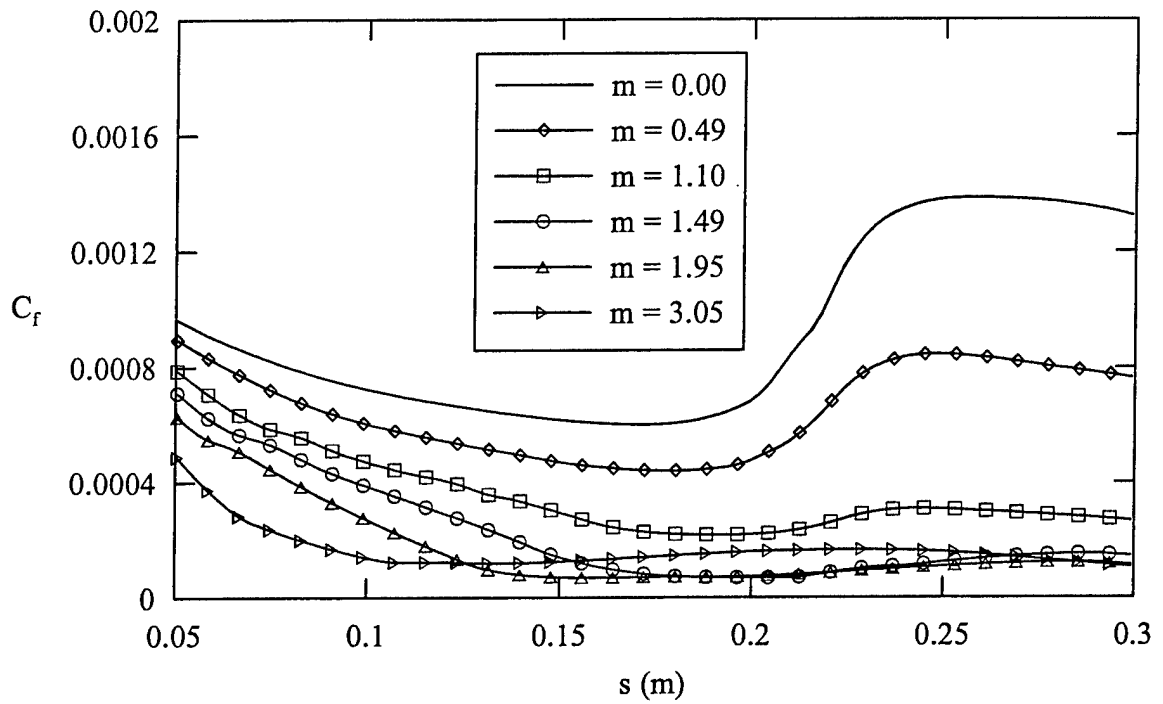
Figure 7-162. Skin friction coefficient (original Baseline model).
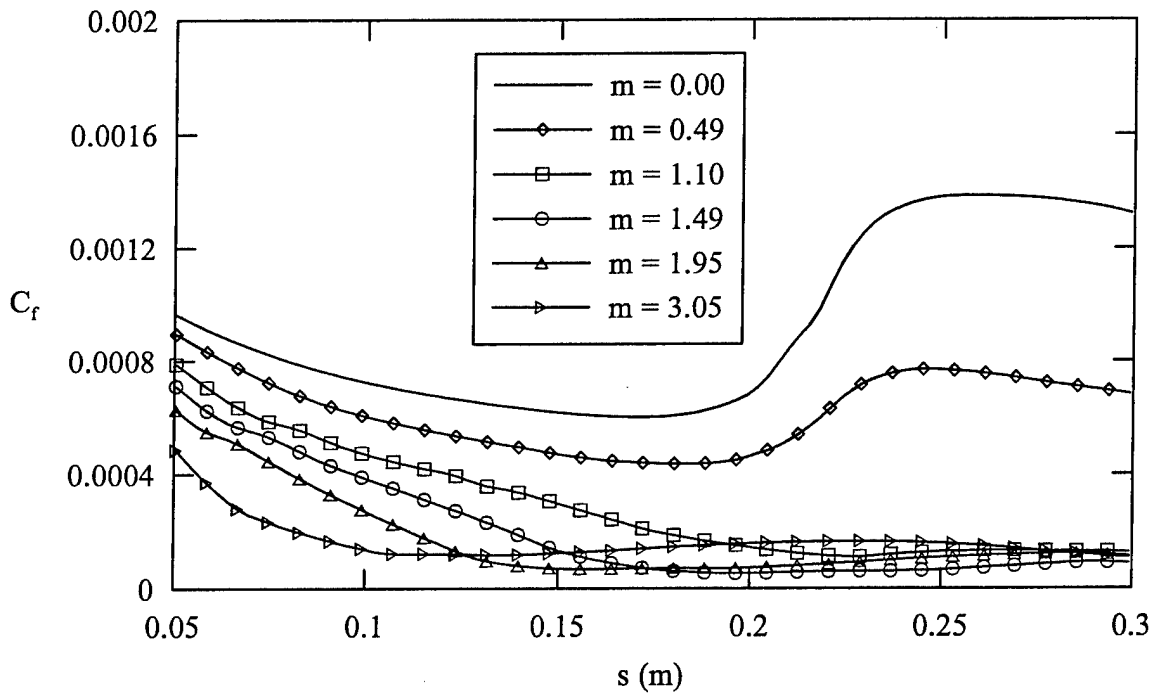
Figure 7-163. Skin friction coefficient (modified Baseline model).
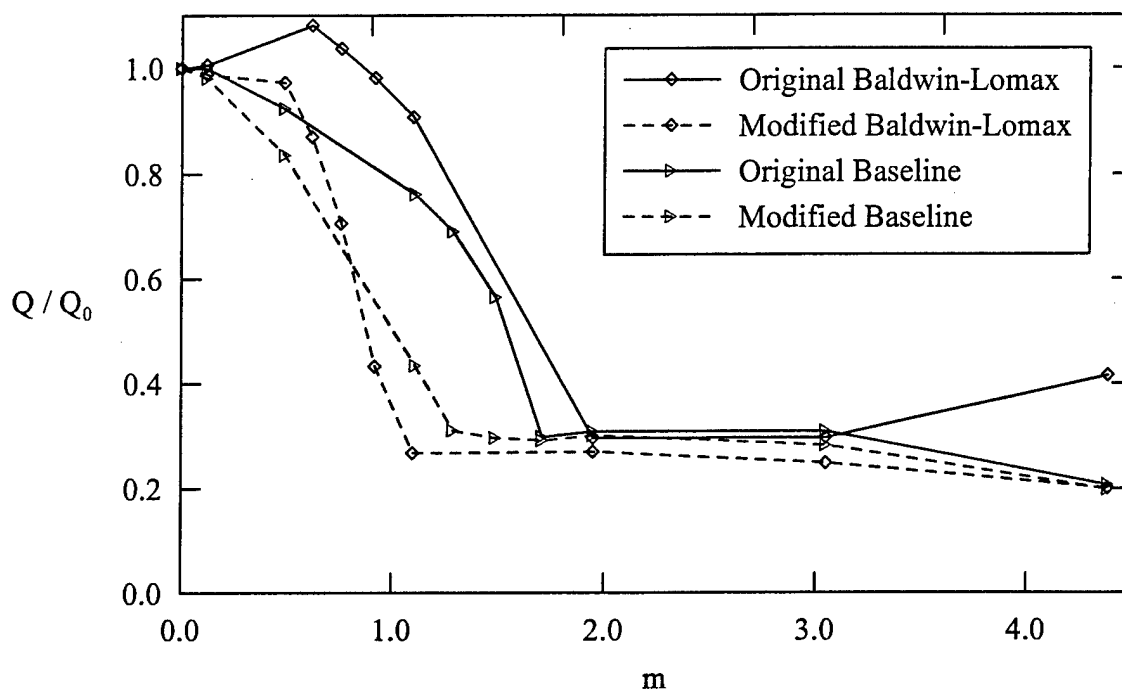
Figure 7-164. Heat rate transfer at $s = 0.28\,m$ versus m.
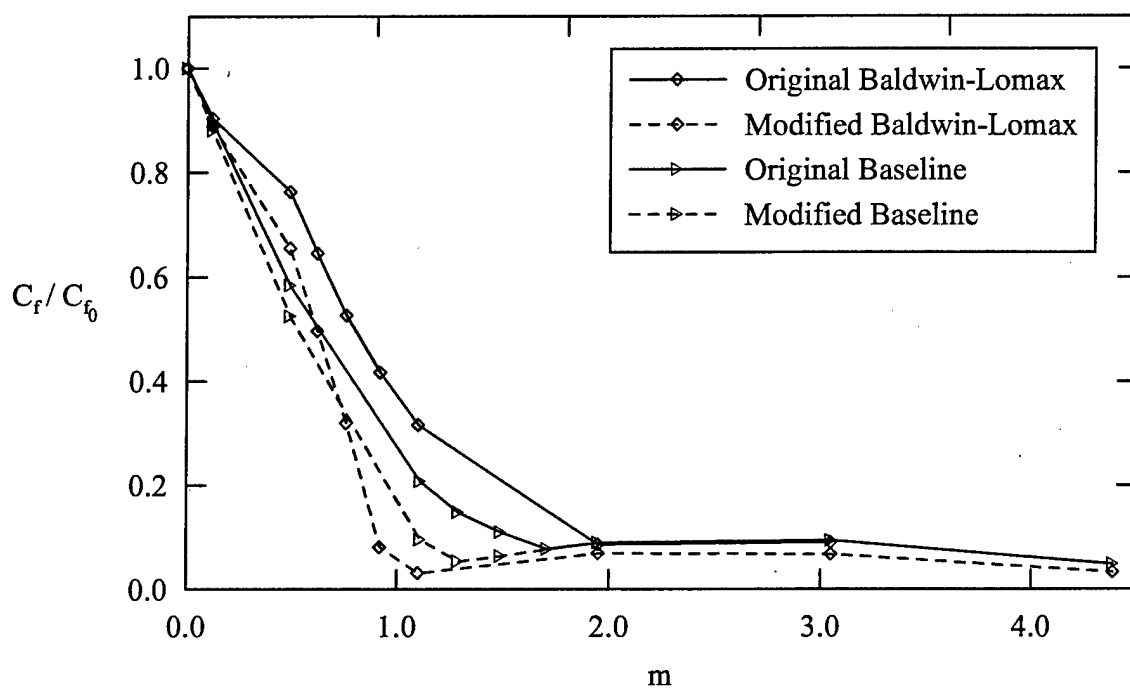
Figure 7-165. Skin friction coefficient at $s = 0.28\,m$ versus m.

163

7.6. Hypersonic Flow Over A Hemisphere In The Low Magnetic Reynolds Number Approximation

7.6.1. Chemically Frozen Flow

Blunt-body configurations generally represent the nose, wing leading edges or any other parts of hypersonic vehicles that are subject to the severe aerodynamic heating. Indeed, heating rates are inversely proportional to the radius of curvature. The blunt-body problem is characterized by a strong detached bow shock wave, which is practically normal near the stagnation streamline. In the postshock region, in particular at the stagnation point, the extreme temperature remains one major impediment to hypersonic flight. However, thermal ionization enhances the electrical conductivity of the gas in the shock layers, so that it is possible to consider magnetic control for this class of flows. Due to the low electrical conductivity of thermally-ionized air, the induced magnetic field is considered negligible and it is not computed. Thus, computations are performed in the so-called low magnetic Reynolds number approximation.

The present numerical simulations illustrate some features of MGD flows over a hemisphere. In an attempt to reproduce the results obtained analytically by Bush [77] and Coakley-Porter [118], the following assumptions are imposed. Air is a calorically perfect gas and the flow is laminar. The electrical conductivity is set to zero in the freestream and to a finite value in the shock layer (due to ionization). The magnetic field distribution, specified in the entire domain of computation and at the boundaries, corresponds to a dipole located at the center of the hemisphere. Freestream conditions are used at the inflow. A zero-order extrapolation scheme is utilized for all primitive variables at the outflow. At the solid surface, the slip velocity condition, zero normal gradient of the sum of static and magnetic pressures, and zero normal temperature gradient are enforced. For validation purposes, the similarity parameters are selected to mimic Poggie and Gaitonde's numerical simulations [119], as specified in Table 7-8. To achieve similarity, the applied magnetic field at the stagnation point is specified in Table 7-9 and the electrical conductivity is $\sigma_{e_{ref}} = 5.012 \times 10^2$ mho·m^{-1}. The computational mesh is depicted in Figure 7-166. Selected magnetic field lines of dipole are shown in Figure 7-167.

Freestream Mach number	$M_{ref} = M_\infty = 5$
Magnetic interaction parameter (varying parameter)	$Q_{ref} \in \{0, 1, 2, 3, 4, 5, 6\}$
Magnetic Reynolds number	$Re_{m_{ref}} = 0.01$
Altitude Freestream conditions	$h = 40$ km $p_\infty = 2.7752 \times 10^2$ Pa, $T_\infty = 251.05$ K
Body radius	$r_b = r_0 = 0.01$ m

Table 7-8. Solution parameters for the flow over the hemisphere.

Q_{ref}	0	1	2	3	4	5	6
B_0 [T]	0.000	1.105	1.562	1.913	2.209	4.470	2.706

Table 7-9. Strength of the applied dipole for the flow over the hemisphere.
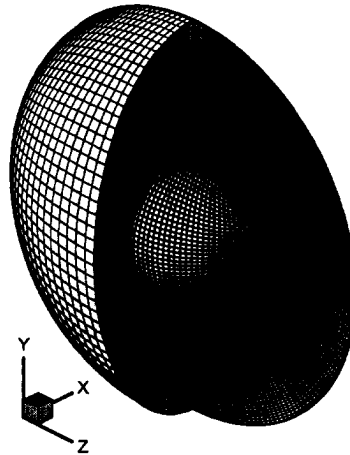
Figure 7-166. Mesh for the hemisphere consisting of 50×50×50 grid points (cutaway plot).
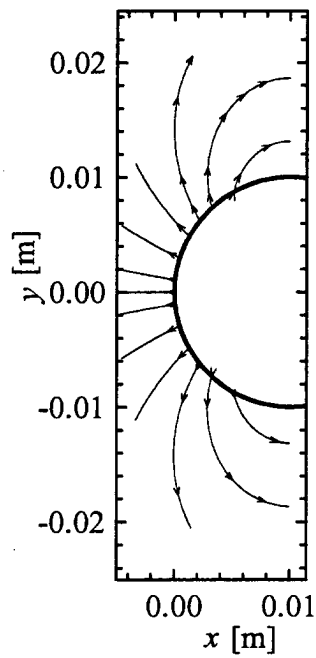
Figure 7-167. Imposed dipolar magnetic field on the hemisphere.
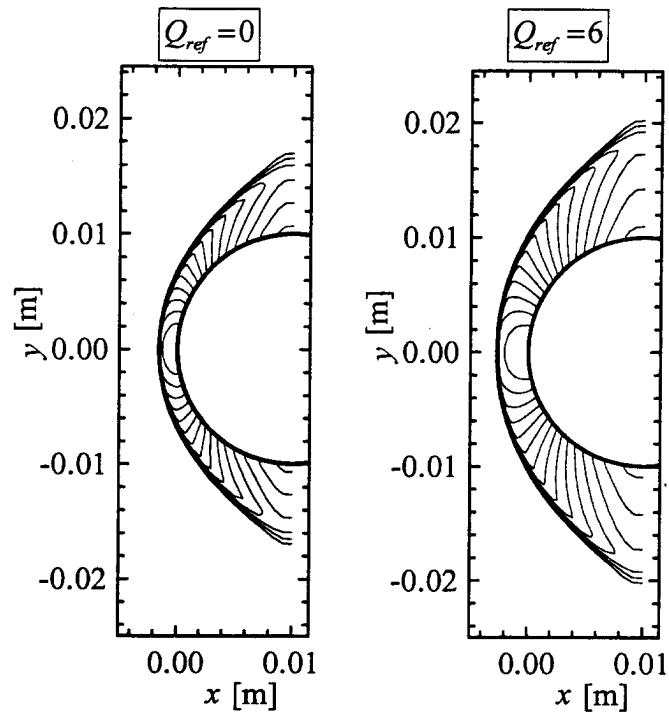
Figure 7-168. Effect of magnetic field on the pressure field over the hemisphere for $M_{ref}=5$, $Re_{m_{ref}}=0.01$, $\gamma=1.4$.

Figure 7-168 illustrates the pressure field for $Q_{ref}=0$ and $Q_{ref}=6$. The application of a strong magnetic field leads to a dramatic increase in the shock standoff distance. No obvious changes in the flow structure are observed. In an attempt to explain the observed phenomena, Figure 7-169, adapted from [118], is considered.
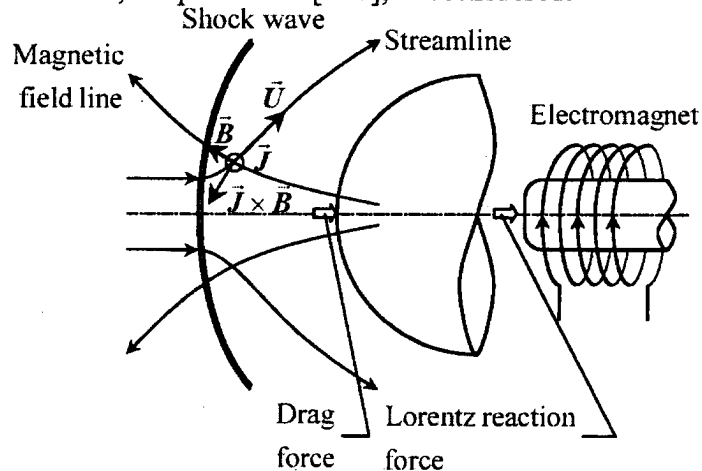
Figure 7-169. Effect of onboard magnetic source on the flow field over a blunt body.

Figure 7-169 illustrates the effect of a magnetic dipole on the bow shock wave that forms in front of the blunt body in hypersonic regime. As in the numerical simulations, the gas is assumed conductor only behind the shock wave due to ionization. An electrical current applied to a coil mounted at the center of curvature of the blunt body generates a dipolar magnetic field $\vec{B}$. The magnetic field interacts with the velocity field in the postshock region only (where the gas is conductor) and induces currents $\vec{J}$ that form loops in a plane normal to the dipole axis. This current interacts with the magnetic field to generate the magnetic force $\vec{f} = \vec{J} \times \vec{B}$. In the absence of electric field, $\vec{f}$ may be rewritten as $\vec{f} = \sigma_e \left(\vec{U} \times \vec{B} \right) \times \vec{B}$ (using Ohm's law). This mathematical expression indicates that $\vec{f}$ presents a component opposing the flow velocity $\vec{U}$, as illustrated in Figure 7-169. $\vec{f}$ tends to decelerate the flow in the postshock region. For conservation of the mass flow rate across the shock wave, an increase in the shock distance is required.

The reasoning above, based on local mathematical relations, provides some insight into the phenomena. However, it fails to justify the increase in the shock standoff distance measured along the stagnation streamline, where the magnetic field vector and velocity vector are collinear ($\vec{U} \times \vec{B} = \vec{0}$), and therefore the local magnetic force is $\vec{f} = \vec{0}$. It should be noted that the phenomena considered here are not local. Indeed, the flow behind the shock, in the vicinity of the stagnation streamline is subsonic and disturbances have a global impact. The flow variables such as density, pressure and temperature adjust to the electromagnetic forces in the entire region to yield the observed phenomena.

In the absence of electric field, the magnetic force leads to a reduction in the stagnation-point velocity gradient as depicted in Figure 7-170. The current numerical solution falls between the values predicted by Bush's theory and Poggie and Gaitonde's solution. However, an excellent agreement in the trend is obtained. For the nonmagnetic case, the stagnation-point velocity gradient predicted by the Newtonian impact theory is less than the other solutions. Figure 7-171 depicts the magnetic effect on the shock wave and the sonic line. It is observed that the region of subsonic flow is extended in the presence of magnetic field.

Figure 7-172 compares the shock standoff distance of the present simulation with results of other investigators, extracted from Reference [119]. An almost perfect match between the present computations and Poggie and Gaitonde's predictions is obtained.
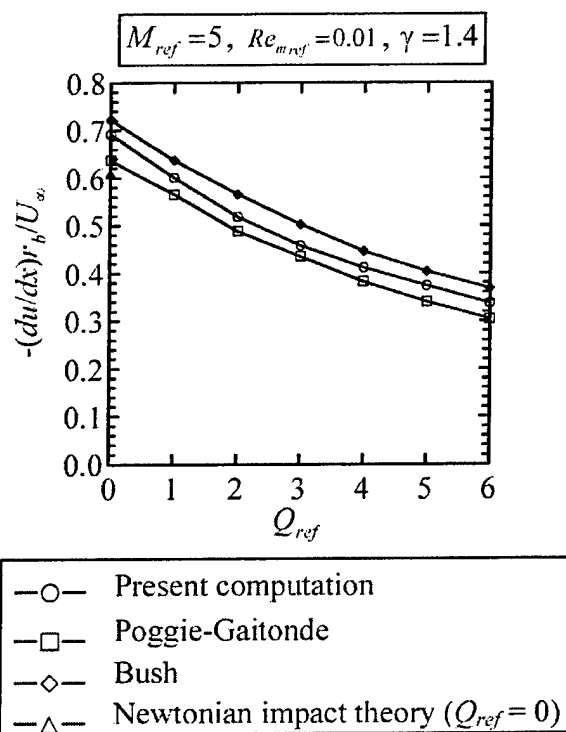
Figure 7-170. Effect of applied magnetic field on the stagnation-point velocity gradient.
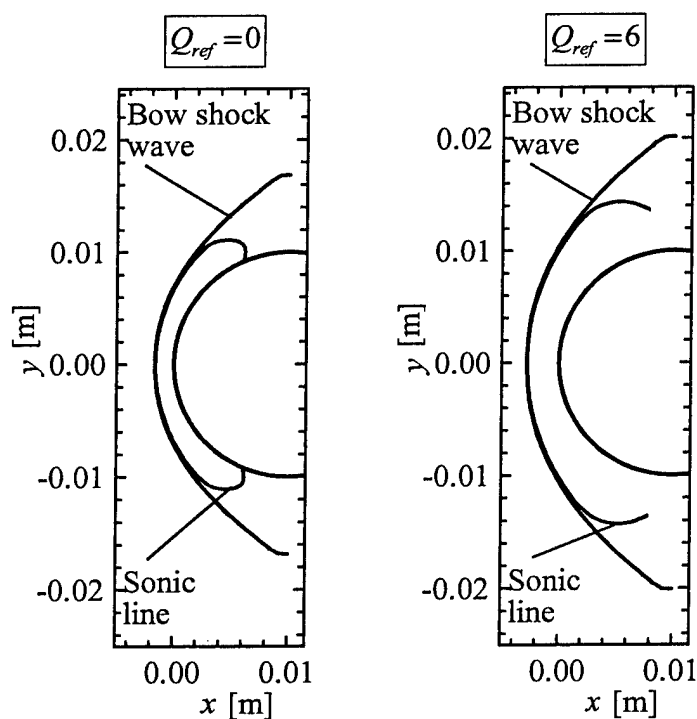
Figure 7-171. Effect of magnetic field on the shock wave and sonic line for inviscid flow over the hemisphere for $M_{ref}=5$, $Re_{mref} = 0.01$, $\gamma=1.4$.

168
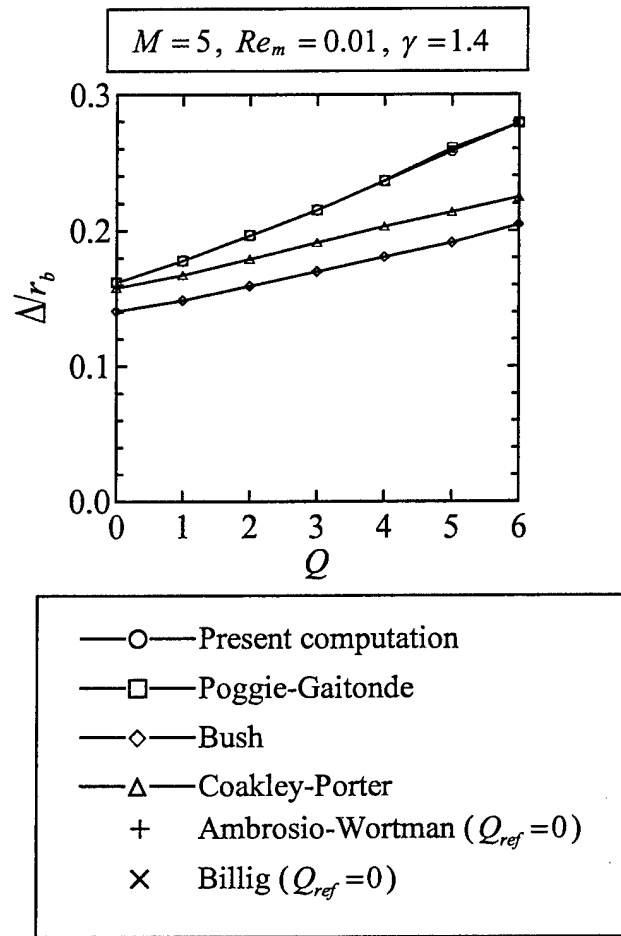
Figure 7-172. Effect of applied magnetic field on the shock standoff distance for $\gamma = 1.4$.

Both Bush's theory and Coakley and Porter's results underestimate the shock standoff distance, the predictions of the latter being however closer to the numerical values. As a reference, the empirical values (Ambrosio-Wortman and Billig) for the shock standoff distance in the absence of magnetic field are also provided and validate the present computations. The relative error between Bush's solution and the present numerical simulation increases from 13% for $Q_{ref} = 0$ up to 27% for $Q_{ref} = 6$. Poggie and Gaitonde [119] attribute the difference observed between the numerical simulations and Bush's solution to the constant-density theory on which the latter solution is based. In this theory, the hypersonic shock layer in the vicinity of the body nose is assumed incompressible, since the Mach number in this region is low. Such an approximation is not well justified and it is not implemented in the present numerical algorithm. Nevertheless, this theory leads to reasonable results in the case of large shock density ratios. The present computations were conducted for a density ratio of $\rho_2 / \rho_1 \approx 5$. Now, a ratio of specific heats of 1.2 (as in Reference [119]) is selected, which leads to a density ratio of $\rho_2 / \rho_1 \approx 7.9$. The shock standoff distance computed in this condition is presented in Figure 7-173. Again, the present numerical solution matches almost exactly Poggie

169

and Gaitonde's solution [119] and is also in relative agreement with Bush's theory (relative error between Bush's solution and present numerical simulation: 9% for $Q_{ref} = 0$ and 23% for $Q_{ref} = 6$).
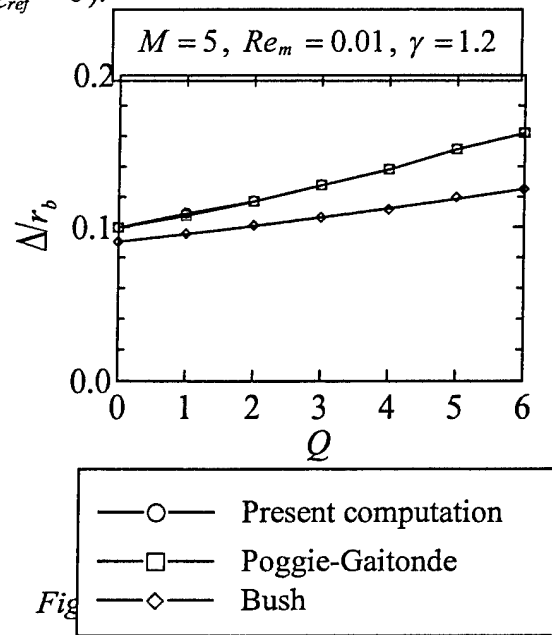
Figure 7-173. Effect of applied magnetic field on the shock standoff distance for $\gamma = 1.2$.

For the present freestream conditions, the chemically frozen flow model predicts stagnation temperature beyond 1,500 K. At this temperature, chemical reactions become considerable and thus need to be taken into account for accurate predictions, which is the object of the next section.

7.6.2. Chemical Equilibrium Flow

In this section, the flow over the hemisphere is computed at an altitude of 40 km, assuming chemical equilibrium, all the nondimensional similarity parameters being kept unchanged from the previous simulations. As shown in Figure 7-174, chemical equilibrium leads to a shock standoff distance less than that predicted in frozen flow.

$$M = 5, \ Re_m = 0.01, \ altitude \ 40 \ km$$
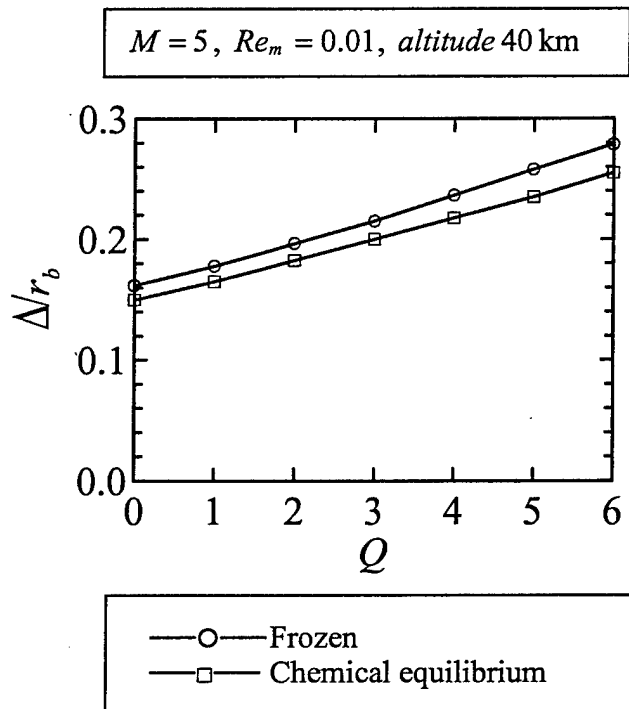
Figure 7-174. Effect of chemistry on the shock standoff distance.

Figure 7-175, illustrates the profiles of density, pressure and temperature (normalized by the freestream values) along the stagnation streamline. In the current simulation, the application of magnetic field at the body surface causes a significant increase in the shock standoff distance, but minor modifications in the flow variables. The Joule heating leads to a little peak in the temperature near the body surface, which in turn causes a trough in the density profile. On the other hand, the chemistry effect causes density to increase by about 7% and temperature to decrease by about 10%. No noticeable effect on pressure is observed.

$M = 5$, $Re_m = 0.01$, *altitude* 40 km
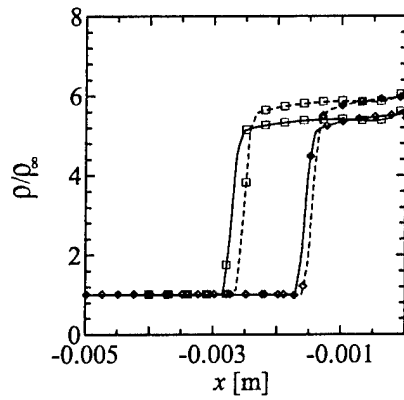
a) *Density*
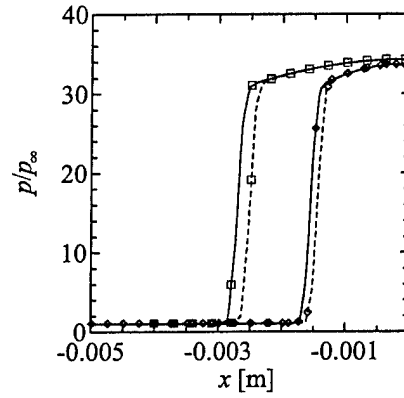
b) *Pressure*
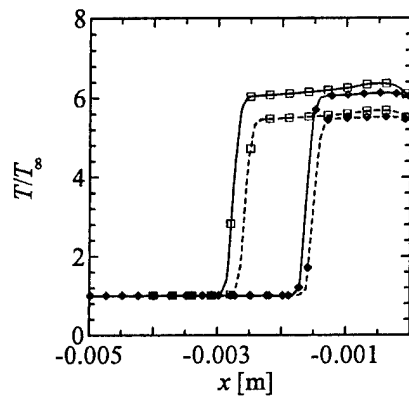
c) *Temperature*
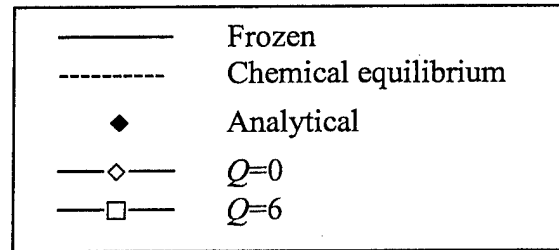
Figure 7-175. Profiles of the flow variables along the stagnation streamline of the hemisphere.

172

7.7. Hypersonic Flow Over A Cylinder

Numerical simulations of flow over a circular cylinder-wedge body are presented in this section. For the purpose of validation, the setup of the present problem is chosen to mimic Gaitonde and Poggie's simulations [91] to the best extent. A magnetic field aligned with the axis of the cylinder, which is coincident with z-axis, is imposed uniformly at the body surface and no electric field is applied. The freestream velocity vector points in the positive x-direction. Since the MGD flow field is expected to be symmetrical about the (x,z) plane, computations are performed in the half-plane $(x, y \geq 0)$ for efficiency purposes. Figure 7-176 illustrates the mesh consisting of 100×100×3 grid points.
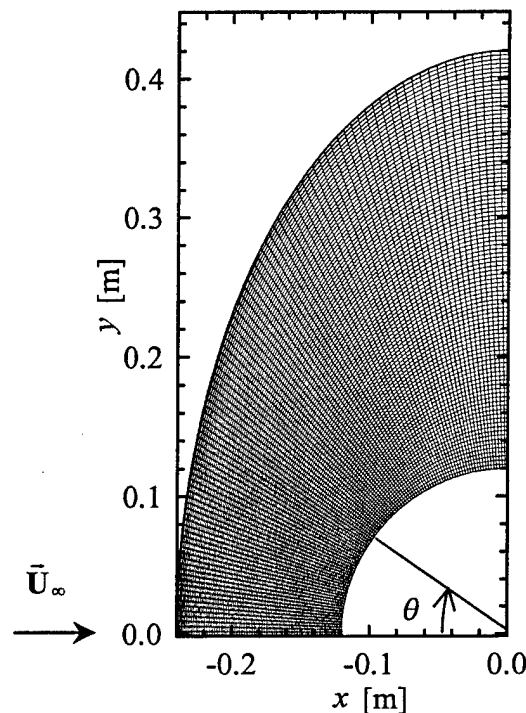
Figure 7-176. Mesh for the cylinder consisting of 100×100×3 grid points.

For symmetry about the x-axis, reflexive boundary conditions along the $i = 1$ line (which is just below the x-axis) are specified. Freestream conditions and zero magnetic field are specified at the inflow. Zero-order extrapolation for all primitive variables is used for the outflow. At the solid surface, the slip velocity condition, zero normal gradient of the sum of static and magnetic pressures, zero normal temperature gradient, and uniform value of magnetic field are specified. Solution parameters for this series of simulations are provided in Table 7-10.

Altitude Freestream conditions	$h = 40 \, \text{km}$ $p_\infty = 2.7752 \times 10^2 \, \text{Pa}$, $T_\infty = 251.05 \, \text{K}$
Freestream Mach number	$M_{ref} = M_\infty = 16$
Magnetic pressure number (varying parameter)	$R_{b_{ref}} \in \{0; \, 0.1; \, 0.5\}$
Magnetic Reynolds number (varying parameter)	$Re_{m_{ref}} \in \{6.25; 12.5; \, +\infty\}$

Table 7-10. Solution parameters for the flow over the cylinder.

7.7.1. Effect Of Magnetic Pressure Number
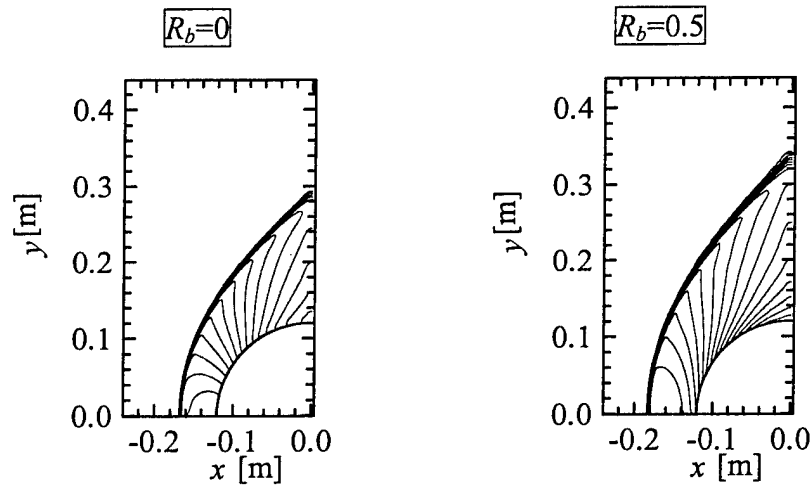
Figure 7-177. Effect of magnetic field on the flow over the cylinder – Pressure contours for $M_{ref} = 16$, $Re_{m_{ref}} = 12.5$.

In this section, the effect of the magnetic pressure number $R_{b_{ref}}$ is numerically investigated. In order to isolate the effect of this parameter, the magnetic Reynolds number is fixed at 12.5. The pressure field in the presence and absence of magnetic field is depicted in Figure 7-177. No fundamental changes in the flow structure are observed. As expected, the shock wave moves upstream with application of magnetic field. For the magnetic case, the inclined contours lines at the body surface suggest that the normal gradient of static pressure is not zero, as it is for the nonmagnetic case. The profiles of static pressure along the stagnation streamline presented in Figure 7-178a confirm that the normal static pressure gradient is indeed not zero if a magnetic field is applied at the wall. It is also observed that surface pressure decreases with increasing magnetic field. Comparison of the present simulation with solution reported in Reference [91] shows good agreement. Due to the use of a relatively fine mesh, the present simulation yields a superior resolution of the shock wave. For the case $R_{b_{ref}} = 1.0$, the magnetic field is

174

attenuated at the shoulder to prevent the occurrence of negative static pressure. In the current investigation, the applied magnetic field at the surface is decreased linearly to zero in the streamwise direction from $\theta = 63.5$ degrees to $\theta = 90$ degrees, which may differ from the attenuation used in Reference [91]. This would explain the discrepancy in the shock standoff distance. However, pressure compares well. As a reference, Billig's correlation [120] for the shock standoff distance in the absence of magnetic field is also provided, which shows excellent agreement with the numerical simulations. Figure 7-178b depicts the variation of temperature along the stagnation streamline. The magnetic field, imposed at the body surface, tends to reduce the surface temperature, although a rise in temperature occurs in a region near the body surface. This temperature "hill" is attributed to the Joulean dissipation. In the present case, the magnetic field is predominant in the vicinity of the body, thus, so is the Joule heating. For comparison purpose, the temperature profile without Joule heating is also provided for the case $R_{b_{ref}} = 0.5$. When Joule heating is omitted, no peak in temperature is observed. It is also observed that the shock standoff is dramatically reduced.
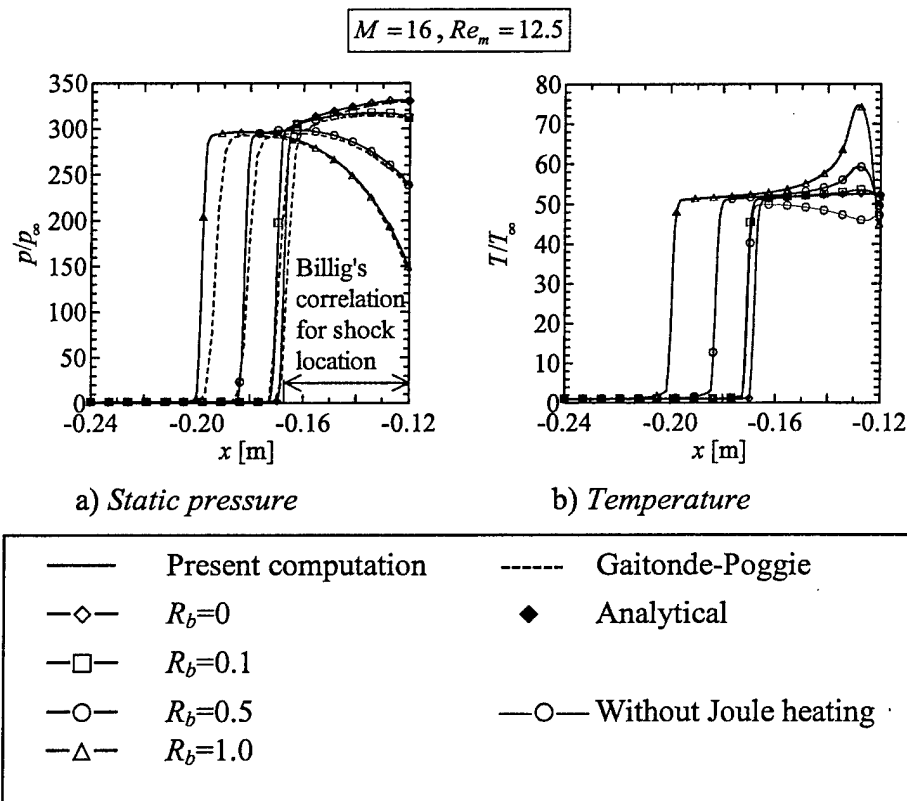
Figure 7-178. Effect of magnetic field on the flow over the cylinder – Profiles of static pressure and temperature along the stagnation streamline.

Figure 7-179 depicts the variation of total pressure along the stagnation streamline. The total pressure is defined as the sum of the static, dynamic and magnetic pressures. The present results compare well with those reported in Reference [91]. Although static pressure decreases with magnetic field, no clear effect on the total

pressure is observed. This suggests no reduction in wave drag. In other words, the reduction in the aerodynamic drag force due to the magnetic interaction is balanced by the Lorentz reaction force.

$$M = 16, Re_m = 12.5$$
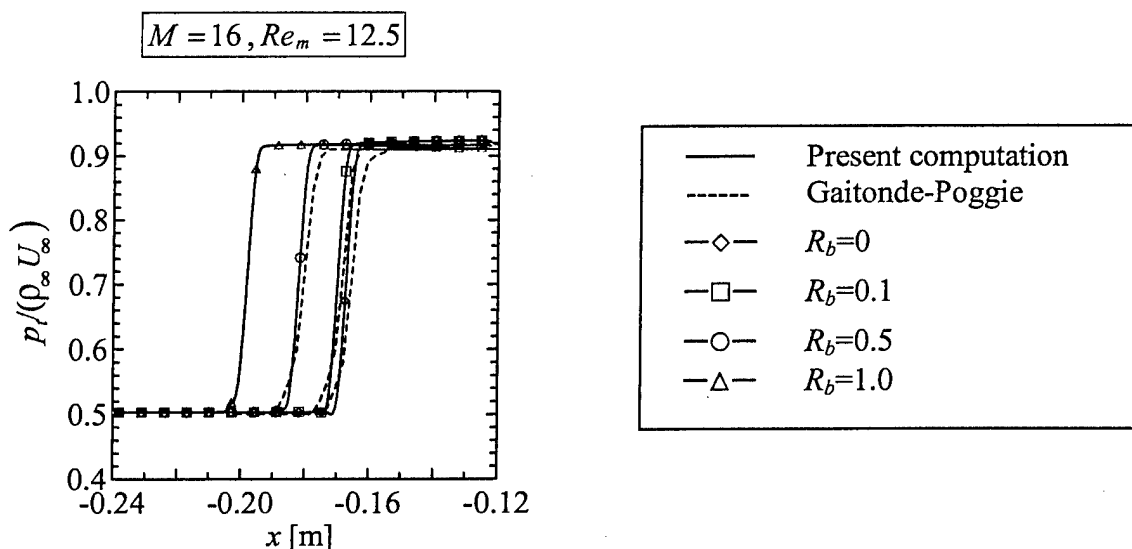
Figure 7-179. Effect of magnetic field on the flow over the cylinder – Profiles of total pressure along the stagnation streamline.

7.7.2. Effect Of Magnetic Reynolds Number

The effect of magnetic diffusion is examined in this section. The relevant parameter is the magnetic Reynolds number $Re_{m_{ref}}$, which determines the diffusion of the magnetic field along the streamlines. To isolate the effect of this parameter, the magnetic pressure number is nominally set to 0.5. Values of $Re_{m_{ref}}$ are varied via the electrical conductivity. It should be noted that this series of experiments is conducted with the full MGD equations, which prohibits the use of zero or very small values of $Re_{m_{ref}}$. For a magnetic Reynolds number equal to zero i.e., for a perfectly electrical insulator fluid, no magnetic interaction is expected. Figure 7-180 illustrates the effect of the magnetic Reynolds number on the pressure field and the magnetic field. An interesting aspect is that the shock standoff distance is greatly affected by the magnetic Reynolds number: the higher the magnetic Reynolds number is, the closer the shock wave to the body. Figure 7-180b provides some clues to better understand this phenomenon. As the magnetic Reynolds number (or electrical conductivity) is increased, the magnetic field permeates the fluid less and less freely. Eventually, for the ideal case of perfectly conducting fluid i.e., for $Re_{m_{ref}} \sim +\infty$, the magnetic field is rigidly coupled with the flow field and is convected by fluid particles. It does not diffuse at all. The rate of diffusion of the magnetic field is negligible compared to the rate of transport of the magnetic field.

176
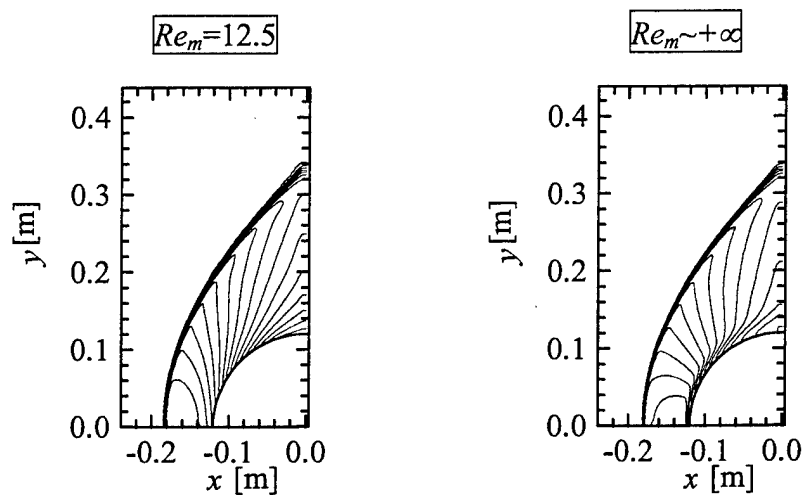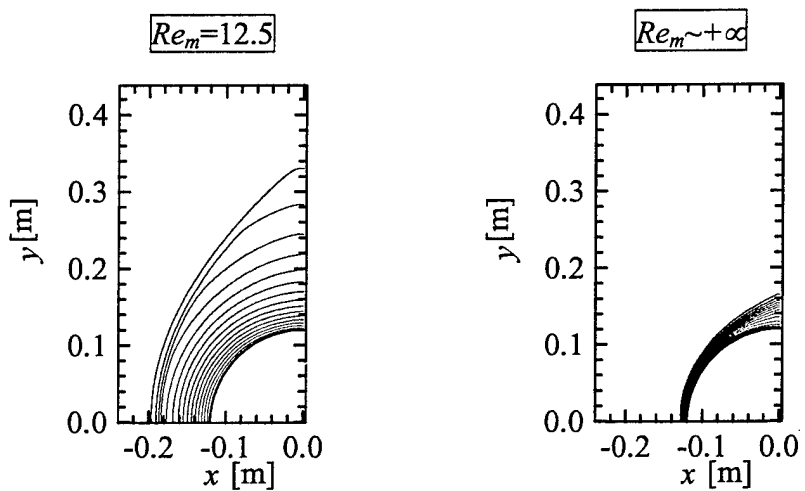
a) *Pressure.*

b) *Axial magnetic field.*

Figure 7-180. Effect of magnetic Reynolds number on the flow over the cylinder –
Pressure and magnetic field contours for $M_{ref} = 16$, $R_{bref} = 0.5$.

$$\boxed{M = 16, \quad R_b = 0.5}$$

a) *Static pressure*

b) *Temperature*

——	Present computation
—◇—	non-magnetic
◆	Analytical
—□—	$Re_m = 6.25$
—O—	$Re_m = 12.50$
—△—	$Re_m \sim +\infty$

c) *Axial magnetic field*
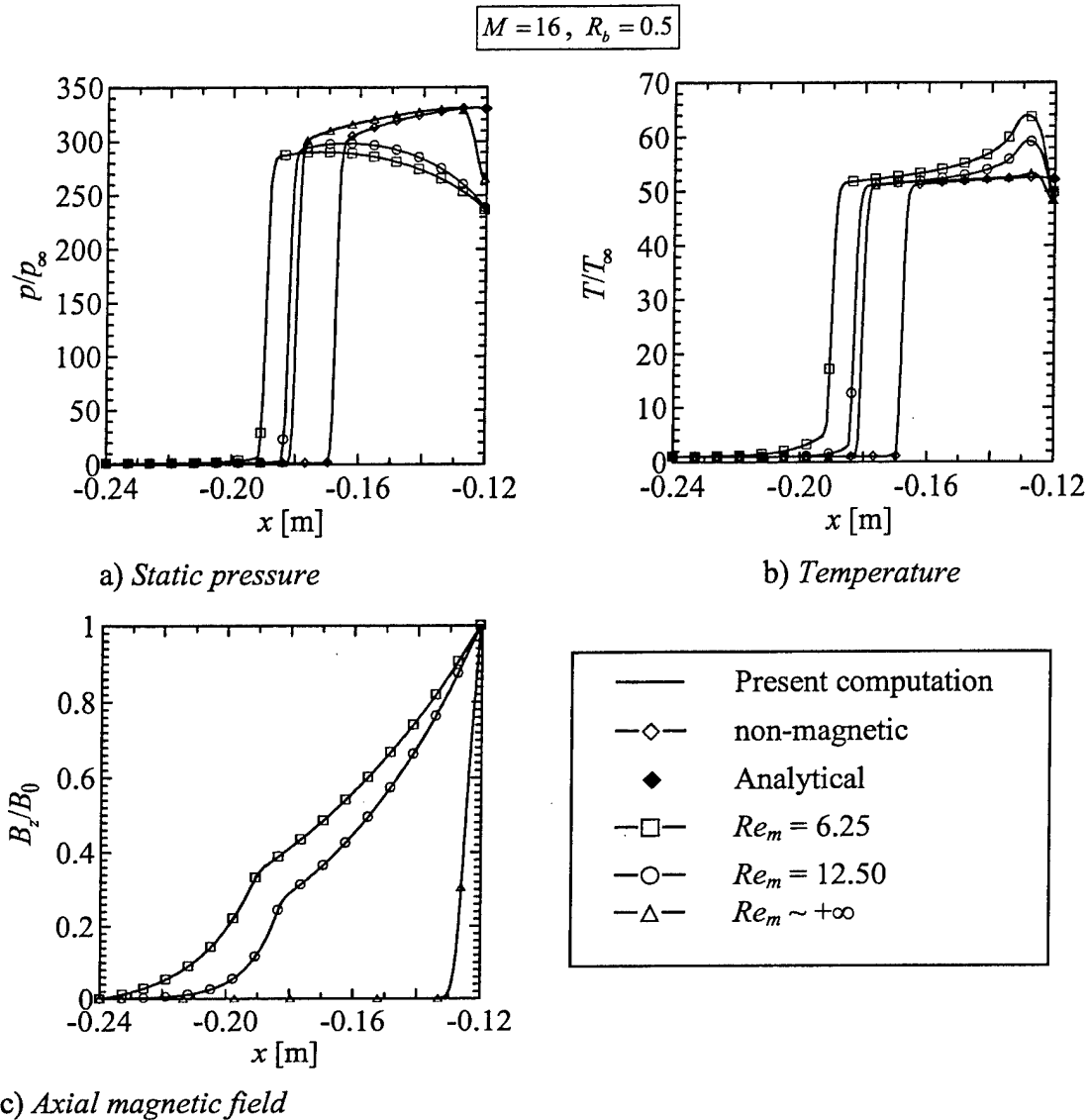
Figure 7-181. Effect of magnetic Reynolds number on the flow over the cylinder –
Profiles of static pressure, temperature, and axial magnetic field along the
stagnation streamline.

The variation of selected flow variables along the stagnation streamline is
presented in Figure 7-181. For finite non-zero magnetic Reynolds number, the flow
undergoes a smooth expansion in the postshock region. In contrast, for infinite magnetic
Reynolds number, a relatively sharp expansion is observed near the body surface.
Temperature, via the Joule heating is also greatly affected. The higher the magnetic
Reynolds number is, the lower the peak in temperature near the body surface. For infinite
magnetic Reynolds number, the magnetic field is confined at the body surface where its
interaction with the fluid is maximal.

7.8. Hypersonic Chemistry For Flow Over A Cylinder

Series of numerical experiments are conducted to explore the effect of altitude and Mach number on hypersonic chemistry for the flow over a circular cylinder. To reduce computation time, the 2-D version of the algorithm is selected, since the flow is 2-D. For these simulations, the mesh consists of 60×80 grid points, as presented in Figure 7-182. The magnetic field applied at the body surface follows the equation $B_z = B_0 \cos\theta$ where θ denotes the angle between the x-axis and a point on the body surface, and B_0 represents magnetic field strength at the stagnation point. For initialization of nonequilibrium simulations, frozen flow computations are performed until a transient detached shock wave forms in front of the body. Subsequently, the nonequilibrium model is switched on. Non-dissociated air (23.5% of O_2 and 76.5% of N_2) is considered for the specification of initial mass fractions.
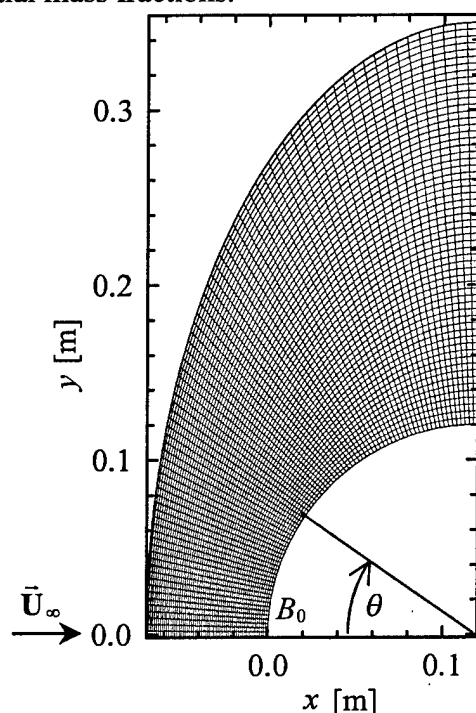
Figure 7-182. Mesh for simulation of hypersonic chemistry over the cylinder, consisting of 60×80 grid points.

7.8.1. Effect Of Altitude

The effect of altitude on the flow structure and chemical composition is investigated. Numerical computations are performed for altitudes ranging from 30 km to 70 km. Changes in altitude are simulated by changes in the flow properties (pressure, density, temperature, etc.), according to the US Standard Atmosphere model [121], as illustrated in Figure 7-183.
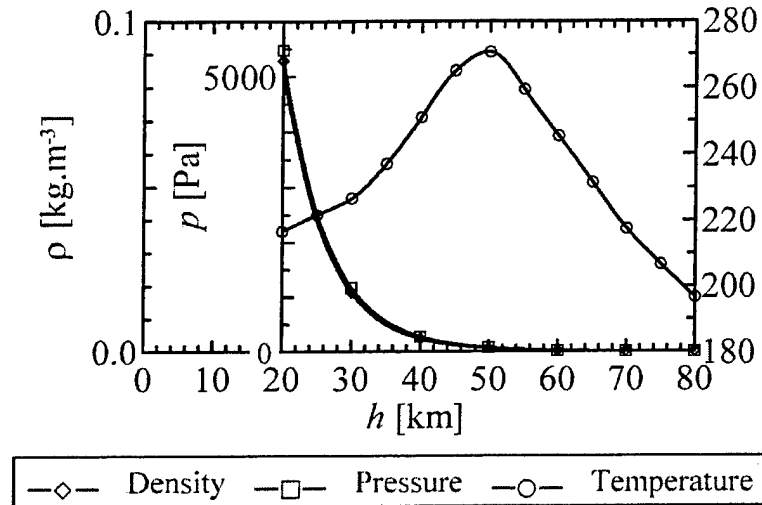
Figure 7-183. US Standard Atmosphere model.

Simulations parameters are specified in Table 7-11. Similarity in terms of Mach number, magnetic pressure number and magnetic Reynolds number for various altitudes is achieved for the dimensional conditions shown in Table 7-12.

Altitude (varying parameter)	$h \in \{30, \quad 50, \quad 70 \quad \text{km}\}$
Freestream Mach number	$M_{ref} = M_\infty = 14$
Magnetic pressure number	$R_{b_{ref}} \in \{0, \quad 0.5\}$
Magnetic Reynolds number	$Re_{m_{ref}} = 12.5$

Table 7-11. Solution parameters for simulation of altitude effect, for the flow over the cylinder.

h [km]	30	50	70
$U_{ref} = U_\infty$ [m·s^{-1}]	3017.414	3297.379	2955.526
B_0 [T]	4.495×10^{-1}	1.144×10^{-1}	2.827×10^{-2}
$\sigma_{e_{ref}}$ [mho·m^{-1}]	1.962×10^4	1.796×10^4	2.003×10^4

Table 7-12. Dimensional conditions for similarity at various altitudes, for the flow over the cylinder.

As observed in Figure 7-183, atmospheric temperature versus altitude presents a maximum at about 50 km. The speed of sound (proportional to the square root of temperature) follows the same trend. Thus, similarity in terms of Mach number is achieved for a freestream velocity proportional to the speed of sound (with a maximum at 50 km). Now, similarity in terms of magnetic Reynolds number requires the electrical conductivity to be inversely proportional to the freestream velocity (with a minimum at

180

50 km). Finally, at constant magnetic pressure number, the applied magnetic pressure is proportional to the dynamic pressure. It can be shown that the freestream dynamic pressure decreases with altitude because air density decreases. As a consequence, the applied magnetic field B_0 is reduced with altitude.

- **Chemically frozen flow model**

Figure 7-184 presents profiles of selected flow variables along the stagnation streamline, at various altitudes, for chemically frozen flow. The perfect overlap of the profiles indicates that similarity has been achieved for each altitude, as expected. Solutions with and without magnetic interaction distinguish by several features. The application of magnetic field leads to an increase in the shock standoff distance and a reduction in the postshock and surface static pressure. Moreover, due to the Joulean dissipation, temperature rises in a postshock region, slightly upstream of the body.

a) Density

b) Pressure

c) Temperature
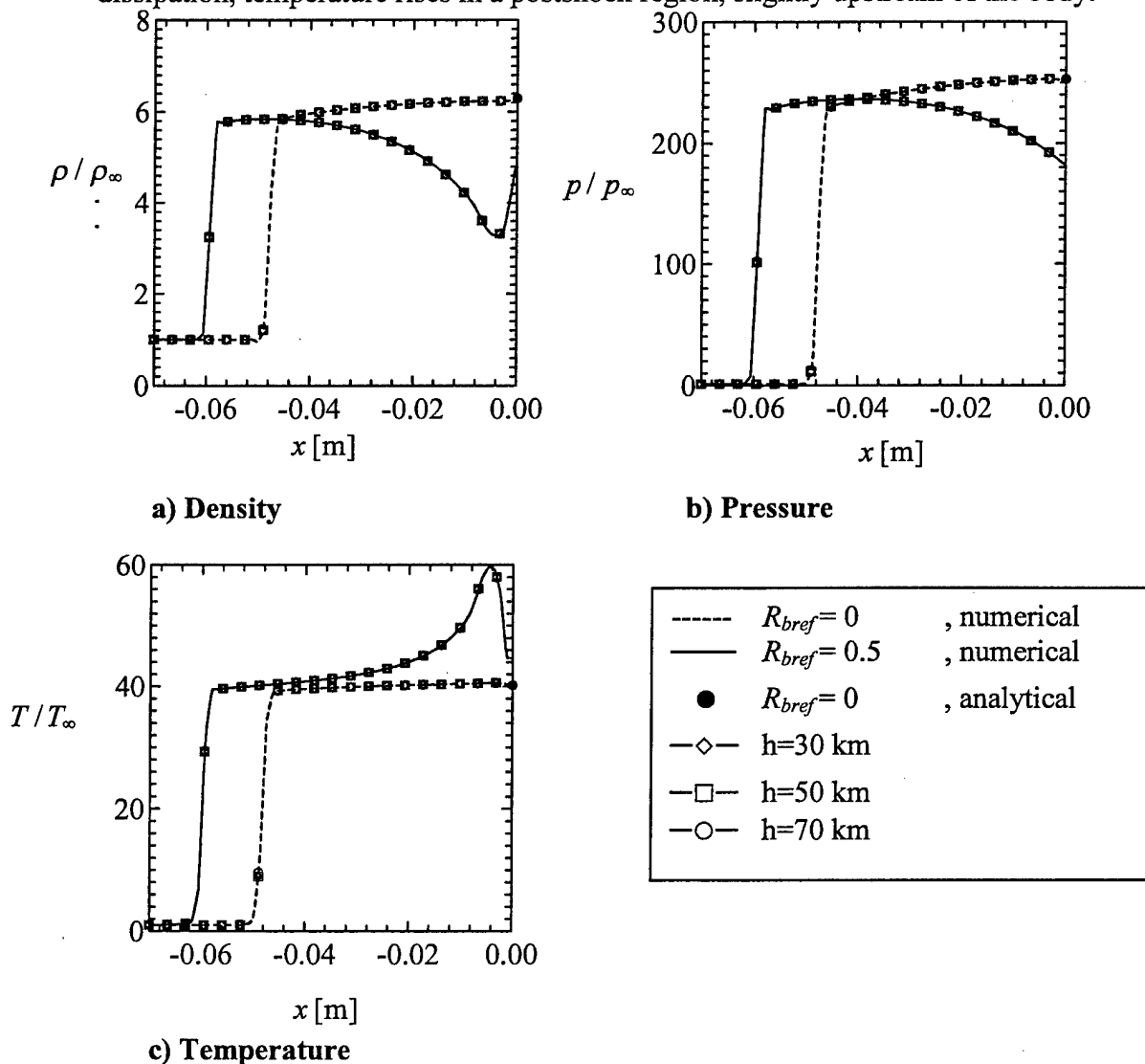
Figure 7-184. Effect of altitude on the flow over the cylinder – Flow variables along the stagnation streamline in chemically frozen state.

181

A corresponding decrease in density results so as to satisfy the equation of state. Analytical values at the stagnation point (in the absence of magnetic field) are also provided, which show an excellent agreement with the numerical simulations.
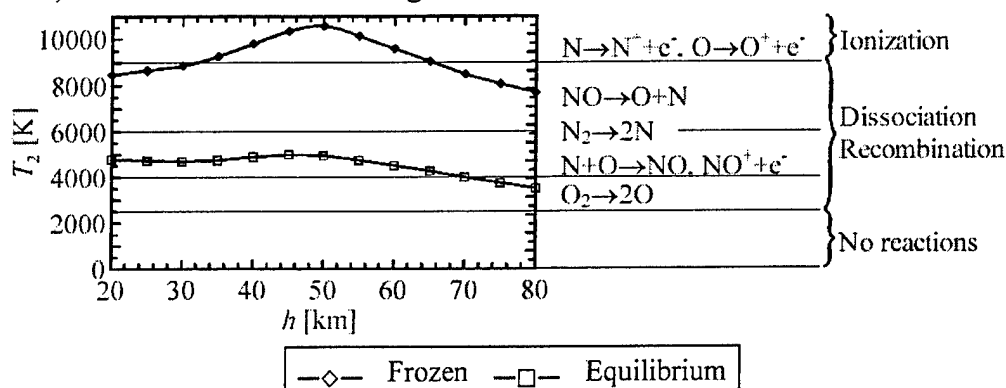
Figure 7-185. Temperature behind a normal shock at Mach 14.

Frozen flow simulations lead to unrealistic postshock temperatures. Figure 7-185 depicts the variation of the postshock temperature with altitude. Postshock temperature evaluated using normal shock relations for frozen flow at Mach 14, exhibits values above 7,000 K for all the altitudes considered, with a maximum reached at an altitude of 50 km. In reality, in the hypersonic high-temperature environment, air undergoes vibrational excitation, dissociation and ionization. These endothermic phenomena absorb energy and cause temperature to fall. Indeed, Figure 7-185 shows that the postshock temperatures, computed using GASEQ, program based on a NASA algorithm for equilibrium air [122], are about half of the frozen flow values. In the range 20-50 km, equilibrium postshock temperature varies very gradually and remains relatively high. Chemical reaction rates, which are exponential functions of temperature are expected to be relatively large. Moreover, in this "low" altitude range, air density is high enough so that the number of molecular collisions is sufficient for the flow to reach thermodynamic equilibrium in the postshock region. In contrast, at higher altitudes, postshock temperature decreases significantly with altitude and air density is also lower. Few molecular collisions take place, thus leading to a nonequilibrium state. The chemical equilibrium model is not expected to be accurate in these conditions.

- **Chemical equilibrium model**

Contrasting with the frozen flow case, the chemical equilibrium model does not preserve similarity with changing altitude, as shown in Figure 7-186. Indeed, one of the nondimensional parameters, namely the ratio of specific heats computed by the equilibrium model varies with the freestream conditions, as depicted in Figure 7-186d. In the preshock region, its value equals the frozen flow value. Indeed, the freestream temperature is too low to initiate chemical reactions. On the other hand, in the postshock region and especially along the stagnation streamline, high temperature and density enhance chemical reactions. Due to the change in the gas chemical composition, thermodynamic properties are modified. In the present case, γ undergoes a dramatic decrease across the shock wave from 1.4 to about 1.2. Chemical phenomena change

182

compressibility, cause temperature to fall, density to increase and lead to a reduction in the shock standoff distance. The effect of chemistry on the postshock pressure is minimal. As a measure of validation of the present effort, density, pressure and temperature right behind the shock wave are compared with the equilibrium values predicted by the program GASEQ (in the absence of magnetic field, behind a normal shock). A good agreement is obtained.

The presence of a magnetic field has an impact on the chemical phenomena, via the Joule heating. In the current simulation, the dissipated magnetic energy causes the temperature to increase in the region surrounding the stagnation point where the magnetic field is the strongest. It should also be noted that temperature is affected by the Joule heating not only in the postshock region, with a peak in the vicinity of the body surface, but also. in the preshock region with values larger than those of the freestream. In the absence of magnetic field, all the flow variables undergo a jump across the shock wave. The flow undergoes a gradual increase in the preshock temperature, as shown in Figure 7-186c. In frozen flow, the shock standoff distance is larger than in equilibrium and the preshock magnetic field is weaker. Therefore, the Joule effect on the preshock temperature is not as noticeable.

a) Density　　　　　　　　　　　　　　b) Pressure

c) Temperature　　　　　　　　　d) Ratio of specific heats

-------	$R_{bref}=0$
———	$R_{bref}=0.5$
Markers ◆■●	$R_{bref}=0$, GASEQ
—◇—	h=30 km
—□—	h=50 km
—○—	h=70 km
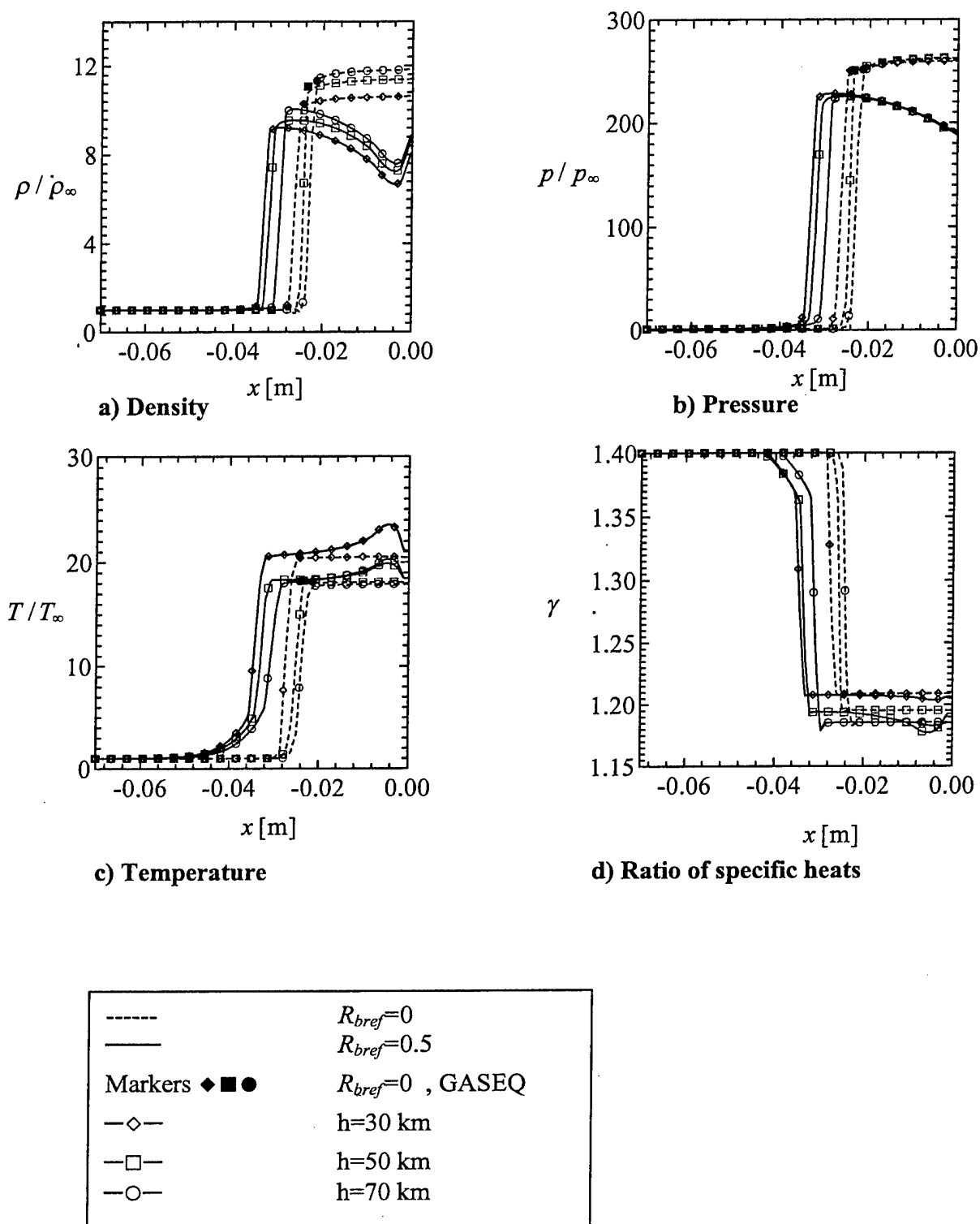
Figure 7-186. Effect of altitude on the flow over the cylinder – Flow variables along the stagnation streamline in chemical equilibrium.

In the presence of magnetic field, the ratio of specific heats follows a trend somewhat inverse to that of the temperature. From the freestream to the body surface, the ratio of specific heats increases gradually in the preshock region, undergoes a jump across the shock wave, and exhibits an undershoot in the vicinity of the body.

- **Chemical nonequilibrium model**

Figure 7-187 depicts the variation of flow properties in chemical nonequilibrium for various altitudes. As altitude increases, air becomes less dense, the number of molecular collisions decreases and thus vibrational and chemical processes slow down. Therefore, nonequilibrium phenomena gain in importance with altitude. Roughly speaking, at low altitudes (say below 50 km), near chemical equilibrium exists. At higher altitudes, nonequilibrium phenomena dominate the flow field and approach chemically frozen state with increasing altitude. As expected, nonequilibrium simulations predict an increase in the shock standoff distance with altitude, which is opposite to the equilibrium predictions. Equilibrium and nonequilibrium solutions present other differences. For instance, in Figure 7-187c, the peak in the temperature right behind the shock wave, which becomes more pronounced as altitude is increased, reveals regions of nonequilibrium. This phenomenon is qualitatively described in Figure 7-188.

a) Density

b) Pressure

c) Temperature

d) Ratio of specific heats

------	$R_{bref}=0$
——	$R_{bref}=0.5$
Markers ◆ ■ ●	$R_{bref}=0$
—◇—	h=30 km
—□—	h=50 km
—○—	h=70 km

Figure 7-187. Effect of altitude on the flow over the cylinder – Flow variables along the stagnation streamline in chemical nonequilibrium.
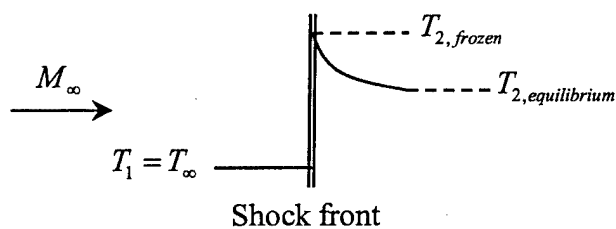
Figure 7-188. Illustration of chemically nonequilibrium temperature behind a shock wave.

In an idealized mathematical model, thermodynamic properties are discontinuous across the shock wave, which is assumed infinitely thin. In reality, the collisions among molecules and atoms, which produce the thermodynamic and chemical changes, occur over a finite thickness. In the preshock region, the flow is chemically frozen. Within the shock front, which is a few mean-free-path thick, only a few molecular collisions take place and the flow barely departs from frozen state. A region of nonequilibrium exists behind the shock wave. As fluid particles move downstream, finite rate reactions take place and flow properties tend to their equilibrium values. The region of nonequilibrium extends more at high altitudes than at low altitudes.

a) h=30 km

b) h=50 km

c) h=70 km

------	$R_{bref} = 0$	, numerical
———	$R_{bref} = 0.5$	, numerical
Markers		
◆ ■ ● ▲ ▼	$R_{bref} = 0$	, GASEQ
—◇—	$O2$	
—□—	$N2$	
—○—	NO	
—△—	O	
—▽—	N	
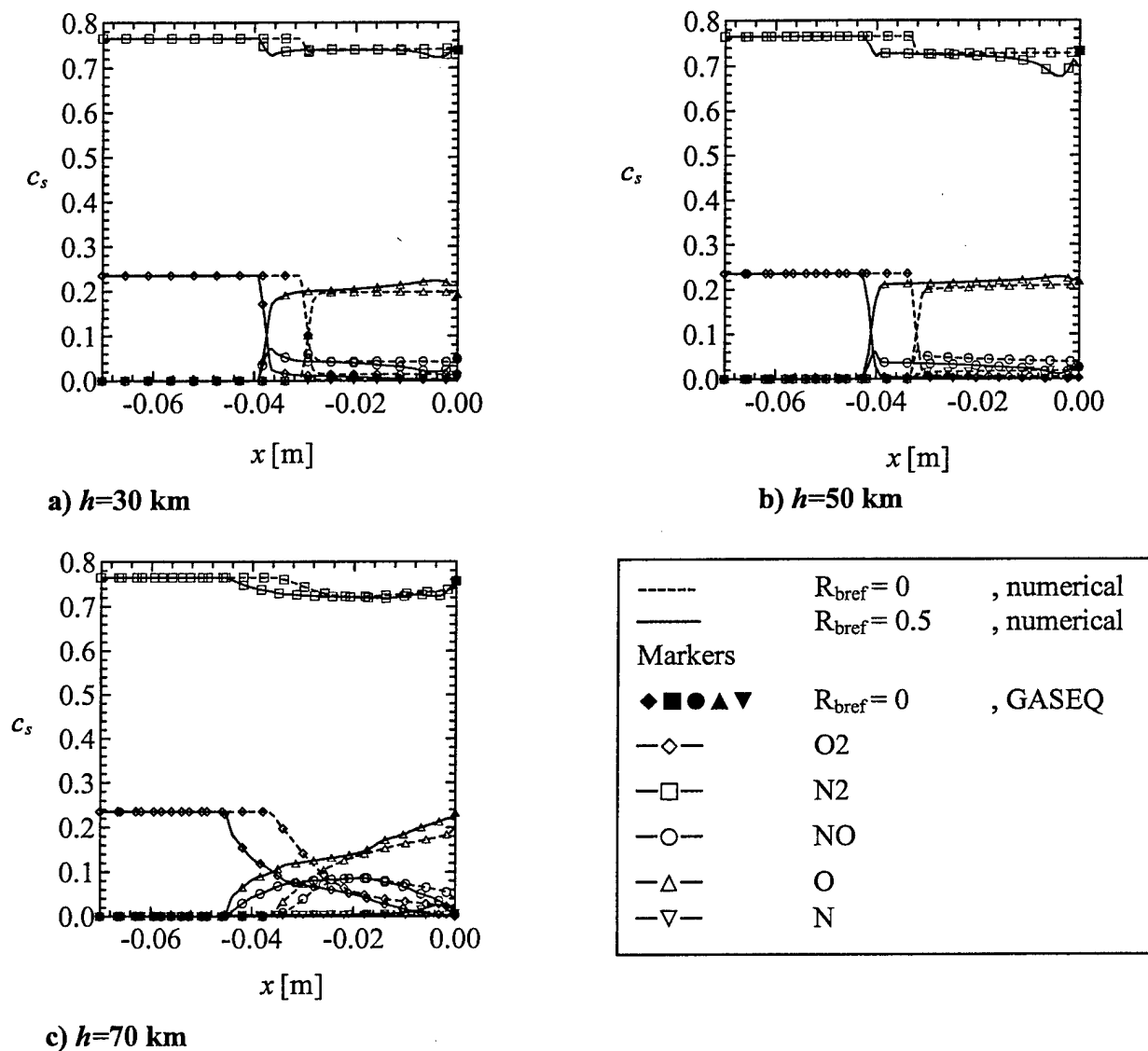
Figure 7-189. Effect of altitude on the flow over the cylinder – Relative distribution of chemical mass fractions along the stagnation streamline in chemical nonequilibrium.

Figure 7-189 depicts the relative variation of the chemical mass fractions with distance along the stagnation streamline. In the postshock region, diatomics O_2 and N_2 dissociate, the dissociation of O_2 being the most important. As expected, the mass fractions of O and N increase, rising from their frozen flow values (essentially zero) ahead of the shock wave and tending to their equilibrium values further downstream. For nonmagnetic cases, in which the postshock flow variables (density, pressure, temperature, etc.) are quasi-uniform along the stagnation streamline, nonequilibrium mass fractions of all chemical species, but nitric oxide NO, range between the two extremes of frozen and equilibrium values.

The NO overshoot observed immediately downstream of the shock wave may be explained as follows, based on the arguments reported in References [123] and [124]. Downstream of the shock wave, diatomics O_2 and N_2 dissociate, which releases O-atoms and N-atoms. The production of O-atoms triggers the NO exchange reactions $O+N_2 \rightleftharpoons N+NO$ and $N+O_2 \rightleftharpoons O+NO$. These reactions are extremely fast and they rapidly lead to a local equilibrium expressed as $O_2+N_2 \rightleftharpoons 2NO$. The net effect of these two reactions is to convert N_2 and O_2 into NO. Since the reactions are very fast, an excess of NO is produced downstream of the shock wave where there is plenty of O_2 and N_2. As O_2 continues to dissociate (further downstream of the shock wave), the shuffle reactions are reversed and nitric oxide NO is reduced towards its final value by this means and also by direct dissociation.

It is observed that the local mass fractions at the stagnation point tend to the equilibrium values. Indeed, along the stagnation streamline, a fluid element decelerates and reaches zero velocity at the stagnation point, where chemical reactions have time to reach equilibrium. It should be recalled that the equilibrium values provided in Figure 7-189 are obtained behind a normal shock wave and not at a stagnation point. They provide a measure of validation of the present effort.

In the current simulations, the chemical mass fractions distributions are affected by the magnetic field. In the absence of magnetic field, the mass fractions vary gradually in the postshock region. Indeed, the postshock temperature, which is the determining factor, is relatively uniform in the present conditions (adiabatic wall, no viscous dissipation at the wall). In the presence of magnetic field, temperature profiles exhibit an overshoot in the vicinity of the body due to the Joule heating. Due to the complexities of the chemical kinetics mechanism associated with such cases, the species mass fractions may exceed the two extremes of frozen and equilibrium values.

7.8.2. Effect Of Mach Number

The effect of the freestream Mach number at a given altitude is investigated in this section. Simulations parameters are specified in Table 7-13.

Altitude	$h=30$ km
Freestream Mach number (varying parameter)	$M_{ref} = M_\infty$, $M_\infty \in \{10,\quad 14,\quad 18\}$
Magnetic pressure number	$R_{b_{ref}} \in \{0,\quad 0.5\}$
Magnetic Reynolds number	$Re_{m_{ref}} = 12.5$

Table 7-13. Solution parameters for simulation of Mach number effect, for the flow over the cylinder.

- **Chemically frozen flow model**

Figure 7-190 depicts the profiles of selected flow variables along the stagnation streamline at various Mach numbers, for frozen flow. Analytical stagnation-point values are also provided, which show an excellent agreement with the numerical simulations. Since the shock temperature ratio becomes larger with the Mach number, chemical processes are expected to be enhanced as the Mach number is increased.

Figure 7-191 illustrates the variation of postshock temperature with the Mach number for both frozen flow and chemical equilibrium. As mentioned previously, the frozen flow approach leads to unrealistic temperature, with error of 42% at Mach 10 and 126% at Mach 18, compared to equilibrium values. Errors of the same order are expected for density. Again, these observations clearly show the necessity to take into account chemistry effect in the computations of hypersonic flows.

a) Density

b) Pressure

c) Temperature

	Rbref=0	, numerical
-------	Rbref=0	, numerical
———	Rbref=0.5	, numerical
Markers		
◆■●▲▼	Rbref=0	, analytical
—◇—	$M_{ref}=10$	
—□—	$M_{ref}=14$	
—○—	$M_{ref}=18$	
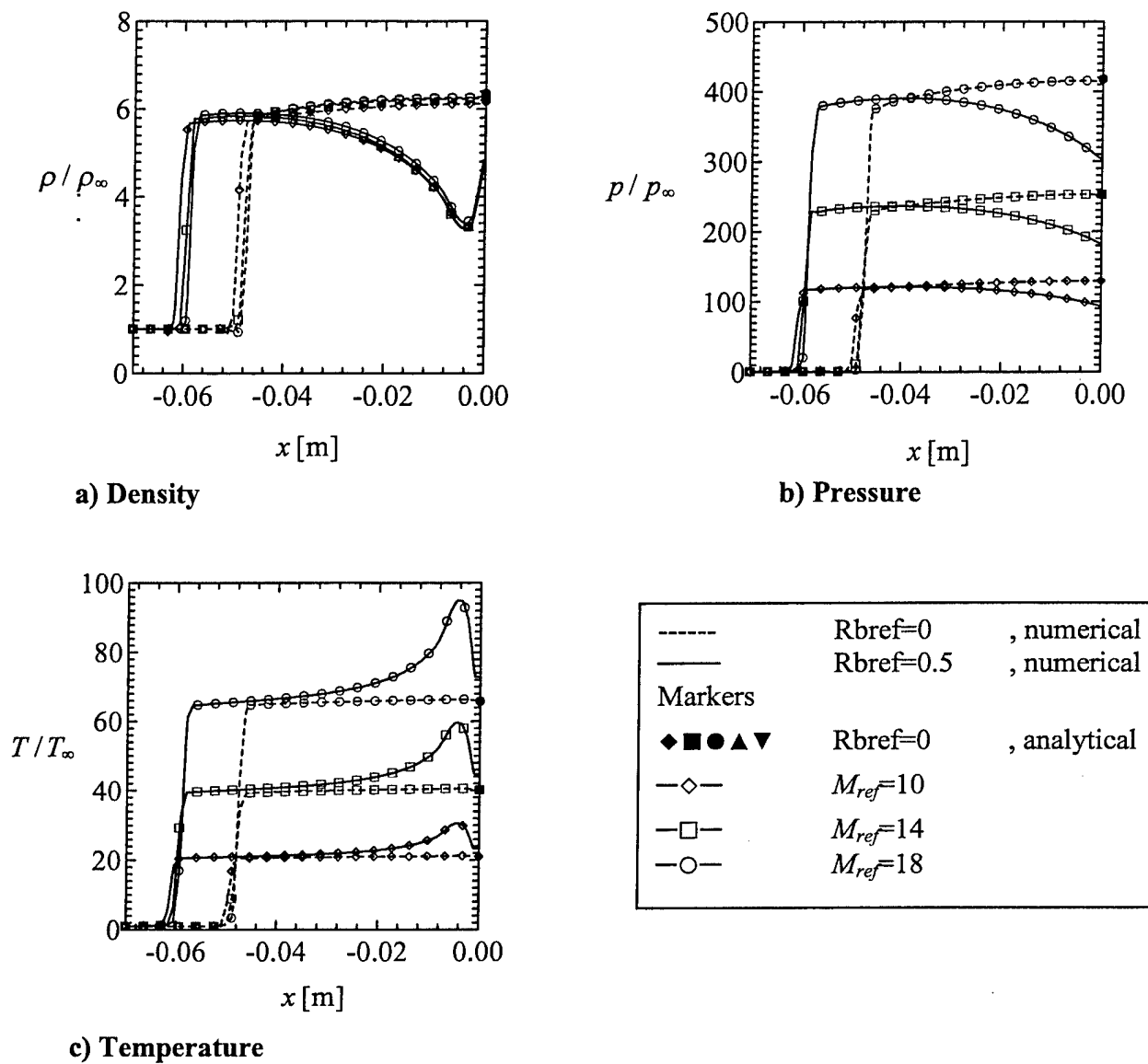
Figure 7-190. Effect of Mach number on the flow over the cylinder – Flow variables along the stagnation streamline in chemically frozen state.
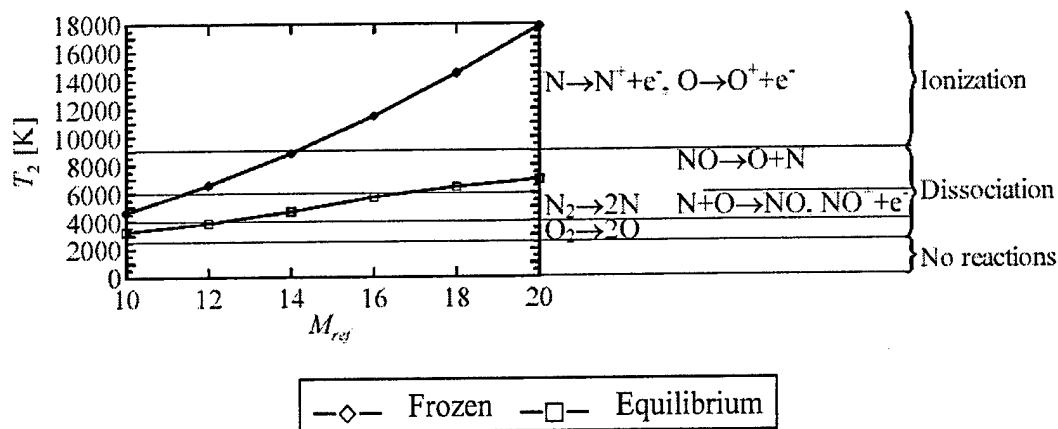
Figure 7-191. Temperature behind a normal shock at an altitude of 30 km.

- **Chemical equilibrium model**

Figure 7-192 depicts the distribution of selected flow variables along the stagnation streamline. As a measure of validation, the equilibrium values obtained with GASEQ (for the nonmagnetic case) are included, which show a good agreement with the current solution. As described in Section 7.8.1, chemical reactions lead to a reduction in temperature, increase in density and no significant effect in pressure, in the postshock region, compared to frozen flow. It is also observed that the variation in the shock standoff distance with the Mach number is amplified in chemical equilibrium compared to frozen flow. The equilibrium model predicts an enhancement of the chemical phenomena with increasing Mach number. The temperature peak associated with the Joule heating is attenuated by chemical reactions, in particular at Mach 18.
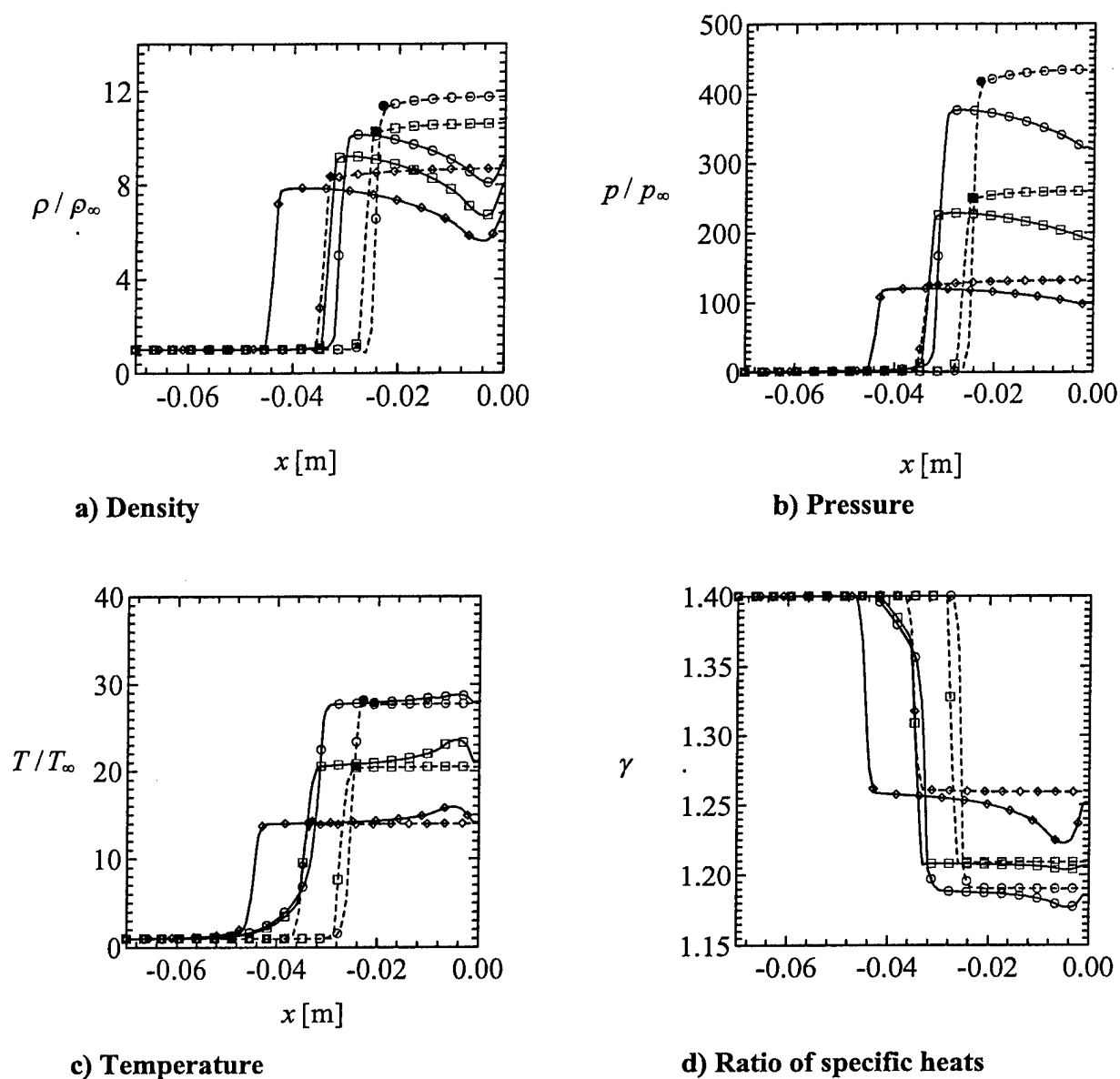
a) Density

b) Pressure

c) Temperature

d) Ratio of specific heats

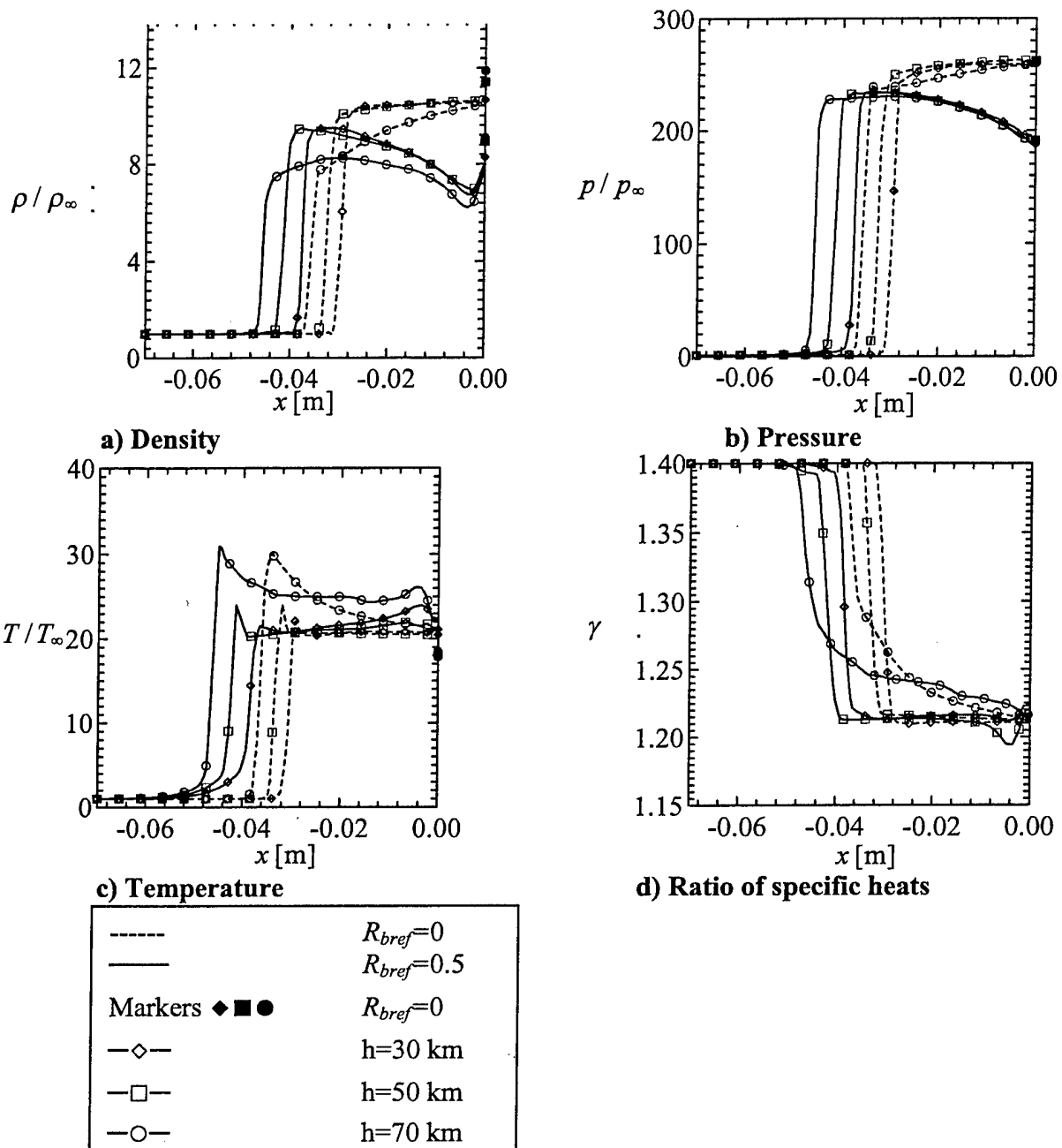|	$R_{bref} = 0$	, numerical
———	$R_{bref} = 0.5$	, numerical
Markers		
◆■●▲▼	$R_{bref} = 0$	, GASEQ
—◇—	$M_{ref} = 10$	
—□—	$M_{ref} = 14$	
—○—	$M_{ref} = 18$	

Figure 7-192. Effect of Mach number on the flow over the cylinder – Flow variables along the stagnation streamline in chemical equilibrium.

192

- **Chemical nonequilibrium model**

The effect of Mach number on nonequilibrium flow is presented in Figure 7-193. At a given altitude, the postshock temperature increases with the Mach number, which enhances the chemical kinetics. Thus, the higher the Mach number is, the faster the flow approaches chemical equilibrium. However, at a given altitude, higher Mach number translates into higher velocity. If the fluid particles cross the shock wave in a time smaller than the time lapse required for the chemical reactions, the flow right behind the shock wave is in chemical nonequilibrium. Peak in temperature, revealing nonequilibrium temperature are observed for all Mach numbers. For the sake of simplicity, the current nonequilibrium model assumes vibrational, rotational and translational temperatures to be the same. As a consequence, the temperature at the first node point behind the shock wave is very high (frozen flow value), and therefore, the chemical reaction rates and their associated Jacobian elements become very large. In reality, the dissociation is preceded by the vibrational excitation (See Table 6-1). Thus, the time at which the vibrational excitation is completed and the time at which the dissociation process begins overlap. Moreover, since vibrational temperature is very low behind the shock wave, associated chemical reactions rates are nearly zero there. Chemical reaction rates become large only after a few node points behind the shock. It is thus expected that a two-temperature model, that treat the translational and rotational temperature separately from the vibrational temperature would provide a mechanism of relaxation.

a) Density

b) Pressure

c) Temperature

d) Ratio of specific heats

-------	$R_{bref} = 0$	, numerical
————	$R_{bref} = 0.5$	, numerical
Markers		
◆■●▲▼	$R_{bref} = 0$	, GASEQ
—◇—	$M_{ref} = 10$	
—□—	$M_{ref} = 14$	
—○—	$M_{ref} = 18$	
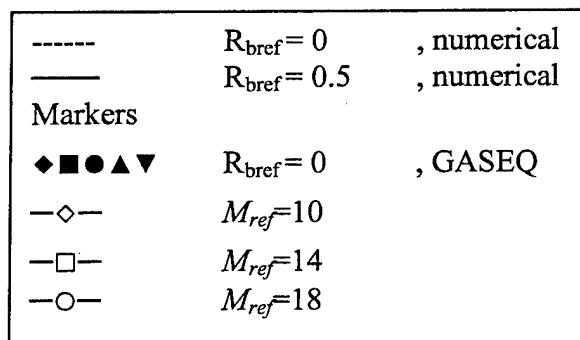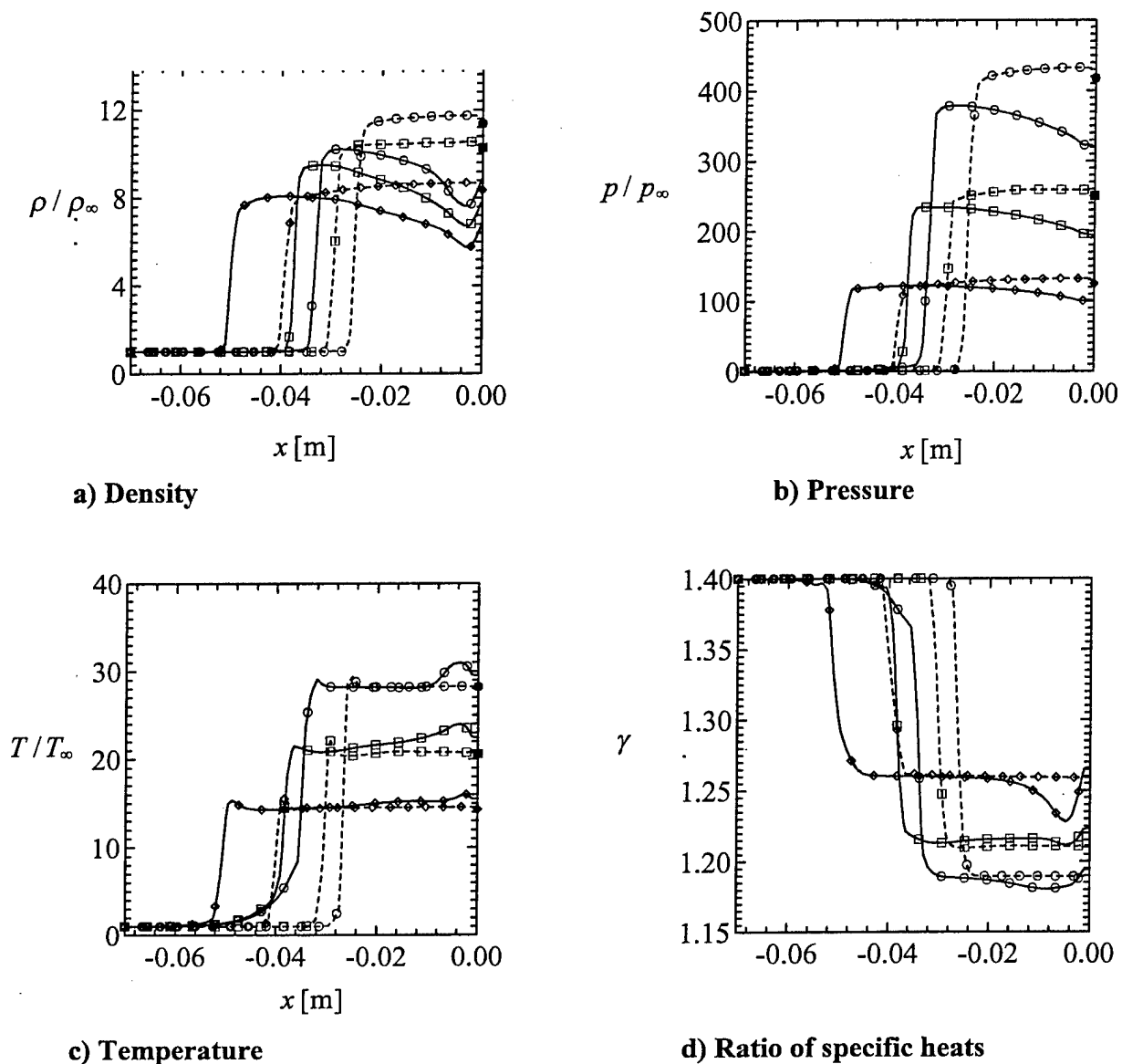
Figure 7-193. Effect of Mach number on the flow over the cylinder – Flow variables along the stagnation streamline in chemical nonequilibrium.

Figure 7-194 shows the effect of the Mach number on the distribution of each of the chemical mass fractions along the stagnation line. For the nonmagnetic case, mass fractions at the stagnation point compares well with the equilibrium values computed with the program GASEQ (behind a normal shock). For the nitric oxide mass fraction, some discrepancy is observed, but it should be noted that Figure 7-194c is a close-up. Figure 7-195 presents the relative distributions of the chemical species, at various Mach numbers. From this perspective, it appears that the mass fractions at the stagnation point agree fairly well with the equilibrium values.

Figures 7-194 and 7-195 show that chemical reactions are enhanced as the Mach number is increased. Dissociation of diatomics O_2 and N_2 balances the release of atoms O and N, and the formation of nitric oxide NO. The dissipation of the magnetic energy in the form of Joule heating modifies chemical kinetics, and enhances thermal dissociations. As a result, a larger amount of O_2 and N_2 is dissociated locally where the Joule effect is considerable.
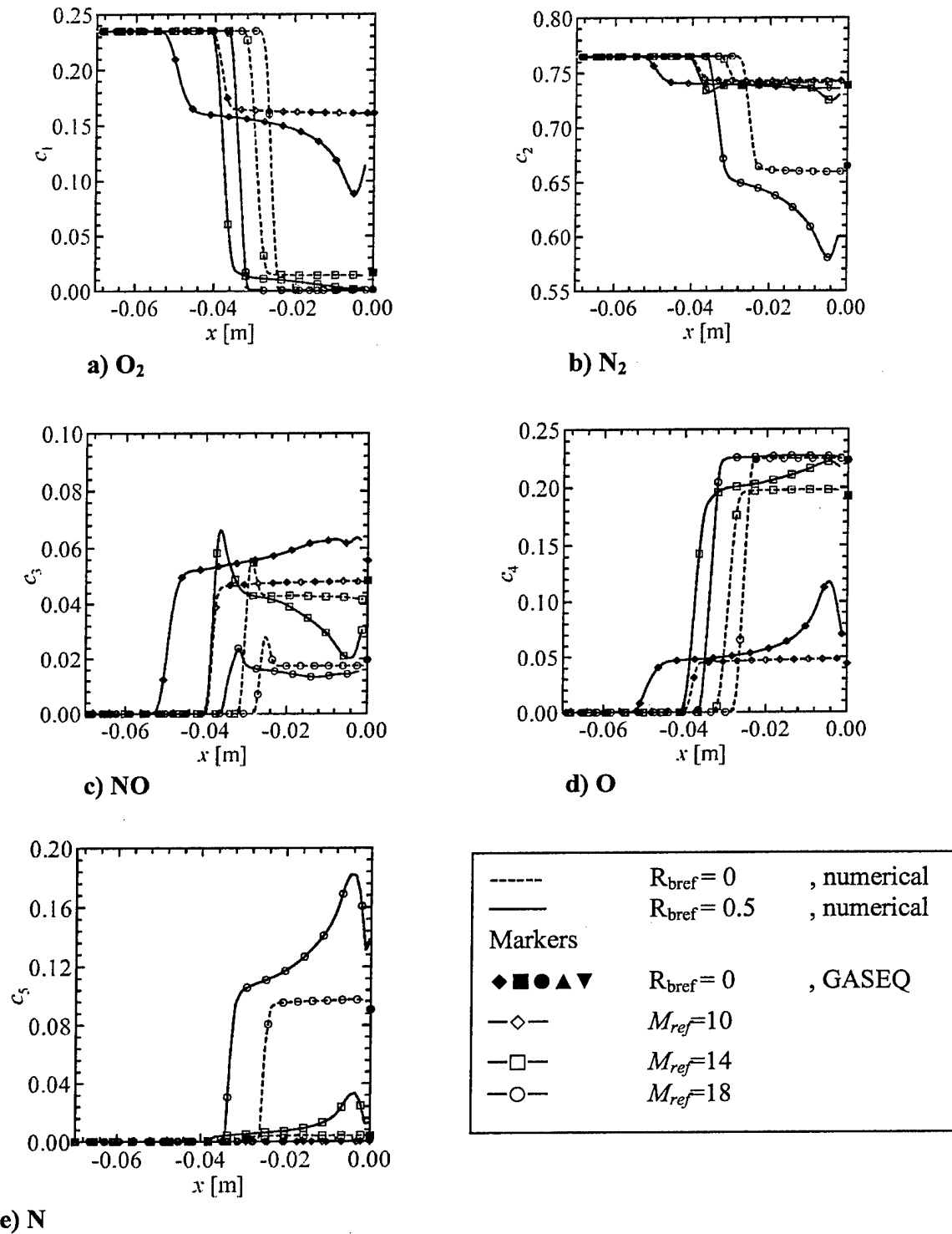
Figure 7-194. Effect of Mach number on the flow over the cylinder – Chemical mass fractions along the stagnation streamline in chemical nonequilibrium.
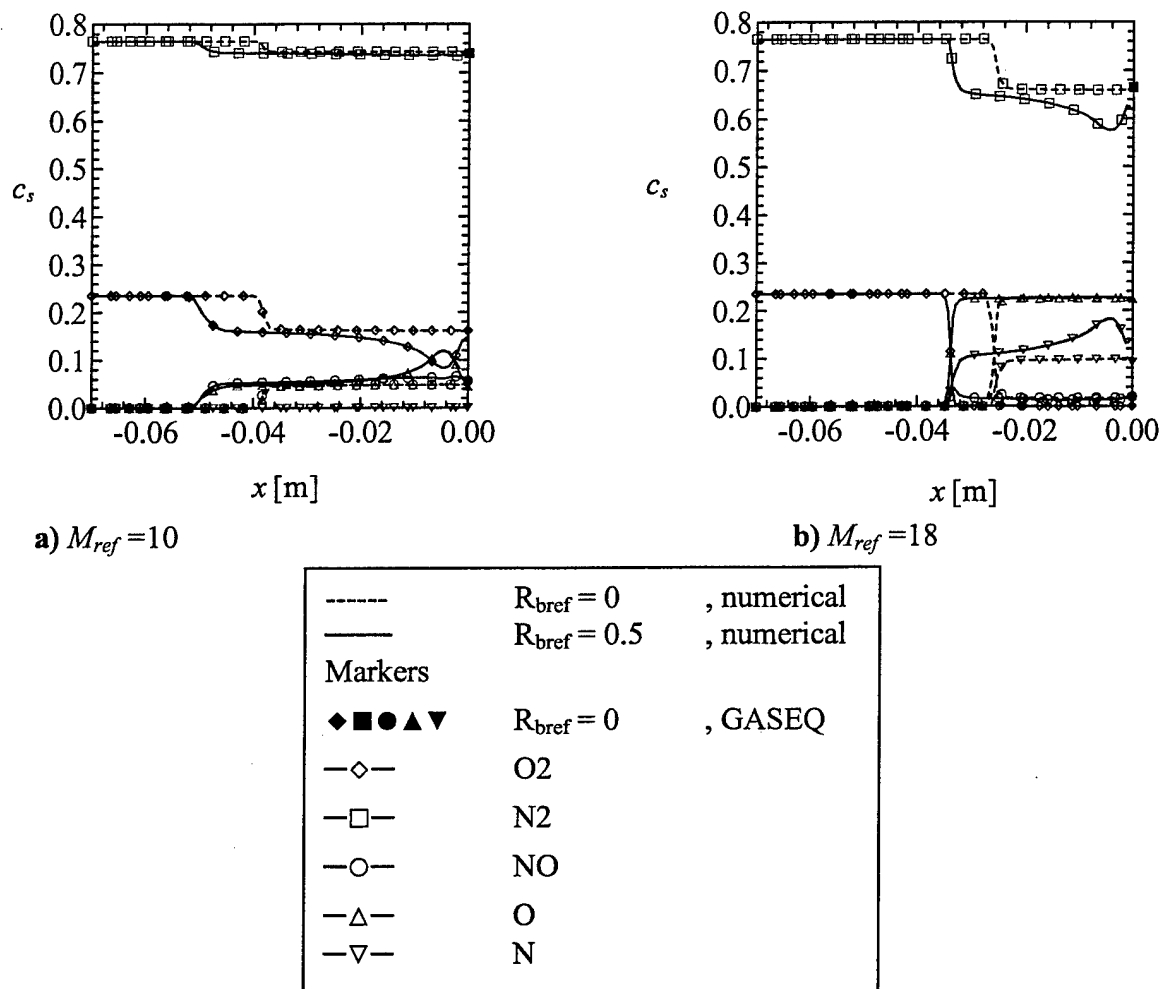
Figure 7-195. Effect of Mach number on the flow over the cylinder – Relative distribution of chemical mass fractions along the stagnation streamline in chemical nonequilibrium.

7.8.3. Examination Of A Nonequibrium Blunt-Body Flow

Some general features of nonequilibrium flow over hypersonic blunt body are addressed in this section. To support this description, the simulation of a Mach 18 flow over the cylinder at an altitude of 30 km is considered.
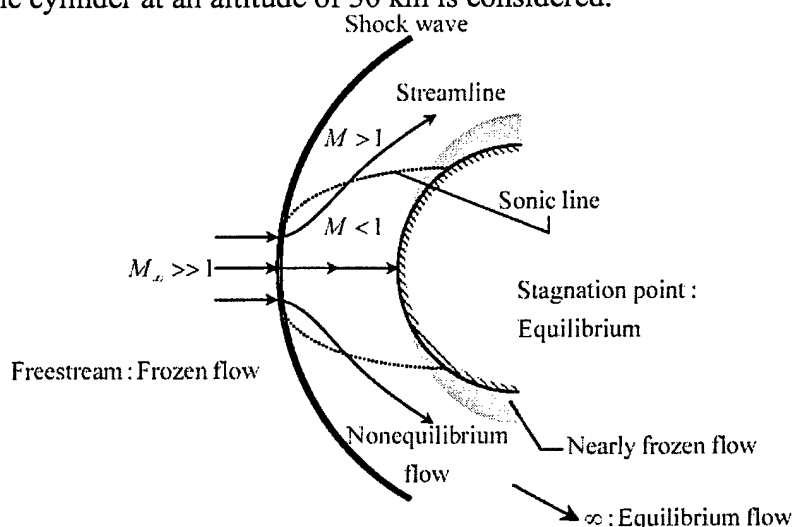
Figure 7-196. High-temperature flow field over a hypersonic blunt body.

On a qualitative basis, the flow field over a blunt body is schematically presented in Figure 7-196, adapted from [125]. The region upstream of the shock wave is the freestream. In the absence of magnetic field, flow properties are uniform in this region and temperature is typically too low to initiate chemical reactions. In the presence of magnetic field, flow properties are not uniform upstream of the shock wave, in particular the Joule heating affects temperature, as mentioned in previous sections. For some flow conditions, the preshock temperature can reach values that initiate chemical reactions. Downstream of the shock wave, fluid particles may undergo various chemical states, depending on their locations. A particle along the stagnation streamline, passes from a state of chemical nonequilibrium immediately downstream of the shock wave to a state of chemical equilibrium at the stagnation point. Indeed, at the stagnation point, flow velocity is zero, and chemical reactions have an infinite time to reach equilibrium. Away from the stagnation streamline, the nonequilibrium region extends downstream. The flow tends to chemical equilibrium further downstream of the body nose. A thin region of nearly frozen flow can be identified along the body downstream of the sonic point. This region is characterized by highly dissociated gas, flowing downstream over the body.

For the sake of comparison, the temperature distributions over the cylinder predicted by frozen flow, equilibrium and nonequilibrium models are presented in Figures 7-197 through 7-199. This allows the identification of the flow features associated with application of magnetic field and those due to hypersonic chemistry.

198
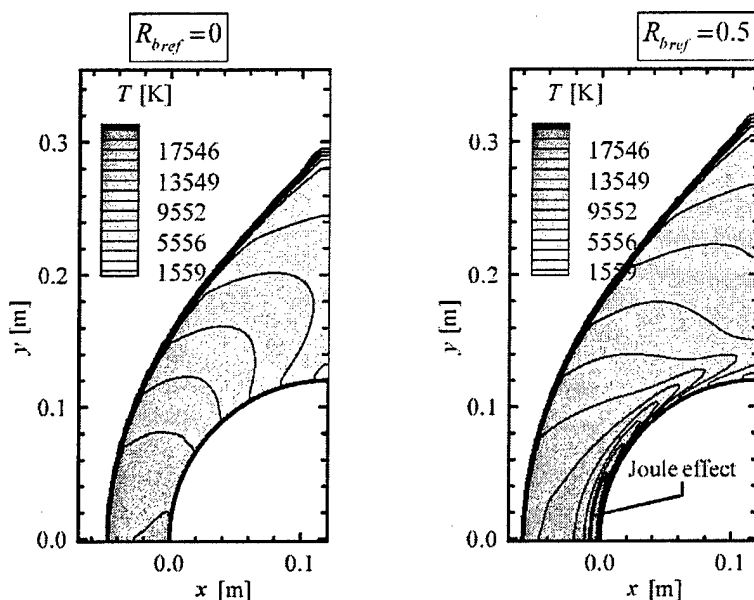
Figure 7-197. Temperature distribution over the cylinder for $M_{ref} = 18$, $Re_{mref} = 12.5$, at an altitude of 30 km, in chemically frozen state.

In frozen flow, temperature is maximal at the stagnation point. Moreover, the application of magnetic field yields an additional rise in temperature along the body surface around the stagnation point. Since the magnetic field decreases along the body surface, as a cosine function, the Joule heating follows the same trend, and thus attenuates at the shoulder of the blunt body.
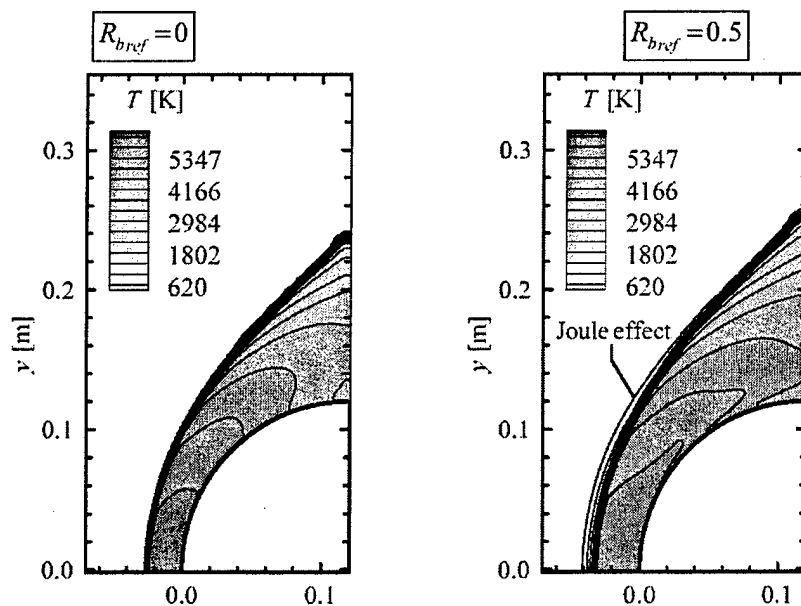
Figure 7-198. Temperature distribution over the cylinder for $M_{ref} = 18$, $Re_{mref} = 12.5$, at an altitude of 30 km, in chemical equilibrium.

199

In chemical equilibrium, the shape of temperature contours resemble that in frozen flow, though the shock standoff distance is reduced. For the magnetic case, a few contour lines are observed in front of the shock wave, corresponding to the gradual increase in temperature due to the Joule heating, as mentioned previously. The high temperatures along the body surface are not as pronounced as in frozen flow.

In the current numerical simulations, nonequilibrium phenomena, identified by regions of high temperature in Figure 7-199b occur mostly right downstream of the shock wave, slightly above the stagnation streamline. Indeed, streamlines and contours plots of velocity magnitude show that fluid particles, downstream of the shock wave, enter regions of various velocity magnitude, depending on their location with respect to the stagnation point.

a) Velocity and streamlines

b) Temperature
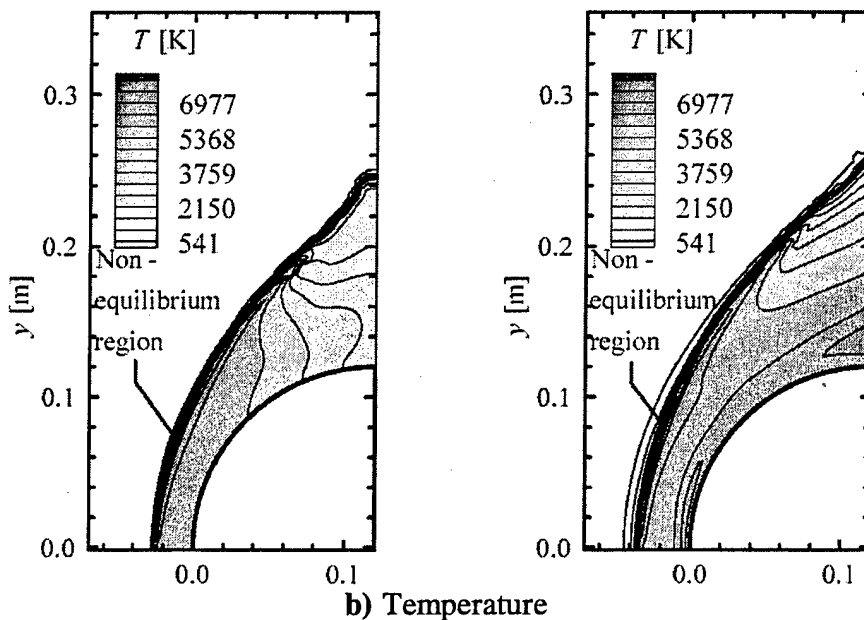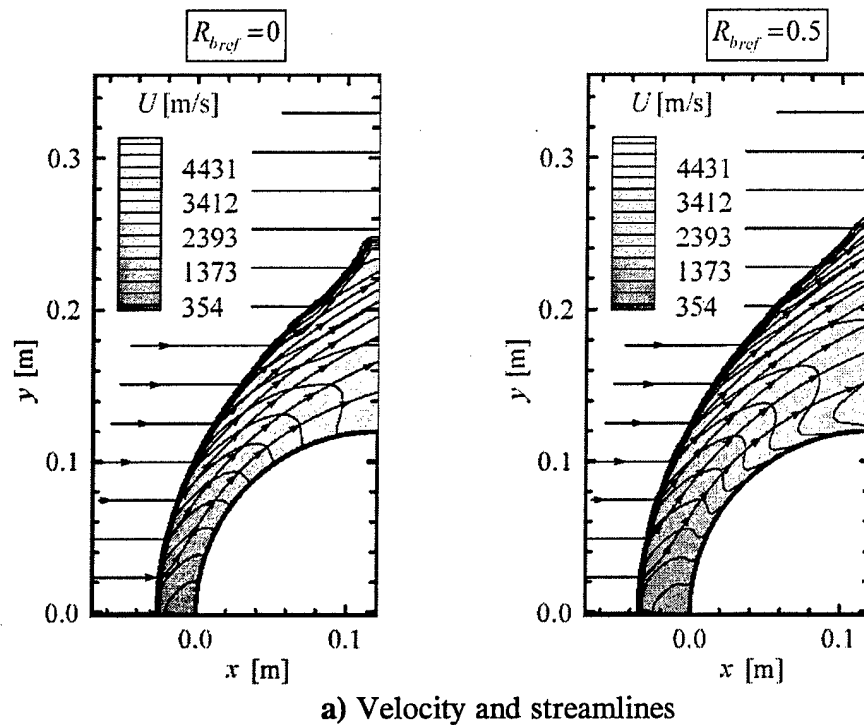
Figure 7-199. Flow field over the cylinder for $M_{ref} = 18$, $Re_{m_{ref}} = 12.5$, at an altitude of 30 km, in chemical nonequilibrium.

Velocity contours are "concentric" around the stagnation point, their value increasing with distance from the stagnation point. Thus, fluid particles entering the shock wave along the stagnation streamline undergo a more dramatic deceleration than particles entering the shock wave above the stagnation streamline. As a result, in the

shock layer, the fluid particles along the stagnation streamline reach chemical equilibrium in a shorter distance than those along other streamlines.

Figure 7-200 depicts the distributions of species mass fractions. It is observed that the molecular oxygen O_2 is almost completely dissociated in the shock layer. Moreover, dissociation proceeds within a short distance behind the shock wave, which is indicated by the accumulation of the contour lines along the shock wave. On the other hand, molecular nitrogen N_2 dissociates gradually in the streamwise direction through the shock layer. The maximum dissociation rate occurs in a region around the stagnation point where the velocity is minimal and the temperature maximal. These chemical phenomena release O-atoms and N-atoms. It is observed that the mass fraction contours of O and N are like photograph negatives of the distributions of O_2 and N_2, respectively. Some of the dissociated O_2 and N_2 contribute to the formation of nitric oxide. The maximum concentration of species NO is observed in a narrow region, adjacent to the shock wave.

Figure 7-200 reveals major differences in the chemical composition and distribution between the nonmagnetic case and the magnetic case. For instance, in the high-temperature region due to the Joule heating, the dissociation of N_2 is enhanced.

a) O_2
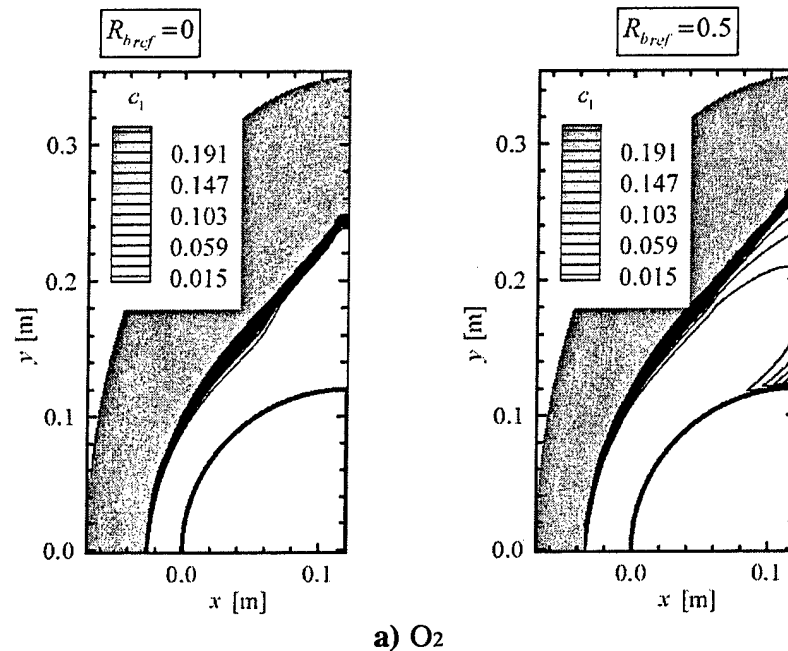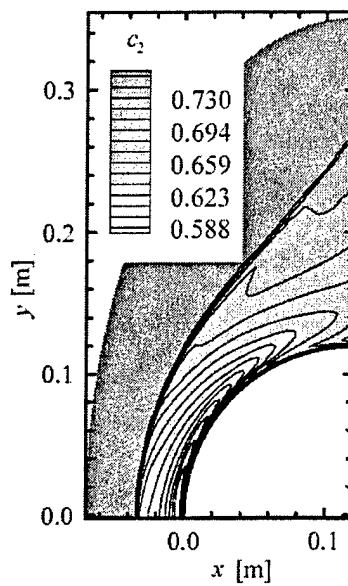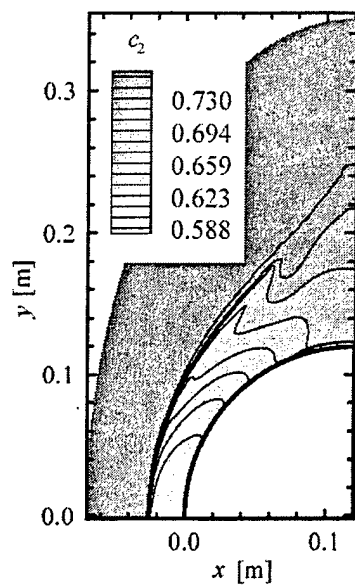
b) N_2
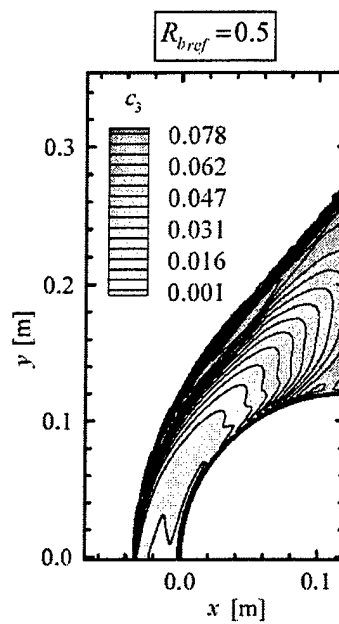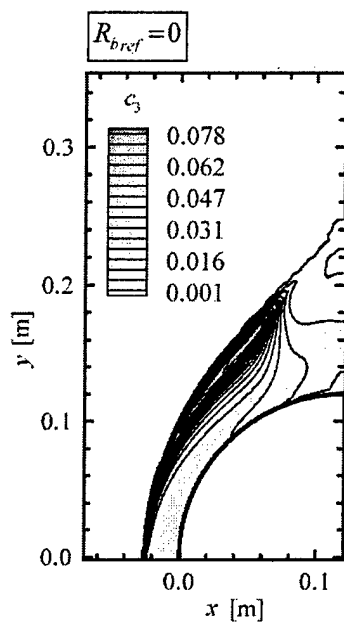
c) NO
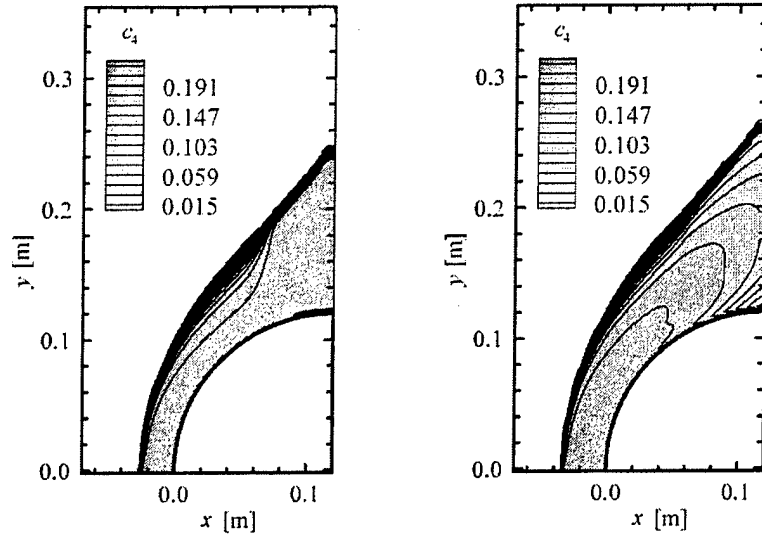
d) O
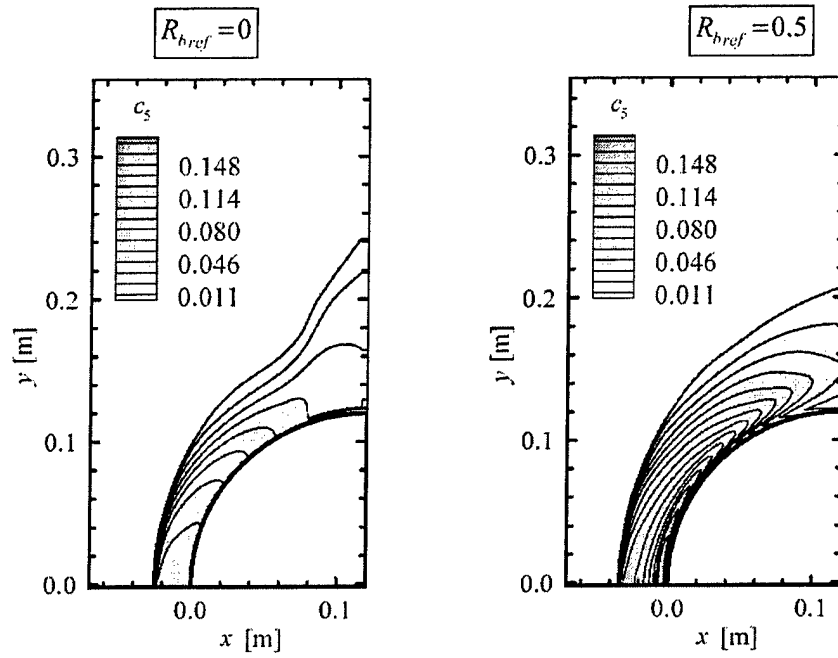
e) N

Figure 7-200. Chemical mass fractions over the cylinder for $M_{ref} = 18$, $Re_{mref} = 12.5$, at an altitude of 30 km, in chemical nonequilibrium.

Among all the cases considered, the flow at Mach 18 at an altitude of 30 km exhibits the highest level of postshock temperature. It is observed in Figure 7-199b that temperature locally reaches values above 8,500 K, but does not exceed 9,000 K, which is the onset of ionization. Therefore, this case is still in the margin of validity of the chemistry model (which does not include ionization).

The current freestream conditions (Mach 18 flow, altitude of 30 km) leads to quasi-chemical equilibrium, though nonequilibrium features are clearly identified in the vicinity of the shock wave. Figure 7-201, compares selected flow variables along the stagnation streamline in various chemical states. As mentioned previously, the frozen flow model yields values of density and temperature, which are off by a factor of two compared to the chemically reacting flow values. All chemistry models predict similar level of postshock pressure. As expected, under the current conditions, the equilibrium and nonequilibrium models lead to nearly identical solutions, which provides another measure of validation of the present effort. However, the small peak in temperature reveals that nonequilibrium features are still present in the flow. As a result, the shock standoff distance in nonequilibrium is slightly larger than in equilibrium.
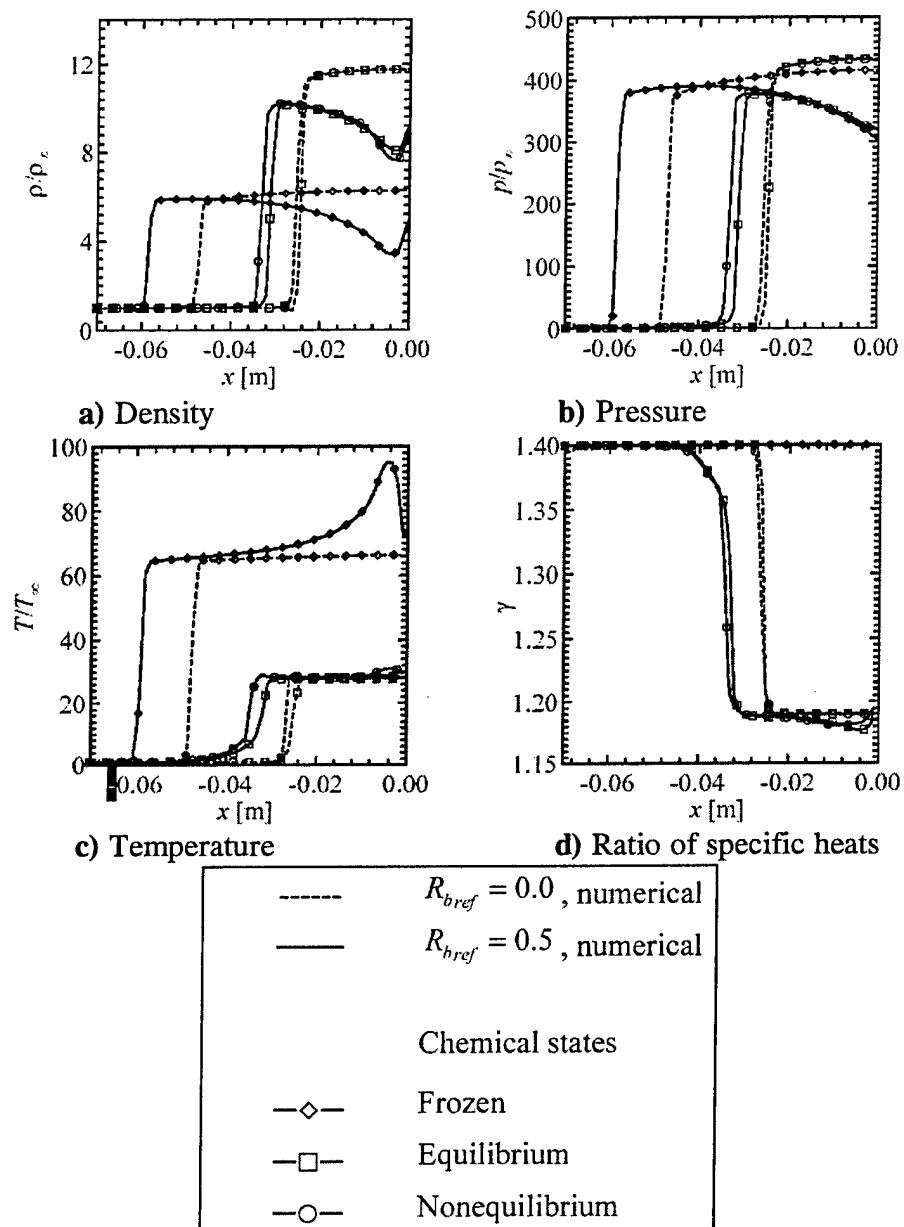
Figure 7-201. Comparison of chemical models for flow over the cylinder for $M_{ref} = 18$, $Re_{m_{ref}} = 12.5$, at an altitude of 30 km – Flow variables along the stagnation streamline.

Chapter 8
Conclusions

The computation of turbulent magnetohydrodynamic flows has been performed using a Reynolds Averaged approach. Two formulations for the magnetohydrodynamic equations have been considered. The full MHD equations were solved for high conductivity fluids, whereas the low magnetic Reynolds number formulation was cinsidered for flows characterized with a low electrical conductivity. The latter formulation does not require the solution of the magnetic induction equation because the induced magnetic field is negligible compared to the applied magnetic field.

The equations of motions were solved by a fourth-order, four stage Runge-Kutta scheme augmented with a Total Variation Diminishing scheme to accurately capture shock-wave discontinuities. The equations were written in a flux vector form and non-dimensionalized before the application of the numerical scheme. Six turbulence models were implemented, ranging from a simple algebraic model to more sophisticated two-equation turbulence models. Their accuracy and limitations have been addressed by comparing the numerical solutions with the experimental data for the flow over a 24-degree compression corner. The performance of each turbulence model varied, and no model could accurately predict both the skin friction and the surface pressure simultaneously. Different formulations for the evaluation of y^+ in the Baldwin-Barth model helped in obtaining a converged solution for this separated flow. The introduction of compressibility correction terms improved the accuracy of the $k-\epsilon$ model in the prediction of the skin friction coefficient. The Reynolds Averaged approach remains the most viable approach for turbulence modeling, due to its relatively reasonable requirement in terms of computational resources.

The MHD solver was validated for the MHD Rayleigh flow and supersonic flow over a blunt body. Good agreement was found with existing analytical solution for the MHD Rayleigh flow. The shock standoff distance compared well with the analytical prediction when the shock wave was not considered concentric with the blunt body.

Each turbulence model was calibrated based on the turbulent Hartmann flow. The objective was to verify the experimental observation, stating that a relaminarization process occurs when the ratio Ha/Re becomes larger than $1/225$. When the Baldwin-Lomax, Baldwin-Barth, Baseline and SST models were used in their original form, they over predicted the skin friction and no relaminarization occurred. The original $k-\epsilon$ model predicted a relaminarization occurring too early. The original Spalart-Allmaras was the most accurate, as it only slightly over predicted the skin friction coefficient. Each model has been modified to account for the presence of a magnetic field. Different types of modifications were introduced within the turbulence models. The Baldwin-Lomax model was modified by introducing a damping term in the evaluation of the mixing length. Additional magnetic terms were added to the $k-\epsilon$ model. The modified version of the Baldwin-Barth model was directly derived from the modified $k-\epsilon$ model. It resulted in the addition of a magnetic term in the turbulent transport equation. By

analogy, additional magnetic terms have been included in the Baseline and SST turbulence models. The Spalart-Allmaras model was modified by proposing one of its closure coefficient to depend on the magnetic field. This simple modification proved to be sufficient since the original model was performing fairly well. The modifications resulted in the accurate prediction of the relaminarization process observed in the turbulent Hartmann flow. The relaminarization process occurred when $Ha/Re = 1/225$, and was not affected by the Reynolds number, ranging from 5,000 to 50,000.

The original and modified turbulence models were applied to a supersonic flow over a flat plate. For a low electrical conductivity fluid, the application of a magnetic field resulted in a decrease of the turbulent skin friction by about 20% when the original models were used and between 20 and 30% when the modified versions of the turbulence models were used. The magnetic field was uniformly applied in the y-direction. A complete relaminarization of the flow could not be obtained because the effect of the magnetic field was more important on the mean flow than on turbulence. As the magnetic field was increased, a separation of the flow occurred before the relaminarization could be reached. Expressions for the laminar and turbulent skin friction coefficients were proposed. They depend explicitly on the magnetic field and are valid for small values of the product mx, for a Mach number ranging from 2 to 4. For very high conductivity fluids, the full MHD equations must be solved because the induced magnetic field is substantial within the boundary layer. In this case, a complete relaminarization of the flow was obtained. It was also determined that the orientation of the applied magnetic field had a strong effect on the reduction of the skin friction. A reduction of 80% was observed when the applied magnetic field was perpendicular to the incoming flow, compared to the case where both applied magnetic field and velocity fields were aligned.

The effect of the magnetic field on the heat transfer was also investigated. The heat transfer was calculated for the hypersonic flow over a cone, and compared with experimental data, in the non-magnetic case. The Baldwin-Lomax and Baseline models provided the most accurate results when no magnetic field was present and therefore, were selected to carry out the numerical simulations when the magnetic field was turned on. A complete relaminarization of the flow could be observed, in the sense that both the skin friction and heat transfer were reduced to their laminar values. The relaminarization process occurred earlier (i.e., for a smaller value of the applied magnetic field) when the modified versions of the turbulence models were implemented.

The numerical efficiency of the two MHD formulations and six turbulence models was discussed. The low magnetic Reynolds number formulation requires less computational time per iteration than the full MHD equation solver. The implementation of turbulence models increased the computational time by 30% for the Baldwin Lomax model, whereas it was multiplied by 5.5 for the $k-\epsilon$ model. The code based on the low magnetic Reynolds number formulation converged faster and was more stable than the full MHD equations solver. The Baldwin-Lomax model was also the model that converged the fastest.

The application of a magnetic field was shown to be beneficial to turbulent MHD flows, by reducing the skin friction and heat transfer. A complete relaminarization of the flow was observed. The Baldwin-Lomax algebraic turbulence model appears to be a good candidate for the computation of relatively simple turbulent MHD flows, due to its computational efficiency and good prediction capabilities.

Two models to simulate hypersonic high-temperature effects were implemented. One is an equilibrium model, based on curve fits of thermodynamic properties. The other is a five-species, seventeen-reaction nonequilibrium model, solved by a flux-vector splitting scheme. For the sake of simplicity, a one-temperature model has been assumed. The chemistry model is loosely coupled with the scheme for solution of the MGD equations.

Blunt-body configurations in 2-D and 3-D were the object of intense investigations. The MGD flow over a hemisphere with an imposed magnetic dipole was simulated in the low magnetic Reynolds number approximation. The magnetic interaction caused the shock wave to move away upstream from the body. For chemically frozen flow, the computed shock standoff distance coincided perfectly with another numerical solution reported in the literature. Simulations in chemical equilibrium indicated a smaller shock standoff distance than in frozen flow.

Inviscid, resistive flow over a circular cylinder-wedge was investigated using the full MGD equations. Good agreement with the existing numerical solutions has been obtained. Increase in the shock standoff distance and reduction in the surface pressure were observed. In the case of the cylinder-wedge, the effect of hypersonic chemistry was investigated in depth using the equilibrium and nonequilibrium chemistry models. Inclusion of chemistry effects in the simulation of hypersonic flow resulted in higher density ratio, lower temperature ratio across the shock wave and reduced shock standoff distance. The effect on postshock pressure was minimal. At low altitudes, the flow was mostly in chemical equilibrium, though small nonequilibrium regions existed behind the shock wave. At higher altitudes, nonequilibrium phenomena dominated the flow field. At a given altitude, chemical kinetics was enhanced with increasing Mach number. The application of a magnetic field had a significant impact on the chemical phenomena. In particular, the Joule heating enhances the thermal dissociation of air.

References

[1]   Rossow, V.J., "On Flow of Electrically Conducting Fluids Over a Flat Plate in the Presence of a Transverse Magnetic Field", NACA TN 3971, May 1957.

[2]   Lykoudis, P.S., "On a Class of Magnetic Laminar Boundary Layers", 1958 Heat Transfer and Fluid Mechanics Institute preprint, June 1958.

[3]   Lykoudis, P.S., "The Newtonian Approximation in Magnetic Hypersonic Stagnation-Point Flow", Journal of the Aero/Space Science, Vol. 28, No. 7, July 1961, pp. 541-546.

[4]   Zachary, A.L., and Collella, P., "A Higher-Order Godunov Method for the Equations of Ideal Magnetohydrodynamics", Journal of Computational Physics, Vol. 99, 1992, pp. 341-347.

[5]   Bell, J.B., Colella, P., and Trangenstein, J.A., "High Order Godunov Methods for General Systems of Hyperbolic Conservation laws", Journal of Computational Physics, Vol. 82, 1989.

[6]   Brio, M., and Wu, C.C., "An Upwind Differencing Scheme for the Equations of Ideal Magnetohydrodynamics", Journal of Computational Physics, Vol. 75, 1998, pp. 400-422.

[7]   Dai, W., and Woodward, P.R., "Extension of the Piecewise Parabolic Method to Multidimensional Ideal Magnetohydrodynamics", Journal of Computational Physics, Vol. 115, 1994, pp. 485-514.

[8]   Dai, W. and Woodward, P.R., "A Simple Riemann Solver and High-Order Godunov Schemes for Hyperbolic Systems of Conservation Laws", Journal of Computational Physics, Vol. 121, 1995, pp. 51-65.

[9]   Dai, W., and Woodward, P.R., "A Second-Order Iterative Implicit-Explicit Hybrid Scheme for Hyperbolic Systems of Conservation Laws", Journal of Computational Physics, Vol. 128, 1996, pp. 181-196.

[10]   Harada, S., Augustinus, J., Hoffmann, K.A., and Agarwal, R.K., "Development of a Modified Runge-Kutta Scheme with TVD Limiters for the Ideal 1-D MHD Equations", AIAA-97-2090, 13th AIAA Computational Fluid Dynamics Conference, June 1997.

[11]   Augustinus, J., Harada, S., Hoffmann, K.A., and Agarwal, R.K., "Numerical Solution of the Eight-Wave Structure Ideal MHD Equations by Modified Runge-Kutta Scheme with TVD", AIAA-97-2398, AIAA 28th Plasmadynamics and Lasers Conference, June 1997.

[12]   Augustinus, J., Hoffmann, K.A., and Harada, S., "Effect of Magnetic Field on the Structure of High –Speed Flows", Journal of Spacecraft and Rockets, Vol. 35, No. 5, September-October 1998, pp. 639-646.

[13]   Harada, S., Hoffmann, K.A., and Augustinus, J., "Numerical Solution of the Ideal Magnetohydrodynamics Equations for a Supersonic Channel Flow", Journal of Thermophysics and Heat Transfer, Vol. 12, No. 4, October-December 1998, pp. 507-513.

[14]   Harada, S., Hoffmann, K.A., and Augustinus, J., "Development of a Modified Runge-Kutta Scheme with TVD Limiters for the Ideal Two-Dimensional MHD Equations", AIAA-98-0981, January 1998.

[15]   Powell, K.G., Roe, P.L., Myong, R.S., Gombosi, T., and De Zeeuw, D., "An Upwind Scheme for Magnetohydrodynamics", AIAA-95-1704-C, June 1995.

[16]   Hoffmann, K.A., Damevin, H.M., Dietiker, J.F., "Numerical Simulation of Hypersonic Magnetohydrodynamic Flows", AIAA-2000-2259, AIAA 31th Plasmadynamics and Lasers Conference, June 2000.

[17]   Shang, J.S., Hayes, J., Harris, S., Umstattd, R., and Ganguly, B., "Experimental Simulation of Magneto-Aerodynamic Hypersonics", AIAA-2000-2258, AIAA 31th Plasmadynamics and Lasers Conference, June 2000.

[18]   Staats, G.E., McGregor, Sprouse, and Frolhlich, "Magnetogasdynamic Experiments Conducted in a Supersonic Plasma ARC Tunnel", AIAA-2000-2566, AIAA 31th Plasmadynamics and Lasers Conference, June 2000.

[19]   Blake, Nagamatsu, Myrabo, and Shear, "MHD Results for Air plasma at Mach 30 and 11,600 K with a 10,300 Gauss Magnetic Field", AIAA-2000-2668, AIAA 31th Plasmadynamics and Lasers Conference, June 2000.

[20]   Batchelor, G.K., "On the Spontaneous Magnetic Field in a Conducting Liquid in Turbulent Motion", Proceedings of the Royal Society A 201, 405,1950.

[21]   Ferraro, V.C.A, and Plumton, C., Magneto-Fluid Mechanics, Oxford University press, 1966.

[22]   Napolitano L.G., "On turbulent Magneto-Fluid Dynamic Boundary Layers", Review of Modern Physics, Vol. 32, October 1960, pp. 785-795.

[23]   Chandrasekhar, "Hydromagnetic Turbulence, I. A Deductive Theory", Proceedings of the Royal Society, A233, 322, 1955.

[24]   Lykoudis P.S., "Transition from Laminar to Turbulent Flow in Magneto-Fluid Mechanic Channels", Review of Modern Physics, Vol. 32, October 1960, pp. 796-798.

[25]   Chandrasekhar, "Hydromagnetic Turbulence, II An Elementary Theory", Proceedings of the Royal Society, A233, 330, 1955.

[26]   Lykoudis, "Magneto Fluid Mechanics Channel Flow. II. Theory", The Physics of Fluids, Vol. 10, No. 5, May 1967, pp. 1002-1007.

[27]   Lee, "Numerical and Experimental Investigation of Flow Channel", Progress in fluid flow research: turbulence and applied MHD, Progress in Astronautics and Aeronautics, Vol. 182, 1998, pp. 437-453.

[28]   Frando, "Study of the MHD Turbulent Flow in Electromagnetic Valve", Progress in fluid flow research: turbulence and applied MHD, Progress in Astronautics and Aeronautics, Vol. 182, 1998.

[29] El-Kaddah, "The Turbulent Recirculating Flow Field in a Coreless Induction Furnace, A Comparison of Theoretical Predictions with Measurements", Journal of Fluid Mechanics, Vol. 133, pp. 37-46.

[30] Shimomura, Y., "Statistical Analysis of Magnetohydrodynamic Turbulent Shear Flows at Low Magnetic Reynolds Number", Journal of the physical Society of Japan, Vol. 57, No. 7, July 1988, pp. 2365-2385.

[31] Kitamura and Hirata, Proc 6th IHTC 3, M-18, 159, 1978.

[32] Yoshizawa, A., "Self-Consistent Turbulent Dynamo Modeling of Reversed Field Pinches and Planetary Magnetic Fields", Physics of Fluids B, Vol. 2, No. 7, 1990.

[33] Yoshizawa, A. Hamba, F., "A Turbulent Dynamo Model for the Reversed Field Pinches of Plasma", Physics of Fluids, Vol. 31, No. 8, 1988.

[34] Hamba, F., "Turbulent Dynamo Effect and Cross Helicity in Magnetohydrodynamic Flows", Physics of Fluids A, Vol. 4, No. 2, 1992.

[35] Kovasznay, "Plasma Turbulence", Magneto Fluid Dynamics, International Symposium on Magneto-Fluid-Dynamics, 1960, pp. 815-822.

[36] Shimomura, "Large Eddy Simulation of Magnetohydrodynamics Turbulent Channel Flows under a Uniform Magnetic Field", Physics of Fluids A3 (12), December 1991, pp. 3098-3106.

[37] Sukoriansky, "Stabilized Negative Viscosity as Sub Grid Scale Representation of Two Dimensional Turbulence", Progress in fluid flow research: turbulence and applied MHD, Progress in Astronautics and Aeronautics, Vol. 182, 1998, pp. 33-47.

[38] Starr, The Physics of Negative Viscosity Phenomena, Mc Graw Hill, 1968.

[39] Moreau, "Why, How and When MHD Turbulence Becomes Two-Dimensional", Liquid-metal flows and magnetohydrodynamics: the third international seminar in the MHD flows and turbulence series, Progress in Astronautics and Aeronautics, Vol. 84, 1983, pp. 20-29.

[40] Caperan, "Transition from 3D to Quasi 2D MHD Grid Turbulence", Single- and multi-phase flows in an electromagnetic field: energy, metallurgical, and solar applications, Progress in Astronautics and Aeronautics, Vol. 100, pp. 89-99

[41] Narasimha, "Relaminarization - MHD and Otherwise", Liquid-metal flows and magnetohydrodynamics: the third international seminar in the MHD flows and turbulence series, Progress in Astronautics and Aeronautics, Vol. 84, 1983, pp. 30-52.

[42] Eckert, "MHD Turbulent Measurements in a Sodium Channel Flow", Progress in fluid flow research: turbulence and applied MHD, Progress in Astronautics and Aeronautics, Vol. 182, 1998, pp. 87-100.

[43] Moisev, "Helical Turbulence and Study of Atmospheric and MHD Laboratory Flows", Progress in fluid flow research: turbulence and applied MHD, Progress in Astronautics and Aeronautics, Vol. 182,1998, pp. 225-241.

[44] Lesieur, M., Comte, P., "Large Eddy Simulations of compressible Turbulent Flows", Turbulence in Compressible Flows, AGARD report No. 819, 1997.

[45] Sagaut, P., Introduction à la Simulation des Grandes Echelles pour les Ecoulements de Fluide Incompressible, Springer-Verlag Berlin, 1998.

[46] Hoffmann, K.A., Chiang, S.T., Computational Fluid Dynamics – Volume II, Engineering Education System, Third Edition, 1998.

[47] Baldwin, B.S., and Lomax, H., "Thin Layer Approximation and Algebraic Model for Separated Turbulent Flows", AIAA 78-257, January 1978.

[48] Baldwin, B.S., Barth, T.J., "A One-Equation Turbulent Transport Model for High Reynolds Number Wall-Bounded Flows", NASA TM 102847, August 1990.

[49] Edwards, J.R., Chandra, S., "Eddy-Viscosity Transport Turbulence Models for High Speed Two-Dimensional Shock-Separated Flowfields", AIAA 94-0310, January 1994.

[50] Spalart, P.R., and Allmaras, S.R., "A One-Equation Turbulence Model for Aerodynamic Flows", AIAA 92-0439, January 1992.

[51] Edwards, J.R., Chandra, S., "Comparison of Eddy-Viscosity Transport Turbulence Models for Three-Dimensional Shock-Separated Flowfields", AIAA Journal, Vol. 334, No. 4, April 1996, pp. 756-763.

[52] Jones, W.P., Launder, B.E., "The Calculation of Low-Reynolds-Number Phenomena with a Two-Equation Model of Turbulence", International Journal of Heat and Mass Transfer, Vol. 16, 1973, pp. 1119-1130.

[53] Kral, L.D., Mani, M., Ladd, J.A., "On the Application of Turbulence Models for Aerodynamic and Propulsion Flowfields", AIAA 96-0564, January 1996.

[54] Coakley, T.J., Huang, P.G., "Turbulence Modeling for High Speed Flows", AIAA 92-0436, January 1992.

[55] Wilcox, D.C., "More Advanced Applications of the Multiscale Models for Turbulent Flows", AIAA 88-0220, January 1988.

[56] Wilcox, D.C., "Supersonic Compression Corner Applications of a Multiscale Model for Turbulent Flows", AIAA Journal, Vol. 28, No. 7, pp. 1194-1198.

[57] Wilcox, D.C., "Progress in Hypersonic Turbulent Modeling", AIAA 91-1785, June 1991.

[58] Wilcox, D.C., "Dilatation-Dissipation Corrections for Advanced Turbulence Models", AIAA Journal, Vol. 30, No. 11, November 1992, pp. 2639-2646.

[59] Menter, F.R., "Influence of Freestream Values on $k-\omega$ Turbulence Models Predictions", AIAA Journal, Vol. 30, No. 6, June 1991, pp. 1657-1659.

[60] Menter, F.R., "Improved Two-Equation $k-\omega$ Models for Aerodynamic Flows", NASA TM-103975, October 1992.

[61] Menter, F.R., "Two-Equation Eddy-Viscosity Turbulence Models for Engineering Applications", AIAA Journal, Vol. 32, No. 8, August 1994, pp. 1598-1605.

[62] Menter, F.R., "Zonal Two-Equation $k - \omega$ Models for Aerodynamic Flows", AIAA 93-2906, 1993.

[63] Suzen, Y.B., Hoffmann, K.A., "Investigation of Supersonic Jet Exhaust Flow by One- and Two-Equation Turbulence Models", AIAA 98-0322, January 1998.

[64] Spalart, P.R., "Strategies for Turbulence modeling and Simulations", 4th Int. Symp. Eng. Turb. Modeling and Measurements, May 1999.

[65] Forsythe, J.R., "Numerical computation of Turbulent Separated Supersonic Flowfields", PhD Dissertation, Wichita State University, 2000.

[66] Resler, E. L. and Sears, W. R., "The Prospects for Magneto-Aerodynamics," Journal of the Aeronautical Sciences, Vol. 25, No. 4, 1958, pp. 235-245, 258.

[67] Resler, E. L. and Sears, W. R., "The Prospects for Magneto-Aerodynamics – Correction and Addition," Journal of the Aero/Space Sciences, Vol. 26, No. 5, 1959, p. 318.

[68] Bleviss, Z. O., "Magnetogasdynamics of Hypersonic Couette Flow," Journal of the Aero/Space Sciences, Vol. 25, No. 10, Oct. 1958, pp. 601-615.

[69] Bush, W. B., "Compressible Flat-Plate Boundary Layer Flow with an Applied Magnetic Field," Journal of the Aero/Space Sciences, Vol. 26, Jan. 1960, pp. 49-58.

[70] Chu, C. K. and Lynn, Y. M., "Steady Magnetohydrodynamic Flow Past a Nonconducting Wedge," AIAA Journal, Vol. 1, No. 5, May 1963, pp. 1062-1067.

[71] Mimura, Y., "Magnetohydrodynamic Flows Past a Wedge with Perpendicular Magnetic Field," AIAA Journal, Vol. 1, No. 10, Oct. 1963, pp. 2272-2279.

[72] Neuringer, J. L. and McIlroy, W., "Incompressible Two-Dimensional Stagnation-Point Flow of an Electrically Conducting Viscous Fluid in the Presence of a Magnetic Field," Journal of the Aeronautical Sciences, Vol. 25, No. 3, Mar. 1958, pp. 194-198.

[73] Neuringer, J. L. and McIlroy, W., "Hydromagnetic Effects on Stagnation-Point Heat Transfer," Journal of the Aeronautical Sciences, Vol. 25, No. 5, May 1958, pp. 332-334.

[74] Rossow, V. J., "Magnetohydrodynamic Analysis of Heat Transfer Near a Stagnation Point," Journal of the Aeronautical Sciences, Vol. 25, No. 5, May 1958, pp. 334-335.

[75] Meyer, R. C., "On Reducing Aerodynamic Heat-Transfer Rates by Magnetohydrodynamic Techniques," Journal of the Aero/Space Sciences, Vol. 25, No. 9, Sept. 1958, pp. 561-566, 572.

[76] Ziemer, R. W. and Bush, W. B., "Magnetic Field Effects on Bow Shock Stand-Off Distance, Space Technology Laboratory," Physical Review Letters, Vol. 1, No. 2, July 1958, pp. 58-59.

[77] Bush, W. B., "Magnetohydrodynamic-Hypersonic Flow Past a Blunt Body," Journal of the Aero/Space Sciences, Vol. 25, No. 11, Nov. 1958, pp. 685-690, 728.

[78] Kemp, N. H., "On Hypersonic Stagnation-Point Flow with a Magnetic Field," Journal of the Aeronautical Sciences, Vol. 25, No. 6, June 1958, pp. 405-407.

[79] Bush, W. B., "A Note on the Magnetohydrodynamic-Hypersonic Flow Past a Blunt Body," Journal of the Aero/Space Sciences, Vol. 26, No. 8, Aug. 1959, pp. 536-537.

[80] Wu, C.-S., "Hypersonic Viscous Flow Near the Stagnation Point in the Presence of Magnetic Field," Journal of the Aero/Space Sciences, Vol. 27, No. 12, Dec. 1960, pp. 882-893, 950.

[81] Levy, R. H., Gierasch P. J. and Henderson, D. G., "Hypersonic Magnetohydrodynamics With or Without a Blunt Body," AIAA Journal, Vol. 2, No. 12, 1964, pp. 2091-2099.

[82] Chen, S. Y., "Magnetic Hypersonic Flow near the Stagnation Point at Low Reynolds Number," Journal of Spacecraft and Rockets, Vol. 6, No. 8, Aug. 1969, pp. 872-877.

[83] Landshoff, R. K. M. (ed.), "Magnetohydrodynamics," Burgers, J., "Penetration of a Shock-wave into a Magnetic Field," pp. 36-56, Stanford University Press, Stanford, CA, 1957.

[84] Sakurai, T., "Two-Dimensional Hypersonic Flow of an Ideal Gas with Infinite Electric Conductivity Past a Two-Dimensional Magnetic Dipole," Journal of the Aero/Space Sciences, Vol. 26, No. 12, Dec. 1959, pp. 841-842.

[85] Romig, M. F., "The Influence of Electric and Magnetic Fields on Heat Transfer to Electrically Conducting Fluids," Advances in Heat Transfer, edited by Irvine, Jr, . F. and Hartnett, J. P., Vol. 1, Academic Press, New York, 1964, pp. 267-354.

[86] Palmer, G., "Magnetic Field Effects on the Computed Flow over a Mars Return Aerobrake," Journal of Thermophysics and Heat Transfer, Vol. 7, No. 2, Apr.-June 1993, pp. 294-301.

[87] Crawford, C.H., Karniadakis G. EM, "Reynolds Stress Analysis of EMHD-Controlled Wall Turbulence. Part I. Streamwise Forcing", Physics of Fluids, Vol. 9, No. 3, March 1997.

[88] Henoch C., Stace J., "Experimental Investigation of Salt Water Turbulent Boundary Layer Modified by an Applied Streamwise Magnetohydrodynamic Body Force", Physics of Fluids, Vol. 7, No. 6, June 1995.

[89] Mutshke G., Shatrov V., Gerbeth G., "Cylinder Wake Control by Magnetic Fields in Liquid Metal Flows", Experimental Thermal and Fluid Science, Vol. 16, 1998, pp. 92-99.

[90] Weier, T., Fey U., Gerbeth G., Mutschke G., Avilov V., "Boundary Layer Control by Means of Electromagnetic Forces". ERCOFTAC bulletin 44, 2000, pp. 36-40.

216

[91] Gaitonde D.V, Poggie J., "Simulation of MHD Flow Control Techniques", AIAA paper 2000-2326, Fluid 2000, June 2000.

[92] Brock, J.S., Ng, W.F., "The Baldwin-Lomax Model for Separated and Wake Flows Using an Entropy Envelope Concept", AIAA paper 92-0148, 30th Aerospace Sciences Meeting & Exhibit, Reno, NV, January 1992.

[93] Lykoudis, "Magneto Fluid Mechanics Channel Flow. I Experiment", The Physics of Fluids, Vol. 10, No. 5, May 1967, pp. 995-1001.

[94] Landrum, D. and Candler, G., "Vibration-Dissociation Coupling in Nonequilibrium Flows," AIAA Paper 91-0466, Jan. 1991.

[95] Park, C., "Assessment of Two-Temperature Kinetic Model for Ionized Air," Journal of Thermophysics and Heat Transfer, Vol. 3, No. 3, July 1989, pp. 233-244.

[96] Tannehill, J. C. and Mugge, P. H., "Improved Curve Fits for the Thermodynamic Properties of Equilibrium Air Suitable for Numerical Computation Using Time-Dependent or Shock Capturing Methods," NASA CR2470, 1974.

[97] Grossman, B. and Cinnella, P., "The Computation of Non-Equilibrium, Chemically- Reacting Flows," Computers and Structures, Vol. 30, No. 1/2, pp. 79-93, 1988.

[98] Candler, G. V. and MacCormack, R. W., "The Computation of Hypersonic Ionized Flows in Chemical and Thermal Nonequilibrium," AIAA Paper 88-0511, Jan. 1988.

[99] Gnoffo, P. A., Gupta, R. N. and Shinn, J. L., "Conservation Equations and Physical Models for Hypersonic Air Flows in Thermal and Chemical Nonequilibrium," NASA Report, TP-2867, Feb. 1989.

[100] Kerrebrock, J. L., "Nonequilibrium Ionization due to Electron Heating: I: Theory," AIAA Journal, Vol. 2, No. 6, pp. 1072-1080, June 1964.

[101] Munipalli, R., "CFD Evaluation of Seeded and Unseeded Air MHD Accelerators," AIAA Paper 2000-0215, Jan. 2000.

[102] Chiang, T. L., "Computation of Nonequilibrium Chemically Reacting Flows in Hypersonic Flow Field," Ph.D. Dissertation, University of Texas, Austin, May 1989.

[103] Park, C., "Convergence of Computation of Chemical Reacting Flows," Progress in Astronautics and Aeronautics: Thermophysical Aspects of Re-Entry Flows, Vol. 103, edited by Moss, J. N. and Scott, C. D., AIAA, New-York, 1986, pp. 478-513.

[104] Chiang, T. and Hoffmann, K. A., "Determination of Computational Time Step for Chemically Reacting Flows," AIAA Paper 89-1855, June 1989.

[105] Hoffmann, K. A., Chiang, S. T., Siddiqui, S., Papadakis, M., Fundamental Equations of Fluid Mechanics, EES, 1996.

217

[106] Settles, G.S., "An experimental Study of Compressible Turbulent Boundary Layer Separation at High Reynolds Numbers", PhD Dissertation, Princeton University, 1975.

[107] Settles, G.S., Vas, I.E., Bogdonoff, S.M., "Details of a Shock Separated Turbulent Boundary at a Compression Corner", AIAA Journal, Vol. 14, No. 12, December 1976, pp. 1709-1715.

[108] Ben Salah, N., Soulaimani, A., Habashi, W.G., Fortin, M, "A Conservative Stabilized Finite Element Method for the Magneto-Hydrodynamic Equations", International Journal for Numerical methods in Fluids, Vol. 29, 1999, pp. 535-554.

[109] Moreau, R., Magnetohydrodynamics, Dordrecht, 1990.

[110] Hughes, W.F., Young, F.J., The Electromagnetodynamics of Fluids, Wiley, 1966.

[111] Spalding, D.B., Chi, S.W, "The Drag of a Compressible Turbulent Boundary Layer on a Smooth Plate with and without Heat Transfer", Journal of Fluid Mechanics, Vol. 18, No. 1, 1964, pp. 117-143.

[112] Kalikhman, L.E., Elements of Magnetogasdynamics, Saunders, 1967.

[113] Eskinazi, S., Vector Mechanics of Fluids and MagnetoFluids, Academic Press, 1967.

[114] Dietiker, J.F., Hoffmann, K.A., "Numerical Simulation of Turbulent magnetohydrodynamic flows", AIAA paper 2001-2737, 32nd AIAA Plasmadynamics and laser Conference, June 2001.

[115] Fischer, M.C., "An Experimental Investigation of Boundary-Layer Transition on a 10° Half-Angle Cone at Mach 6.9", NASA TN D-5766, April 1970.

[116] Suzen, Y.B., and Hoffmann, K. A., "Performance study of Turbulence Models for Heat Transfer Predictions", AIAA paper 97-2568, 32nd Thermophysics Conference, June 1997.

[117] Siddiqui, M.S., Hoffmann, K.A., Chiang, S.T., and Ruthledge, W.H., "A Comparative study of the Navier-Stokes Solvers with Emphasis on the Heat Transfer Computations of High Speed Flows", AIAA 92-0835, January 1992.

[118] Coakley, J. F. and Porter, R. W., "Time-Dependent Numerical Analysis of MHD Blunt Body Problem," AIAA Journal, Vol. 9, No. 8, Aug. 1971, pp. 1624-1626.

[119] Poggie, J. and Gaitonde, D. V., "Computational Studies of Magnetic Control in Hypersonic Flow," AIAA Paper 2001-0196, Jan. 2001.

[120] Billig, F. S., "Shock-Wave Shapes around Spherical- and Cylindrical-Nosed Bodies," Journal of Spacecraft and Rockets, Vol. 4, No. 6, June 1967, pp.822-823.

[121] U.S. Standard Atmosphere, 1976, U.S. Government Printing Office, Washington, D.C., Oct. 1976.

[122] Gordon, S. and McBride, B. J., "Computer Program for Calculation of Complex Chemical Equilibrium Composition and Applications". Part I - Analysis, NASA RP-1311, NASA Lewis Research Center, Cleveland, OH, 1994.

[123] Palmer, H. B., "Chemical Kinetics and Hypersonic Flow," Fundamental Phenomena in Hypersonic Flow, edited by Hall, G. J., Cornell University Press, New York, 1966, pp. 175-190.

[124] Wray, K. L., "Prepared Comments," Fundamental Phenomena in Hypersonic Flow, edited by Hall, G. J., Cornell University Press, New York, 1966, pp. 190-194.

[125] Hypersonic and High Temperature Gas Dynamics, Anderson, J. D., McGraw-Hill Book Company, 1989.

Appendices

Appendix A
MHD Viscous Terms in Computational Space

The viscous flux vectors in the computational space are expressed as

$$\overline{E}_v = \frac{1}{J} \begin{bmatrix} 0 \\ \dfrac{\mu}{Re_\infty}\left(a_1 u_\xi + a_3 v_\xi + c_1 u_\eta + c_3 v_\eta\right) \\ \dfrac{\mu}{Re_\infty}\left(a_3 u_\xi + a_2 v_\xi + c_4 u_\eta + c_2 v_\eta\right) \\ \dfrac{\mu}{Re_\infty}\left(a_4 w_\xi + c_5 w_\eta\right) \\ \dfrac{1}{Re_{m\infty}\sigma_e}\left[a_4\left(B_x\right)_\xi + c_5\left(B_x\right)_\eta\right] \\ \dfrac{1}{Re_{m\infty}\sigma_e}\left[a_4\left(B_y\right)_\xi + c_5\left(B_y\right)_\eta\right] \\ \dfrac{1}{Re_{m\infty}\sigma_e}\left[a_4\left(B_z\right)_\xi + c_5\left(B_z\right)_\eta\right] \\ \dfrac{\mu}{Re_\infty}\left[\dfrac{1}{2}a_1\left(u^2\right)_\xi + \dfrac{1}{2}a_2\left(v^2\right)_\xi + \dfrac{1}{2}a_4\left(w^2\right)_\xi + a_3\left(uv\right)_\xi \right. \\ \left. + \dfrac{1}{Pr(\gamma-1)M_\infty^2}a_4 T_\xi + \dfrac{1}{2}c_1\left(u^2\right)_\eta + \dfrac{1}{2}c_2\left(v^2\right)_\eta \right. \\ \left. + \dfrac{1}{2}c_5\left(w^2\right)_\eta + c_3 uv_\eta + c_4 vu_\eta + \dfrac{1}{Pr(\gamma-1)M_\infty^2}c_5 T_\eta \right] \end{bmatrix} \qquad (A.1)$$

$$\overline{F}_v = \frac{1}{J} \begin{bmatrix} 0 \\ \dfrac{\mu}{Re_\infty}\left(b_1 u_\eta + b_3 v_\eta + c_1 u_\xi + c_4 v_\xi\right) \\ \dfrac{\mu}{Re_\infty}\left(b_3 u_\eta + b_2 v_\eta + c_3 u_\xi + c_2 v_\xi\right) \\ \dfrac{\mu}{Re_\infty}\left(b_4 w_\eta + c_5 w_\xi\right) \\ \dfrac{1}{Re_{m\infty}\sigma_e}\left[b_4 \left(B_x\right)_\eta + c_5 \left(B_x\right)_\xi\right] \\ \dfrac{1}{Re_{m\infty}\sigma_e}\left[b_4 \left(B_y\right)_\eta + c_5 \left(B_y\right)_\xi\right] \\ \dfrac{1}{Re_{m\infty}\sigma_e}\left[b_4 \left(B_z\right)_\eta + c_5 \left(B_z\right)_\xi\right] \\ \dfrac{\mu}{Re_\infty}\left[\dfrac{1}{2}b_1\left(u^2\right)_\eta + \dfrac{1}{2}b_2\left(v^2\right)_\eta + \dfrac{1}{2}b_4\left(w^2\right)_\eta + b_3\left(uv\right)_\eta\right. \\ + \dfrac{1}{Pr(\gamma-1)M_\infty^2}b_4 T_\eta + \dfrac{1}{2}c_1\left(u^2\right)_\xi + \dfrac{1}{2}c_2\left(v^2\right)_\xi \\ \left. + \dfrac{1}{2}c_5\left(w^2\right)_\xi + c_3 vu_\xi + c_4 uv_\xi + \dfrac{1}{Pr(\gamma-1)M_\infty^2}c_5 T_\xi\right] \end{bmatrix} \qquad (A.2)$$

where

$$a_1 = \frac{4}{3}\xi_x^2 + \xi_y^2 \qquad (A.3a) \qquad , \qquad a_2 = \xi_x^2 + \frac{4}{3}\xi_y^2 \qquad (A.3b)$$

$$a_3 = \frac{1}{3}\xi_x\xi_y \qquad (A.3c) \qquad , \qquad a_4 = \xi_x^2 + \xi_y^2 \qquad (A.3d)$$

$$b_1 = \frac{4}{3}\eta_x^2 + \eta_y^2 \qquad (A.4a) \qquad , \qquad b_2 = \eta_x^2 + \frac{4}{3}\eta_y^2 \qquad (A.4b)$$

$$b_3 = \frac{1}{3}\eta_x\eta_y \qquad (A.4c) \qquad , \qquad b_4 = \eta_x^2 + \eta_y^2 \qquad (A.4d)$$

$$c_1 = \frac{4}{3}\xi_x\eta_x + \xi_y\eta_y \quad \text{(A.5a)} \qquad , \qquad c_2 = \xi_x\eta_x + \frac{4}{3}\xi_y\eta_y \quad \text{(A.5b)}$$

$$c_3 = \xi_y\eta_x - \frac{2}{3}\xi_x\eta_y \quad \text{(A.5c)} \qquad , \qquad c_4 = \xi_x\eta_y - \frac{2}{3}\xi_y\eta_x \quad \text{(A.5d)}$$

$$c_5 = \xi_x\eta_x + \xi_y\eta_y \quad \text{(A.5e)}$$

The subscripts ξ and η represent differentiation with respect to this variable. For example $u_\xi = \dfrac{\partial u}{\partial \xi}$ and $u_\eta = \dfrac{\partial u}{\partial \eta}$. They are approximated by a second order central difference approximation

$$u_\xi = \frac{\partial u}{\partial \xi} \approx \frac{u_{i+1,j} - u_{i-1,j}}{2\Delta\xi} \qquad \qquad \text{(A.6a)}$$

$$u_\eta = \frac{\partial u}{\partial \eta} \approx \frac{u_{i,j+1} - u_{i,j-1}}{2\Delta\eta} \qquad \qquad \text{(A.6b)}$$

Appendix B
Electrical Conductivity of Selected Fluids

Fluid	Electrical conductivity σ_e $\left(\mathrm{mho}/m\right)$
Distilled water	$\approx 10^{-4}$
Sea water	4.0
Weak electrolytes	10^{-4} to 10^{-2}
Strong electrolytes	10^{-4} to 10^{-2}
Water + 20% Na Cl (20°C)	21.6
Pure H_2SO_4 (20°C)	73.6
Molten Glass (1400°C)	10 to 10^2
"Cold" Plasmas ($T \approx 10^4 K$)	$\approx 10^3$
"Hot" Plasmas ($T \approx 10^6 K$)	$\approx 10^6$
Totally ionized gas	$\approx 10^7 T^{3/2}$
Ionized hydrogen	$\approx 5.3 \times 10^4$
Interstellar space	$\approx 10^3$
Interplanetary space (solar wind)	$\approx 10^5$
Liquid metals	10^6 to 10^7
Steel (1500°C)	0.7×10^6
Mercury (20°C)	10^6
Aluminum (700°C)	5×10^6
Sodium (400°C)	6×10^6

Table B-1. Electrical conductivity of selected fluids.

Table B-1 shows the electrical conductivity for various fluids. Hot plasmas, referring to plasmas encountered in astrophysical applications or thermonuclear fusion, are very good conductors, but they cannot be fully described by the laws of fluid

mechanics. They do not satisfy the assumptions of thermodynamic equilibrium and a detailed description of the interaction between particles is required.

Cold plasmas are less conducting but can be described by fluid models. Since they are very light, the electromagnetic forces affect them in a similar fashion as liquid metals that have a higher conductivity but are much heavier.

Appendix C
Compressibility Correction Terms

The following table summarizes the compressibility correction terms available within the turbulence models.

Turbulence Model	Replace (from the original Model)	By (to obtain the modified version)	Comment	Objective
Baldwin-Barth	$y^+ = \dfrac{\rho_w u^+ y}{\mu_w}$	$y^+ = \dfrac{1}{v}\left[\dfrac{c_\mu(\tilde{v}\tilde{R}_t)}{\kappa} + \beta R_{e\infty}\|\vec{V}\|y\right]$		Prevent damping functions from approaching zero in the separation and reattachment regions
$k-\epsilon$	$\rho\epsilon$	$\rho\epsilon\left(1+\alpha M_t^2\right)$	$\alpha = 1.0$	Designed for shear layer flows
$k-\epsilon / k-\omega$	$\beta^* \rho\omega k$	$\beta^* \rho\omega k\left[1+\alpha_1 M_t^2(1-F_1)\right]$	In the k-equation	
	—	$\beta^* \alpha_1 M_t^2 \rho\omega^2\left(1-F_1\right)$	Added to the ω-equation	
Spalart-Allmaras	$S = \left\|\dfrac{\partial u}{\partial y} - \dfrac{\partial v}{\partial x}\right\|$	$S^2 = \left(\dfrac{\partial u_i}{\partial x_j} + \dfrac{\partial u_j}{\partial x_i}\right)\dfrac{\partial u_i}{\partial x_j} - \dfrac{2}{3}D^2$	$D = \dfrac{\partial u_k}{\partial x_k}$	Avoid numerical singularity near the wall
	$\tilde{S} = S + \dfrac{\tilde{v}}{\kappa^2 d^2}$	$\tilde{S} = \sqrt{S}\left(\dfrac{1}{\chi} + f_{v1}\right)$		
	$r = \tilde{v}/\left(\kappa^2 d^2 \tilde{S}\right)$	$r = \dfrac{\tanh\left(\tilde{v}/\left(\kappa^2 d^2 \tilde{S}\right)\right)}{\tanh(1.0)}$		
$k-\epsilon$	$c_{\epsilon 1} f_1 \epsilon\tau_{ij}\dfrac{\partial u_i}{\partial x_j}\dfrac{\epsilon}{k}$	$c_{\epsilon 1} f_1 \dfrac{\epsilon}{k}\mu_t S^2 - \alpha_\epsilon \rho\epsilon D$	$\alpha_\epsilon = 2.0$	Obtain a larger separation region
$k-\epsilon / k-\omega$	$\dfrac{\alpha\rho}{\mu_t}\tau_{ij}\dfrac{\partial u_i}{\partial x_j}$	$\alpha\rho S^2 - \alpha_\omega \rho\omega D$	$\alpha_\omega = \dfrac{4}{3}$	Obtain a larger separation region (only for the Baseline model)
$k-\epsilon / k-\omega$	—	$(1-F_1)\overline{p''d''}$	Added to the ϵ-equation	Designed for axisymmetric jet flows
	—	$-(1-F_1)\dfrac{\overline{p''d''}}{v_t}$	Added to the ω-equation	

Table C-1. Summary of the compressibility correction terms.

Appendix D
Calculation of the Shock Standoff Distance

In this appendix, the analytical calculation of the non-dimensional shock standoff distance obtained by Lykoudis [5] is reviewed. The procedure is used to calculate the ratio $\frac{\Delta s}{\Delta s_0}$, where Δs and Δs_0 are the nondimensional shock standoff distances with and without a magnetic field, respectively. The following assumptions are made:

The magnetic field is constant in the region between the shock and the body. It is perpendicular to the incoming streamlines.

The induced electric current is negligible.

The shock wave is cylindrical in shape.

The pressure is not altered by the magnetic field in the stagnation region.

A Newtonian pressure distribution with constant density is assumed.

The electrical conductivity is assumed constant.

Viscosity has little effect on the solution.

Under these assumptions, the cylindrical shock standoff distance, in presence of a magnetic field is given by

$$\Delta s = \frac{r_s - r_b}{r_s} = \frac{\varepsilon}{(1-P)^{(1-m)/2}(1-Q)^{(1+m)/2}} \int_P^1 \frac{dz}{(z-P)^{(1+m)/2}(z-Q)^{(1-m)/2}} \qquad (D.1)$$

where

$$P = \frac{-S\varepsilon + \sqrt{(S\varepsilon)^2 + 12\varepsilon}}{2} \qquad (D.2)$$

227

$$Q = \frac{-S\varepsilon - \sqrt{(S\varepsilon)^2 + 12\varepsilon}}{2}$$

(D.3)

$$m = \frac{-P - Q}{P - Q}$$

(D.4)

$$S = \frac{\sigma_e B^2 r}{\rho_\infty V_\infty}$$

(D.5)

$$\varepsilon = \frac{\rho_\infty}{\rho}$$

(D.6)

In the case where there is no magnetic field, the shock standoff distance reduces to

$$\Delta s_0 = \frac{r_0 - r_b}{r_0} = \frac{\varepsilon}{\sqrt{1 - 3\varepsilon}} \cosh^{-1}\left(\frac{1}{\sqrt{3\varepsilon}}\right)$$

(D.7)

where

r_0 is the shock radius of curvature in the non-magnetic case,

r is the shock radius of curvature in presence of magnetic field,

r_b is the blunt body radius.

Figure D-1 illustrates the standoff distance for two values of the density ratio across the shock.
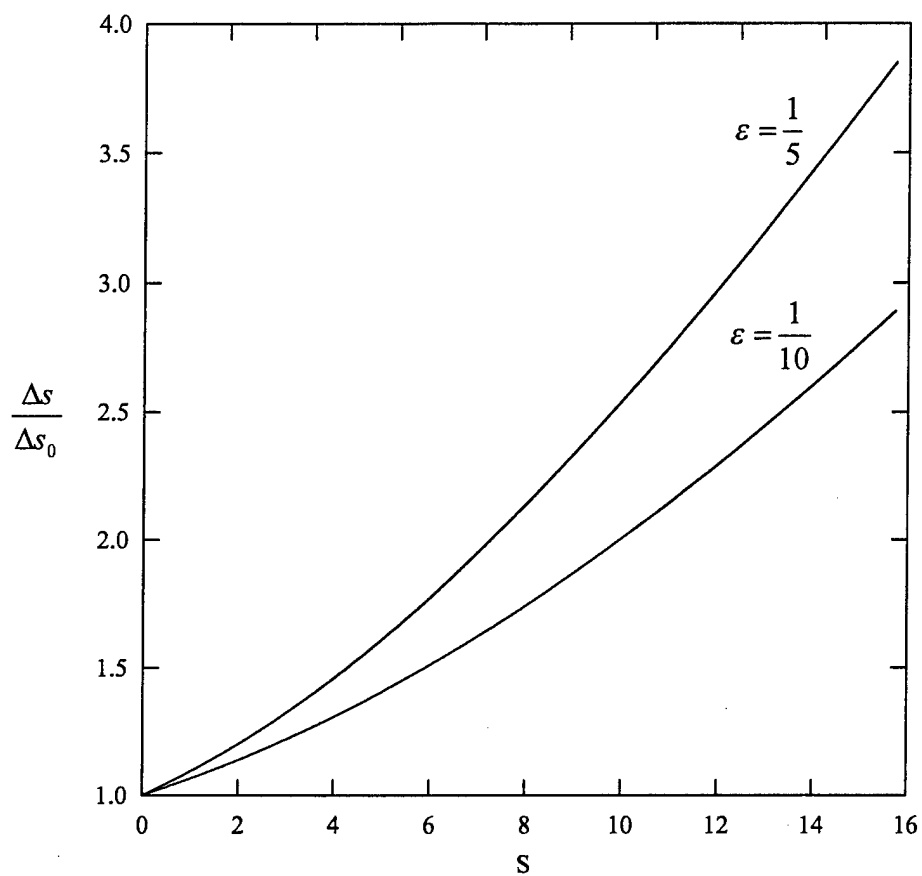
Figure D-1. Shock standoff distance for a cylindrical shock versus the parameter S.

Appendix E
Chemical DATA

The properties of the five species considered in the chemical model are specified in Table E-1.

Index s	1	2	3	4	5
Species	O_2	N_2	NO	O	N
M_s [g·mol^{-1}]	31.9988	28.0134	30.0061	15.9994	14.0067
$h_{0,s}$ [J·g^{-1}]	0	0	2.995×10^3	1.544×10^4	3.364×10^4
$\theta_{v,s}$ [K]	2275.2	3394.4	2740.7		

Table E-1. Properties of the chemical species.

Dimensional analysis shows that the units of the chemical rate constants are reaction dependent. To determine the dimensions of the rate constants of a given chemical reaction, the dimensions equations associated with the rate equations are written as shown in Table E-2. n, L and t denote the dimensions for the number of moles, length and time, respectively.

Rate equation	Associated dimensions equation
Forward rate $$\left.\frac{d[A_s]}{dt}\right|_f = \left(v_s^P - v_s^R\right) K_f \prod_{s=1}^{SM} [A_s]^{v_s^R}$$	$$n \cdot L^{-3} \cdot t^{-1} = K_f \left(n \cdot L^{-3}\right)^{\sum_{s=1}^{SM} v_s^R}$$
Backward (or reverse) rate $$\left.\frac{d[A_s]}{dt}\right|_b = \left(v_s^R - v_s^P\right) K_b \prod_{s=1}^{SM} [A_s]^{v_s^P}$$	$$n \cdot L^{-3} \cdot t^{-1} = K_b \left(n \cdot L^{-3}\right)^{\sum_{s=1}^{SM} v_s^P}$$

Table E-2. Dimensional analysis.

Thus, the dimensions of K_f, K_b and $K_e = K_f / K_b$ follow as

$$K_f : \left(n \cdot L^{-3}\right)^{-\alpha_f} \cdot t^{-1} \text{ with } \alpha_f = \sum_{s=1}^{SM} v_s^R - 1$$

$$K_b : \left(n \cdot L^{-3}\right)^{-\alpha_b} \cdot t^{-1} \text{ with } \alpha_b = \sum_{s=1}^{SM} v_s^P - 1$$

$$K_e : \left(n \cdot L^{-3}\right)^{\alpha_b - \alpha_f}$$

If international units are used, the CGS unit system is more suitable for chemistry than the MKS system. In the CGS system, units are as listed below.

$$n : [\text{mol}]$$
$$L : [\text{cm}]$$
$$t : [\text{s}]$$
$$K_f : \left[\left(\text{mol} \cdot \text{cm}^{-3}\right)^{-\alpha_f} \cdot \text{s}^{-1}\right]$$
$$K_b : \left[\left(\text{mol} \cdot \text{cm}^{-3}\right)^{-\alpha_b} \cdot \text{s}^{-1}\right]$$
$$K_e : \left[\left(\text{mol} \cdot \text{cm}^{-3}\right)^{\alpha_b - \alpha_f}\right]$$

Table F-2 provides the constants used in the chemical model, expressed in the CGS system.

Table E-3. Numerical constants used in calculation of chemical rates.

Chemical reaction	Reaction set r	Third body M	Forward rate Constant $K_{f,r}$ ($K_{f,r}$ units)	C units	α	e_a/k units	Backward rate Constant $K_{b,r}$ ($K_{b,r}$ units)	K_e units	Equilibrium rate Constant $K_{e,r}$ — A_1	A_2	A_3	A_4	A_5
$O_2+M \rightleftharpoons 2O+M$	1	N, O	cm³·mol⁻¹·s⁻¹	2.90^{23} cm³·mol⁻¹·s⁻¹·K²·⁰	-2.0	59750 K	cm⁶·mol⁻²·s⁻¹	cm⁻³·mol	2.855 ln(cm⁻³·mol)	0.988	-6.181	-0.023	-0.001
	2	N₂, O₂, NO	cm³·mol⁻¹·s⁻¹	9.68^{22} cm³·mol⁻¹·s⁻¹·K²·⁰			cm⁶·mol⁻²·s⁻¹	cm⁻³·mol					
$N_2+M \rightleftharpoons 2N+M$	3	N	cm³·mol⁻¹·s⁻¹	1.60^{22} cm³·mol⁻¹·s⁻¹·K¹·⁶	-1.6	113200 K	cm⁶·mol⁻²·s⁻¹	cm⁻³·mol	1.858 ln(cm⁻³·mol)	-1.325	-9.856	-0.174	0.008
	4	O	cm³·mol⁻¹·s⁻¹	4.98^{21} cm³·mol⁻¹·s⁻¹·K¹·⁶			cm⁶·mol⁻²·s⁻¹	cm⁻³·mol					
	5	N₂, O₂	cm³·mol⁻¹·s⁻¹	3.70^{21} cm³·mol⁻¹·s⁻¹·K¹·⁶			cm⁶·mol⁻²·s⁻¹	cm⁻³·mol					
	6	NO	cm³·mol⁻¹·s⁻¹	4.98^{21} cm³·mol⁻¹·s⁻¹·K¹·⁶			cm⁶·mol⁻²·s⁻¹	cm⁻³·mol					
$NO+M \rightleftharpoons N+O+M$	7	N, O, N₂, O₂, NO	cm³·mol⁻¹·s⁻¹	7.95^{23} cm³·mol⁻¹·s⁻¹·K²·⁰	-2.0	75500 K	cm⁶·mol⁻²·s⁻¹	cm⁻³·mol	0.792 ln(cm⁻³·mol)	-0.492	-6.761	-0.091	0.004
$NO+O \rightleftharpoons N+O_2$	8		cm³·mol⁻¹·s⁻¹	8.37^{12} cm³·mol⁻¹·s⁻¹	0.0	19450 K	cm³·mol⁻¹·s⁻¹		-2.063	-1.480	-0.580	-0.114	0.005
$O+N_2 \rightleftharpoons N+NO$	9		cm³·mol⁻¹·s⁻¹	6.44^{17} cm³·mol⁻¹·s⁻¹·K	-1.0	38370 K	cm³·mol⁻¹·s⁻¹		1.066	-0.833	-3.095	-0.084	0.004

Appendix F
Chemical Rate Equations

The rates of change of species concentration due to each chemical reaction are expressed as follows.

$O_2 + M \rightleftharpoons 2O + M$
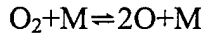
$$\frac{d[O_2]}{dt} = [O]^2 \{ K_{b,1}([N] + [O]) + K_{b,2}([N_2] + [O_2] + [NO]) \}$$
$$- [O_2] \{ K_{f,1}([N] + [O]) + K_{f,2}([N_2] + [O_2] + [NO]) \} \tag{F-1}$$
$$= R_1$$

$$\frac{d[O]}{dt} = -2R_1 \tag{F-2}$$

$N_2 + M \rightleftharpoons 2N + M$
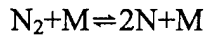
$$\frac{d[N_2]}{dt} = [N]^2 \{ K_{b,3}[N] + K_{b,4}[O] + K_{b,5}([N_2] + [O_2]) + K_{b,6}[NO] \}$$
$$- [N_2] \{ K_{f,3}[N] + K_{f,4}[O] + K_{f,5}([N_2] + [O_2]) + K_{f,6}[NO] \} \tag{F-3}$$
$$= R_2$$

$$\frac{d[N]}{dt} = -2R_2 \tag{F-4}$$

$NO + M \rightleftharpoons N + O + M$
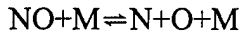
$$\frac{d[NO]}{dt} = \left(K_{b,7}[N][O] - K_{f,7}[NO] \right)\left([N] + [O] + [O_2] + [N_2] + [NO]\right) \tag{F-5}$$
$$= R_3$$

$$\frac{d[N]}{dt} = \frac{d[O]}{dt} = -R_3 \tag{F-6}$$

$NO + O \rightleftharpoons N + O_2$
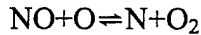
$$\frac{d[NO]}{dt} = \frac{d[O]}{dt} = K_{b,8}[N][O_2] - K_{f,8}[NO][O] = R_4 \tag{F-7}$$

$$\frac{d[N]}{dt} = \frac{d[O_2]}{dt} = -R_4 \tag{F-8}$$

$O + N_2 \rightleftharpoons N + NO$
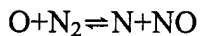
$$\frac{d[O]}{dt} = \frac{d[N_2]}{dt} = K_{b,9}[NO][N] - K_{f,9}[N_2][O] = R_5 \tag{F-9}$$

$$\frac{d[N]}{dt} = \frac{d[NO]}{dt} = -R_5 \tag{F-10}$$

The net changes of species concentration due to the five chemical reactions are

$$\frac{d[O_2]}{dt}\bigg|_{net} = R_1 - R_4 \tag{F-11}$$

$$\frac{d[N_2]}{dt}\bigg|_{net} = R_2 + R_5 \tag{F-12}$$

$$\frac{d[NO]}{dt}\bigg|_{net} = R_3 + R_4 - R_5 \tag{F-13}$$

$$\frac{d[O]}{dt}\bigg|_{net} = -2R_1 - R_3 + R_4 + R_5 \tag{F-14}$$

$$\frac{d[N]}{dt}\bigg|_{net} = -2R_2 - R_3 - R_4 - R_5 \tag{F-15}$$

The mass production rates are expressed as

$$\dot{w}_1 = \frac{d(\rho c_1)}{dt} = M_1 \frac{d[O_2]}{dt}\bigg|_{net} = M_1(R_1 - R_4) \tag{F-16}$$

$$\dot{w}_2 = \frac{d(\rho c_2)}{dt} = M_2 \frac{d[N_2]}{dt}\bigg|_{net} = M_2(R_2 + R_5) \tag{F-17}$$

$$\dot{w}_3 = \frac{d(\rho c_3)}{dt} = M_3 \frac{d[NO]}{dt}\bigg|_{net} = M_3(R_3 + R_4 - R_5) \tag{F-18}$$

$$\dot{w}_4 = \frac{d(\rho c_4)}{dt} = M_4 \frac{d[O]}{dt}\bigg|_{net} = M_4(-2R_1 - R_3 + R_4 + R_5) \tag{F-19}$$

$$\dot{w}_5 = \frac{d(\rho c_5)}{dt} = M_5 \frac{d[N]}{dt}\bigg|_{net} = M_5(-2R_2 - R_3 - R_4 - R_5) \tag{F-20}$$

Appendix G

Chemical Jacobian Matrix $\overline{\mathbf{D}}_c$

Jacobian matrix $\overline{\mathbf{D}}_c$ is defined as $\overline{\mathbf{D}}_c = \dfrac{\partial \overline{\dot{W}}}{\partial \overline{\mathbf{Q}}_c} = \dfrac{\partial \dot{W}}{\partial \mathbf{Q}_c}$. The elements $D_{s_i s_j}$ are expressed as

$$D_{s_i,s_j} = \frac{\partial \dot{w}_{s_i}}{\partial Q_{cs_j}} = \frac{1}{M_{s_j}} \frac{\partial \dot{w}_{s_i}}{\partial [\mathrm{A}_{s_j}]} \tag{G-1}$$

Thus,

$$D_{1,s_j} = \frac{M_1}{M_{s_j}} \frac{\partial}{\partial [\mathrm{A}_{s_j}]} (R_1 - R_4) \tag{G-2}$$

$$D_{2,s_j} = \frac{M_2}{M_{s_j}} \frac{\partial}{\partial [\mathrm{A}_{s_j}]} (R_2 + R_5) \tag{G-3}$$

$$D_{3,s_j} = \frac{M_3}{M_{s_j}} \frac{\partial}{\partial [\mathrm{A}_{s_j}]} (R_3 + R_4 - R_5) \tag{G-4}$$

$$D_{4,s_j} = \frac{M_4}{M_{s_j}} \frac{\partial}{\partial [\mathrm{A}_{s_j}]} (-2R_1 - R_3 + R_4 + R_5) \tag{G-5}$$

$$D_{5,s_j} = \frac{M_5}{M_{s_j}} \frac{\partial}{\partial [\mathrm{A}_{s_j}]} (-2R_2 - R_3 - R_4 - R_5) \tag{G-6}$$

where

$$\frac{\partial R_1}{\partial [\mathrm{A}_1]} = \frac{\partial R_1}{\partial [\mathrm{O}_2]} = K_{b,2}[\mathrm{O}]^2 - K_{f,1}([\mathrm{O}]+[\mathrm{N}]) - K_{f,2}(2[\mathrm{O}_2]+[\mathrm{N}_2]+[\mathrm{NO}]) \tag{G-7}$$

$$\frac{\partial R_1}{\partial [\mathrm{A}_2]} = \frac{\partial R_1}{\partial [\mathrm{N}_2]} = K_{b,2}[\mathrm{O}]^2 - K_{f,2}[\mathrm{O}_2] \tag{G-8}$$

$$\frac{\partial R_1}{\partial [\mathrm{A}_3]} = \frac{\partial R_1}{\partial [\mathrm{NO}]} = K_{b,2}[\mathrm{O}]^2 - K_{f,2}[\mathrm{O}_2] \tag{G-9}$$

$$\frac{\partial R_1}{\partial [\mathrm{A}_4]} = \frac{\partial R_1}{\partial [\mathrm{O}]} = 2[\mathrm{O}]\{K_{b,1}([\mathrm{O}]+[\mathrm{N}]) + K_{b,2}([\mathrm{O}_2]+[\mathrm{N}_2]+[\mathrm{NO}])\} + K_{b,1}[\mathrm{O}]^2 - K_{f,1}[\mathrm{O}_2] \tag{G-10}$$

$$\frac{\partial R_1}{\partial [\mathrm{A}_5]} = \frac{\partial R_1}{\partial [\mathrm{N}]} = K_{b,1}[\mathrm{O}]^2 - K_{f,1}[\mathrm{O}_2] \tag{G-11}$$

$$\frac{\partial R_2}{\partial [\mathrm{A}_1]} = \frac{\partial R_2}{\partial [\mathrm{O}_2]} = K_{b,5}[\mathrm{N}]^2 - K_{f,5}[\mathrm{N}_2] \tag{G-12}$$

$$\frac{\partial R_2}{\partial [\mathrm{A}_2]} = \frac{\partial R_2}{\partial [\mathrm{N}_2]} = K_{b,5}[\mathrm{N}]^2 - K_{f,3}[\mathrm{N}] - K_{f,4}[\mathrm{O}] - K_{f,5}([\mathrm{O}_2]+2[\mathrm{N}_2]) - K_{f,6}[\mathrm{NO}] \tag{G-13}$$

$$\frac{\partial R_2}{\partial [\mathrm{A}_3]} = \frac{\partial R_2}{\partial [\mathrm{NO}]} = K_{b,6}[\mathrm{N}]^2 - K_{f,6}[\mathrm{N}_2] \tag{G-14}$$

$$\frac{\partial R_2}{\partial [A_4]} = \frac{\partial R_2}{\partial [O]} = K_{b,4}[N]^2 - K_{f,4}[N_2] \tag{G-15}$$

$$\frac{\partial R_2}{\partial [A_5]} = \frac{\partial R_2}{\partial [N]} = 2[N]\{K_{b,3}[N] + K_{b,4}[O] + K_{b,5}([O_2]+[N_2]) + K_{b,6}[NO]\}$$
$$+ K_{b,3}[N]^2 - K_{f,3}[N_2] \tag{G-16}$$

$$\frac{\partial R_3}{\partial [A_1]} = \frac{\partial R_3}{\partial [O_2]} = K_{b,7}[O][N] - K_{f,7}[NO] \tag{G-17}$$

$$\frac{\partial R_3}{\partial [A_2]} = \frac{\partial R_3}{\partial [N_2]} = K_{b,7}[O][N] - K_{f,7}[NO] \tag{G-18}$$

$$\frac{\partial R_3}{\partial [A_3]} = \frac{\partial R_3}{\partial [NO]} = K_{b,7}[O][N] - K_{f,7}([O_2]+[N_2]+2[NO]+[O]+[N]) \tag{G-19}$$

$$\frac{\partial R_3}{\partial [A_4]} = \frac{\partial R_3}{\partial [O]} = K_{b,7}[N]([O_2]+[N_2]+[NO]+2[O]+[N]) - K_{f,7}[NO] \tag{G-20}$$

$$\frac{\partial R_3}{\partial [A_5]} = \frac{\partial R_3}{\partial [N]} = K_{b,7}[O]([O_2]+[N_2]+[NO]+[O]+2[N]) - K_{f,7}[NO] \tag{G-21}$$

$$\frac{\partial R_4}{\partial [A_1]} = \frac{\partial R_4}{\partial [O_2]} = K_{b,8}[N] \tag{G-22}$$

$$\frac{\partial R_4}{\partial [A_2]} = \frac{\partial R_4}{\partial [N_2]} = 0 \tag{G-23}$$

$$\frac{\partial R_4}{\partial [A_3]} = \frac{\partial R_4}{\partial [NO]} = -K_{f,8}[O] \tag{G-24}$$

$$\frac{\partial R_4}{\partial [A_4]} = \frac{\partial R_4}{\partial [O]} = -K_{f,8}[NO] \tag{G-25}$$

$$\frac{\partial R_4}{\partial [A_5]} = \frac{\partial R_4}{\partial [N]} = K_{b,8}[O_2] \tag{G-26}$$

$$\frac{\partial R_5}{\partial [A_1]} = \frac{\partial R_5}{\partial [O_2]} = 0 \tag{G-27}$$

$$\frac{\partial R_5}{\partial [A_2]} = \frac{\partial R_5}{\partial [N_2]} = -K_{f,9}[O] \tag{G-28}$$

$$\frac{\partial R_5}{\partial [A_3]} = \frac{\partial R_5}{\partial [NO]} = K_{b,9}[N] \tag{G-29}$$

$$\frac{\partial R_5}{\partial [A_4]} = \frac{\partial R_5}{\partial [O]} = -K_{f,9}[N_2] \tag{G-30}$$

$$\frac{\partial R_5}{\partial [A_5]} = \frac{\partial R_5}{\partial [N]} = K_{b,9}[NO] \tag{G-31}$$

Appendix H
Flux-Splitting for 2-D Chemistry Equations

Due to the good stability of implicit numerical methods, an implicit finite difference formulation is applied as follows.

$$\frac{\overline{Q}_c^{n+1} - \overline{Q}_c^n}{\Delta t_c} + \left(\frac{\partial \overline{E}_c}{\partial \xi}\right)^{n+1} + \left(\frac{\partial \overline{F}_c}{\partial \eta}\right)^{n+1} - \overline{W}_c^{n+1} = 0 \tag{H-1}$$

The time derivative is approximated by a first-order backward finite difference. The remaining terms in the equation are expressed at the $n+1$ time level. The change in the unknown vector $\overline{Q}_c$ per time step is

$$\Delta \overline{Q}_c = \overline{Q}_c^{n+1} - \overline{Q}_c^n \tag{H-2}$$

A finite difference formulation in terms of $\Delta \overline{Q}_c$ (known as the delta formulation) is considered. In the implicit formulation, the nonlinear terms given by the flux vectors $\overline{E}_c$, $\overline{F}_c$ and $\overline{W}_c$ are at the unknown time level. Thus, a linearization is required. From Taylor series expansion about time level n,

$$\overline{E}_c^{n+1} = \overline{E}_c^n + \left(\frac{\partial \overline{E}_c}{\partial t_c}\right)^n \Delta t_c + O(\Delta t_c)^2 \tag{H-3}$$

Using the definition of flux Jacobian matrix $\overline{A}_c$,

$$\overline{E}_c^{n+1} = \overline{E}_c^n + \overline{A}_c^n \frac{\partial \overline{Q}_c}{\partial t_c} \Delta t_c + O(\Delta t_c)^2 \tag{H-4}$$

Considering the approximation, $\dfrac{\partial \overline{Q}_c}{\partial t_c} \approx \dfrac{\Delta \overline{Q}_c}{\Delta t_c}$, one obtains

$$\overline{E}_c^{n+1} = \overline{E}_c^n + \overline{A}_c^n \Delta \overline{Q}_c + O(\Delta t_c)^2 \tag{H-5}$$

Likewise,

$$\overline{F}_c^{\,n+1} = \overline{F}_c^{\,n} + \overline{B}_c^{\,n} \Delta \overline{Q}_c + O(\Delta t_c)^2 \qquad \text{(H-6)}$$

and

$$\overline{\dot{W}}_c^{\,n+1} = \overline{\dot{W}}_c^{\,n} + \overline{D}_c^{\,n} \Delta \overline{Q}_c + O(\Delta t_c)^2 \qquad \text{(H-7)}$$

Substitution of these expressions into the finite difference Equation (H-4) yields

$$\Delta \overline{Q}_c + \Delta t_c \left[\frac{\partial \left(\overline{A}_c^{\,n} \Delta \overline{Q}_c \right)}{\partial \xi} + \frac{\partial \left(\overline{B}_c^{\,n} \Delta \overline{Q}_c \right)}{\partial \eta} - \overline{D}_c^{\,n} \Delta \overline{Q}_c \right] = -\Delta t_c \left(\frac{\partial \overline{E}_c^{\,n}}{\partial \xi} + \frac{\partial \overline{F}_c^{\,n}}{\partial \eta} - \overline{\dot{W}}_c^{\,n} \right) \qquad \text{(H-8)}$$

In the flux-vector splitting method, the flux vectors $\overline{E}_c$, $\overline{F}_c$ and the flux Jacobian matrices $\overline{A}_c$, $\overline{B}_c$ are split according to the sign of their respective eigenvalues. Jacobian matrices $\overline{A}_c$ and $\overline{B}_c$ admit the multiple eigenvalues $\lambda_{c\xi} = \overline{U}$, $\lambda_{c\eta} = \overline{V}$, respectively. The splitting process is as follows.

$$\begin{cases} \lambda_{c\xi} \geq 0 \Rightarrow \begin{cases} \overline{A}_c^+ = \overline{A}_c & \overline{A}_c^- = 0 \\ \overline{E}_c^+ = \overline{E}_c & \overline{E}_c^- = 0 \end{cases} \\ \lambda_{c\xi} < 0 \Rightarrow \begin{cases} \overline{A}_c^+ = 0 & \overline{A}_c^- = \overline{A}_c \\ \overline{E}_c^+ = 0 & \overline{E}_c^- = \overline{E}_c \end{cases} \end{cases}, \qquad \text{(H-9)}$$

$$\begin{cases} \lambda_{c\eta} \geq 0 \Rightarrow \begin{cases} \overline{B}_c^+ = \overline{B}_c & \overline{B}_c^- = 0 \\ \overline{F}_c^+ = \overline{F}_c & \overline{F}_c^- = 0 \end{cases} \\ \lambda_{c\eta} < 0 \Rightarrow \begin{cases} \overline{B}_c^+ = 0 & \overline{B}_c^- = \overline{B}_c \\ \overline{F}_c^+ = 0 & \overline{F}_c^- = \overline{F}_c \end{cases} \end{cases}, \qquad \text{(H-10)}$$

The flux-split form of Equation (H-8) is

$$\Delta \overline{Q}_c + \Delta t_c \left\{ \frac{\partial}{\partial \xi} \left[\left(\overline{A}_c^+ + \overline{A}_c^- \right)^n \Delta \overline{Q}_c \right] + \frac{\partial}{\partial \eta} \left[\left(\overline{B}_c^+ + \overline{B}_c^- \right)^n \Delta \overline{Q}_c \right] - \overline{D}_c^{\,n} \Delta \overline{Q}_c \right\}$$

$$= -\Delta t_c \left[\frac{\partial}{\partial \xi} \left(\overline{E}_c^+ + \overline{E}_c^- \right)^n + \frac{\partial}{\partial \eta} \left(\overline{F}_c^+ + \overline{F}_c^- \right)^n - \overline{\dot{W}}_c^{\,n} \right] \qquad \text{(H-11)}$$

238

The space derivatives corresponding to the positive (negative) terms are approximated by a backward (forward) difference. If first-order approximations are used, the following finite difference equation is obtained.

$$\forall i \in \{2, IM - 1\}, \; \forall j \in \{2, JM - 1\},$$

$$
\begin{aligned}
&CAM_{i,j} \, \Delta\overline{Q}_{ci-1,j} + CAP_{i,j} \, \Delta\overline{Q}_{ci+1,j} \\
&+ CBM_{i,j} \, \Delta\overline{Q}_{ci,j-1} + CBP_{i,j} \, \Delta\overline{Q}_{ci,j+1} \\
&+ \left[I + \frac{\Delta t_c}{\Delta \xi} \left(\overline{A}^+_{c\,i,j} - \overline{A}^-_{c\,i,j} \right)^n + \frac{\Delta t_c}{\Delta \eta} \left(\overline{B}^+_{c\,i,j} - \overline{B}^-_{c\,i,j} \right)^n - \Delta t_c \overline{D}^n_{c\,i,j} \right] \Delta\overline{Q}_{ci,j} \\
&= RHS_{i,j}
\end{aligned}
\tag{H-12}
$$

where

$$CAM_{i,j} = -\frac{\Delta t_c}{\Delta \xi} \left(\overline{A}^+_{c\,i-1,j} \right)^n \tag{H-13a}$$

$$CAP_{i,j} = \frac{\Delta t_c}{\Delta \xi} \left(\overline{A}^-_{c\,i+1,j} \right)^n \tag{H-13b}$$

$$CBM_{i,j} = -\frac{\Delta t_c}{\Delta \eta} \left(\overline{B}^+_{c\,i,j-1} \right)^n \tag{H-13c}$$

$$CBP_{i,j} = \frac{\Delta t_c}{\Delta \eta} \left(\overline{B}^-_{c\,i,j+1} \right)^n \tag{H-13d}$$

$$
\begin{aligned}
RHS_{i,j} = &-\left[\frac{\Delta t_c}{\Delta \xi} \left(\overline{E}^+_{c\,i,j} - \overline{E}^+_{c\,i-1,j} + \overline{E}^-_{c\,i+1,j} - \overline{E}^-_{c\,i,j} \right)^n \right. \\
&\left. + \frac{\Delta t_c}{\Delta \eta} \left(\overline{F}^+_{c\,i,j} - \overline{F}^+_{c\,i,j-1} + \overline{F}^-_{c\,i,j+1} - \overline{F}^-_{c\,i,j} \right)^n - \Delta t_c \overline{W}^n_{c\,i,j} \right]
\end{aligned}
\tag{H-13e}
$$

This implicit formulation for a two-dimensional configuration results in a pentadiagonal coefficient matrix. The solution of such a system is computationally time consuming. In order to alleviate this problem, an approximate factorization is introduced so as to reduce the pentadiagonal matrix system into two tridiagonal matrix systems for which efficient solution procedures exist. The equations are thus solved in two steps as follows.

$$\forall i \in \{2, IM-1\}, \quad \forall j \in \{2, JM-1\},$$

$$CBM_{i,j} \Delta \overline{Q}'_{ci,j-1} + CB_{i,j} \Delta \overline{Q}'_{ci,j} + CBP_{i,j} \Delta \overline{Q}'_{ci,j+1} = RHS_{i,j} \qquad \text{(H-14)}$$

$$CAM_{i,j} \Delta \overline{Q}_{ci-1,j} + CA_{i,j} \Delta \overline{Q}_{ci,j} + CAP_{i,j} \Delta \overline{Q}_{ci+1,j} = \Delta \overline{Q}'_{ci,j} \qquad \text{(H-15)}$$

where

$$CA_{i,j} = I + \frac{\Delta t_c}{\Delta \xi} \left(\overline{A}^+_{c\,i,j} - \overline{A}^-_{c\,i,j} \right)^n \qquad \text{(H-16a)}$$

$$CB_{i,j} = I + \frac{\Delta t_c}{\Delta \eta} \left(\overline{B}^+_{c\,i,j} - \overline{B}^-_{c\,i,j} \right)^n - \Delta t_c \overline{D}^n_{c\,i,j} \qquad \text{(H-16b)}$$

Given $RHS_{i,j}$, Equation (H-14) can be solved for $\Delta \overline{Q}'_{ci,j}$. This provides the right hand side of Equation (H-15), which is then solved for $\Delta \overline{Q}_{ci,j}$. The required boundary conditions for the blunt-body grid system are expressed as follows.

At the solid surface ($j = 1$) zero-order extrapolation leads to

$$\Delta \overline{Q}'_{ci,1} = \Delta \overline{Q}'_{ci,2} \qquad \text{(H-17a)}$$

Application of the freestream conditions ($j = JM$) yields

$$\Delta \overline{Q}'_{ci,JM} = 0 \qquad \text{(H-17b)}$$

After application of the boundary conditions (H-17a) and (H-17b), Equation (H-14) is written in matrix form as

$$\forall i \in \{2, IM-1\}$$

$$
\begin{bmatrix}
CBM_{i,2} + CB_{i,2} & CBP_{i,2} & 0 & \cdots & & 0 \\
CBM_{i,3} & CB_{i,3} & \ddots & \ddots & & \vdots \\
0 & CBM_{i,4} & \ddots & CBP_{i,JM-3} & & 0 \\
\vdots & & \ddots & \ddots & CB_{i,JM-2} & CBP_{i,JM-2} \\
0 & & \cdots & 0 & CBM_{i,JM-1} & CB_{i,JM-1}
\end{bmatrix}
\begin{bmatrix}
\Delta \overline{Q}'_{ci,2} \\
\Delta \overline{Q}'_{ci,3} \\
\vdots \\
\Delta \overline{Q}'_{ci,JM-2} \\
\Delta \overline{Q}'_{ci,JM-1}
\end{bmatrix}
$$

$$
=
\begin{bmatrix}
RHS_{i,2} \\
RHS_{i,3} \\
\vdots \\
RHS_{i,JM-2} \\
RHS_{i,JM-1}
\end{bmatrix}
\tag{H-18}
$$

Subsequently, Equation (H-15) is expressed in a matrix form as

$$\forall j \in \{2, JM-1\},$$

$$
\begin{bmatrix}
CAM_{2,j} + CA_{2,j} & CAP_{2,j} & 0 & \cdots & & 0 \\
CAM_{3,j} & CA_{3,j} & \ddots & \ddots & & \vdots \\
0 & CAM_{4,j} & \ddots & CAP_{IM-3,j} & & 0 \\
\vdots & & \ddots & \ddots & CA_{IM-2,j} & CAP_{IM-2,j} \\
0 & & \cdots & 0 & CAM_{IM-1,j} & CA_{IM-1,j}
\end{bmatrix}
\begin{bmatrix}
\Delta \overline{Q}_{c2,j} \\
\Delta \overline{Q}_{c3,j} \\
\vdots \\
\Delta \overline{Q}_{cIM-2,j} \\
\Delta \overline{Q}_{cIM-1,j}
\end{bmatrix}
$$

$$
=
\begin{bmatrix}
\Delta \overline{Q}'_{c2,j} \\
\Delta \overline{Q}'_{c3,j} \\
\vdots \\
\Delta \overline{Q}'_{cIM-2,j} \\
\Delta \overline{Q}'_{cIM-1,j}
\end{bmatrix}
\tag{H-19}
$$

When Equation (H-8) is applied on the body surface, the flux-splitting method is still valid for the ξ-derivatives. However, for the η-derivatives, one-sided differences must be used. If second-order approximations are used, the following finite difference equation is obtained.

$\forall j \in \{2, JM-1\}$,

$$\Delta \overline{Q}_{ci,1} + \frac{\Delta t_c}{\Delta \xi}\left(\overline{A}^+_{c\,i,1}\,\Delta \overline{Q}_{ci,1} - \overline{A}^+_{c\,i-1,1}\,\Delta \overline{Q}_{ci-1,1}\right.$$

$$\left. + \overline{A}^-_{c\,i+1,1}\,\Delta \overline{Q}_{ci+1,1} - \overline{A}^-_{c\,i,1}\,\Delta \overline{Q}_{ci,1}\right)^n - \Delta t_c \overline{D}^n_{c\,i,1}\,\Delta \overline{Q}_{ci,1}$$

$$= -\left[\frac{\Delta t_c}{\Delta \xi}\left(\overline{E}^+_{c\,i,1} - \overline{E}^+_{c\,i-1,1} + \overline{E}^-_{c\,i+1,1} - \overline{E}^-_{c\,i,1}\right)^n\right. \tag{H-20}$$

$$\left. + \frac{\Delta t_c}{2\Delta \eta}\left(-3\overline{F}_{ci,1} + 4\overline{F}_{ci,2} - \overline{F}_{ci,3}\right)^{n+1} - \Delta t_c \overline{\overline{W}}^{n+1}_{c\,i,1}\right]$$

Note that, for a non-porous solid surface,

$$\overline{V} = \eta_x u + \eta_y v = 0 \Rightarrow \overline{F}_{ci,1} = 0 \tag{H-21}$$

For the sake of simplicity, the following auxiliary variables are introduced.

$$CAM_{i,1} = -\frac{\Delta t_c}{\Delta \xi}\left(\overline{A}^+_{c\,i-1,1}\right)^n \tag{H-22a}$$

$$CAP_{i,1} = \frac{\Delta t_c}{\Delta \xi}\left(\overline{A}^-_{c\,i+1,1}\right)^n \tag{H-22b}$$

$$CA_{i,1} = \mathbf{I} + \frac{\Delta t_c}{\Delta \eta}\left(\overline{A}^+_{c\,i,1} - \overline{A}^-_{c\,i,1}\right)^n - \Delta t_c \overline{D}^n_{c\,i,1} \tag{H-22c}$$

$$RHS_{i,1} = -\left[\frac{\Delta t_c}{\Delta \xi}\left(\overline{E}^+_{c\,i,1} - \overline{E}^+_{c\,i-1,1} + \overline{E}^-_{c\,i+1,1} - \overline{E}^-_{c\,i,1}\right)^n\right.$$

$$\left. + \frac{\Delta t_c}{2\Delta \eta}\left(\overline{F}_{ci,3} - 4\overline{F}_{ci,2}\right)^{n+1} - \Delta t_c \overline{\overline{W}}^n_{c\,i,1}\right] \tag{H-22d}$$

With the assumptions

$$\Delta \overline{Q}_{c1,1} = \Delta \overline{Q}_{c2,1} \tag{H-23a}, \qquad \Delta \overline{Q}_{cIM,1} = \Delta \overline{Q}_{cIMM1,1} \tag{H-23b}$$

the following block tridiagonal system is obtained.

$$
\begin{bmatrix}
CAM_{2,1}+CA_{2,1} & CAP_{2,1} & 0 & \cdots & & 0 \\
CAM_{3,1} & CA_{3,1} & \ddots & \ddots & & \vdots \\
0 & CAM_{4,1} & \ddots & CAP_{IM-3,1} & & 0 \\
\vdots & \ddots & \ddots & CA_{IM-2,1} & & CAP_{IM-2,1} \\
0 & \cdots & 0 & CAM_{IM-1,1} & & CA_{IM-1,1}+CAP_{IM-1,1}
\end{bmatrix}
\begin{bmatrix}
\Delta \overline{Q}_{c2,1} \\
\Delta \overline{Q}_{c3,1} \\
\vdots \\
\Delta \overline{Q}_{cIM-2,1} \\
\Delta \overline{Q}_{cIM-1,1}
\end{bmatrix}
\quad \text{(H-24)}
$$

$$
=
\begin{bmatrix}
RHS_{2,1} \\
RHS_{3,1} \\
\vdots \\
RHS_{IM-2,1} \\
RHS_{IM-1,1}
\end{bmatrix}
$$